The use of Terrestrial Laser Scanning in characterizing active tectonic processes from postseismic slip to the long term growth of normal faults

WILKINSON, MAXWELL

Department of Earth Sciences, University of Durham

The use of Terrestrial Laser Scanning in characterizing active tectonic processes from postseismic slip to the long term growth of normal faults

A thesis submitted to the University of Durham

for the degree of Doctor of Philosophy in the

Faculty of Science

Maxwell Wilkinson

2012

Abstract

This thesis investigates two main hypotheses regarding uncertainty in the measurement of paleoseismic offsets used to estimate fault activity and paleoearthquake magnitudes on normal faults: (1) That variations in fault geometry have a significant effect on throw-rates and fault offsets; and (2) that postseismic deformation can be a significant component of the total fault slip for moderate magnitude earthquakes.

These hypotheses are tested using high resolution terrestrial laser scan datasets of normal fault topographic offsets and surface ruptures. The first hypothesis is addressed by studying the crustal scale Campo Felice active normal fault in the Central Apennines, Italy. Variation in throw-rate along strike since the last glacial maximum (15 ka ±3) is measured from an offset periglacial surface at two hundred and fifty sites using cross sectional data derived from a high resolution terrestrial laser scan (TLS) dataset. The measurements are used to create a detailed throw-rate profile. Field measurements of fault geometry (strike, dip and kinematic slip direction) are also gathered. Variation in fault throw-rate is found to correlate with fault strike. A study of weathered band thickness on the exposed Miocene limestone bedrock fault scarp, thought to have been created by single past slip events on the fault also appears to correlate with fault strike. A strain-rate profile is calculated using the throw-rate profile and the field measurements of kinematic slip. In contrast to throw-rate, strain-rate is independant of changes in fault strike and dip. It is suggested that strain-rate in comparison to throw-rate provides a more robust measure of fault activity as it is unaffected by changes in fault geometry. The outcome of this study is that paleoseismic studies on active faults should take into account fault geometry before

choosing sites which may have anomalously high or low paleoseismic offsets. Fault geometry introduces significant uncertainty into the estimation of inferred paleoearthquake magnitudes from paleoseismic offsets and hence seismic hazard analysis.

The second hypothesis is addressed through the study of near-field postseismic deformation (surface rupture afterslip) following the 6th April 2009 6.3 Mw L'Aquila earthquake, created by slip on the Paganica normal fault in the Central Italian Apennines. A novel use of TLS technology allowed the postseismic deformation at four sites along the L'Aquila surface rupture to be measured between 8 – 126 days after the earthquake. Complimentary measurements of postseismic deformation at a fifth site using a robotic total station were combined with the TLS datasets to describe the along strike variation in postseismic deformation. The near-field postseismic deformation measured occurred mostly in the immediate hangingwall of the surface rupture and increased with decreasing rate over time. The postseismic deformation measured is comparable to theoretical and empirical models which have been used to describe afterslip for previous earthquakes. The magnitude of near-field postseismic deformation was up to 60% that of the coseismic offset in the near-field and suggests that postseismic deformation can form a significant component of paleoseismic offsets of moderate magnitude. Postseismic deformation was also found to be greatest above regions of the fault zone where a high coseismic slip gradient existed, suggesting that postseismic deformation occurs at the periphery of the coseismic slip patch within the fault zone.

Regression relationships which relate surface offset to moment magnitude are populated by field observations of surface offsets where earthquake magnitude is known. These regression relationships are then used to infer paleoearthquake

magnitudes from paleoseismic offsets. The field studies used to populate regression relationships do not routinely take into account the potential effects of fault geometry and significant postseismic slip. As a result paleoearthquake magnitudes inferred from such regression relationships are maybe over estimated. It is suggested that future regression relationships of surface offset and moment magnitude should factor in the effects of fault geometry and postseismic deformation in order to produce a relationship in which surface offset (both coseismic and postseismic) is described for a range of magnitudes and, where possible, any local effects of fault geometry are removed from the input dataset. The production of such a relationship will allow paleoseismologists to measure combined coseismic and postseismic offsets from field studies and to infer paleoearthquake magnitude with decreased uncertainty.

Table of Contents

List of Figures

Chapter 4

Chapter 5

Chapter 6

List of Tables

Chapter 5

Acknowledgements

I would like to thank my supervisors, Ken McCaffrey, Gerald Roberts and Patience Cowie for their direction, support and advice during this research. It is they who have enabled me to make the most of this opportunity and I greatly appreciate their willingness to include me in discussions relating to their wider research. In addition to my supervisors, Richard Jones is thanked for a series of brief, but insightful discussions on the inner workings of terrestrial laser scanners and appropriate point cloud meshing algorithms. Jeroen van Hunen and Richard Hobbs are thanked for initial discussions on how the code for the program *Crossint* could be designed. I would like to thank Dave Stevenson and Gary Wilkinson for maintaining computing support, in particular with regard to providing access to a 64-bit workstation. Those who assisted me in the field following the L'Aquila earthquake, including Richard Phillips, Nicola de Paola, Alessandro Michetti, Eutizio Vittori, Luca Guerrieri, Anna Maria Blumetti, Adam Yates and Giancanio Sileo are thanked for their patience, level headedness and commitment. Mauro Degasperi of the Geological Survey of Trento is also thanked for providing access to a dataset of total station measurements following the L'Aquila earthquake. This data enriched the subsequent study of postseismic deformation. I would like to thank the Durham Doctoral Fellowship selection committee for their decision to provide stipend funding for my period of study. I hope I have returned the favour by enhancing academic research within the Department of Earth Sciences. Finally, I would like to thank my parents, close friends and family and my partner Alodie Bubeck for their encouragement and support, and for distracting me away from my work once in awhile!

Declaration

No part of this thesis has previously been submitted for a degree at this or any other university. The work described in this thesis is entirely that of the author, except where reference is made to previously published or unpublished work.

Maxwell Wilkinson

University of Durham

Department of Earth Sciences

February 2012

Chapter 1: Introduction

Empirical relationships between fault length, surface offset and earthquake magnitude have been established [Wells & Coppersmith, 1994] and are widely used to infer paleoearthquake magnitudes from measurement of discrete offsets on faults cutting datable sediments. These paleoearthquake magnitudes are in turn used as an input for seismic hazard analysis. The Wells & Coppersmith statistical dataset has been compiled from data of fault length and surface offset obtained from field studies of recent earthquakes, where the magnitude is known.

This thesis investigates two main hypotheses which could create uncertainty in the measurement of paleoseismic offsets used to estimate fault activity and paleoearthquake magnitudes:

1. That variation in fault geometry has a significant effect on throw-rates and fault offsets.

A study of changes in throw-rates across breached relay zones [e.g. Faure Walker et al., 2009] suggested that the throw-rate can change around a breached relay zone given a constant slip direction along the entire fault. It is proposed that changes in fault geometry (dip, strike and kinematic slip direction) will affect fault throw-rates (fig. 1.0) and in turn paleoearthquake offsets, as throw-rates are a measurement of multiple slip events over a given period. Fault geometry is not routinely considered when choosing sites for paleoseismic study or during the process of estimating paleoearthquake magnitude and so ignoring geometry may be a source of significant uncertainty. Fault geometry is also not routinely considered during the process of collecting surface offset measurements from recent earthquakes for use in defining regression relationships between surface

slip and moment magnitude. Regression relationships provide a mathematical function relating one parameter to another over a range of scales, for example surface offset to earthquake magnitude. Regression relationships allow the prediction of one parameter based on the observation of another.

2. That postseismic deformation can be a significant component of the total long-term fault slip for moderate magnitude earthquakes (fig. 1.1).

Paleoearthquake offsets are commonly assumed to have been created wholly by coseismic deformation. These offsets are measured in the field and the empirical surface offset – magnitude regression relationships of Wells & Coppersmith (1994) are then used to infer their magnitude. However, if postseismic deformation occurs, paleoearthquake magnitudes could be incorrectly estimated if it is assumed that all slip occurred coseismically. This would lead to overestimation of paleoearthquake coseismic offsets, through the unintentional inclusion of significant postseismic deformation, which in turn would lead to an overestimation of paleoearthquake magnitudes. The creation of regression relationships which include postseismic deformation will reduce the uncertainty of paleoearthquake magnitude estimates, which should lead to improved seismic hazard analysis.

The field area in this study is the central Apennines in the Lazio-Abruzzo provinces of central Italy. This area has some of the best exposure of bedrock normal fault scarps in the world, making it a suitable field area in which to investigate the hypotheses outlined above. The central Apennine region contains an extensive array (155 km x 55 km) of crustal scale normal faults, up to 40 km in length, trending North-West – South-East (Fig. 1.2) [Roberts & Michetti, 2004]. The normal fault

array has developed due to NE-SW crustal extension that followed NE thrusting related to the convergence of the African and Eurasian plates which ceased in the Pliocene [Patacca et al., 1990]. The normal faults have cumulative offsets of up to 2 km and are exposed as bedrock fault scarps in Mesozoic carbonates. Paleoseismic studies reveal that the recurrence intervals for the active normal faults of the central Apennines are on the order of 500 years [Michetti et al., 1996, Galli et al., 2008], which is longer than the current usable historical record. In order to properly assess the seismic hazard in this region it is necessary to study fault activity over numerous, recent seismic cycles [Roberts et al., 2004] and also to learn as much as possible about the seismic cycle from earthquakes which occur within the instrumental record.

The importance of reducing and quantifying uncertainty of paleoearthquake magnitudes in order to improve seismic hazard analyses is highlighted by Peruzza (2010) who stated that "*Italy has experienced approximately 350 deaths per year due to earthquakes in the last millennium* (Fig. 1.3)*, a shocking number, which rises to even more than 1,000 casualties per year if we consider the twentieth century only."*.

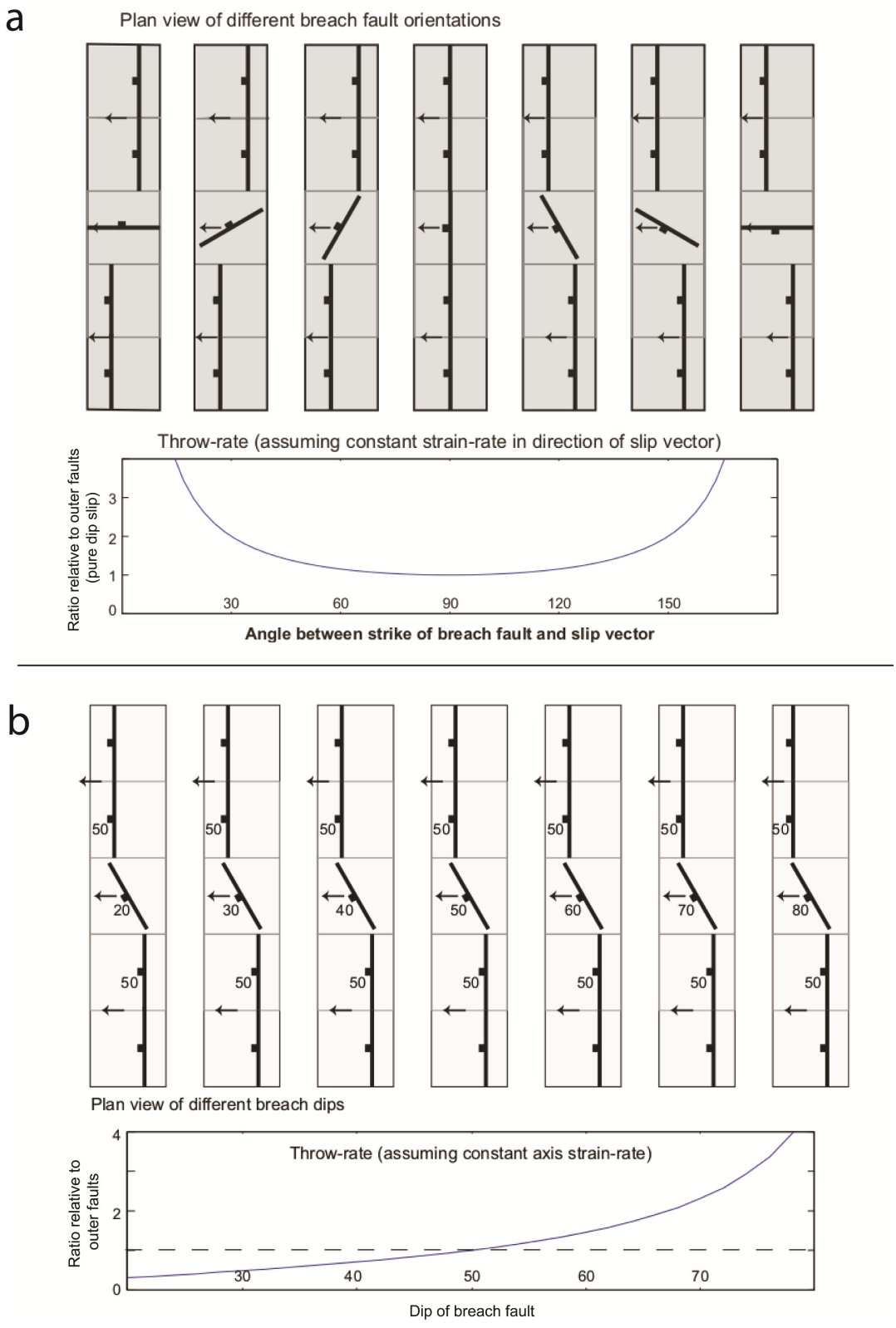

Figure 1.0: Modelled changes in throw-rate, due to changes in (a) fault strike or (b) fault dip (after Faure-Walker et al., 2009). Note that each box is modelled as an isolated segment. No stress transfer is modelled between the boxed regions.

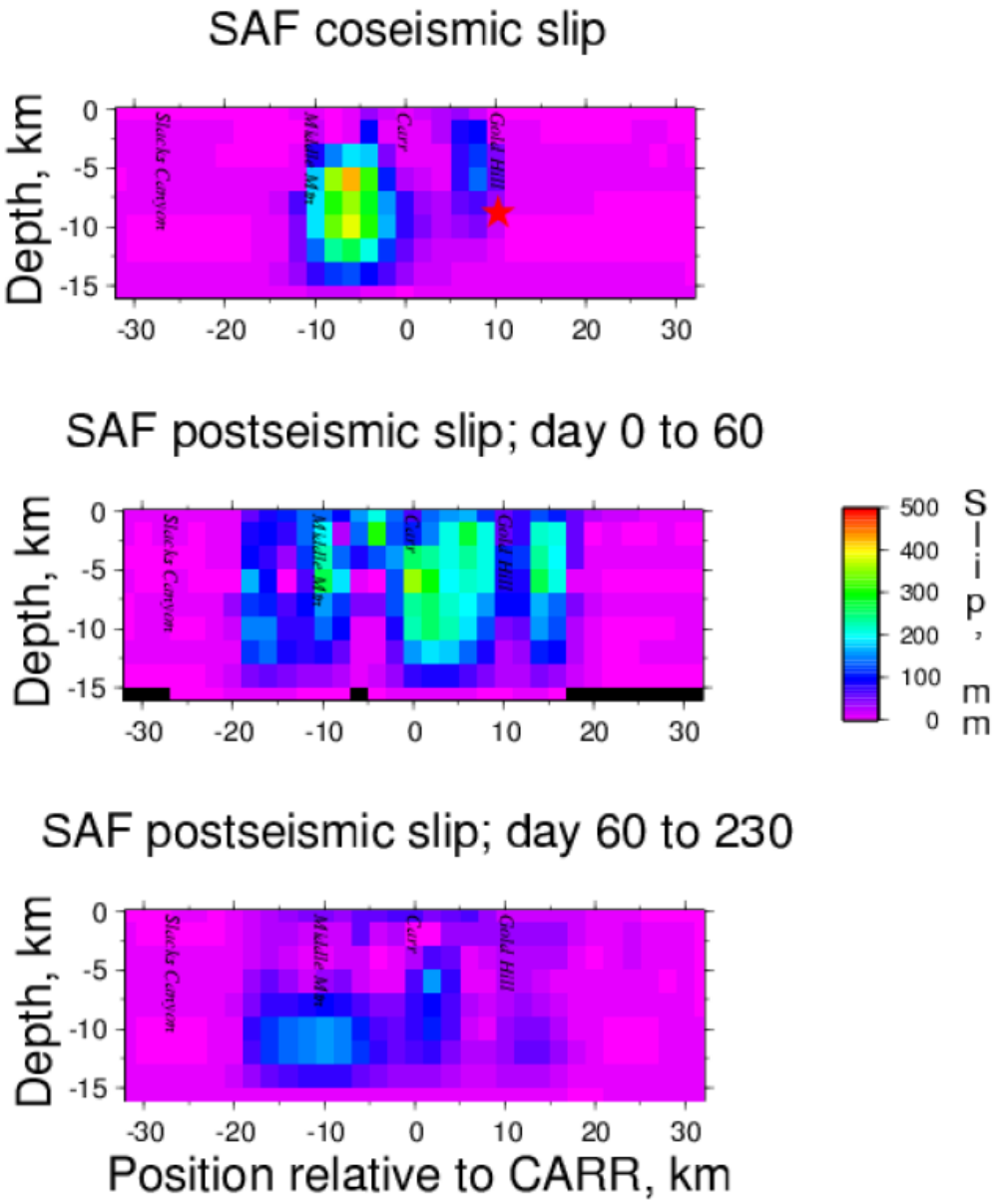

Figure 1.1: Coseismic and postseismic slip on the San Andreas Fault following the 2004 Parkfield earthquake (after Langbein et al., 2006). The coseismic slip occurs instantaneously as rapid slip on the fault plane. Postseismic slip occurs in the hours to years following an earthquake with a decreasing rate with time. Postseismic slip often occurs at the periphery of coseismic slip patches within the fault zone.

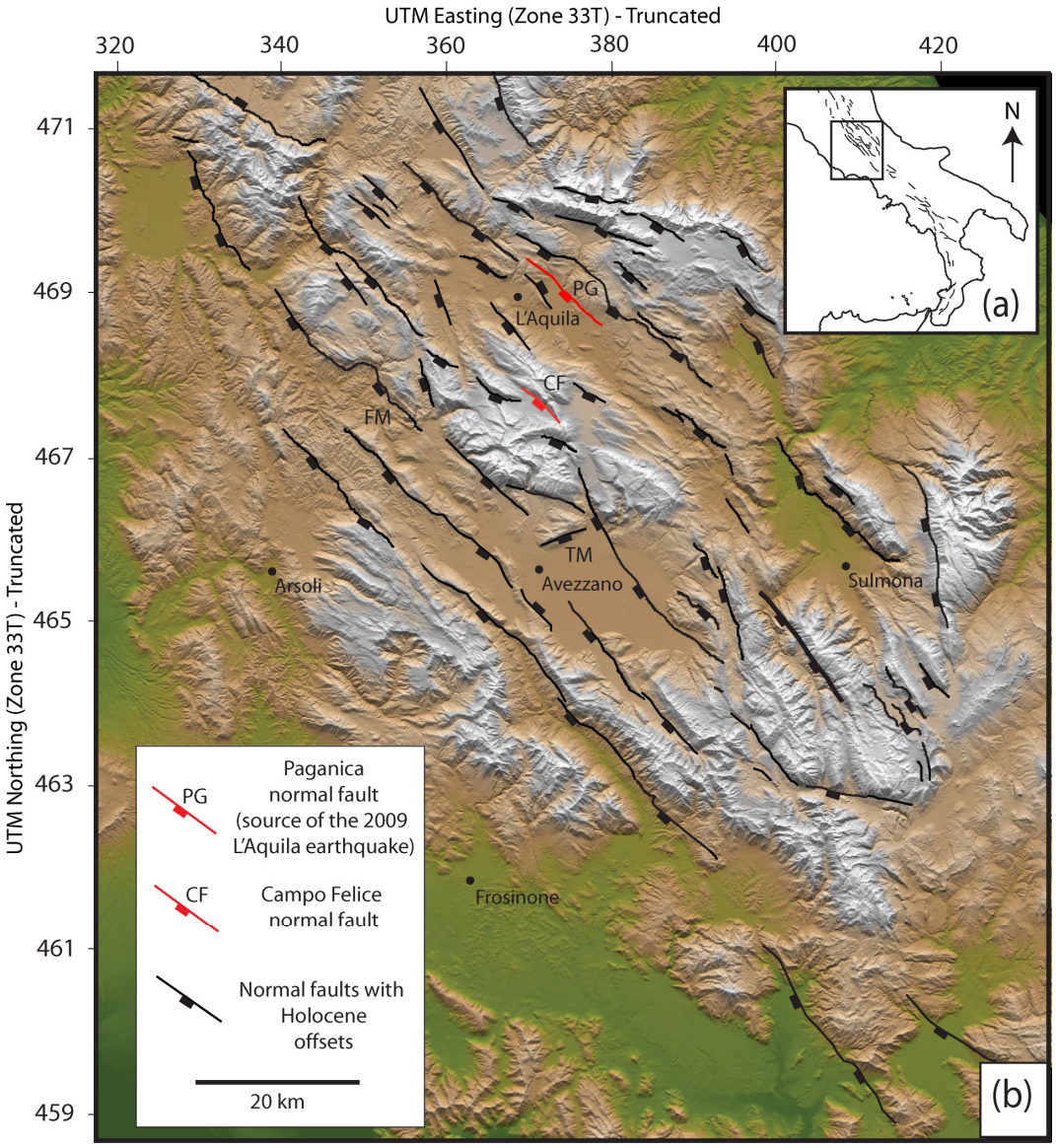

Figure 1.2: (a) Location map of the Italian peninsula. Active faults are shown as black lines. (b) Active normal fault map for the central Apennines. The faults studied in this thesis (the Pagancia and Campo Felice faults) are highlighted in red. The Fiamignano and Tre Monti faults, referred to in section 3.1.2 are denoted by 'FM' and 'TM' respectively. The map grid represents 20 km spacings in the UTM co-ordinate system, zone 33T. Figure adapted from Roberts et al., 2010.

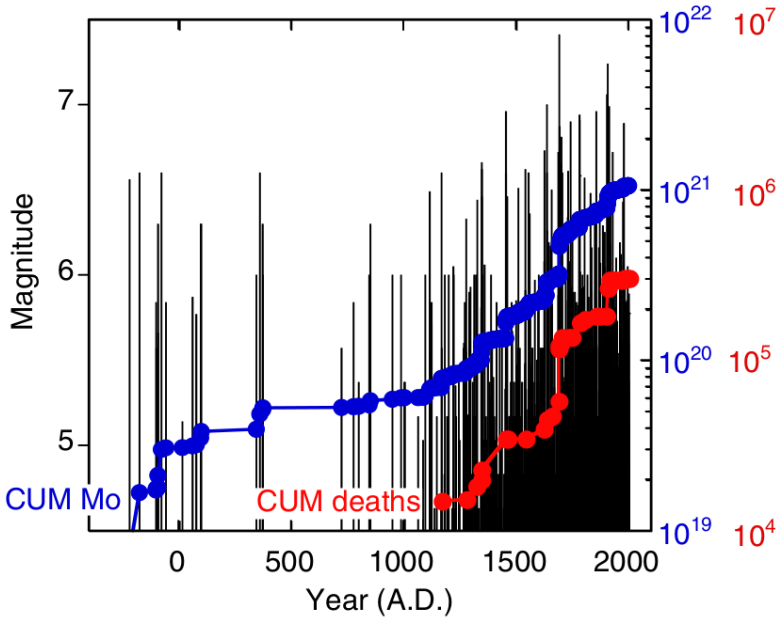

Figure 1.3: A simplified representation of the Italian earthquake catalogue (after CPTI Working Group, 2004). Black lines represent earthquakes of a given time and magnitude. The blue line represents cumulative seismic moment release (based on interpretation of historical accounts for the pre-instrumental age). The non-linear increase in cumulative moment can be partly attributed to increased accuracy in the seismic catalog since the late middle ages. The red represents cumulative casualties (after Peruzza et al., 2010).

In this study, the effect of fault geometry on throw-rates is investigated using topographic fault offsets measured in cross section from a high resolution topographic dataset created using a terrestrial laser scanner. A program to measure topographic offsets (*crossint*) was developed by the author specifically for this process. The use of a high resolution topographic dataset and the *crossint* program enabled an unprecedented number of topographic profiles (250 cross sections) to be analysed along a 4.5 km length of the Campo Felice fault scarp in the central Apennines (Chapter 4). Throw-rate and strain-rate profiles for the length of the fault were created

from these measurements. Field data collected along the fault were used to investigate the effect of fault geometry (strike, dip and kinematic slip direction) on throw-rate and strain-rate.

The hypothesis that significant postseismic deformation occurs following moderate-magnitude earthquakes and is routinely unaccounted in surface offset – magnitude datasets was investigated in this study by the use of repeat terrestrial laser scanning along the surface rupture of the 2009 Mw 6.3 L'Aquila earthquake (Chapter 5). The surface rupture of the L'Aquila earthquake was laser scanned numerous times at four sites for a period of up to 126 days after the earthquake. An innovative new method was developed in this thesis to model postseismic deformation from such repeat terrestrial laser scan datasets (no such method existed prior to this work). The magnitude of postseismic deformation was investigated in relation to inferred coseismic slip within the fault zone and from field observations of the surface rupture during the days following the earthquake.

A brief outline of the thesis is as follows:

- Chapter 2 provides a review of the current relevant literature on the progression of field techniques and technology used to measure fault offsets and postseismic deformation. The chapter also covers the role of terrestrial laser scan technology in these studies as well as background literature on earthquake geology in the Apennines and the 2009 L'Aquila earthquake.
- Chapter 3 describes the methods developed during this study to map the geomorphology of active normal faults and to calculate fault throw-rate and strain-rate from geological offsets within terrestrial laser scan datasets. This

chapter also describes a new method by which near-field postseismic deformation can be monitored and measured using repeat terrestrial laser scan datasets.

- Chapter 4 describes the results and implications of an analysis of variable throw-rate measured along the Campo Felice normal fault using a terrestrial laser scan dataset. The study found that fault geometry can influence throw-rates and its uncertainty and that the measurement of strain-rate, rather than throw-rate is a more reliable indicator of fault activity, as it is unaffected by fault geometry. In cases where fault geometry is not taken into account during paleoseismic studies, it is implied that fault geometry has the potential to affect the magnitude of paleoseismic offsets, leading to uncertainty in paleoearthquake magnitude estimation and seismic hazard analysis.
- Chapter 5 describes a study of postseismic deformation using repeat terrestrial laser scanning following the 2009 6.3 Mw L'Aquila earthquake. The study found that postseismic deformation forms an appreciable component of the total surface rupture offset of this moderate-magnitude earthquake. The study provides information on the magnitude and spatial distribution of near-field postseismic deformation. This study has highlighted the importance of considering postseismic deformation as an appreciable component of surface offset for moderate-magnitude earthquakes. Field studies of earthquakes from within the instrumental record, where magnitude is known often do not factor in significant postseismic deformation, for use in surface-offset – magnitude regressions used to estimate earthquake magnitudes from paleoseismic offsets. Postseismic deformation is also not generally accounted for when calculating paleoearthquake magnitudes. This study highlights the need to consider

postseismic deformation in order to reduce uncertainty in paleoearthquake maximum magnitudes and seismic hazard analyses.

- Chapter 6 integrates the outcomes from the two studies in Chapters 4 and 5 into an example workflow which provides suggested improvements in working practices in order to estimate earthquake magnitude with reduced uncertainty from the measurement of a paleoseismic offset, surface rupture offset or fault length. The reduction in uncertainty of earthquake magnitude estimates provided will in turn improve estimates required for seismic hazard analysis and building design, such as peak ground acceleration and size of the affected area.
- Chapter 7 provides general concluding remarks for the thesis.

This thesis has lead to the following publications:

Slip distributions on active normal faults measured from LiDAR and field mapping of geomorphic offsets: an example from L'Aquila, Italy, and implications for modelling seismic moment release. Wilkinson et al., submitted, *Geomorphology special issue 'Geomorphology of Active faults'* (Covered in Chapters 3, 4 & 6).

Partitioned postseismic deformation associated with the 2009 Mw 6.3 L'Aquila earthquake surface rupture measured using a terrestrial laser scanner. Wilkinson et al., 2010, *Geophys Res Lett*, 37*,* L10309 (Covered in Chapters 3, 5 & 6, Appendix vi).

Distribution and Magnitude of Postseismic Deformation of the 2009 L'Aquila Earthquake (M6.3) Surface Rupture Measured Using Repeat Terrestrial Laser

Scanning. Wilkinson et al., 2012, *Geophys. J. Int.* (Covered in Chapters 3, 5 & 6, Appendix vii).

The studies and methods within this thesis have also contributed to the following publications:

The tectonic geomorphology of bedrock scarps on active normal faults in the Italian Apennines mapped using combined ground penetrating radar and terrestrial laser scanning. Bubeck et al., submitted, *Geomorphology special issue 'Geomorphology of Active faults'*.

Combining Ground Penetrating Radar and Terrestrial LiDAR to produce 3D Virtual Outcrop Models. Bubeck et al., in prep.

Relationship between topography, rates of extension and mantle dynamics in the actively-extending Italian Apennines. Faure Walker et al., 2012, *Earth Planet Sc Lett*.

Shallow subsurface structure of the 2009 April 6 M w 6.3 L'Aquila earthquake surface rupture at Paganica, investigated with ground-penetrating radar, Roberts et al., 2010, *Geophys. J. Int.*, 183, 774-790.

Surface faulting of the April 6th 2009 Mw 6.3 L'Aquila earthquake in central Italy. Vittori et al., 2011, *B. Seismol. Soc. Am.,* 101, 1507-1530.

Chapter 2: Literature review

2.1. Introduction

Traditional field methods of mapping faults using compass and tape measure have provided limited quantitative description of tectonic processes, including the study of fault growth through the measurement of topographic and stratigraphic offsets [e.g. Muraoka & Kamata, 1983, Walsh & Watterson, 1987, Peacock & Sanderson, 1991] and coseismic and postseismic deformation from earthquake surface ruptures [e.g. Smith & Wyss, 1968]. These studies yielded sparse datasets which formed the basis of our insight into these tectonic processes in the pre-digital age. New digital geospatial technologies have enabled a substantial increase in the amount, coverage and resolution of measurements of tectonic processes, which continue to provide new insights [e.g. McCaffrey et al., 2005].

2.2. Offsets on active faults at the surface

In topographic fault offset studies, the surface expression of fault offsets on a surface of known age is measured to investigate fault slip-rates. Exampes of offset surfaces of known age used to inform fault slip-rates include the Bishop tuff 3.09 ± 0.08 ka, California [Lee et al., 2001] and the planar upper slope present in the footwall of the normal faults in the central Apennines, formed during periglacial conditions at 15 ±3 ka [Roberts & Michetti, 2004]. Normal fault topographic offsets are traditionally measured by producing cross sections through the topography in the direction of fault slip, using a tape measure and compass. The slip-rate is calculated by measuring the offset between the intersection of the upper slope and the degraded fault scarp in the footwall, and the lower slope and the base of the fault scarp in the hangingwall (as shown in Fig. 2.2.0). Careful measurement is required in order to avoid the perceived fault offset being modified by the deposition of a colluvial wedge in the hangingwall or lowering of the hangingwall through the process of landsliding or channel erosion. The main issue associated with conducting topographic fault offset studies using traditional field methods is that it is time consuming in the field, which limits the number of topographic profiles which can be collected along a fault. The collection of a limited number of topographic profiles means that it is not possible to gain a statistically robust estimate of the uncertainty in these types of measurements, or to identify and investigate any subtle systematic variability in measurements which may be present while moving along fault strike. New field survey methods involving digital technology (of which terrestrial laser scanning is one such example) allow for increased data gathering capabilities which in turn provide new insights into the variability of fault offsets and fault growth mechanisms.

Studies of topographic fault offsets of normal faults have been conducted using digital total station / laser theodolite surveying instruments (i.e. Dawers et al., 1993 and Cowie & Shipton, 1998). The use of this new technology allowed displacement profiles and fault tip gradients of normal faults of varying lengths to be constructed from regular measurments along the faults and also for the uncertainty in these measurements to be quantified and presented. These studies provided the first step towards quantitative, high resolution mapping of normal fault displacement profiles on a range of scales. However they were still limited by the time required to survey faults of significant length, meaning that the spacing between each measurement was still relatively large.

The use of GPS technology to conduct topographic surveys (digital mapping) of faults and fault offset horizons provided a step forward in terms of the amount of data which could be acquired, the size of fault systems which could be studied and the precision of the topographic measurements. A study of structures in three-dimensions was conducted for the Chimney Rock fault system, central Utah, using GPS (Maerten et al., 2001). Survey of a limestone horizon offset by a fault using this new technology allowed for variations in dip-slip fault displacement to be estimated by extrapolating the offset surface in three-dimensions using modelling. This type of study could not have been conducted with reasonable precision using laser theodolite survey equipment, as the fault offsets are observed in locations where there is little line of sight between them. The significant advantage of GPS here is that line of sight between survey points is not required in order to collect position and elevation measurements. The drawback of this study is that a GPS system must be physically positioned at each location where a measurement is to be taken, meaning that the number of measurements taken is still limited by the time available in the field.

The use of terrestrial laser scanning (TLS) technology by geoscientists has allowed for the rapid collection of high resolution topographic data (generally between 0.1 – 4 m spacing between individual measurements) at distances of up to 100 – 2000 m from the scanner, allowing for faults with lengths of up to 10 km and above to easily be surveyed in unprecedented detail. Recent studies using terrestrial laser scanning have focussed on detailing fault displacement from offset lake shorelines in order to compared fault displacement on geological vs. geodetic timeframes [e.g. Oldow et al., 2008] as well as the measurement of kinematic slip vectors in three dimensions through the identification of offset channels [e.g. Gold et al., 2012]. The use of TLS has enabled the measurement of fault offsets through the identification of subtle fault offset topographic features, such as paleoshorelines and the banks of streams and channels, which would have been difficult to measure sufficiently using laser theodolite or GPS.

A further advancement of terrestrial laser scan technology is through the use of airborne laser scanning, often termed airborne laser swath mapping (ALSM) in which a laser scanner is mounted within an aircraft and data is collected while the aircraft is in flight. The advantages of ALSM over terrestrial laser scanning include the ability to acquire data from an aerial view, which is advantageous for mapping strike-slip offsets, but can be a hindrance for mapping normal fault offsets. ALSM surveys can also cover much larger areas than terrestrial laser scan surveys. The disadvantages of ALSM surveys include the additional cost, planning and authorisation of survey flights, the need to collect GPS ground data in order to calculate the exact position and orientation of the aircraft, the potential of loss of flight time through low cloud as well as a reduced point density compared to TLS surveys (~10 points per m^2). For the reasons discussed above, ALSM surveys are

often carried out by a contracted operator, rather than by the researchers who will use the data. The cost associated with acquring the data often means that surveys are carried out in the interest of many researchers and data is released to allow researchers to work on different aspects at the same time (i.e. the B4 Southern San Andreas dataset available from www.opentopography.org). The B4 Southen San Andreas ALSM dataset has recently been used to measure strike-slip topographic offsets on the Carrizo segment of the Southern San Andreas Fault [Zielke et al., 2010]. The study revealed through the restoration of offset channels and other landforms that the average slip of the 1857 earthquake on this segment was 5.3 ±1.4 m, which suggests that the Carrizo segment did not rupture in a manner that would identify it as a discrete segment in relation to the rest of the Southern San Andreas Fault system. Using further restoration, the study suggested that the cumulative slip on this segment of the San Andreas may have formed with a characteristic slip size of ~5 m. The use of ALSM as the data collection method for this study, as opposed to TLS is appropriate, given the strike-slip nature of the offsets and the large scale of the study area required to measure a sufficient number of reliable offsets.

Other remote sensing datasets, such as shuttle radar tomography mission (SRTM) DEM data can be used as an alternative to ALSM in order to measure topographic offsets and fault activity. SRTM DEM data has been used to infer the post-glacial evolution of active faults in the North German basin through the study of lineations, fault parallel drainage networks and tectonic block bounded lakes [Reicherter et al., 2005]. This type of approach is novel in relation to ALSM and TLS based studies as it provides an insight into tectonic processes, fault activity and paleostress orientations approaching a plate tectonic scale. The drawbacks of such studies include the lack of ground truthing of many features seen in STRM datasets,

mainly due to their number and the large areas over which they are mapped. However regional-scale SRTM-type datasets do provide a means to interrogate large expanses of terrain in order to identify key study areas, which can then be visited for ground truthing and further detailed study. Many such study areas could not have been identified in any other way.

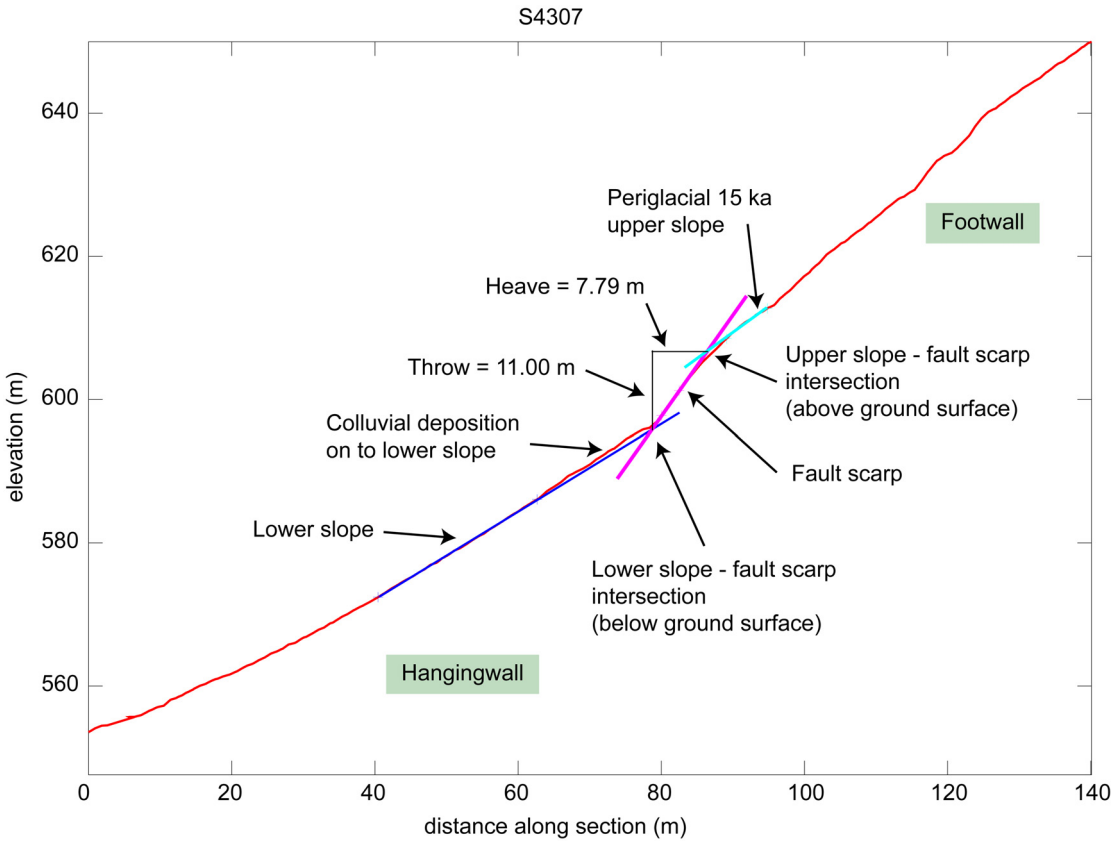

Figure 2.2.0: Topographic cross section of a normal fault, showing the lower slope, fault scarp and upper slope. The topography is shown in red. The throw and heave are calculated as the vertical and horizontal distances between the intersection of the lower slope and the base of the fault scarp and the intersection of the upper slope and the top of the fault scarp.

2.2.1. Subsurface offset studies

Inferring fault activity through the measurement of fault offsets in the subsurface is a complimentary approach to the measurement of topographic fault offsets at the surface. Geological and geophysical subsurface investigations of fault offsets often provide a record of successive slip events, in the case where a fresh set of sediments are deposited after each earthquake and subsequently offset by the next.

Direct geological observations

In cases where direct observations can be made, the ability to date offset sediments using radiocarbon techniques (i.e. Pantosti et al., 1996, Rockwell et al., 2009) provides information on the timing of slip events, the recurrence interval of the studied fault, as well as its average slip-rate and elapsed time. For instance, the subsurface offsets formed by the 1915 Fucino earthquake and earlier slip events on the Fucino fault system was investigated by trenching the fault at several locations [Michetti et al., 1996]. The dating of offset sediments revealed two previous slip events on the Fucino fault system, the first between 885 and 1349 A.D. and a second between 550 and 885 A.D. A slip-rate of 1.6 mm/yr was inferred from a 2.4 m offset of sediments whose age is younger than 550 A.D., however the long term slip-rate for this part of the fault system since the mid-Pleistocene is much lower (0.4 mm/yr). This discrepancy highlights the challenges present in these types of studies, as fault slip measured over different time frames can vary significantly. There is therefore a need to integrate inferences on fault slip from multiple studies spanning different time frames.

Subsurface studies where direct observations are made have traditionally been carried out by digging a trench across the fault and using a tape measure and a quadrat

grid which is pinned to the trench wall in order to aid hand sketching of the fault zone and offsets sediments. In more recent times, digital technology has allowed for the use of photographic documentation of the trench walls and photoshop-style computer programs have become readily available in order to create photo-mosaics. These photo-mosaics can then be used as a template on which to create accurate trench wall sketches within vector drawing software packages (e.g. Fig. 2.2.1, from Rockwell at al., 2009). The digital overlay of sketches onto a photo-mosaic also provides other researchers with an appreciation of how the trench wall looked in real life, rather than just providing an interpretative sketch without presenting the uninterpreted view.

More recently TLS has begun to be used to document trench walls (i.e. Arrowsmith et al., 2009). The acquisition of TLS datasets in trenches provides a means to document and archive the exposed trench wall, which is advantageous in situations where the trench may have to be filled in after a specified period of time. The use of TLS also allows for offsets to be measured with greater precision than using photo-mosaics. Also using numerous TLS datasets from closely spaced trenches allows features such as bedding interfaces, channels and faults to be projected from one dataset to the next in order to build a three dimensional model of faults and offset sedimentary units (i.e. Arrowsmith et al., 2009).

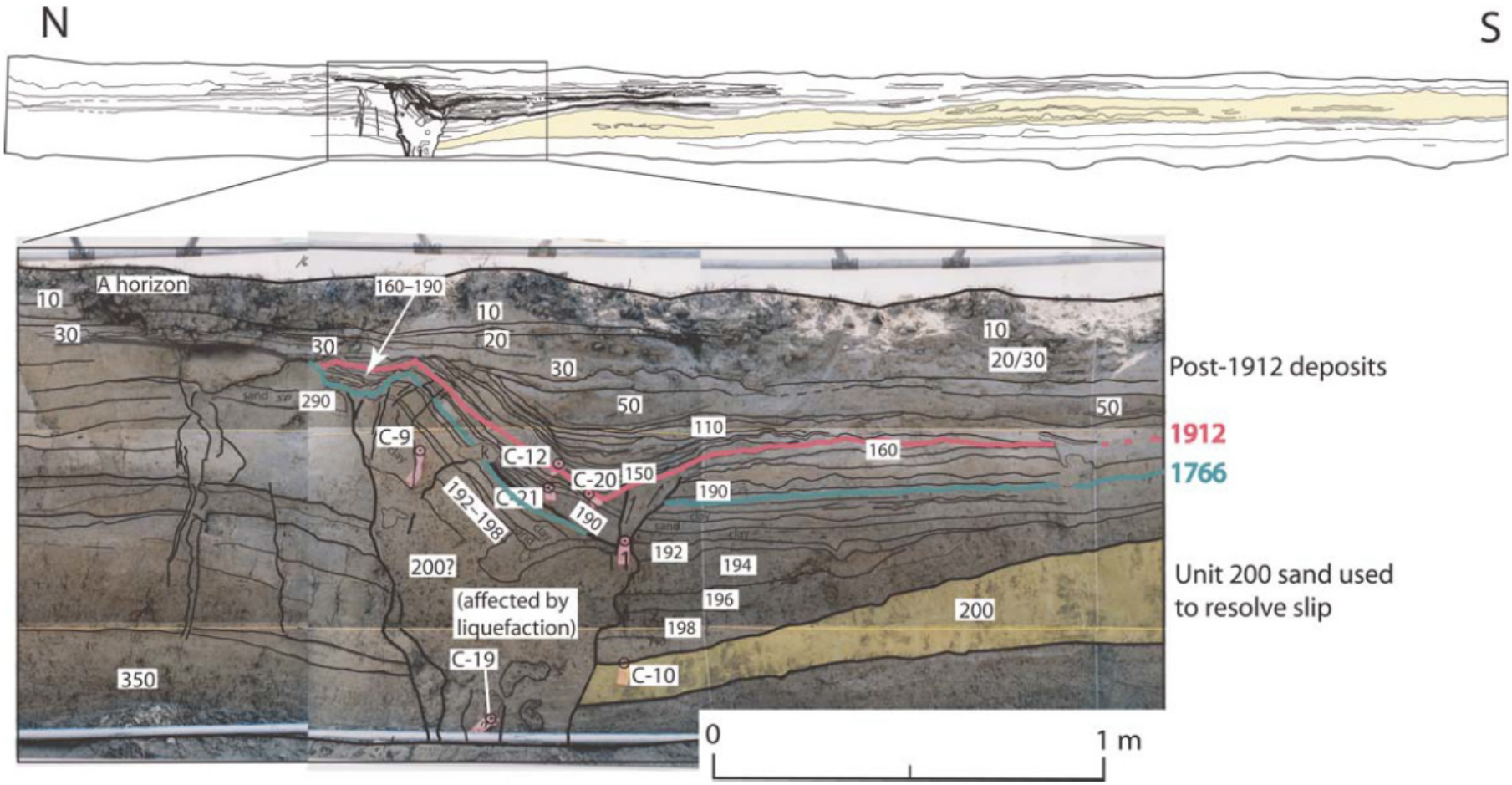

Figure 2.2.1: An example of a photo-mosaic of a trench wall, overlain by a digital sketch interpretation of the fault zone and various offset sediments (see Rockwell et al., 2009 for details)

Indirect geophysical observations

Indirect geophysical observations of fault offsets can provide information of the existence and magnitude of fault offsets in locations where it is not possible to make direct observations. Applications of indirect observations include where faults are located offshore, for example in the Gulf of Corinth [i.e. Moretti et al., 2003 and Bell et al., 2011] and where faults are located beneath roads or in locations where it is not permissible to excavate to obtain direct observations, for example the central portion of the 2009 L'Aquila earthquake surface rupture in the town of Paganica [i.e. Roberts et al., 2010].

Geophysical methods (seismic reflection surveys and ground penetrating radar (GPR) surveys) provide a means to indirectly measure offsets on active faults. Recent examples of the use of GPR include a study of the August 1999 earthquake ruptures on the North Anatolian fault near Izmit [Ferry et al., 2004], in which two survey lines were acquired at either size of a study trench to provide complementary information of paleoseismic offsets. The study was able to identify two earthquake events in the GPR data which supported the interpretation obtained from trenching. The study noted that GPR is a useful tool to use for imaging the fault zone and potential offsets prior to excavating trenches. A GPR study of the 2009 L'Aquila earthquake surface rupture [Roberts et al., 2010] found evidence for offsets of Holocene-Pleistocene age in the top 10 m of the subsurface. A throw-rate of 0.23 – 0.30 mm/yr was obtained by measuring the vertical offset of the base of the Holocene which is in agreement with other offsets of Mid Pleistocene tephras. The study also found that the 2009 rupture stepped between two faults in an en-echelon configuration, both of which clearly show Holocene offsets. The use of GPR on the 2009 L'Aquila earthquake surface rupture has provided vital information on the long term slip-rate of the Paganica fault.

A GPR study of paleoseismic offsets on the Hope fault, New Zealand was conducted [Beaupretre et al., 2012] because there has been significant sedimentation over the fault trace, leading to buried fault offsets. The fault was imaged in three dimensions using GPR, which revealed alluvial terraces of varying age. TLS was also used to complement the GPR survey by mapping the topographic expression of an anastamosing stream network as it crossed the fault. A stream network had incised terraces in the subsurface and the study was able to measure 48 lateral offsets which ranged between 6 – 108 m. The study interpreted up to 30 large earthquakes offsetting the Hope fault in the last 6 – 7 kyr, with coseismic slip of ~3.2 ±1 m, an average recurrence interval of ~200 years and moment magnitudes of 7 – 7.4. Such a complete record in the near subsurface is unique. However it is possible that multiple offsets on different stream channels could have been formed by a single-slip event, thus lowering the slip-rate and increasing the recurrence interval. This study shows the exciting capabilities of shallow subsurface GPR studies, but it also highlights the need in many cases to obtain direct evidence of offsets in order to back up interpretations made from indirect observations, in particular the age of offset sediments.

The Gulf of Corinth rift, in central Greece is a good example of where seismic reflection survey technology has been used to good effect to quantify the activity of offshore normal faults, through the indirect measurement of offset sediments. A study of three seismic lines across the Gulf of Corinth [Bell et al., 2011] revealed that long term extension rates increase from the centre of the rift to the Western end of the rift, as would be expected from the overall rift morphology where its width, basement subsidence and sediment accumulation are greatest. They compare their rates of extension to those from geodetic measurements averaged over 5 – 100 yr and find that maximum present day geodetic extension is located in the West of the rift. They

explain the disparity between the long term extension maximum in the centre of the rift and the present day extension maximum in the West to the growth and linkage of faults during the history of the Corinth Rift. Such studies provide a detailed insight into the long-term activity and growth of faults, which are difficult to obtain from onshore studies of fault offsets. There are limitations to this approach, mainly due to the difficulty in obtaining the seismic data needed to conduct such studies. A source of uncertainty in such studies is the assumption of the age of offset sediments, as measured in the seismic data, in the case where the data cannot be tied to direct observations taken from boreholes. In regions such as Corinth, onshore fault offset studies using TLS, ALSM and satellite data can complement offshore studies to provide a greater insight into fault systems which span the terrestrial and marine domains.

Seismic reflection data has also been used to investigate the growth and development of ancient fault zones. Seismic reflection data from the Northern North Sea has been used to investigate the development of fault overlap zones during the growth of normal faults [Childs et al., 1995]. Through the study of displacement profiles from normal faults in seismic data, the study found that bends in fault geometry were originally formed as overlap zones. As displacement continued on the faults within an overlap zone, fault tip propagation caused through going faults to form and for the overlap zone to become hard linked. High resolution fault displacement mapping using 3D seismic data of growth faults in the Gulf of Mexico [Mansfield & Cartwright, 1996] revealed local decreases in throw at discrete sections along the faults. These anomalous changes in throw are inconsistent with fault growth models which require repeated slip of the entire fault surface in order for fault tip propagation. The anomalous changes in throw have been found to persist as the fault

grew through repeated slip events. It is therefore suggested that local changes in throw are due to a local decrease towards fault tips in areas where fault segments overlap in an en échelon configuration. Variations in fault displacement along strike were studied using seismic data from the Strathspey-Brent-Statfjord fault array, formed by an extenional event in the Late Jurassic northern North Sea rift basin [McLeod et al., 2000]. Displacement variations along strike were found to coincide with fault paleo-segments, suggesting displacement variations along strike were generated by discrete fault segments which existed prior to fault linkage (Fig. 2.2.2). Seismic stratigraphic techniques were used to show that the fault array began as a series of small fault segments, which eventually linked and the strain localised to form a main through going fault and an antithetic counterpart. The outlying fault segments which did not link to become part of the main through-going faults ceased activity within 3 – 4 Myr of the beginning of the extension.

The temporal development of the northeastern section of the Murchison-Statfjord North Fault Zone in the northern North Sea was investigated using 3D seismic data and syn-rift stratigraphy [Young et al., 2001]. Study of fault stratigraphic offsets at different intervals revealed the complex development of the fault zone. The fault zone developed in three discrete stages (Fig. 2.2.3), initially six isolated fault stands formed, which controlled the stratigraphy in the area for the first 13 Myr. These fault strands then linked along strike through the process of fault tip propagation during increased displacement to form two 9 km long fault segments separated by a wide relay ramp. This configuration existed for the next 10 Myr. Finally, during the last 7 Myrs of the fault system, the two fault segments breached the relay zone and become hard linked. The study shows that the combination of 3D seismic and syn-rift stratigraphic study can reveal the complex temporal development

of fault systems. A study of syn-sedimentary fault growth [Childs et al., 2003], where faults were mapped in 3D seismic data revealed differing fault propagation rates for individual faults. Ten fault tips were mapped using this technique, which revealed maximum tip propagation rates of 15 km/Myr for gravity driven faults and 3 km/Myr for tectonically driven faults. The study found that fault tip propagation rates decrease with elapsed time from the start of faulting. Fault tip retreat was found to occur in the later stages of fault growth in situations where the strain field became overlapped by another fault during the formation of relay zones.

High-resolution 3D seismic data from a listric growth fault system in South East Asia has been used to investigate changes in geometry and kinematics of minor basin faults in relation to along strike changes in the structure and position of the basin bounding fault [Imber et al., 2003]. In cases where the basin bounding fault remained fixed, a landward migration and decrease in age of the hangingwall growth faults were observed. In cases along strike where the footwall collapsed, causing the basin bounding fault to step back into the footwall, casued the punctuated migration of the rollover hinge (the limit of syn-sedimentary thickening against a buried growth fault) and buried hanigingwall growth faults towards the footwall. The study highlights the ability to observe a detailed record of fault growth in complex configurations using 3D seismic data. The study notes that the migration of hangingwall growth faults can occur in fault configurations whereby the basin bounding fault is fixed or progressively migrates into the footwall.

Studies of fault growth and interaction using seismic data, coupled with stratigraphic observations have provided unique insights into the temporal development of fault systems. Such observations have allowed for investigation into

the growth of individual faults as well as their interaction and the development of fault arrays as a whole.

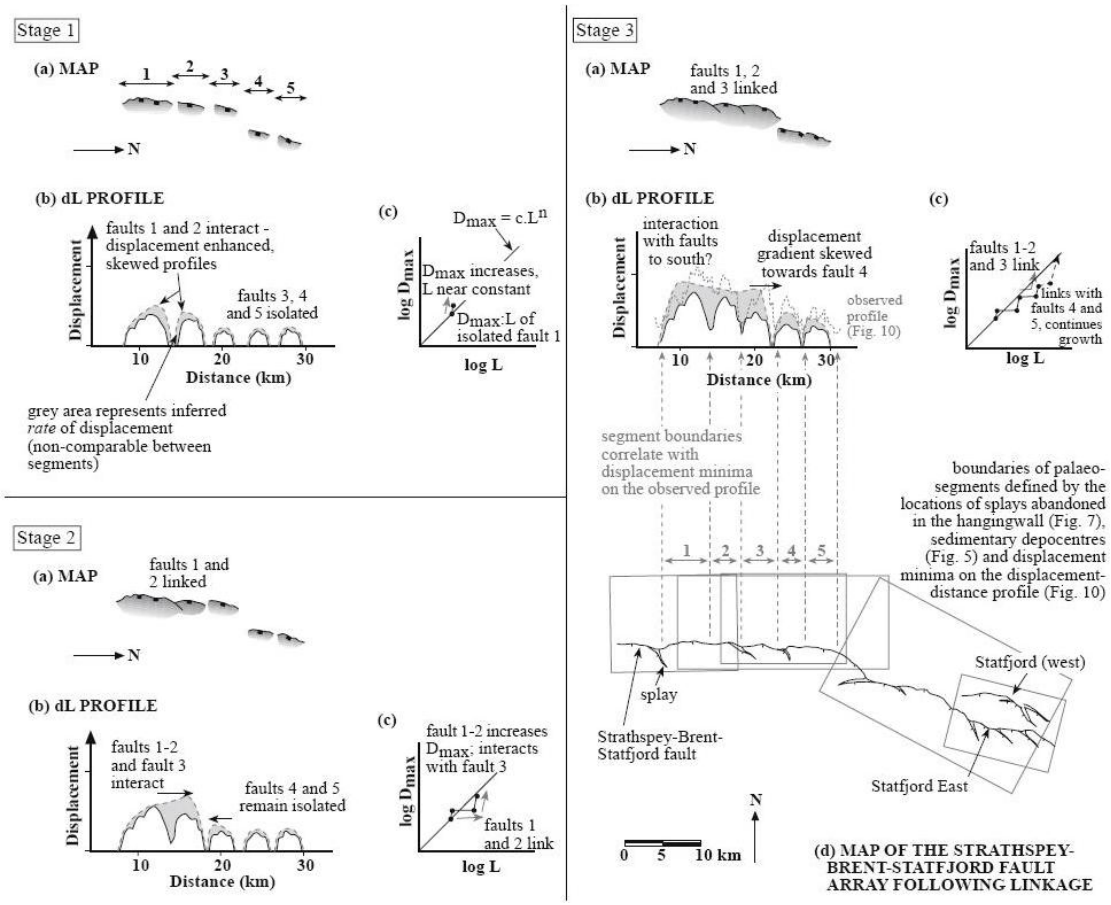

Figure 2.2.2: A model of fault growth for the Strathspey-Brent-Statfjord fault system, highlighting the creation of an irregular displacement profile, through the linkage of discrete fault segments (after McLoed et al., 2000).

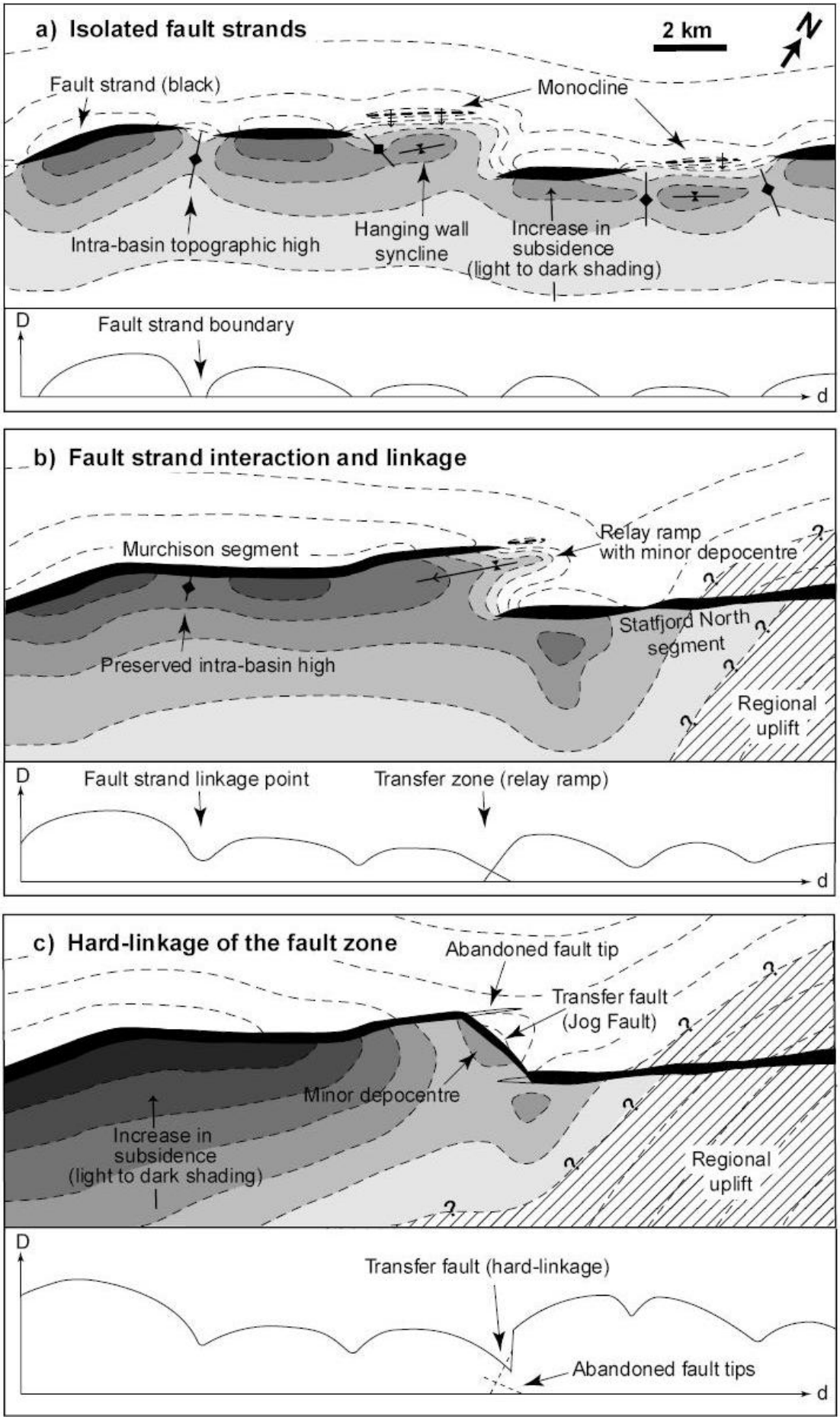
a) Isolated fault strands
2 km
N
Fault strand (black)
Monocline
Intra-basin topographic high
Hanging wall syncline
Increase in subsidence (light to dark shading)
D
Fault strand boundary
d
b) Fault strand interaction and linkage
Murchison segment
Relay ramp with minor depocentre
Statfjord North segment
Preserved intra-basin high
Regional uplift
D
Fault strand linkage point
Transfer zone (relay ramp)
d
c) Hard-linkage of the fault zone
Abandoned fault tip
Transfer fault (Jog Fault)
Minor depocentre
Increase in subsidence (light to dark shading)
Regional uplift
D
Transfer fault (hard-linkage)
Abandoned fault tips
d

Figure 2.2.3: The three stage development of the Murchison-Statfjord North Fault Zone, obtained from study of 3D seismic data and stratigraphy (after Young et al., 2001).

2.2.2. The role for TLS in fault offset studies

Terrestrial laser scan technology provides a means to efficiently collect high resolution topographic data. The main advantage of TLS technology over all other methods when measuring fault offsets is that it allows a small team of researchers, typically between one to three people to collect their own high resolution data from a fault or sets of faults of their choice. Further advantages include the fact that researchers must be in reasonably close proximity to the fault they are studying, typically within 1000 m. This allows for further close inspection of the fault and for ground truthing using traditional structural mapping, measurement of fault dip, strike, slip direction, plus integration with other site specific data such as GPR. The use of ALSM and SRTM datasets can provide insights into fault offsets and fault activity over much larger areas than is possible with TLS technology, but they are mostly suited to strike-slip fault offsets due to their downward-looking view of topography. Other topographic survey methods such as total station and GPS provide a means of surveying topographic fault offsets at reduced cost, as long as the drawback of reduced data coverage and density can be reconciled. In the case of subsurface studies of fault offsets, TLS provides a complimentary dataset that can be used to measure onshore topographic fault offsets and to map geomorphic features in three-dimensions which can be compared to those that are seen in subsurface datasets. TLS also provides a means to document and preserve a digital copy of topography or

subsurface trench walls which show detailed fault offsets. A further advantage of TLS technology is that a three-dimensional dataset can be acquired during fieldwork, following which the processing and interpretation of the data can be carried out on a computer in the lab upon returning from fieldwork. This approach allows for efficient use of fieldwork time, in fact a general reduction in fieldwork time when using TLS for a given project is often the case. The use of TLS for measuring topographic fault offsets forms the basis of the study of the Campo Felice normal fault in the Italian Apennines, covered in Chapter 4.

2.2.3. Active fault offsets in the study area

Fault activity in the central Apennines has been mainly quantified through paleoseismic study of multiple coseismic offsets (i.e. Pantosti, et al., 1996, D'Adezzio et al., 1996, Michetti et al., 1996, Galli et al., 2002, Galli et al., 2008) which are dated using radiocarbon techniques to define a recurrence interval, range of earthquake magnitudes and slip-rate for each fault. Recurrence intervals for the Apennine faults defined from paleoseismic studies are typically on the order of 500 years [Michetti et al., 1996, Galli et al., 2008].

Other studies have focused on the measurement of post-glacial throw-rates by measuring the offset of a periglacial surface formed ~15 ±3 ka (i.e. Morewood & Roberts, 2000, Roberts & Michetti, 2004, Roberts et al., 2004, Papanikolaou et al., 2005, Roberts, 2006, Faure Walker et al., 2009, Faure Walker et al., 2010). In these studies, topographic fault offsets have been measured by surveying cross-sectional transects across normal faults. The periglacial upper slope in the footwall, the bedrock normal scarp and the lower slope in the hangingwall are projected as planar surfaces.

The throw-rate is then determined by measuring the vertical offset between the intersection of lower slope in the hangingwall and the base of the scarp and the upper slope in the footwall and the top of the scarp (see Section 3.2.2 and Figs. 3.2.1 & 4.1.1). Throw-rates obtained using this method for the Apennine normal faults are in the range of 0.03 – 1.67 mm/yr [Morewood & Roberts, 2000, Roberts & Michetti, 2004, Papanikolaou et al., 2005, Papanikolaou & Roberts, 2007, Faure Walker et al., 2009, Faure Walker et al., 2010, Faure Walker et al., 2012]. Throw-rates can then be used as a proxy for recurrence interval, as recurrence intervals will decrease (earthquakes become more frequent) as throw-rate increases [Roberts et al., 2004]. These studies have provided insights into the activity of active faults in the Apennines, through the measurement of tens of topographic cross sections at each fault using total station and traditional map and compass techniques. The use of terrestrial laser scan technology, however, allows for hundreds of cross sections to be created and studied along each normal fault. This approach has been conducted for a study of the Campo Felice fault in Chapter 4 of this thesis. The ability to measure throw-rates at all suitable sites along a fault using TLS technology allows for a better understanding of the variability in throw-rate and what the maximum throw-rate is for a particular fault.

More recently ^{36}Cl exposure dating has been carried out on bedrock fault scarps in the Apennines (i.e. Schlagenhauf et al., 2010, Schlagenhauf et al., 2011) in which the slip history of a fault can be revealed by sampling the exposure age of the fault scarp. A study of the Magnola fault [Palumbo et al., 2004] revealed evidence for between 5 – 7 slip events, with individual slip in the range of 1.5 – 3.0 m. However it is uncertain as to whether these slip events represent single discrete earthquakes or

periods of time containing clusters of several smaller earthquakes. The slip-rate over the last 12 ka was defined as ~0.8 mm/yr.

Geodetic measurements using campaign GPS (i.e. long term measurements from permanently installed GPS stations) have been measured in the Apennines over various timespans (1875 – 2001, Hunstad et al., 2003, 1991 – 2002, Serpelloni et al., 2005, 1994 - 2010, D'Agostino et al., 2011) with the aim of inferring the current strain field within the Apennines. In all cases the Apennines are found to be extending in a NE-SW direction, perpendicular to the mountain chain, with extension velocities ranging from 1.6 – 5 mm / yr, which is in broad agreement with estimates of the extension rate inferred from geological fault offsets since the Late Pleistocene [Roberts and Michetti, 2004, Faure-Walker et al., 2010]. These studies have suggested that present day strain is now only focussed on a number of major through-going faults due to a rapid decrease in GPS velocities away from the centre of the Apennine chain [D'Agostino et al., 2011], or that strain released during earthquakes over the GPS survey period does not account for all of the measured strain, suggesting off-fault extension of the crust is also occurring [Hunstad et al., 2003]. However the discrepancy between the rate and width of the zone of active deformation inferred from present day strain obtained from geodetic studies and strain inferred by geological fault offset studies can be rationalised by comparing the timespan of the geodetic measurements (10 – 20 yr) in relation to the recurrence intervals of the Apennine faults (~500 yr). The GPS survey time span is not sufficient in order to define the strain which operates on the order of a single complete seismic cycle, as the regional rate of extension may not be consistent throughout the entire seismic cycle. Periods of anomalously high strain and lower strain in relation to the long-term

geological average may occur during and after earthquakes, which may happen to have been captured by present day GPS measurements.

2.3. Coseismic and postseismic deformation (afterslip) on active faults

Coseismic deformation is the deformation of the ground surface that occurs during an earthquake. If the earthquake magnitude is sufficient (>6.0 Mw), coseismic deformation can occur where a fault intersects the surface, often forming a surface rupture or offset in the near-field [Wells & Coppersmith, 1994]. Coseismic deformation can also occur as broad deformation in the far-field, in certain cases up to 10's of kilometres from the surface expression of the fault [e.g. Ryder et al., 2007; Papanikolaou et al., 2010]. Coseismic deformation is driven by fault slip during earthquakes and occurs instantaneously as the fault zone ruptures at depth within the seismogenic zone [Scholtz, 1990]. The coseismic rupture propagates up the fault zone towards the surface as well as down the fault zone and into the lithosphere. Postseismic deformation, in contrast, is the deformation which occurs following an earthquake over the subsequent minutes to years, whose rate of deformation decreases with time [Marone et al., 1991, e.g. Smith & Wyss, 1968; Bucknam et al., 1978; Williams & Magistrale, 1989]. Postseismic deformation encompasses all surface and fault zone deformation which occurs following an earthquake, in the far-field or as deformation in the near-field on the surface rupture and the fault zone, which is termed afterslip [Scholtz, 1990]. Afterslip was first noticed following the 1966 Parkfield earthquake in California [Smith & Wyss, 1968].

A model for earthquake afterslip, based on rate and state variable friction laws was proposed by Marone et al., (1991). The model is based on a two-layer configuration, a velocity-weakening layer at depth within the fault zone in which the fault gouge is consolidated and an upper velocity-strengthening layer in which the fault gouge is poorly consolidated (Fig. 2.3.1, Marone, 1998). The velocity weakening

layer incorporates the seismogenic zone from where earthquakes originate. When coseismic slip occurs within the velocity weakening layer, the layer responds in a manner which does not resist the propagation of slip throughout the layer. The coseismic slip propagates upwards into the velocity-strengthening layer, which due to its unconsolidated state, reacts to resist and perturb rapid coseismic slip. This perturbation creates a coseismic slip-deficit between the two layers. The velocity-strengthening layer then responds to equalize this deficit through the process of gradual creep over time, causing afterslip with decaying rate over time. The thickness of the velocity-strengthening layer (comprised of unconsolidated sediment) is expected to increase afterslip in relation to coseismic slip at the surface. It is suggested that younger faults with little fault gouge are expected to exhibit less afterslip. The decay-law model for afterslip is based around a logarithmic function, which provides comparable decay curves of afterslip vs. time for earthquakes with significant afterslip (Fig. 2.3.2).

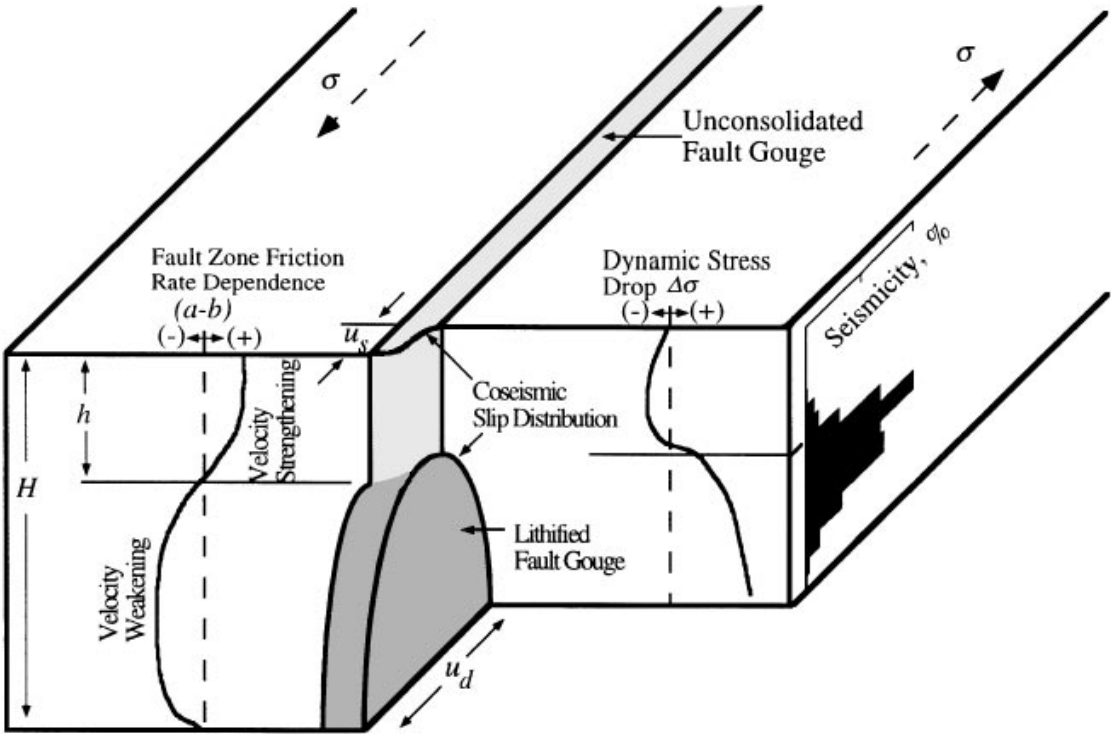

Figure 2.3.1: The two layer model of a strike-slip fault zone, used to explain the source of afterslip. The lower velocity weakening layer of the fault zone is situated within the seismogenic zone which consists of consolidated material. This velocity weakening layer does not resist rapid slip and coseismic slip rapidly propagates up the fault zone. The upper velocity strengthening layer of the fault zone consists of consonsolidated material (fault gouge), which resists rapid slip following earthquakes. Coseismic slip propagates up the fault zone through this region, but is perturbed. The difference between coseismic slip at the surface and at the base of the velocity strengthening layer drives the process of afterslip, whereby the velocity strengthening layer slips slowly over time to re-equilibriate the difference (after Marone, 1998).

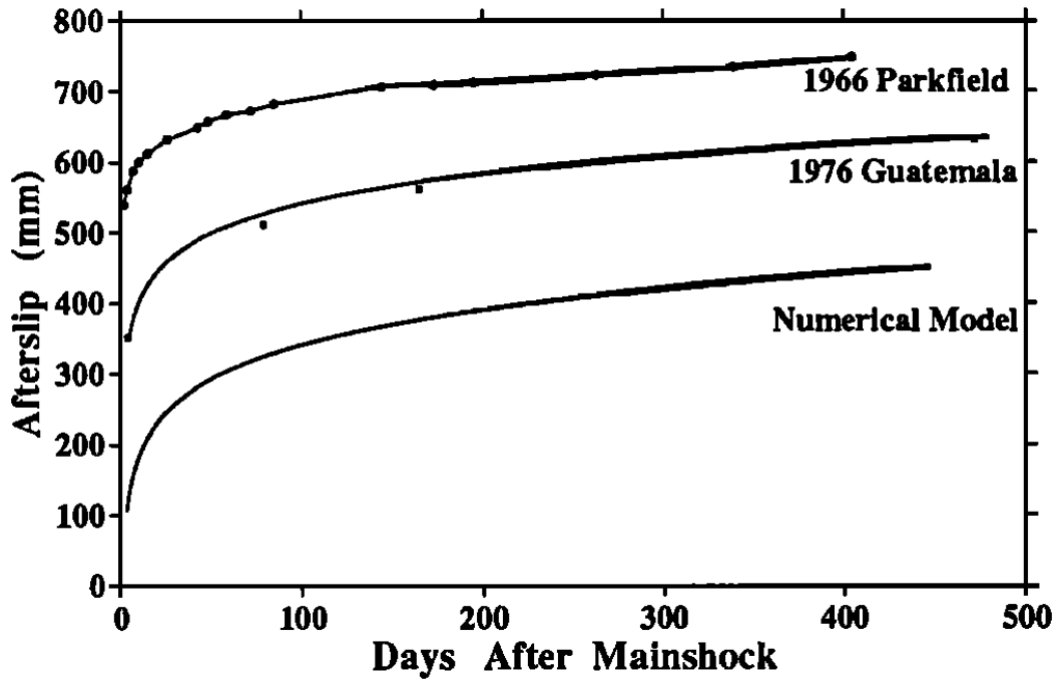

Figure 2.3.2: Comparison of the two-layer numerical model for afterslip and the afterslip observed for the 1966 Parkfield and 1976 Guatemala earthquakes (after Marone et al., 1991).

The magnitude of near-field postseismic deformation in comparison to coseismic slip was ~60% for the 2009 L'Aquila moderate magnitude earthquake (6.3 Mw, see Chapter 5). It is suggested that larger earthquakes have a lower proportion of postseismic deformation, in relation to coseismic slip (i.e. 20% following the 1997 Mw 7.6 Manyi earthquake [Ryder et al., 2007]) as coseismic slip within the seismogenic zone increases during these earthquakes and means that more of the slip at depth can travel to the surface coseismically, leading to a lower proportion of postseismic slip. A way of explaining the significant decrease in postseismic deformation for higher magnitude earthquakes, compared with those of lower magnitude is that more coseismic slip travels to the surface as earthquake magnitude increases, due to increased slip magnitude and area within the seismogenic zone, with more energy being released. The unconsolidated velocity strengthening material within the fault zone perturbs the rapid propagation of coseismic slip from depth to the surface through the process of grains interlocking as coseismic slip propagates through the confined unconsolidated sediment within the fault zone [i.e. Marone et al., 1991]. There is however an upper limit to the amount of coseismic slip which this process can perturb, above which coseismic slip causes the interlocking grains to be fractured and a through-going slip surface is eventually formed. The potential of the unconsolidated velocity strengthening material to resist the propagation of coseismic slip may also depend on the amount of sediment cover and its depth within the fault zone [e,g, Bucknam et al, 1978] . As a greater amount of coseismic slip propagates to the surface in earthquakes of increasing magnitude there is no more of a slip deficit created between the surface and depth than in smaller magnitude eathquakes and hence there is less potential for significant postseismic deformation in relation to coseismic deformation to be observed.

The 2009 L'Aquila earthquake provided an opportunity to test the hypothesis that significant postseismic deformation will occur following a moderate magnitude earthquake (~6.3 Mw). A new method was developed to measure postseismic deformation on the surface rupture of the L'Aquila earthquake using terrestrial laser scanning technology. The study is covered in Chapter 5. This hypothesis has implications for studies of earthquake geology and paleoseismology. If significant postseismic deformation is shown to exist for moderate magnitude earthquakes, then paleoseismic studies must account for postseismic deformation when inferring earthquake magnitude from paleoseismic offsets.

Studies of coseismic and postseismic deformation of earthquakes which occur within the historical record can be used to provide valuable field data where moment magnitude, coseismic surface offset, postseismic deformation and rupture length can be independently observed. These parameters can then be used in regression analyses to produce empirical relationships which relate, for example coseismic surface offset to moment magnitude (e.g. Wells & Coppersmith, 1994, Fig. 2.3.3). These empirical regression relationships enable paleoseismic studies to estimate the moment magnitude of a paleoearthquake by measuring its offset. The mapped length of an active fault can also be used as a proxy for potential maximum earthquake magnitude, in the case where the entire fault was to rupture.

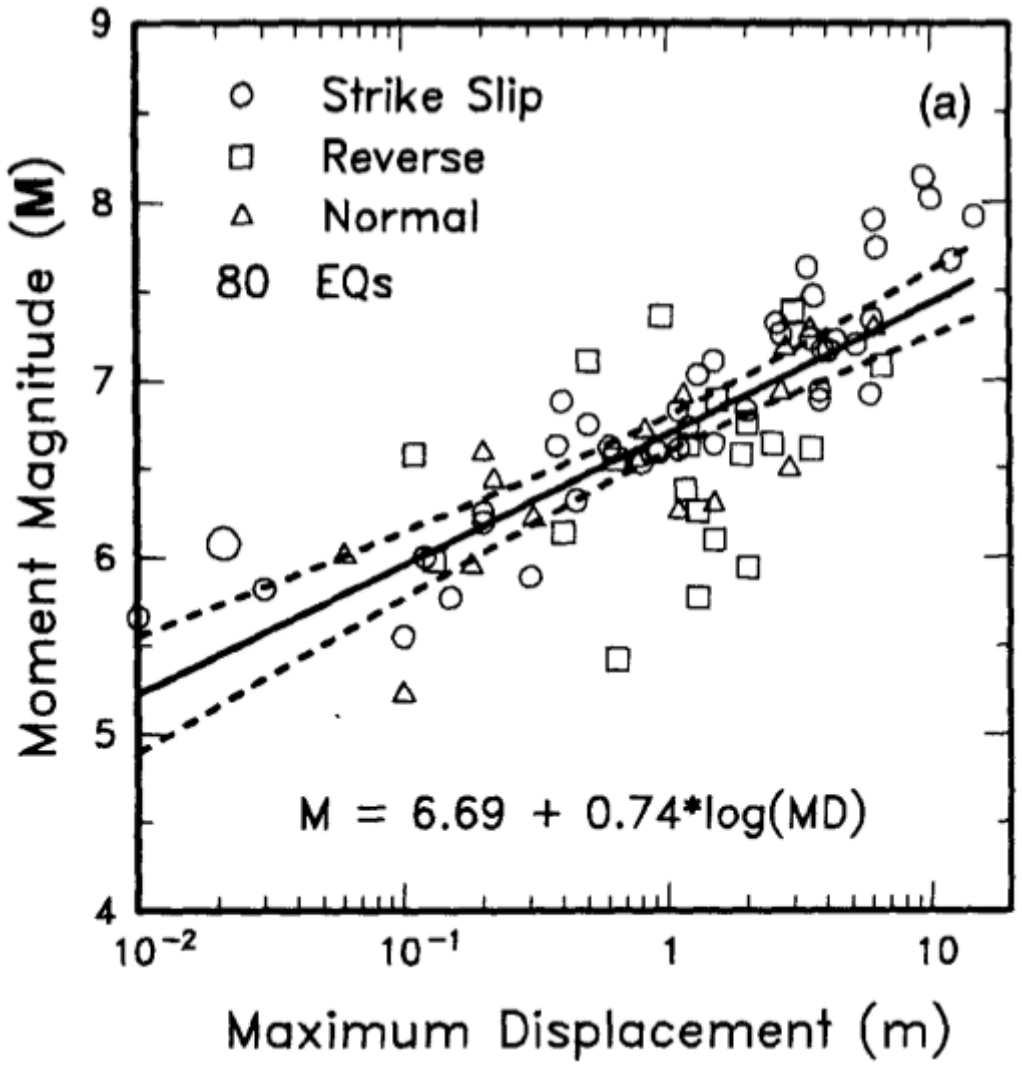

Figure 2.3.3: Regression of maximum surface displacement on moment magnitude. Regression line is for all slip types combined. The dashed lines represent ±95% confidence interval. (after Wells & Coppersmith, 1994).

2.3.1. Measuring postseismic deformation

Studies of postseismic deformation and afterslip have been carried out since it was first noticed following the 1966 Parkfield earthquake [Smith & Wyss, 1968]. The use of new technology since this time has allowed for studies to be conducted with increasing detail and precision, and are enabling new insights into the nature and

magnitude of postseismic deformation. The study of displacement following the 1966 Parkfield earthquake (~6 Mw) was carried out by surveying a small scale geodetic network to the SE of Parkfield using a theodolite [Smith & Wyss, 1968]. Measurements were taken at distances of up to 100 m across the fault at intervals of every three days during the first month, then every ten to thirty days. In the same study a strainmeter and tiltmeter were installed following the 1966 Parkfield earthquake. The strainmeter covered an 8 m length across the fault and was buried in a trench at 2 m depth. The rate of displacement following the earthquake decreased in a logarithmic fashion from 10 mm / day two days after the earthquake to 0.17 mm / day one year after. The postseismic deformation was measured to be ~21 cm, which is double the estimated coseismic offset of 10.3 cm, based on the seismic moment. The use of geodetic surveying equipment as well as strain and tilt meters allowed postseismic deformation to be accurately documented for the first time. The study identified the characteristic decay rate and the large relative magnitude of postseismic deformation in relation to coseismic slip for the Parkfield 1966 moderate magnitude earthquake (~6 Mw).

Afterslip following the 1976 7.5 Mw Guatemala earthquake [Bucknam et al., 1978] was recorded using a total station survey at seven locations along the surface rupture. The earthquake displacement was measured at 60cm, four days after the earthquake, which through the process of afterslip increased to ~91 cm in the twenty months following the earthquake. Given the moderately high magnitude of this earthquake, significant afterslip (up to 50% of the coseismic displacement) was observed following the earthquake. The afterslip measured at all sites was found to follow a logarithmic law with time. The use of total station technology available at this time allowed for afterslip measurements to be taken with sufficient precision

(measurements are quoted in the range of half a millimetre to a millimeter) to enable the definition of the decay law and magnitude of afterslip at each site.

Near-field postseismic deformation was measured following the 1992 7.3 Mw Landers earthquake, which ruptured four separate major faults, covering a distance of 85 km [Sylvester, 1993]. The measurements were recorded using a total station distance meter, across six separate quadrilateral arrays six months after the earthquake. Using this method the authors of the study defined the precision of the measurements as ±2 mm. The ratio of afterslip to coseismic slip was found to be very low for this earthquake. In most cases coseismic slip was on the order of 3 m, whereas the afterslip measured was between 2 – 40 mm (±2 mm), between 10 – 190 m distance from the fault. The authors cite the lack of alluvial cover and the presence of basement rocks at the surface as a potential reason why significant afterslip did not occur in this region following the earthquake. The use of up to date total station technology allowed precise measurements at a limited number of locations to be made at significant distances from the fault and the limited amount of afterslip following this earthquake was precisely defined.

A study of postseismic creep following the 2003 6.5 Mw Chengkung earthquake (Eastern Taiwan) was carried out at three surface rupture sites using a combination of creep meter, levelling, total station and GPS measurements [Lee et al., 2006]. Creep meter measurements were carried out on a daily basis, with the other measurements taken 20–25 days before, 20–25 days after, and 120–125 days after the earthquake. The measurements show 1-2 cm of coseismic displacement, while significant near-field postseismic deformation of 7-9 cm was recorded within the first 120 – 125 days after the earthquake. The study accounts for the significant near-field postseismic deformation observed due to the velocity strengthening properties of

unconsolidated material (mudstone) within the fault zone, which is estimated to be between 25 – 100 m depth and is thought to have locked during coseismic slip. The near-field deformation of this thrust fault earthquake was observed as anticlinal folding in the hangingwall and synclinal folding in the footwall. Far-field measurements of postseismic deformation were collected using three continuous GPS stations, which showed shortening at distances of up to 2 – 3 km from the surface rupture. The magnitude of the far-field measurements were reduced compared to the near-field and the study did not have sufficiently dense GPS coverage to define the rate of decrease with distance from the surface rupture, although the authors do note that the high magnitude of near-field postseismic deformation suggests that postseismic deformation is a shallow mechanism within the fault zone.

GPS technology has been used in the past to study postseismic deformation following a number of earthquakes, including the 2004 Parkfield and 2009 L'Aquila earthquakes [Langbein et al., 2006, Freed, 2007, Cheloni et al., 2010]. The main advantage of GPS technology is that it is the only widespread technology which can measure far-field deformation. Permanent, continually run GPS networks provide an insight into far-field coseismic deformation, while temporary networks with denser coverage provide far-field measurements of postseismic deformation. The precision and rate of modern dual-frequency GPS equipment means that deformation can be measured with errors of around ±2 mm at intervals as low as thirty seconds. The coseismic and postseismic deformation field measured by GPS can be inverted to provide models of coseismic and postseismic slip within the fault zone, as was conducted for the 2004 Parkfield [Langbein et al., 2006] and 2009 L'Aquila earthquakes [Cheloni et al., 2009]. From these models of fault slip, it was found that postseismic slip in the fault zone generally occurs at the periphery of the coseismic

slip patch, due to the differences in stress between the coseismic slip patch and the fault zone at its periphery. The disadvantage of GPS studies is that they do not define near-field postseismic deformation, due to the large multi-kilometer spacings of GPS stations. Also, any deformation field which is calculated is only based on GPS measurements from a limited number of stations, usually less than ten. This means that the resolution of the measurements is coarse and it is difficult to identify and eliminate any anomalous GPS measurements created due to ground instability.

The introduction of InSAR (Interferometric Synthetic Aperture Radar) during the early 1990's, in which the phase difference between microwaves emitted from satellites is measured, provided a new method to remotely sense surface deformation. InSAR is used to measure coseismic and postseismic surface deformation following earthquakes [e.g. Ryder et al., 2007] and to monitor volcano surface deformation [e.g. Pritchard & Simons, 2004]. The advantage of InSAR studies over GPS is that the entire deformation field can be calculated in the far-field at a resolution of around 100 m. Observations in the near-field are limited by the 100 m pixel spacing. The precision of InSAR is often quoted on the order of 1 - 2 mm, however the deformation fields calculated (so called interferograms) only show close to vertical deformation due to the downward looking view from a satellite and often have patches of noise where the signal becomes incoherant due to variations in vegetation, snow cover, cloud cover, moisture content and temperature of the air. The interferometric nature of this method means that large surface displacements over very short distances cannot be measured. This is due to the fact that only the phase difference between emitted and returning microwaves can be calculated, while large deformations may be on the order of multiple wavelengths. The period of acquisition of InSAR is limited by the orbit schedule of available satellites, which varies with time and location, but often

means periods of up at thirty days are common between measurements. The network of satellites capable of collecting data for use in InSAR studies is expanding and efforts are made following earthquakes to acquire data from as many satellites as possible.

A study of postseismic deformation following the 1997 7.6 Mw Manyi earthquake was conducted using InSAR observations for a period of 4 years after the earthquake [Ryder, et al., 2007]. The earthquake caused over 7 m of left-lateral displacement on the 200 km long Kunlun fault in Northern Tibet. A postseismic interferogram was produced using time-series analysis of 26 interferograms (Fig. 2.3.4). The postseismic interferogram reveals the northern side of the fault is downthrown with respect to the southern side (Figs. 2.3.4 & 2.3.5). The deformation decreases in rate over time. Three different models were used to try to understand the variation in surface displacement seen in the postseismic interferogram. The study found that a first order poroelastic model and a Maxwell viscoelastic halfspace did not fit the observed displacements. A model of viscoelastic stress relaxation, with linear solid rheology beneath an elastic lid provided a closer fit to the deformation, with two relaxation times used to fully characterise the postseismic transient. The study also found that the maxima for coseismic and postseismic deformation within the fault zone coincided and suggested afterslip as a plausible mechanism. The maximum modelled afterslip was 0.72 m after three years, representing 20% of the coseismic moment release.

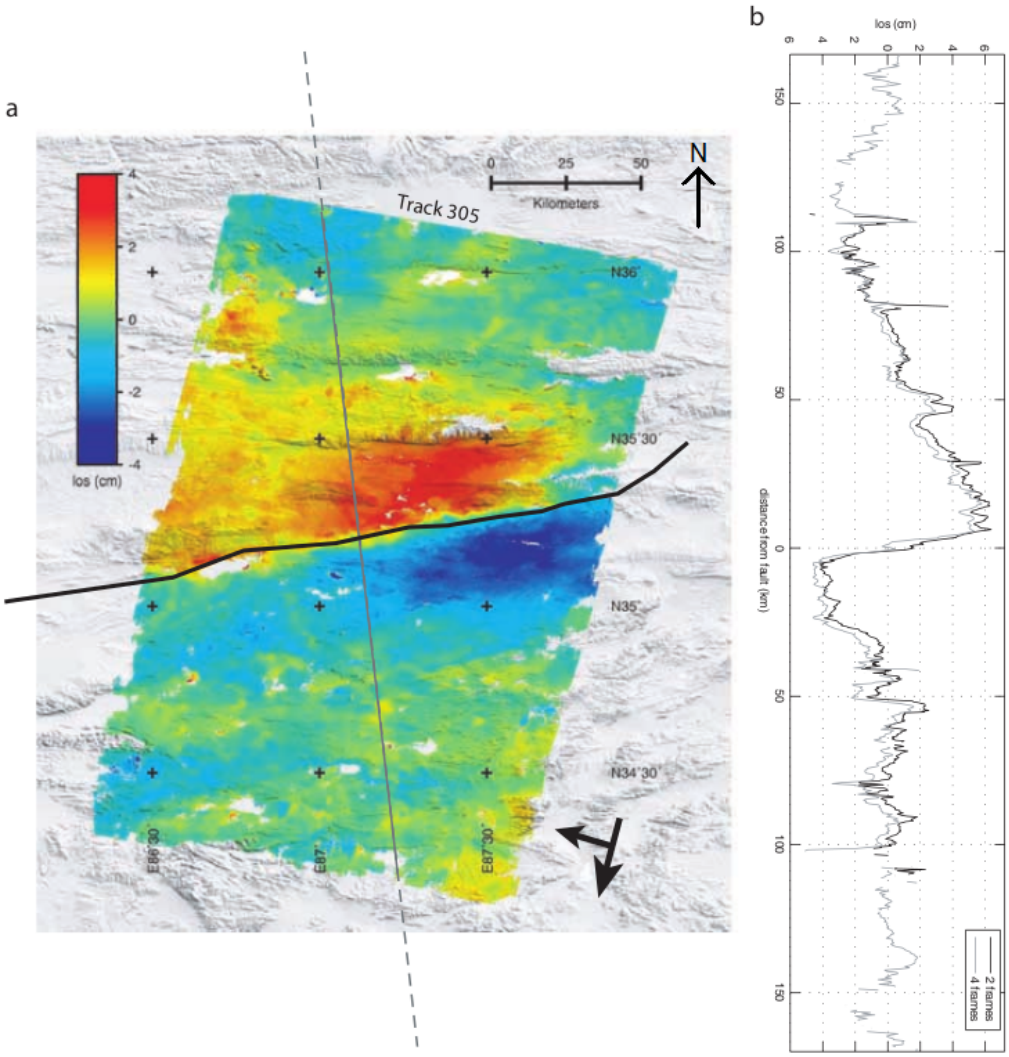

Figure 2.3.4: (a) Postseismic InSAR interferogram for time period 1997-12-02 – 1998-08-04. (b) Profiles through the interferogram along the gray line in (a), for two frames and four frames respectively (after Ryder et al., 2007).

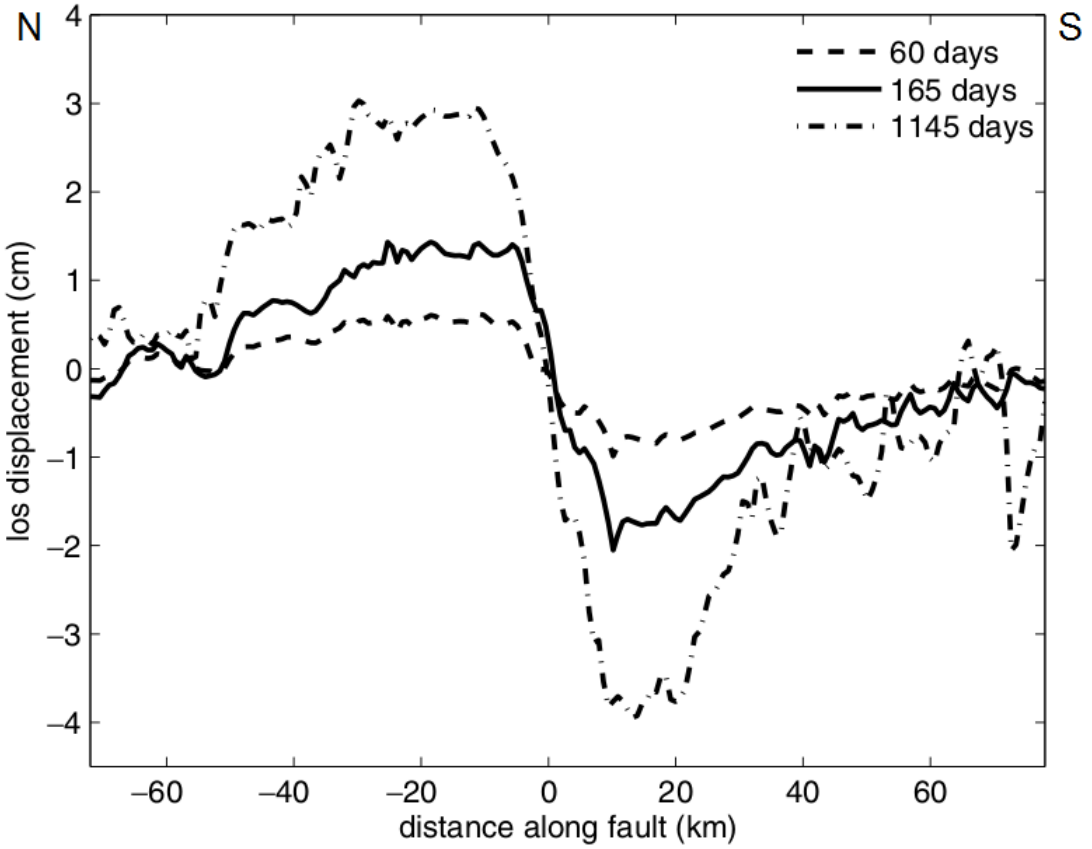

Figure 2.3.5: InSAR interferogram profiles perpendicular to strike for line of sight displacement through the centre of the fault (see fig. 2.3.4). Time spans are 60, 165 & 1145 days (after Ryder et al., 2007).

The use of airborne LiDAR (ALSM) technology has recently allowed data to be collected which begins to bridge the gap between far-field and near-field datasets. The first study of this kind was conducted using differential-LiDAR to reveal near-field deformation following the 2010 7.2 Mw El Mayor-Cucapah strike-slip earthquake (Baja California) [Oskin et al., 2012]. A high resolution ALSM dataset of the earthquake surface rupture (up to 9 measurements per square metre) was acquired following the earthquake and compared with a lower resolution pre-earthquake ALSM dataset. The elevation of the terrain was compared pre- and post-earthquake in order to produce a map of the postseismic deformation in the near to far-field

following the earthquake (Fig. 2.3.6). The resultant deformation map shows the distribution of deformation as the earthquake slip propagated from the termination of one fault and across onto a neighbouring fault. The deformation map also shows how the ground has moved downwards on one side of the fault and upwards on the opposite side of the fault, in agreement with the slip direction. The deformation map also shows deformation past the present tip of one of the faults, where slip at depth has deformed the surface across a broad area. The use of ALSM technology to measure coseismic and postseismic deformation provides a means to measure deformation precisely from the near-field to the far-field in one dataset. The disadvantage of ALSM in relation to ground based studies is the need for pre-earthquake datasets, which are growing in number, but still relatively sparse. There is also the extra cost and organisation required to acquire each dataset, especially in the case where multiple flights are required to measure the development of postseismic deformation. The results however provide a significant step forward in providing the data required to increase understanding of the relationship between near-field and far-field postseismic deformation.

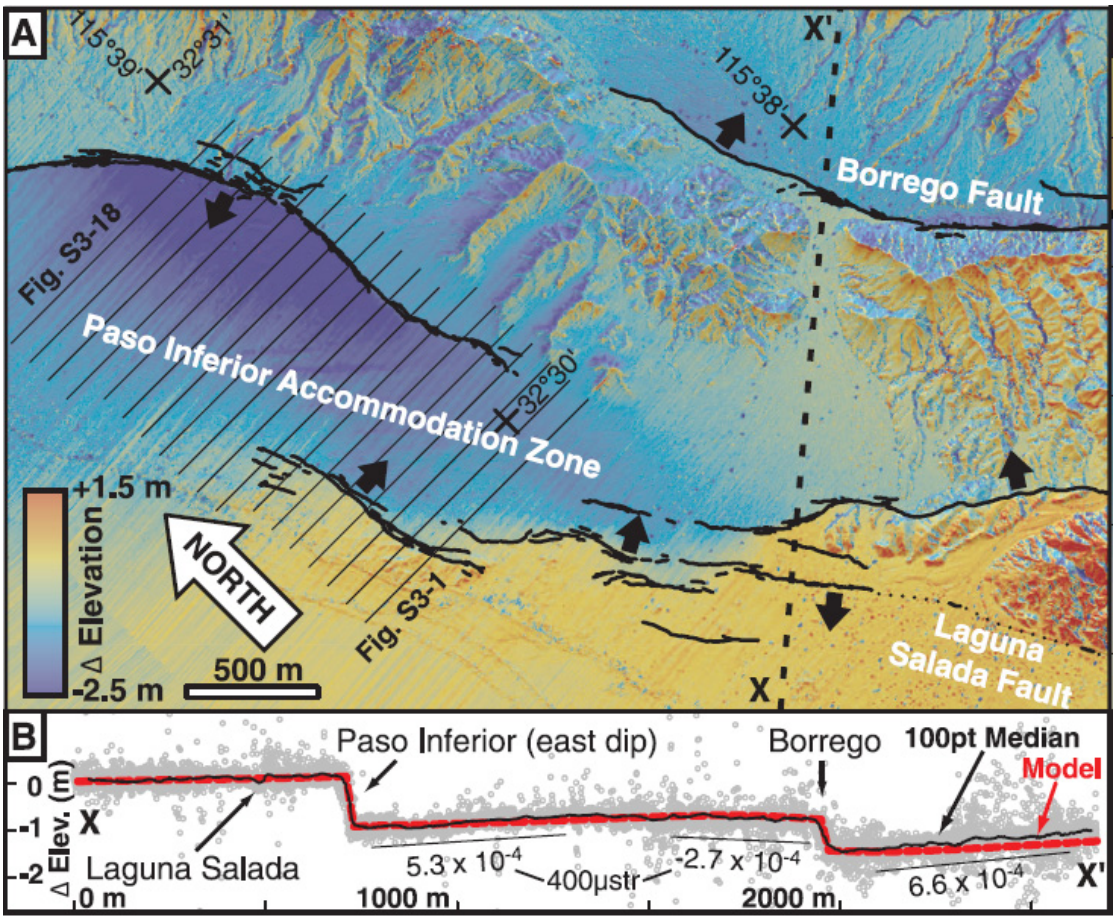

Figure. 2.3.6: (a) Differential LiDAR map showing the distributed deformation between pre- and post-earthquake. (b) Cross section between X – X' showing downward deformation and uplift / backtilting in correspondence with the observed slip direction on the major faults (after Oskin et al., 2012).

2.3.2. The role of TLS in postseismic offset studies

Terrestrial laser scan (TLS) technology provides a means to acquire high resolution data of earthquake surface ruptures at distances of up to 1000 m from the scanner. TLS can be used to measure postseismic deformation in the near-field by repeat scanning surface ruptures in the days, weeks and months following an earthquake. The initial dataset can then be compared to all subsequently collected datasets in order to produce a highly detailed map of postseismic deformation and

afterslip. TLS has the ability at close range to make measurements with spacing of less than ten centimetres. Such datasets can be used to create incredibly detailed and precise maps of surface deformation. The main advantages of TLS technology over theodolite, ALSM, InSAR and GPS studies is the ability for the equipment to be operated by one or two people in the field, the unprecedented detail of the data acquired and the ability to collect measurements on a daily basis. TLS technology can complement traditional survey methods of near-field postseismic deformation and can be used to compare the magnitude of near-field deformation with measurements of far-field deformation using other technologies. One of the most exciting applications is the merging of TLS and ALSM datasets, which will allow for seemless comparison of postseismic deformation from the near-field in high resolution to the far-field. The application of TLS technology to measure near-field postseismic deformation forms the basis of the study covered in Chapter 5.

2.3.3. The 2009 L'Aquila earthquake

The 2009 6.3 Mw L'Aquila earthquake was the most recent major earthquake to occur in the central Apennines. The earthquake produced a discontinuous surface rupture, along the base of the Paganica fault. The rupture was mapped during a number of studies which defined the primary surface rupture length to be between 2.6 – 18 km and the maximum vertical coseismic surface offset was 10 cm [Falcucci et al., 2009, Boncio et al., 2010, Vittori et al., 2011, Emergeo Working Group, 2010] (Fig. 2.3.7). The study by Vittori et al., (2010) commented that evidence of surface rupturing was likely to be only within a 2.6 km length, with ground cracks outside of this length attributed to sympathetic affects and secondary slip on an array of other faults around the Paganica fault. A fault rupture length of ~2.5 km was also proposed

by the Emergeo working group [Emergeo Working Group, 2010]. The strike of the surface rupture was between 130 – 140° [Boncio et al., 2010]. The direction of slip of the earthquake on the fault plane was defined to be 218° ±5°, by measuring of opening direction of the rupture [Roberts et al., 2010, Wilkinson et al., 2010]. The dip of the Paganica fault was defined as 54°, through analyses of coseismic InSAR and body wave seismology [Walters et al., 2009]. The source of the L'Aquila seismicity was attributed to the Paganica fault, through study of body wave seismology [Walters et al., 2009] and InSAR studies of coseismic deformation [Atzori, et al., 2009, Walters et al., 2009, Lanari, et al., 2010, Papanikolaou et al., 2010]. The far-field coseismic deformation was measured to be up to 30 cm downward deformation in the hangingwall of the Paganica fault, with a 1/3 footwall uplift to hangingwall subsidence ratio after the mainshock [Papanikolaou et al., 2010]. Studies of coseismic deformation obtained from InSAR [Atzori, et al., 2009, Walters et al., 2009, Lanari, et al., 2010, Papanikolaou et al., 2010] and geodetic measurements [Cheloni et al., 2010] are in broad agreement.

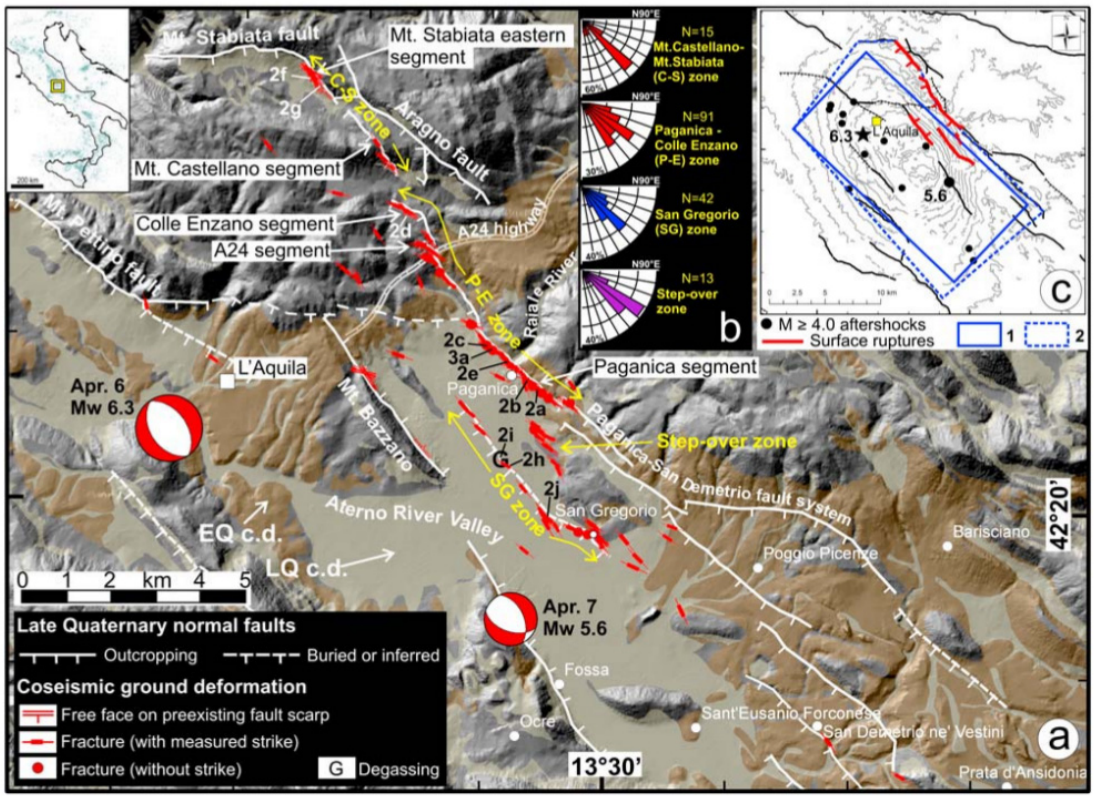

Figure 2.3.7: (a) Surface rupture and fracture map of the Paganica fault zone and surrounding areas. Surface rupture and fractures shown in red, active normal faults with Late Quaternary offsets are shown in white. The main surface rupture is to the north of the village of Paganica. The epicentre of the April 6th earthquake is shown by the focal mechanism to the South-West of L'Aquila. (b) Rose diagrams for strike of the different fault strands in (a). (c) Map of slip within the fault zone, the main earthquakes of the 6th and 7th April and the largest aftershocks (after Boncio et al., 2010).

The postseismic deformation of the L'Aquila earthquake was measured in the near-field using a robotic total station across the surface rupture near the village of Paganica [Degasperi, 2010] and using two laser strain meters in two tunnels at 1400m depth, 20km to the North-East of the epicentre [Amoruso & Crescentini, 2009]. Far-field postseismic studies were conducted using campaign GPS [Cheloni et al., 2010]

and InSAR [Lanari et al., 2010]. The near-field postseismic deformation measured using a robotic total station decayed in rate over time, which is indicative of the process of afterslip within the fault zone [Marone et al., 1991] and is comparable to deformation measured using similar methods from other earthquakes [Bucknam et al., 1978, Williams & Magistrale, 1989, Koukouvelas & Doutsos, 1996]. The regions in the far-field which experienced significant postseismic deformation in both the GPS and InSAR measurements were found to be located on the periphery of the coseismic slip patch within the fault zone (Fig. 2.3.8, after Cheloni et al., 2010), in a similar manner to that observed following the 1966 and 2004 Parkfield earthquakes (Fig. 2.3.9, after Bakun et al., 2005).

Paleoseismic study of the Paganica fault revealed evidence for two past earthquakes dated 1703 A.D. & 801 A.D. and a last glacial maximum (20 ka) to present day slip-rate of 0.4 mm/yr [Galli et al., 2010]. Evidence for Late Pleistocene - Holocene activity from radiocarbon dating from separate studies of offset colluvium [Falcucci et al., 2009] defined a slip-rate of ~0.24 mm/yr [Boncio et al., 2010]. The recurrence interval of the Paganica fault after ~1000 A.D. was estimated to be on the order of ~500 yrs, however only two events occurred in the preceding 4000 years before ~1000 A.D., suggesting a much longer recurrence interval (1000-2000 yrs) over this time period [Cinti et al., 2011]. The segmented en-echelon structure of the Paganica fault and a slip-rate of 0.23 – 0.4 mm/yr was revealed through a study of subsurface paleoseismic offsets using ground penetrating radar [Roberts et al., 2010]. Surface mapping of the 2009 surface rupture showed that it bypassed the en-echelon segmentation by stepping across a relay zone onto another fault strand, highlighting the complexity and variability of repeated surface rupture along this fault. A paleoseismic offset for the L'Aquila earthquake was unable to be reliably identified

from trenching studies, due to its small magnitude [Galli et al., 2010]. This conclusion has implications for the ability of paleoseismic studies to detect a complete record of moderate-magnitude earthquakes, which in turn has implications for hazard analyses, given the significant death toll of 308 for the 2009 L'Aquila earthquake. The relatively low slip-rate of the Paganica fault, compared to the major range bounding normal faults in the region has lead to a poor geomorphic expression in the present day topography [Walters et al., 2009], which meant that the activity of the fault was underestimated during hazard analysis. This unfortunate oversight has important implications for hazard analysis in the Apennines. The L'Aquila earthquake has taught us that faults such as the Paganica fault with low Late Pleistocene - Holocene slip-rates (0.24 - 0.5 mm/yr) can have poor geomorphic expressions, but can still pose a significant seismic hazard. Further paleoseismic investigation of this fault and other faults like it is required to define their recurrence interval and slip-rate over a range of time periods and to understand their potential seismic hazard.

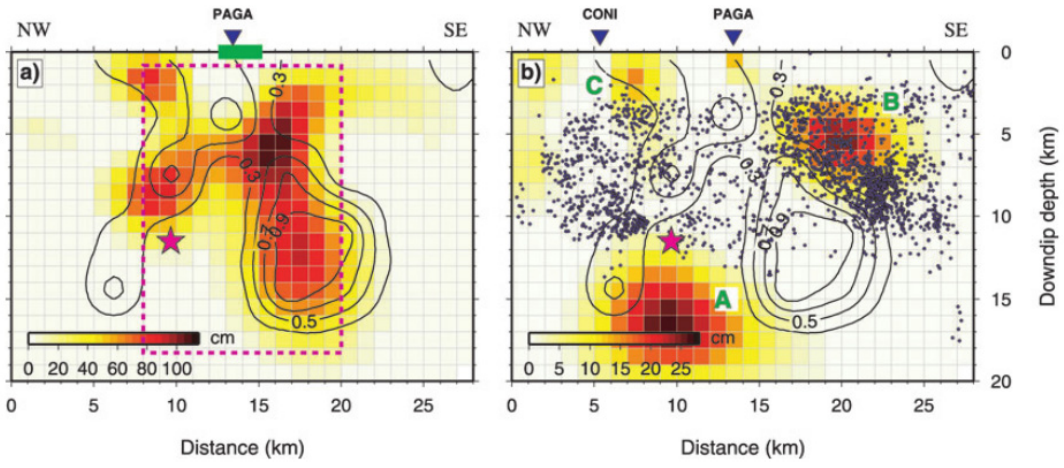

Figure 2.3.8: (a) Modelled coseismic slip within the fault zone for the L'Aquila earthquake. The zone of surface rupturing is shown by the green box. (b) Modelled postseismic slip within the fault zone, occurring at the periphery of the regions of

coseismic slip and correlated with high density regions of aftershocks (after Cheloni et al., 2010).

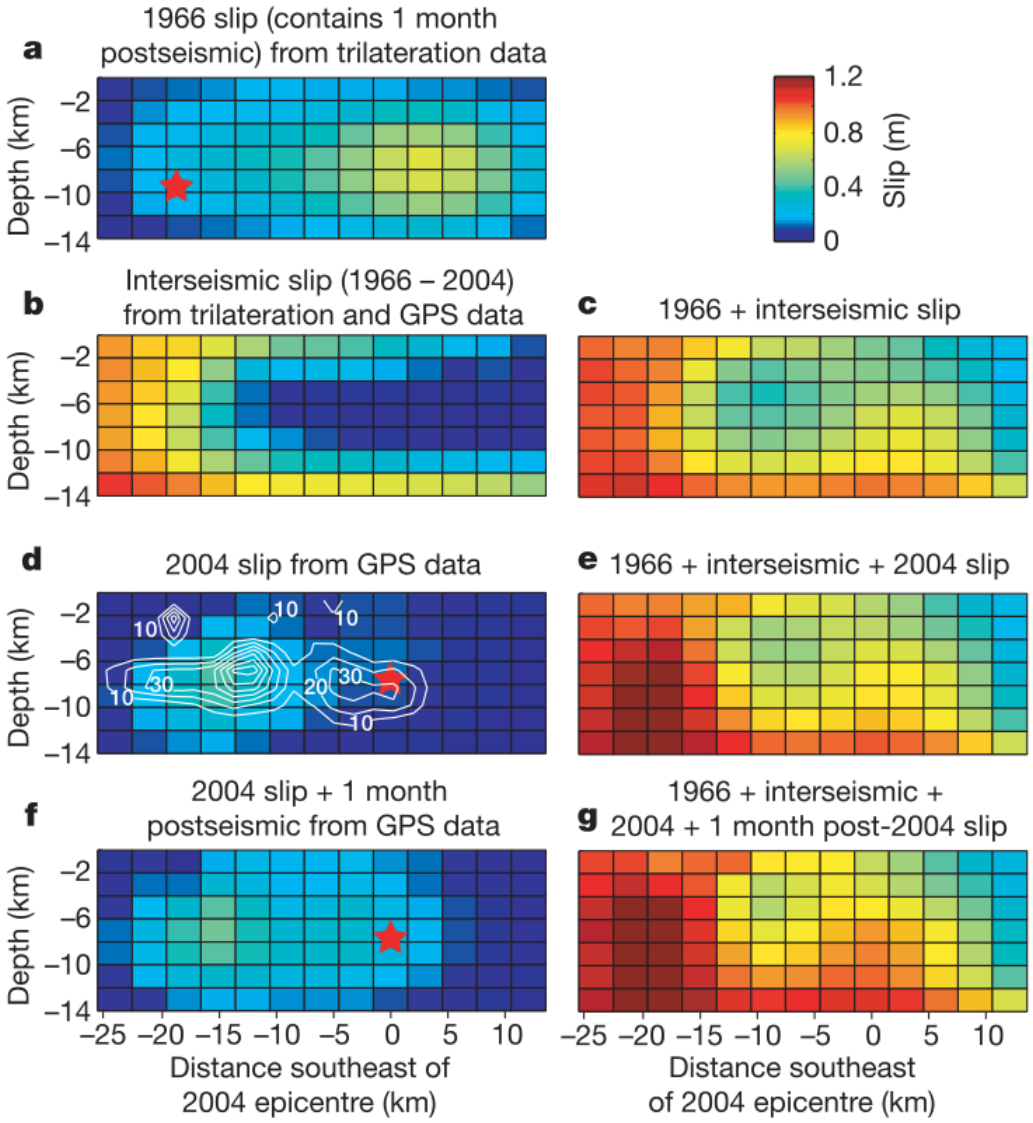

Figure 2.3.9: Distribution of slip along the San Andreas Fault since 1966, estimated from geodetic data. The slip models show how slip during earthquakes (coseismic and postseismic) combines with aseismic slip between earthquakes to generate a cumulative offset across the fault (after Bakun et al., 2005).

Chapter 3: Methods

This chapter introduces the methods developed for use in the various studies within this thesis. Three methods are described in separate sections with conclusions at the end of each section. The sections are as follows:

3.1. Mapping the geomorphology of active normal faults using terrestrial laser scan datasets

3.2. Extracting normal fault throw-rate profiles from terrestrial laser scan datasets

3.3. Modelling postseismic surface motion using repeat terrestrial laser scanning

3.1. Mapping the geomorphology of active normal faults using terrestrial laser scan datasets

3.1.1. Introduction and rationale

Studies of normal fault surface offsets [Roberts & Michetti, 2004, Mouslopoulou et al., 2009] and ^{36}Cl exposure dating of fault scarps [Palumbo et al., 2004, Schlagenhauf et al., 2010] aim to reveal the slip-rate and earthquake recurrence interval of individual faults and fault systems. These studies rely on the creation of surface offset and scarp exposure purely through the mechanism of fault slip during earthquakes. Geomorphic processes that take place along active normal faults are also able to reduce surface offset and scarp exposure and thus compete against fault slip. In order to select suitable study sites for slip-rate determination, it is necessary to map the geomorphology and understand the effects of active geomorphic processes present along the fault to be studied.

Terrestrial laser scan (TLS) datasets provide a new approach to mapping the geomorphology of active normal faults. TLS datasets provide an accurate

representation of the real world topography, to such a degree that subtle changes in slope can be used to identify important geomorphic features. A terrestrial laser scanner is a tripod mounted ranging machine (Fig 3.1.0) which acquires a point cloud dataset by using the time of flight of sequentially emitted and reflected laser pulses to calculate the range between the laser scanner and objects within its line of sight (Fig. 3.1.1). By incrementally adjusting the emission direction in horizontal and vertical steps, the scanner is able to sample reflections on a regularly spaced grid within the line of sight of the scanner. For each laser return a unique point in 3D space is calculated, with individual returns populating a point cloud dataset (Fig. 3.1.2). Laser returns can occur from the ground surface, bare rock, vegetation or other similar objects such as fence posts and buildings. In order to locate (geo-reference) the 3D point cloud datasets in their real-world position, it is necessary to survey the location of four or more cylindrical reflectors (11.0 – 22.5 cm diameter) using a GPS system. A real time kinematic (RTK) GPS system provides a means to acquire reflector positions with sub-centimetre precision, with the GPS being located at each reflector for only a couple of seconds. The cylindrical reflectors are scanned with a high density of laser returns, in order that the scanner can calculate their exact position relative to itself. The point cloud dataset is then translated and rotated in a real world co-ordinate system until the surveyed GPS positions of the reflectors co-locate with the reflector positions within the point cloud dataset. Each individual point measurement within the laser scan point cloud dataset now has a real world co-ordinate attached and this data can now be extracted and used to measure distances between features, areas and volumes.

3.1.2. Methods

Vegetation removal from point cloud datasets

The first step in processing the point cloud is to remove all points which are not ground returns. This step can be carried out manually in the case of small study areas with limited vegetation by selecting and deleting vegetation from within a 3D viewer, such as *RiSCAN*. This process can preserve most of the ground points, with little degradation, although it can be unrealistically time consuming in the case of larger study areas. A sensible compromise is to remove the most easily identifiable patches of vegetation and lone trees manually before applying a vegetation filter or algorithm to the point cloud. In this study, a pseudo-vegetation filter was applied to the point cloud using the GEON *points2grid* software [Crosby et al., in review]. *Points2grid* was developed to create raster elevation grids from point cloud data. The software operates by allowing the user to define an output grid spacing *S*, which will determine the uniform point spacing in map view of the output pointset. The software also requires a search radius to be defined, and for the case of the pseudo-vegetation filter, the minimum elevation option selected. *Points2grid* in this case calculates the elevation value for each output point according to the minimum elevation found in the input pointset within the specified search radius *R* (Fig. 3.1.3). As a general rule, the search radius should be:

$$R = \frac{\sqrt{2}}{2} * S$$

The effect is that the points with vegetation have higher elevation values than the ground surface and are removed from the output pointset. A side effect of the process is that the input point cloud has a reduced point density and is re-sampled as a regularly spaced pointset. This can be beneficial, as the fewer points which are used to

represent the topography the more options are available for intensive post-processing to create derivatives for use in analysis. It is important however not to over-filter the data which can lead to over-simplification of the output pointset and the removal of the important topographic features which exist beneath the vegetation. As a rule, the work from this thesis found that an output point spacing of between 2 – 4 meters, with corresponding search radius R between 1.41 – 2.8 meters seems to be most suitable for the TLS datasets of active normal faults collected during this study. This search radius filters out vegetation from the point cloud dataset while preserving sharp changes in topography. Output point spacings of less than 2 m and corresponding search radiuses did not filter vegetation from the datasets, while point spacings greater than 4 m with corresponding search radiuses smoothed out important topographic features, such as the upper parts of fault scarps and upper slope surfaces in the footwall. Once the point cloud has been filtered to remove vegetation there are a number of derivatives which can be created from the dataset in order to identify geomorphic features.

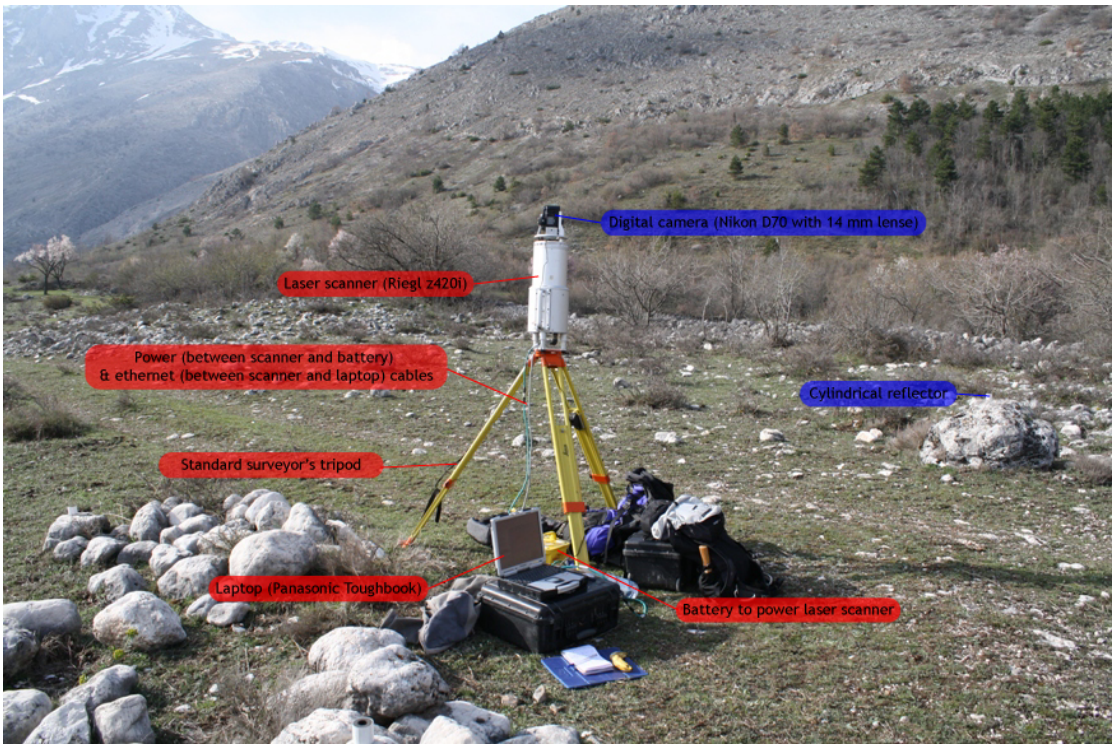

Figure 3.1.0: The components of a typical TLS setup. Essential components for acquiring a point cloud dataset are shown in red, optional components for acquiring a coloured, geo-referenced point cloud (camera & cylindrical reflectors) are shown in blue.

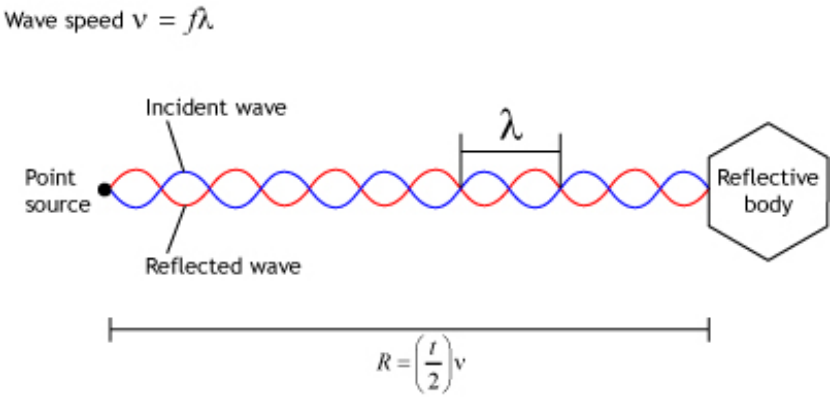

Figure 3.1.1: The use of light detection and ranging (LiDAR) to calculate the range (R) to a reflective body from a point source (the laser scanner). f = Wave frequency, λ = Wavelength.

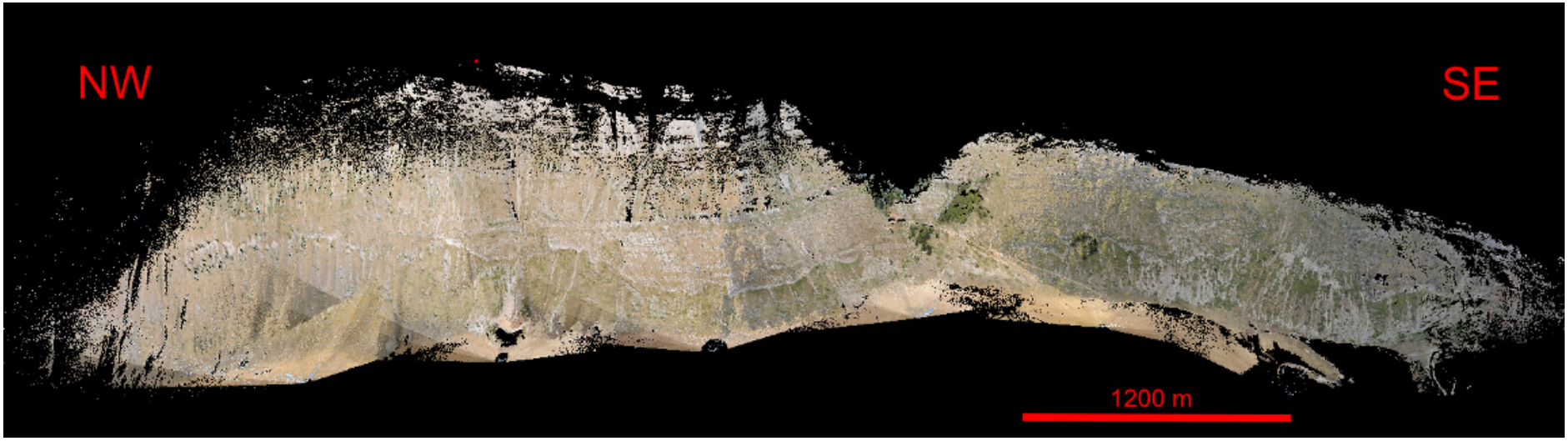

Figure 3.1.2: A raw laser scan point cloud dataset from the Campo Felice fault (location denoted by ‘CF’, Fig 1.1).

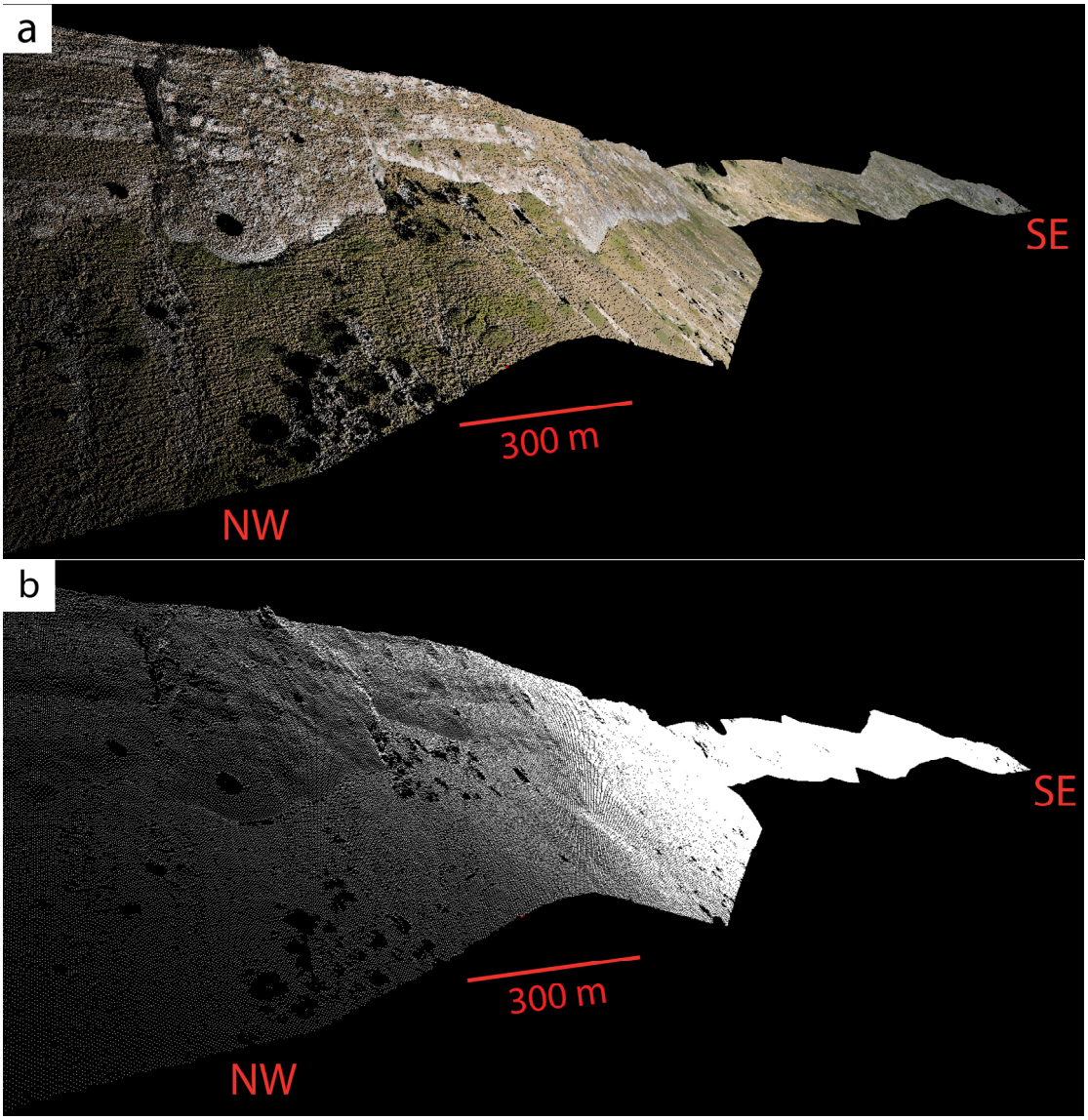

Figure 3.1.3: The point cloud dataset from Figure 3.1.2 filtered using: (a) Manual removal of points representing vegetation, followed by (b) the *points2grid* pseudo-vegetation filter with output spacing 0.5 m. In the regions which passed the vegetation filter, the points are now regularly spaced. This provides a dataset of homogeneous point density to work with.

Surface generation

The generation of a solid surface from a point cloud dataset produces an advantageous visualisation of the topographic point cloud dataset. A solid surface

representation of the topography is created using the vegetation filtered pointset as input. The simplest way to create a representative surface from a pointset is by the creation of a triangular irregular network (TIN). A TIN is a triangulated mesh, whereby the vertices of each triangle are located using the input pointset. It is essentially a method of joining the points together and filling the internal space between three points with a plane. The most common method of choosing groups of three points to form triangles is through Delaunay triangulation [Delaunay, 1934], whereby all points are used as triangle vertices, such that no triangles can be subdivided using points located within a triangle and that the smallest angle of each triangle is the largest that it can be. The process favours the triangulation options which produce equilateral triangles and so triangles with very large differences between their side lengths are avoided. A major advantage of surface generation by TIN using Delaunay triangulation over more complex routines is that the process is computationally efficient. The point cloud processing software *RiSCAN* is able to generate TIN surfaces from point cloud datasets using Delaunay triangulation (Fig. 3.1.4). The generation of a TIN surface, with lighting applied from a unidirectional source allows immediate identification of the base of the fault scarp. Footwall gullies, hangingwall erosional channels, the larger landslips and alluvial fans are also immediately identifiable (Fig 3.1.4).

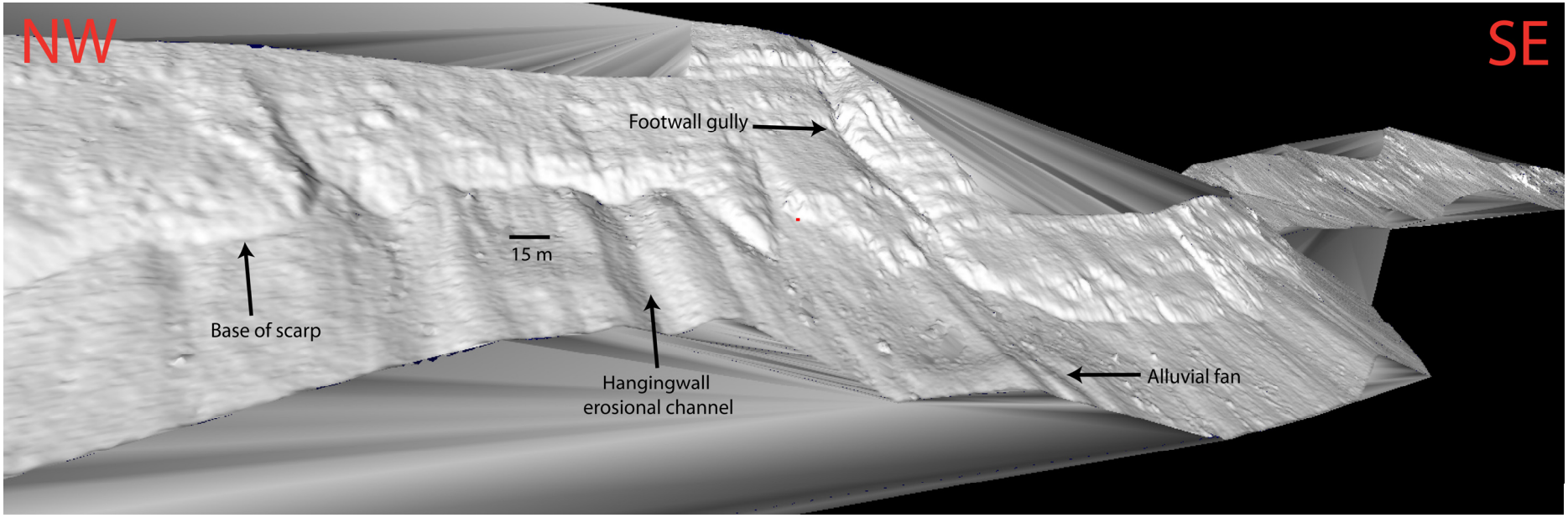

Figure 3.1.4: A TIN surface generated in *RiSCAN* for the filtered point cloud dataset shown in Figure 3.1.3. Note the base of the scarp, as well as the presence of footwall gullies, hangingwall erosional channels and alluvial fans.

Hillshade generation

Surface generation through triangulation methods is a useful tool for those users who have access to the necessary programs with which to view such surfaces in an interactive 3D environment, such as *RiSCAN*. A big drawback exists when the needs comes to share the data with a colleague who does not have access to such programs. A suitable workaround is to generate a hillshade raster from the point cloud dataset and embed this within a *Google Earth* .kmz file. This approach allows the data to be viewed by any individual with *Google Earth* installed on their machine. The command line program *las2dem* is part of *lastools* [Isenberg & Shewchuk], a set of tools for processing, converting and viewing lidar point cloud data. *Las2dem* can be used to create a hillshade raster from a point cloud dataset using the command line:

```
las2dem.exe -i input_pointset.txt -o output_raster.png -
utm 33T -hillshade -step 0.5 -light 1 1 3
```

The above command line will read the input pointset 'input_pointset.txt', triangulate the pointset using Delaunay triangulation into a TIN, then convert this TIN into a hillshade raster and output as the file '*output_raster.png*'. The argument '*-utm 33T*' will create a *Google Earth* .kml file to correctly georeference *output_raster.png* for viewing inside *Google Earth*. The argument '*-step 0.5*' produces a raster grid size of 0.5 meters. The argument '*-light 1 1 3*' controls the direction vector of the light source, used to illuminate the raster. The direction of the light source can be changed to illuminate features of interest in the resultant hillshade.

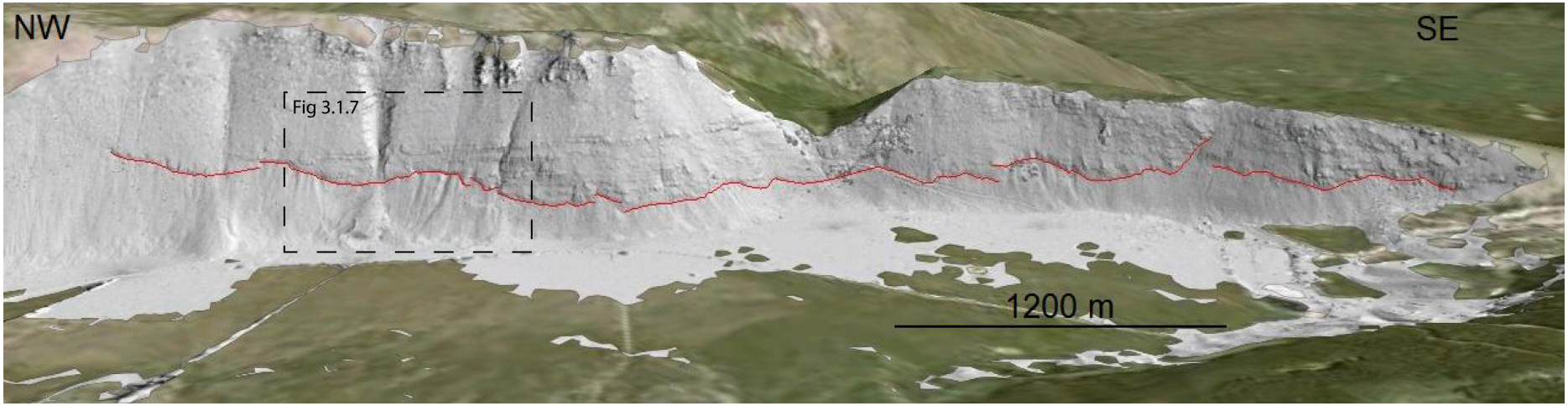

Figure 3.1.5: A hillshade raster for the dataset shown in Figure 3.1.3, created using *las2dem*, displayed in *Google Earth*. The trace of the Campo Felice fault is shown by the red line.

Surface dip map generation

A further enhancement to a TIN surface is to calculate the dip of each triangle from horizontal using the dip calculation algorithm in the program *goCAD*, and then to interpolate this data over the entire surface. These interpolated data can then be used to colour the surface according to the local dip, using a colour map, creating a surface dip map as shown in Figure 3.1.6. Surface dip maps allow a quantitative assessment of the surface to be carried out. Geomorphic features such as bowl shaped rotational slips and alluvial fans are clearly defined using this technique, as opposed to viewing the surface without a dip colourmap applied. The creation of a surface dip map also allows for the dip of the fault scarp, the hangingwall and the footwall to be visualised in their entirety, providing an important overview for the selection of suitable study sites for slip-rate cross-section analysis and ^{36}Cl exposure dating.

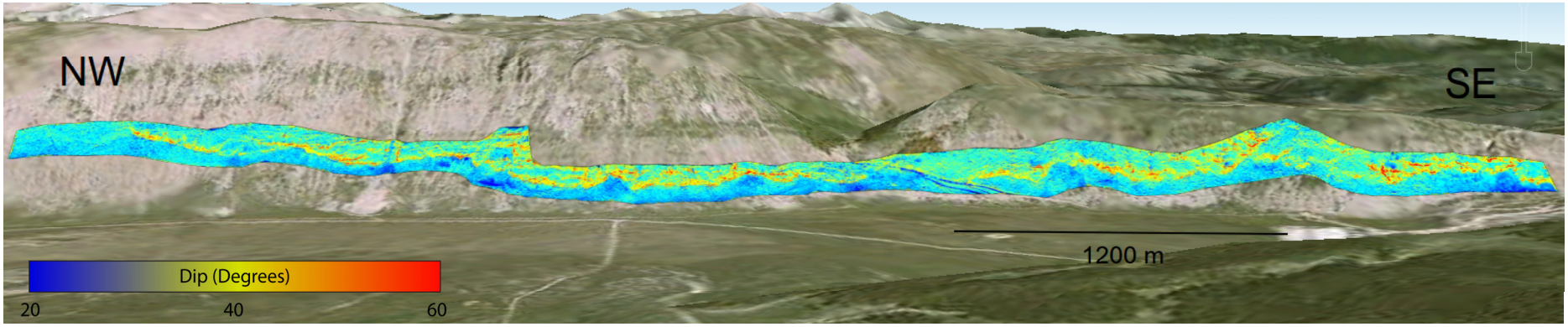

Figure 3.1.6: A surface dip map for the dataset shown in Figure 3.1.5, created using the dip calculation algorithm in *goCAD* and displayed in *Google Earth*. Blue colours correspond to low values of dip ~ 20 degrees. Yellow colours correspond to moderate values of dip ~ 40 degrees. Red colours correspond to high values of dip ~ 60 degrees.

Surface contouring

The generation of topographic contours (lines connecting points of equal elevation) allow a further method of surface assessment. Topographic contours are generated in *goCAD* using the contour algorithm from within *surface attributes* and are displayed on the surface, as shown in Figure 3.1.7. Topographic contours provide a means with which to measure the uniformity of a slope, for example the hangingwall of an active normal fault. Contours in a particular region of the hangingwall that are linear and equally spaced signify that this region of the hangingwall has not been modified by the geomorphic processes which could affect the measured fault slip. On the other hand topographic contours which are curved and non-equally spaced could signify geomorphic features such as rotational slips (Fig. 3.1.8), alluvial fans, erosional channels and footwall bedrock gullies.

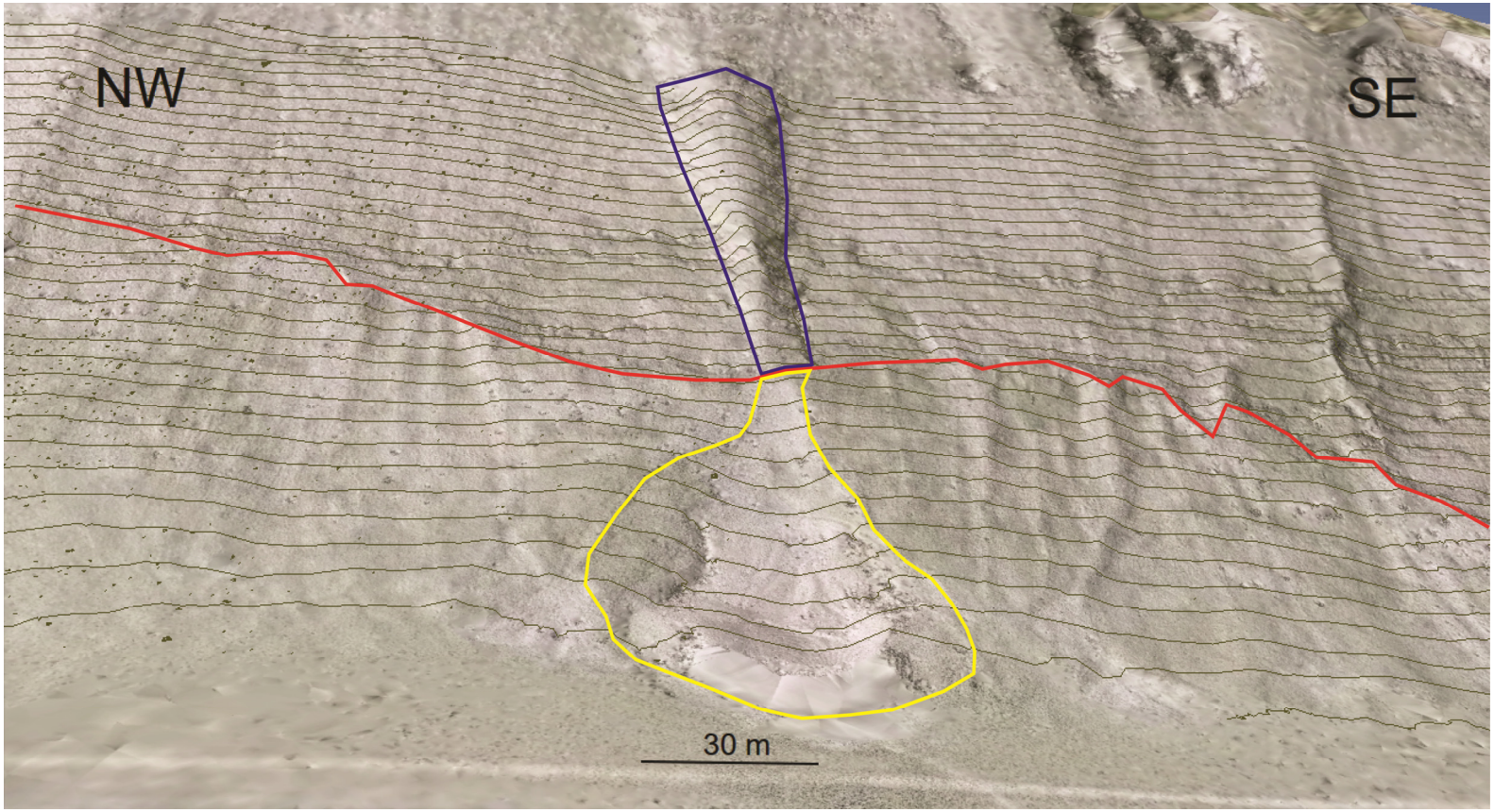

Figure 3.1.7: A hillshade raster for the dataset shown in Figure 3.1.3, with topographic contours of 10 m overlain and visualised in *Google Earth*. The red line shows the base of the fault scarp. The blue polygon depicts the extent of a footwall gully, with the yellow polygon showing the extent of a hangingwall alluvial fan fed by this gully.

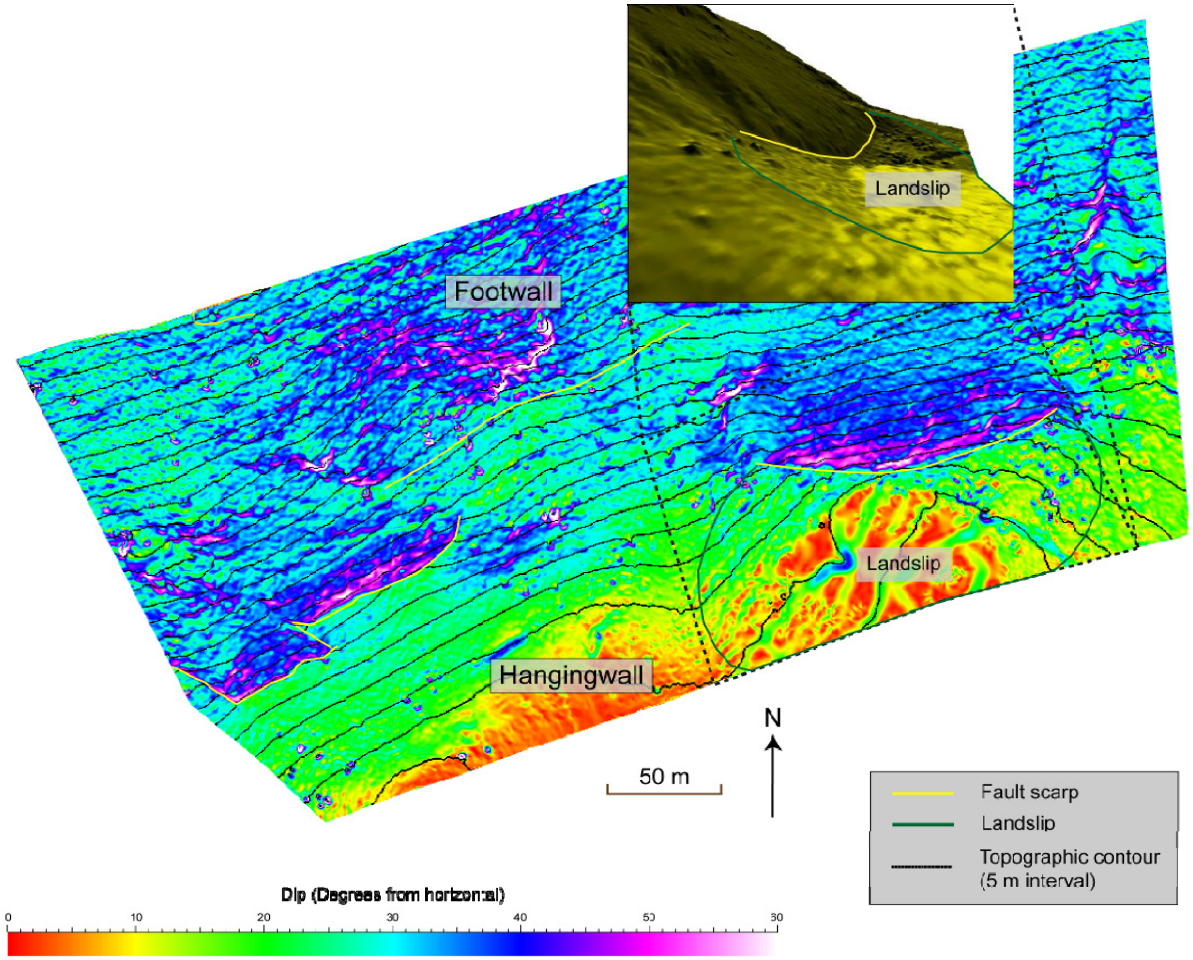

Figure 3.1.8: An example of a bowl shaped rotational slip in the hangingwall of the Tre Monti fault (location: TM, Fig. 1.1), distinguished by curved and irregularly spaced topographic contours. Colours represent surface dip.

Flow routing

Flow routing analysis produces a synthetic channel network of high flow accumulation channels across a TLS derived topographic surface. The analysis operates using the D8 algorithm [O'Callaghan & Mark, 1984], whereby the direction of flow from one pixel of a DEM to its neighbours is calculated, based on their relative elevations. The process is repeated for all pixels within the DEM to produce a representative channel network. The channel network can be used to visualise subtle changes in topography, based on local changes in surface aspect, which may allow the visualisation of particular topographic responses related to fault activity which would not be produced by other means. Classic examples of topographic response include the focussing of sediment transport through the relay zones of crustal scale normal faults [Densmore et al., 2003], as well as channel profiles which describe the change from incision in regions of uplift, to deposition in regions of subsidence [Kirby et al., 2003]. A flow routing analysis can be carried out on TLS data in most GIS packages, once the data has been interpolated to a surface raster. An example of a completed flow routing analysis for the Campo Felice fault is shown in Figure 3.1.9. The direction of flow within the footwall changes along strike in relation to the fault geometry. The direction of flow is always close to perpendicular to the strike of the fault. Changes in footwall flow direction can be used to infer the geometry of a fault whose exact geometry is obscured by a sedimentary drape.

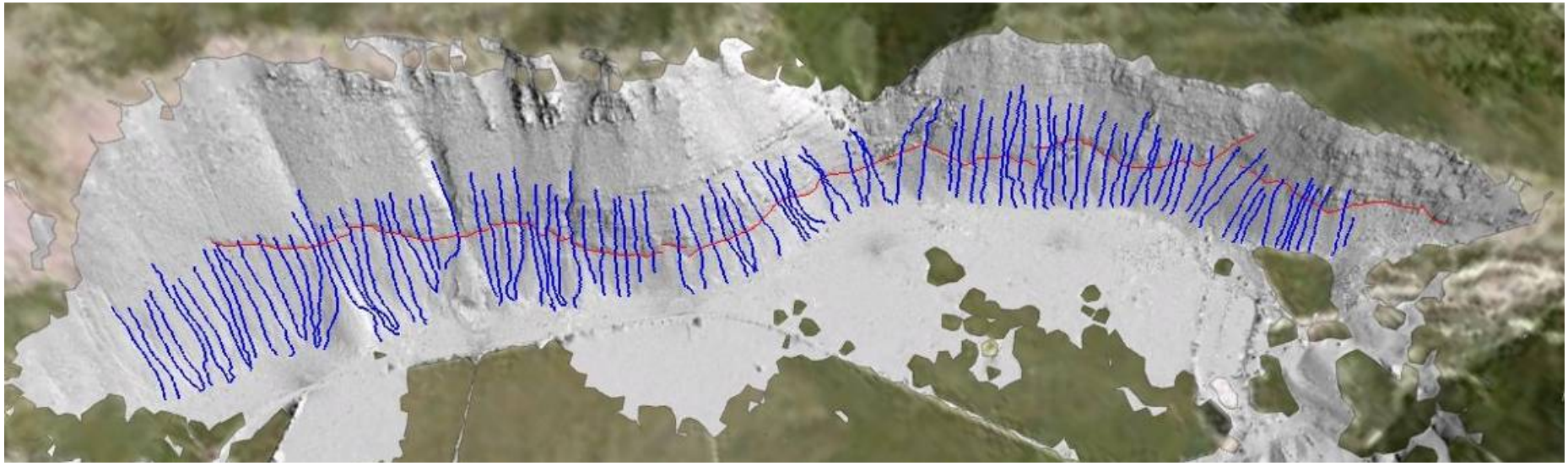

Figure 3.1.9: Flow routing analysis for the Campo Felice fault, displayed in *Google Earth* alongside the hillshade raster for the dataset shown in Figure 3.1.3. Blue lines represent regions of flow accumulation. The red lines represent the trace of the Campo Felice fault. Note the change in flow direction in response to fault strike.

Visualisation of subsurface data (GPR) alongside TLS data

Ground penetrating radar (GPR) is a geophysical method which samples the dielectric properties of the subsurface. A GPR survey can be used to provide subsurface reflectance data similar to seismic surveys. The portability of the GPR equipment as well as the high spatial resolution achievable makes GPR suitable for shallow, small scale surveys. Practical lengths of survey lines range from 3 m to many kilometres, with penetration depths of up to 15 m.

The hangingwall of a number of active normal faults in the Apennines have been surveyed with GPR, as part of an MSci thesis [Bubeck, 2009] that aimed to characterise the hangingwall geomorphology and shallow subsurface structure. The geomorphology of the hangingwall is an important property to quantify and map, as processes such as gullying and landsliding could increase the perceived throw on certain parts of the fault scarp despite not being related to seismic slip. The sites which were surveyed using GPR have also been laser scanned using the Riegl LMS-420i terrestrial laser scanner. A bowl-shaped landslip was identified in the TLS data for the Fiamignano Apennine normal fault (Fig 3.1.10). A GPR survey across the feature revealed a similar feature in the subsurface, complete with deformed strata (Fig. 3.1.11).

In order to visualise the GPR trace alongside the TLS derived topography of the survey site, a program *img2points* (Appendix i) was written for GNU octave to convert the processed GPR trace image into a pointset. The processed GPR trace image is loaded into *img2points* by the user. The pixel spacing of the length and depth axes are supplied to the program, as well as the co-ordinates of the start of the survey line and the bearing direction. *img2points* uses this information to convert each pixel

in the GPR trace image into a unique point on a vertically orientated plane, such that the trace image is converted into a correctly located and orientated pointset.

Once the GPR image is converted to a colour xyzrgb pointset, the pointset can be loaded into *RiSCAN* and visualised alongside the TLS data. Combining the two datasets into a 3D visualisation produces a model of the surface-to-subsurface geometry of the landslip (Fig. 3.1.12). The application of combined TLS and GPR can be applied to any scenario where the external outcrop geometry needs to be linked to the subsurface geometry. GPR surveys also rely on the input of topography (z-values) for each individual survey line. Often the topography is surveyed along the line at meter scale intervals using a total station or GPS. The acquisition of a TLS dataset which covers the GPR survey area allows topography on a much higher sub-meter resolution to be extracted and applied to GPR survey lines. In some cases the application of TLS-derived topography to GPR survey lines can increase the coherence of subsurface reflectors in comparison to those with GPS or total station-derived topography [Bubeck et al., submitted] (Fig. 3.1.13).

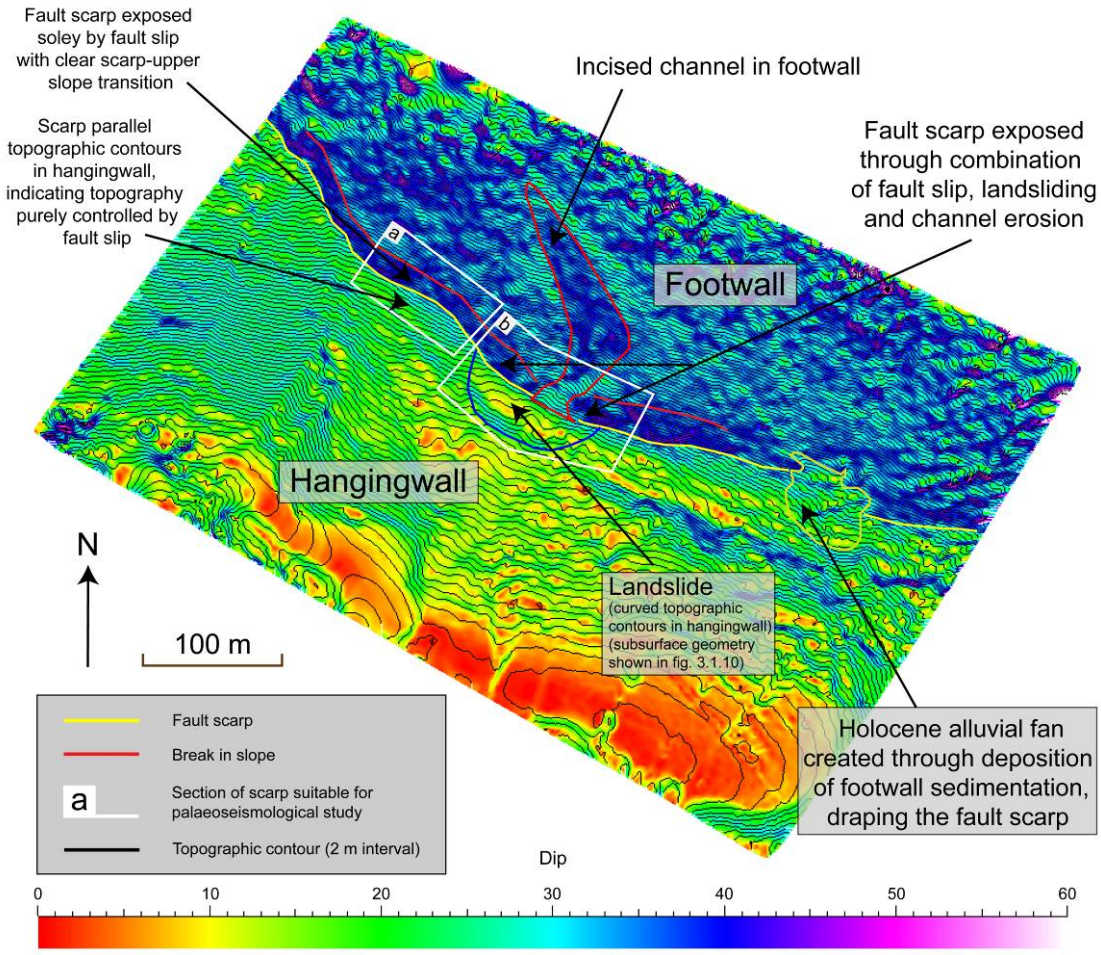

Figure 3.1.10: TLS derived dip and contour map of the Fiamignano fault (location: FM, Fig. 1.1), detailing curved contours in area *b*, a bowl shaped depression in the hangingwall, believed to be a landslip, after Bubeck et al., submitted.

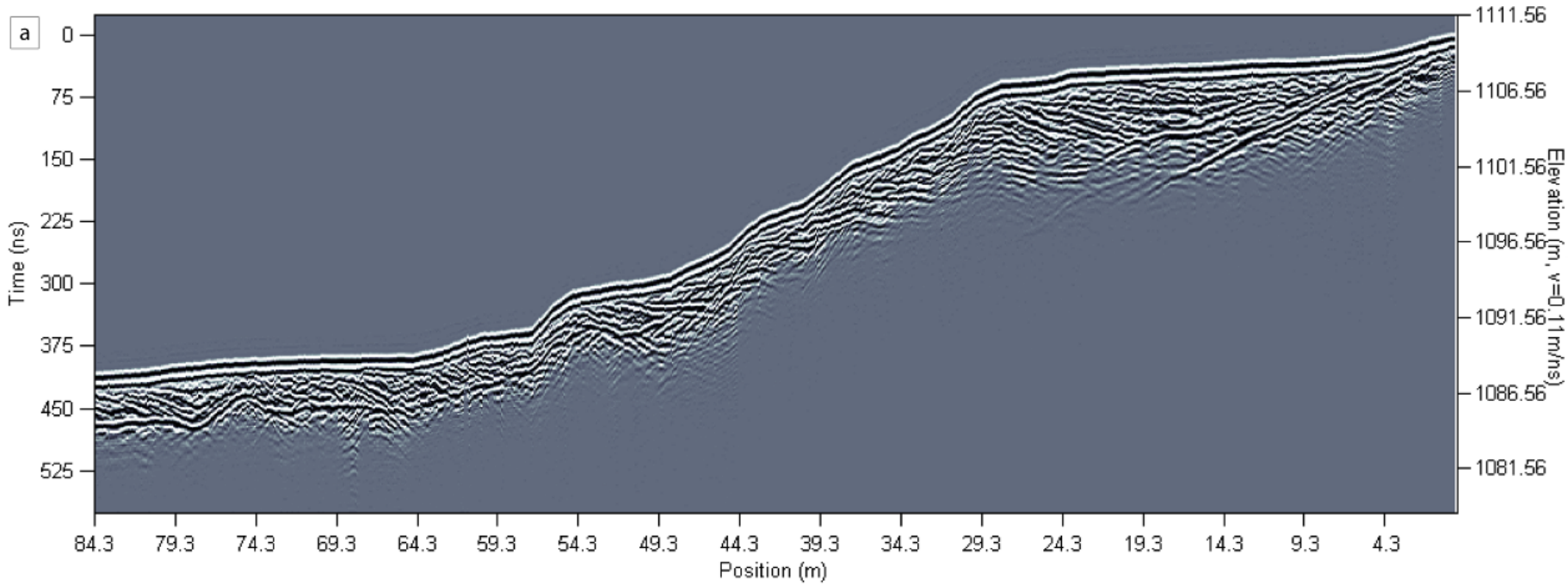

Figure 3.1.11: (a) Processed GPR trace image across the bowl shaped depression in Figure 3.1.10.

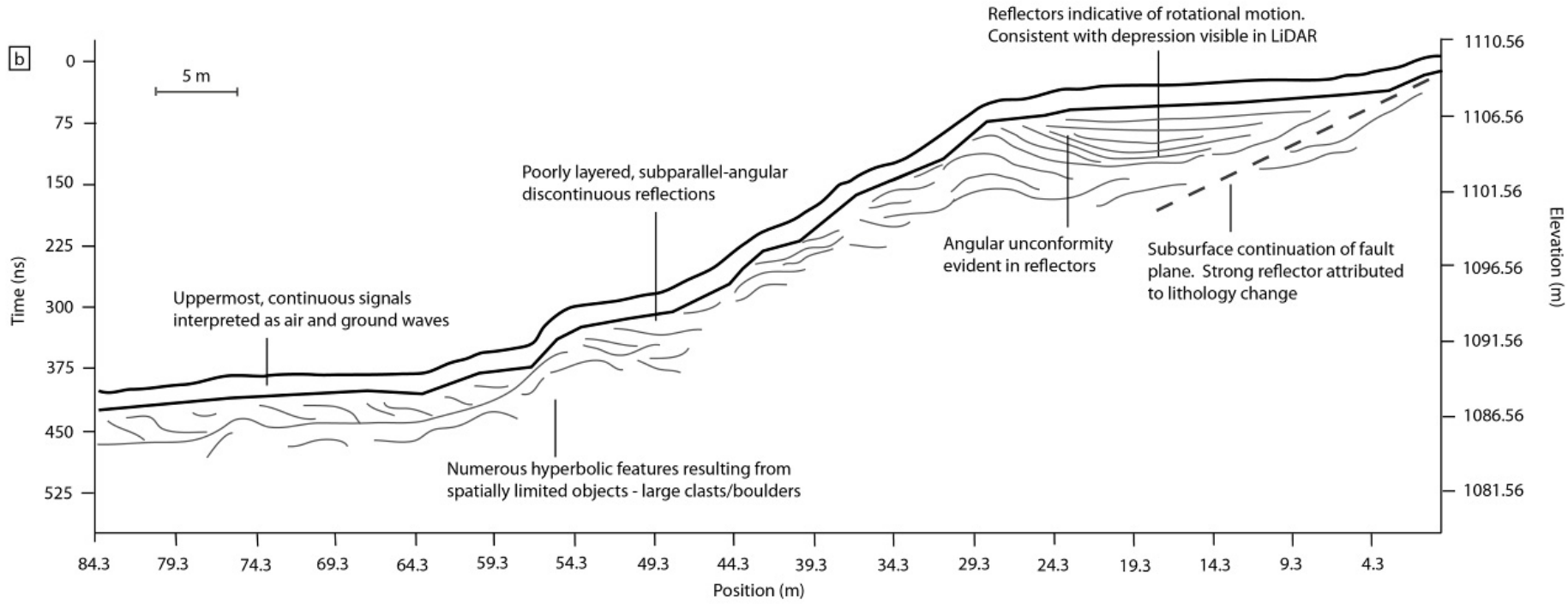

(b) Interpretation of GPR profile. Between 5 - 35m, to a depth of ~10 m, the reflectors exhibit geomorphic geometries consistent with gravitational movements, after Bubeck et al., submitted.

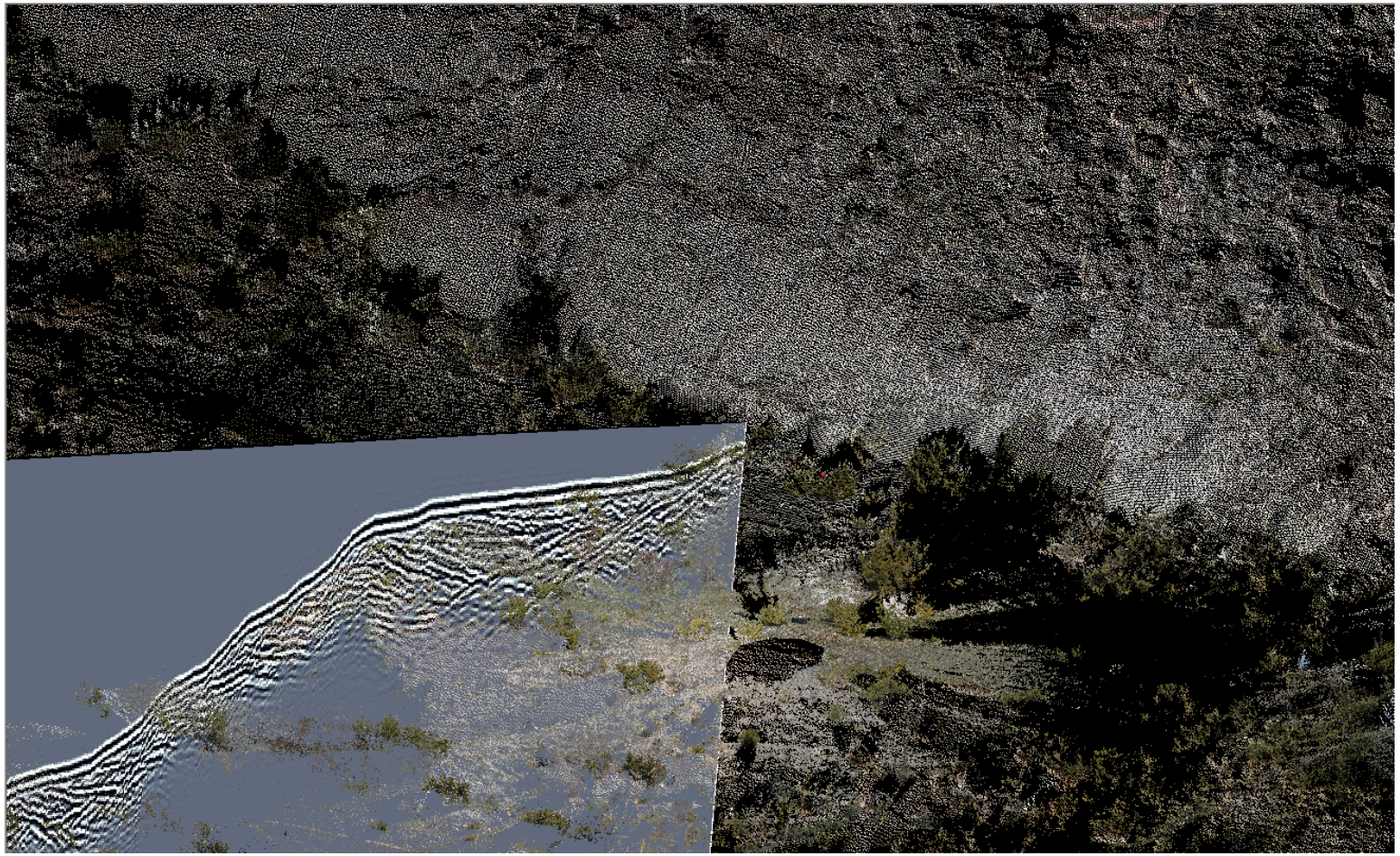

Figure 3.1.12: Co-visualisation of the combined TLS pointset and the GPR trace image, following conversion of the data to a pointset using *img2points*, after Bubeck et al., submitted.

a

GPR profile with total station elevations (every 5 m) applied

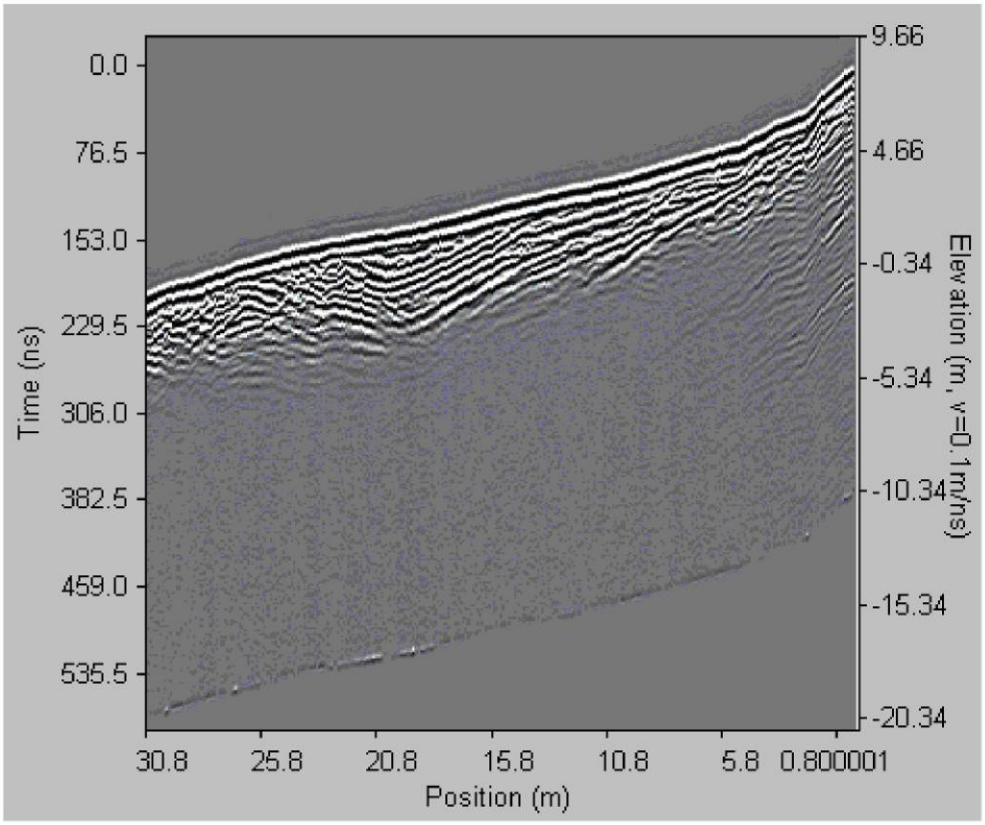

b

GPR profile with TLS elevations (every 0.1 - 0.5 m) applied

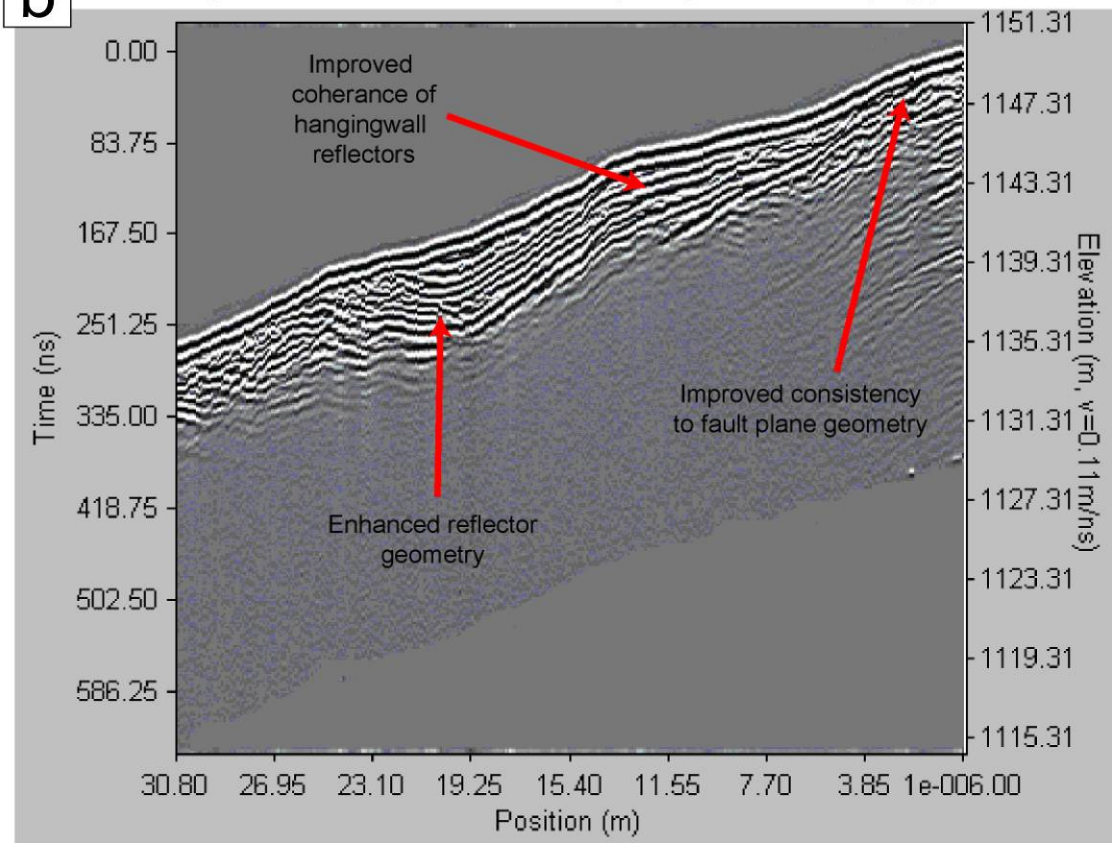

Figure 3.1.13: The effect of applying terrestrial laser scan topography to a GPR survey line vs. total station topography. (a) The GPR survey line with total station topography applied. (b) The GPR survey line with terrestrial laser scan-derived topography applied, after Bubeck et al., submitted.

3.1.3. Conclusions - Mapping the geomorphology of active normal faults using terrestrial laser scan datasets

Terrestrial laser scan (TLS) datasets provide a new approach to mapping the geomorphology of active normal faults. Unprocessed point cloud datasets, direct from the scanner can be used to gain a basic appreciation of the surface geomorphology. A significant advance on this approach includes a number of derivative datasets which can be produced from the point cloud. The filtering of vegetation is a major processing step, allowing the true topography to be revealed from within the point cloud. From this point TIN surfaces and a hillshade raster can be produced in order to provide initial identification of geomorphic features. Further interrogation of the dataset through the generation of surface dip maps, topographic contouring and flow routing analysis allow subtle geomorphic features and topographic responses to tectonics to be visualized, quantified and mapped. The combination of subsurface GPR data and surface TLS data provide a powerful tool with which to visualise and map the geometry, orientation and spatial distribution of features from the topographic and outcrop domains into the subsurface.

3.2. Extracting normal fault throw-rate profiles from terrestrial laser scan datasets

3.2.1. Introduction and rationale

Fault throw-rate is an important parameter for assessing earthquake recurrence intervals in seismic hazard analyses. As throw-rates increase, earthquake recurrence decreases and the hazard of any particular fault increases [Roberts et al., 2004]. Throw-rates for the normal faults in the Apennines have been calculated over geological time periods containing multiple earthquakes using offsets from a periglacial upper slope formed in the footwall at 15.3 ± 3 ka (initial age of the last glacial maximum: 18 ka, [Giraudi & Frezzotti, 1997]; age refined to 15.3 ± 3 ka, [Faure Walker et al., 2010]). Faulted offsets of periglacial slopes are measured from topographic profiles in order to define a long term throw-rate for a fault [Roberts & Michetti, 2004, Roberts, 2006]. These cross sections are constructed using end-to-end inclinometer measurements over 1 meter intervals [Faure Walker et al., 2009], or total station measurements [Tucker et al., 2011]. These surveys quantify the geological throw-rate for particular faults, but they are conducted from a limited number of sites along the fault and are not extensive enough to indicate how characteristic a particular throw-rate from one site is in relation to the entire fault. The method described below shows how terrestrial laser scan datasets acquired from normal fault scarps may to be used to extract and interpret multiple cross sections at numerous sites along their length. The method allows along-fault variability in throw-rate to be investigated.

The first step is to map the geomorphology of the fault from the TLS dataset as presented in Section 3.1. An understanding of the geomorphology is important prior to choosing locations for cross section creation, to be sure that the surface offset

observed can be attributed solely to the action of fault slip during and after earthquakes, rather than through other unrelated geomorphic processes, such as landsliding or gullying. The interpretation of multiple cross sections from various sites along the fault provides an indication of the uncertainty and variability in the final measurement in relation to the rest of the fault, as well as any natural variability in throw-rate due fault geometry. An understanding of the methodological and natural variability of such parameters is important in order to properly weight the throw-rate for a particular fault within probabilistic seismic hazard analyses.

3.2.2. Methods

The common morphological features of Apennine normal fault scarps in cross sectional view are shown in Figure 3.2.1.a. In order to extract accurate values for throw-rate, the intersections of the upper slope and fault scarp, and of the lower slope and the fault scarp must be identified. Commonly the upper slope – scarp intersection has been degraded and cut-off in the topography due to the affects of erosion over the last 15 ka. The lower slope-scarp intersection is also buried in places beneath a deposit of colluvium at the base of the scarp. To solve this problem, the lower slope, fault scarp and upper slope must be identified as planar regions within cross section (Fig. 3.2.1.b). Once these regions have been identified, the points of intersection can be located through extrapolation (Fig. 3.2.1.c). The throw can then be calculated using the vertical difference between the two points of intersection (Fig. 3.2.1.d). Such extrapolation of planar surfaces above ground, or underneath colluvium is difficult to conduct in the field. A solution to this problem is to measure throw through the interpretation of topographic cross sections.

To begin the process of measuring throw-rate, the acquired point cloud is initially processed using the method described in Section 3.1.2 in order to filter vegetation and to produce a point cloud representative of the topographic surface. The geomorphology of the fault scarp is then mapped using a combination of hillshade raster, surface dip and contour maps derived from the point cloud.

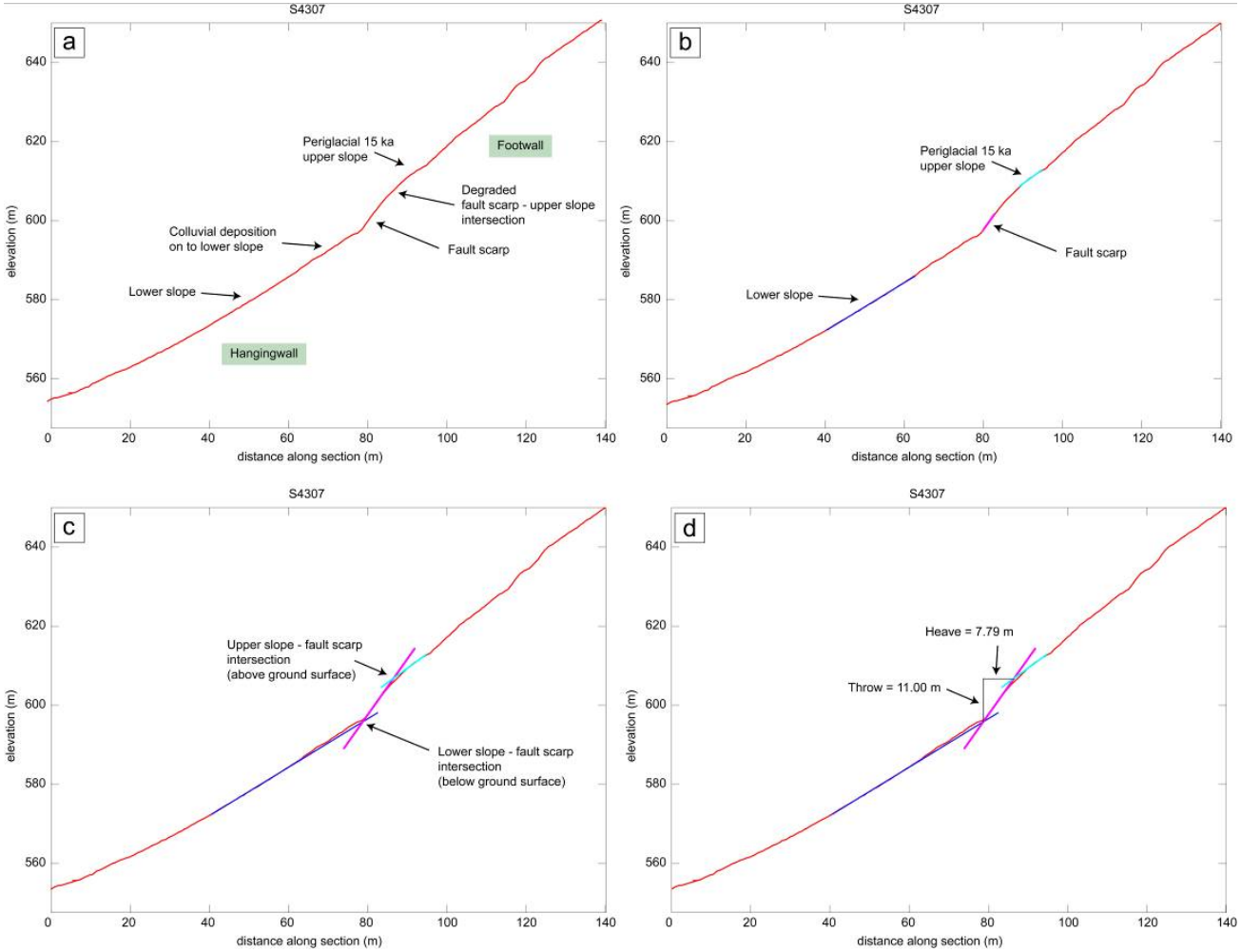

Figure 3.2.1: (a) Common morphological features of Apennine fault scarps in cross section. (b) The identification of planar regions representing the upper slope, fault scarp and lower slope. (c) Extrapolation of the planar regions to identify the upper slope - scarp intersection and the lower slope – scarp intersection. (d) The vertical difference between the two intersection points is a measure of throw. The horizontal difference between the two points is a measure of heave in the direction of the bearing of the cross section.

Cross section generation

A TIN is created from the filtered point cloud within *RiSCAN* (Fig. 3.2.2), using the volume creation tool. A vertical plane is created in *RiSCAN*, which is rotated and translated so that it intersects the TIN in the chosen location and trend to create a cross section close to perpendicular to the strike of the fault (Fig. 3.2.3). The location of the cross section to be generated is checked against the mapped geomorphology to ensure the site is suitable. A batch of ten cross sections, spaced 1 m apart are created using the cross section tool in *RiSCAN*. The tool uses the intersection of the TIN and the vertically dipping plane to create the first cross section, the next cross section is then created at a spacing of 1 m from the first, measured perpendicular to the plane. The process continues until ten cross sections have been created (Fig. 3.2.4). The vertically dipping plane is then translated along the fault scarp to the next suitable site for cross section generation, the plane is rotated perpendicular to strike, the geomorphology of the site is checked and the next set of cross sections are generated. The process is repeated until cross sections have been generated for all suitable sites along the fault (Fig. 3.2.5).

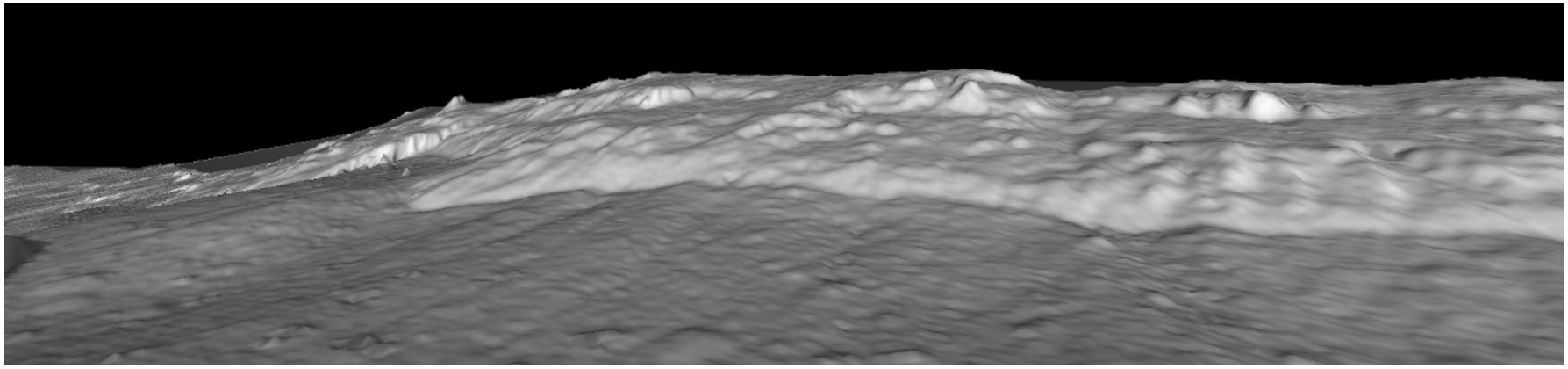

Figure 3.2.2: A TIN created from the filtered point cloud dataset using the volume tool in *RiSCAN*.

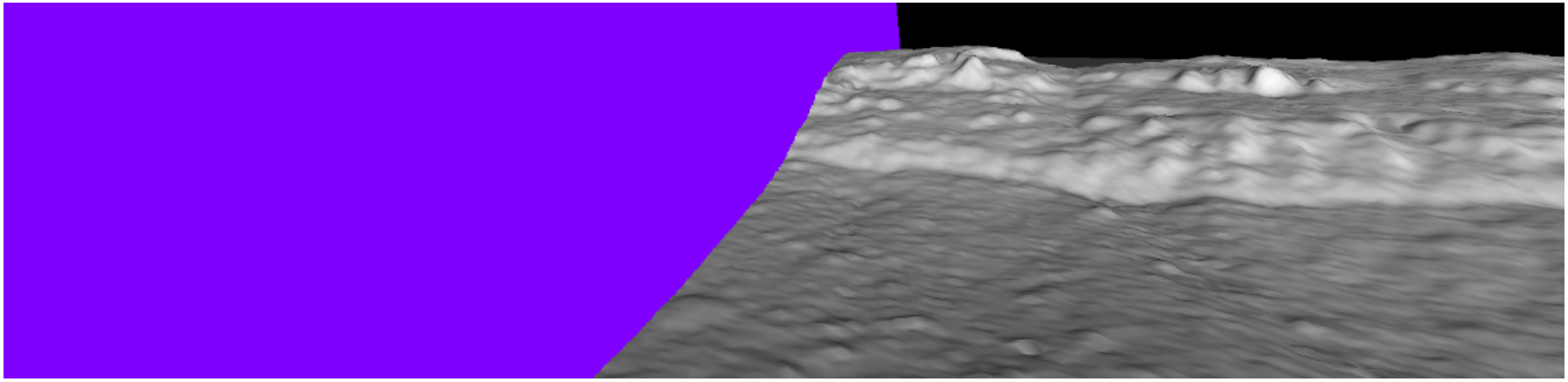

Figure 3.2.3: A vertically dipping plane positioned to intersect the TIN for the creation of a cross section.

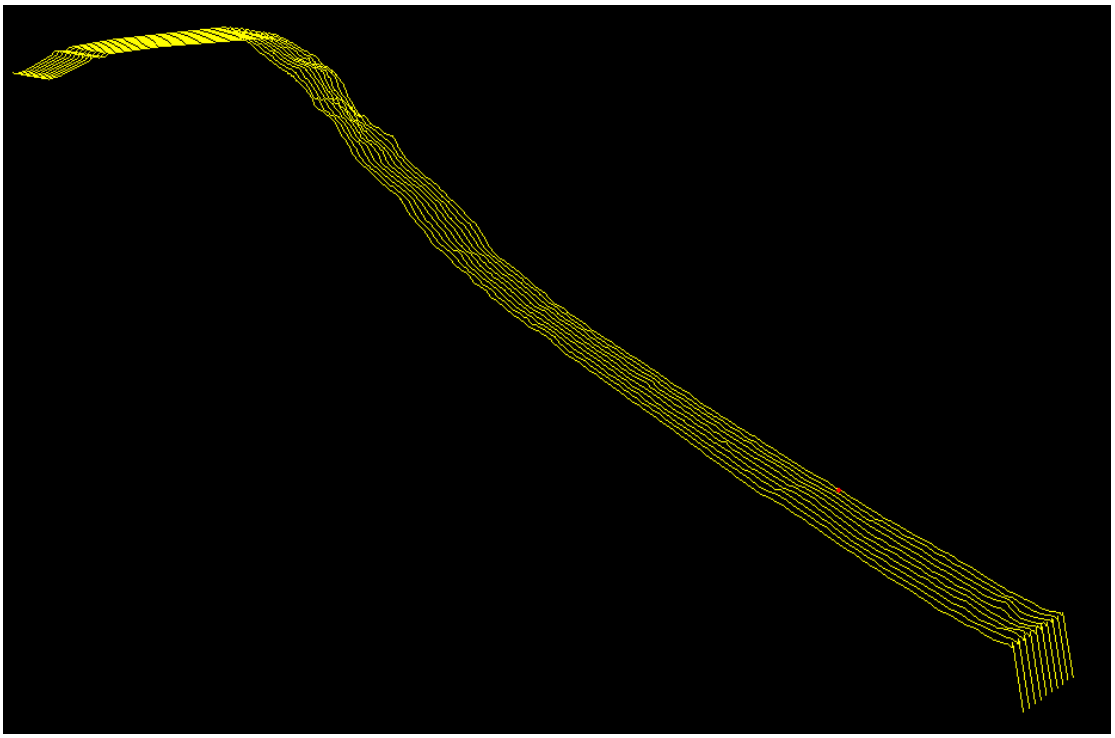

Figure 3.2.4: A batch of ten cross sections, spaced at 1 m intervals, created from the initial position of the plane in Figure 3.2.3.

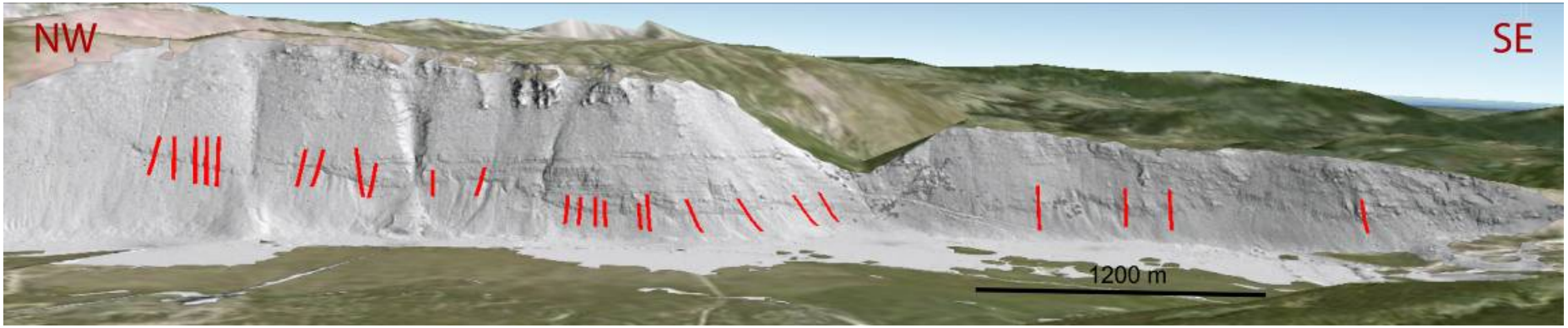

Figure 3.2.5: The complete batches of cross sections, shown in red, generated for all suitable sites along the fault.

Cross section interpretation using Crossint

The generated cross sections are exported from *RiSCAN* in .dxf format. *goCAD* is used to convert the .dxf format files to space delimited ascii text in the form x y z. Subsequently, each of the cross section files are interpreted using the *Crossint* program which has been written by the author specifically for this thesis. *Crossint* is an interactive tool for the interpretation of normal fault cross sections. The program is written in the GNU octave language. The full code can be found in Appendix ii. *Crossint* is loaded from within the GNU octave terminal and prompts the user to enter the name of the cross section to be interpreted. The user enters the filename of the first cross section to process the first cross section. The xyz data from the cross section file is read by the program, and displayed as a cross sectional plot (Fig. 3.2.6). The user then picks two points in the hangingwall, defining a representative portion of the lower slope (Fig. 3.2.7). *Crossint* then produces a linear regression through all points between the selected points, plots a best fit line and reports the dip of the line (Fig. 3.2.7). The user confirms they are happy with this line as an interpretation of the lower slope surface. The user is then prompted to pick two points on the fault plane. Once the user has picked these two points, *Crossint* repeats the linear regression for the picked section of the scarp, plots the best fit line and reports the dip of the line (Fig. 3.2.8). The user confirms they are happy with the regression line as a representation of the fault plane. The user then picks two points in the footwall, between which an appropriate representation of the upper slope exists. *Crossint* repeats the regression for those points and plots the best fit line (Fig. 3.2.9). The intersection of the lower slope regression line and the scarp regression line is given as the lower point of the fault plane. The intersection of the fault plane regression line and the upper slope regression line is given as the upper point of the fault plane. The

throw and heave displayed in this cross section are the vertical and horizontal differences between these two points. *Crossint* displays the throw and heave for the present interpretation, based on the picked points. The user confirms that they are happy with the interpretation, or have the option to start over. If the user confirms they are happy, the interpreted plot, with the picked points and the regression lines are output to a graphics file, along with the dip of the regression lines, the calculated throw and heave (Fig. 3.2.10).

Following calculation of the throw-rate for each cross section, the section file name, throw, heave, and dips of the hangingwall, scarp and footwall regression lines as well as the slip-rate are appended as a line to an output file in space delimited format. The user then loads in the next cross section in the sequence and the interpretation processes is repeated. As more cross sections are processed, new lines are appended to the output file, which can be used for further data analysis once all cross sections have been interpreted (Fig. 3.2.11).

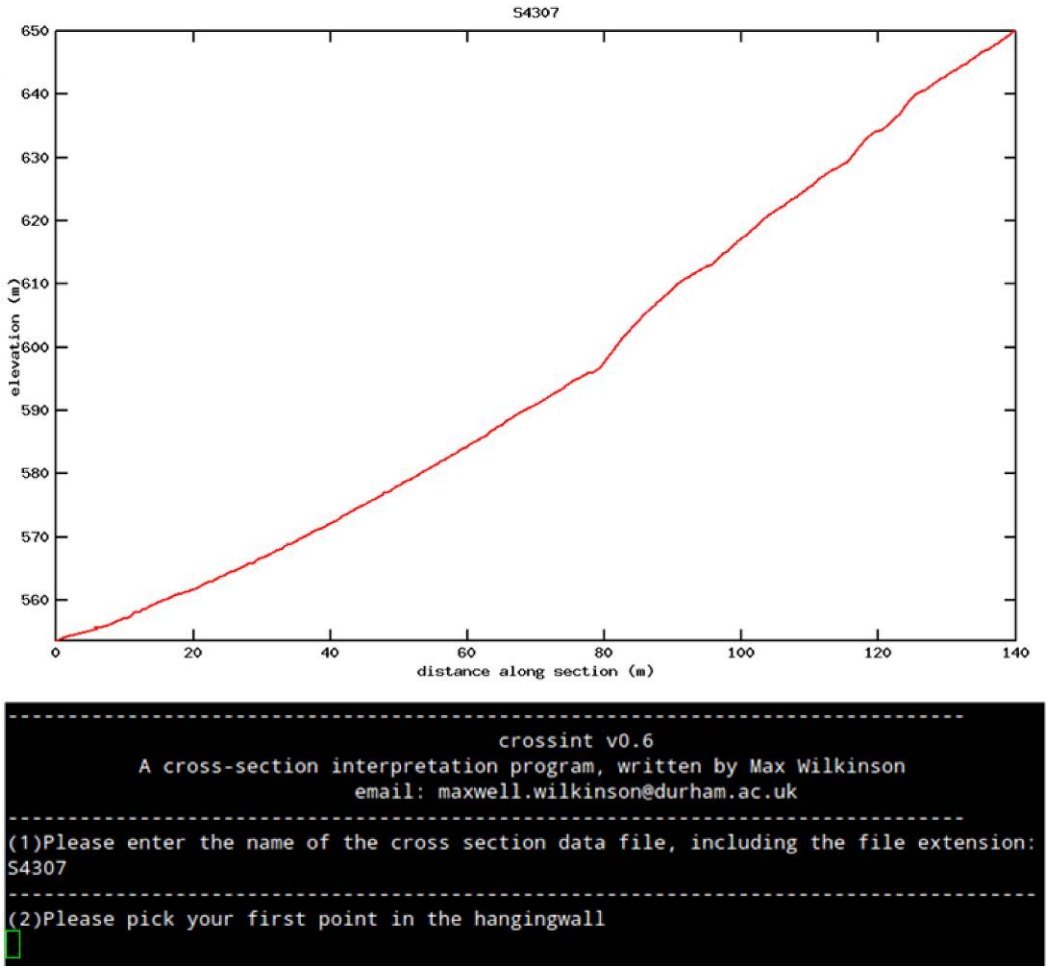

Figure 3.2.6: The *Crossint* interface, with a cross section loaded and displayed ready for interpretation.

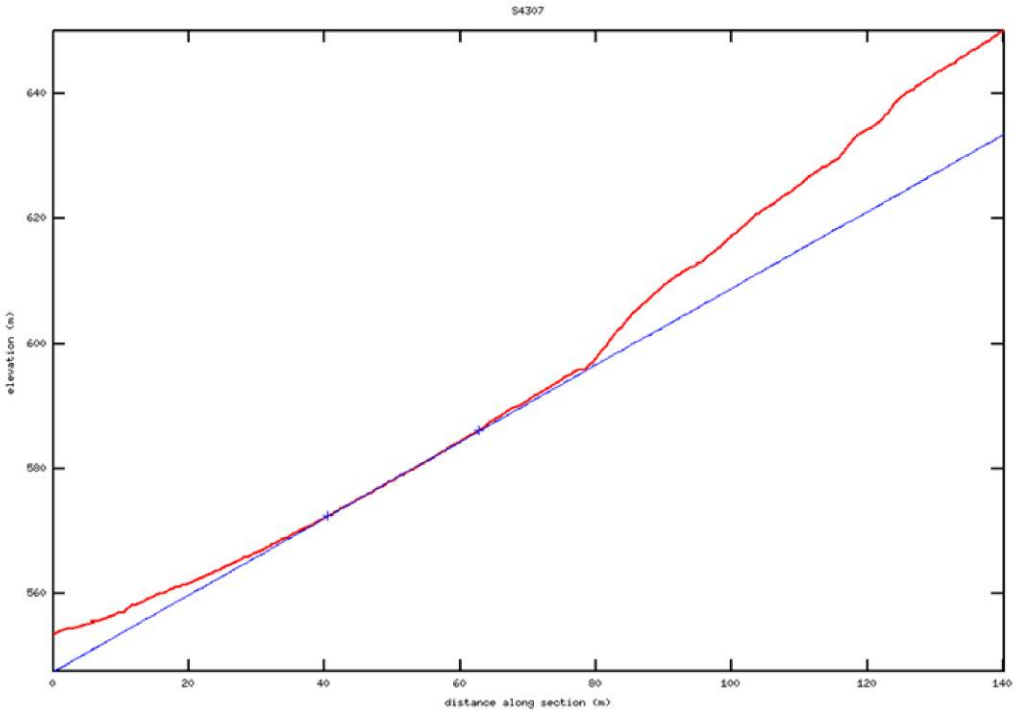


```
(3)Are you happy with your first hangingwall pick?
Press right mouse button to confirm, or left mouse button to retry the pick
--------------------------------------------------------------------------------
(4)Please pick your second point in the hangingwall
--------------------------------------------------------------------------------
(5)Are you happy with your second hangingwall pick?
Press right mouse button to confirm, or left mouse button to retry the pick
--------------------------------------------------------------------------------
(6)The dip of the hangingwall interpretation line you have picked is:
31.497
Are you happy with this hangingwall interpretation line?
Press right mouse button to confirm, or left mouse button to retry the hangingwall pick
 process
```

Figure 3.2.7: The two lower slope picks selected by the user, between which a representative portion of the hangingwall exists. The regression line (in blue) calculated by *Crossint* using the points between the two hangingwall picks displayed on the cross section. The dip of the regression line is displayed in the terminal window.

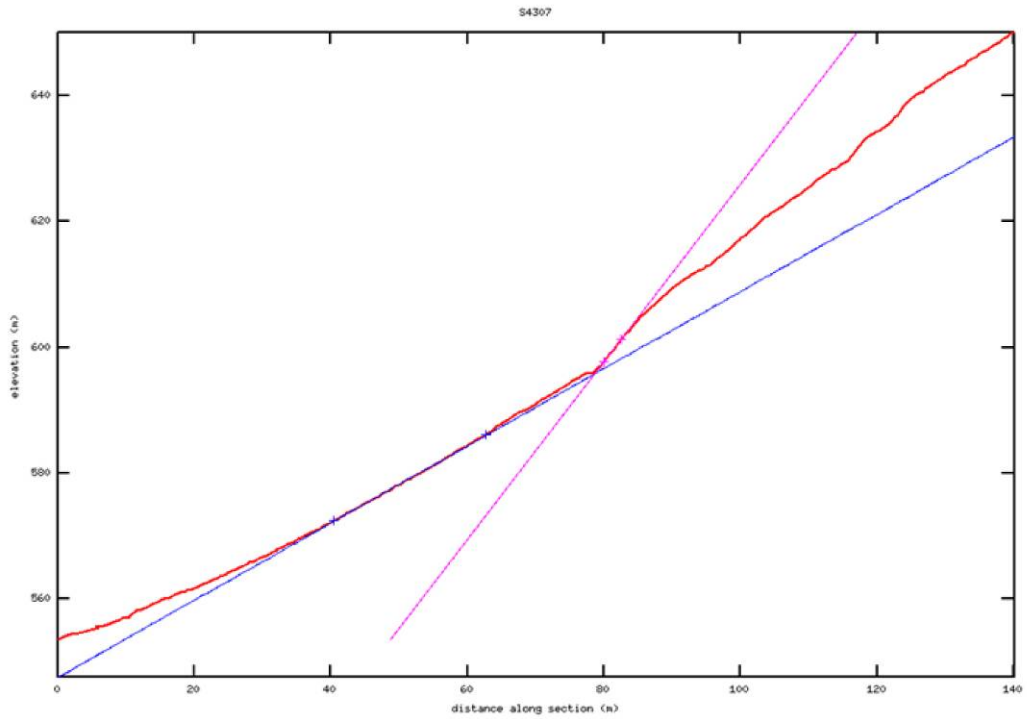


```
(7)Please pick your first point on the scarp
--------------------------------------------------------------------------------
(8)Are you happy with your first scarp pick?
Press right mouse button to confirm, or left mouse button to retry the pick
--------------------------------------------------------------------------------
(9)Please pick your second point on the scarp
--------------------------------------------------------------------------------
(10)Are you happy with your second scarp pick?
Press right mouse button to confirm, or left mouse button to retry the pick
--------------------------------------------------------------------------------
(11)The dip of the scarp interpretation line you have picked is:
54.694
Are you happy with this scarp interpretation line?
Press right mouse button to confirm, or left mouse button to retry the scarp pick proce
ss
```

Figure 3.2.8: The two user picked points for a representative portion of the fault plane and the calculated regression line displayed on the cross section. The dip of the fault plane regression line is displayed in the terminal window.

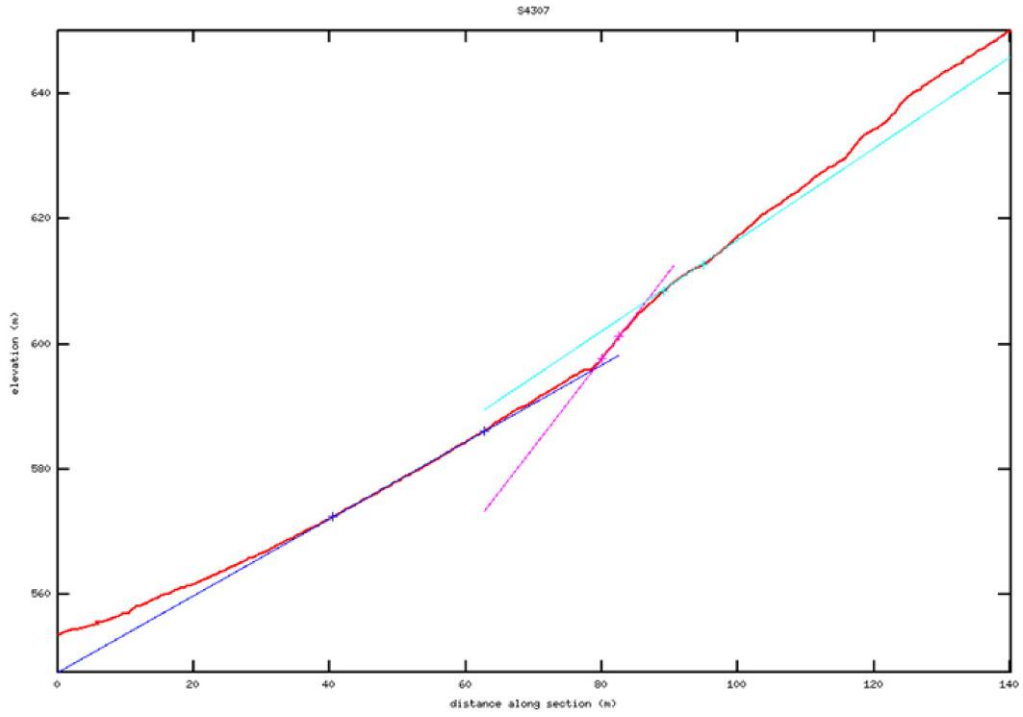


```
(12)Please pick your first point in the footwall
--------------------------------------------------------------------------------
(13)Are you happy with your first footwall pick?
Press right mouse button to confirm, or left mouse button to retry the pick
--------------------------------------------------------------------------------
(14)Please pick your second point in the footwall
--------------------------------------------------------------------------------
(15)Are you happy with your second footwall pick?
Press right mouse button to confirm, or left mouse button to retry the pick
--------------------------------------------------------------------------------
(16) The dip of the footwall interpretation line you have picked is: 36.098
     The throw for your interpretation is: 11.001224
     The heave for your interpretation is: 7.790934
     Are you happy with this footwall interpretation line?
     Press right mouse button to confirm, or left mouse button to retry the footwall pi
ck process
```

Figure 3.2.9: The two user picked points for a representative portion of the upper slope and the regression line displayed on the cross section. The dip of the upper slope regression line as well as the throw and heave for the current interpretation are displayed in the terminal window.

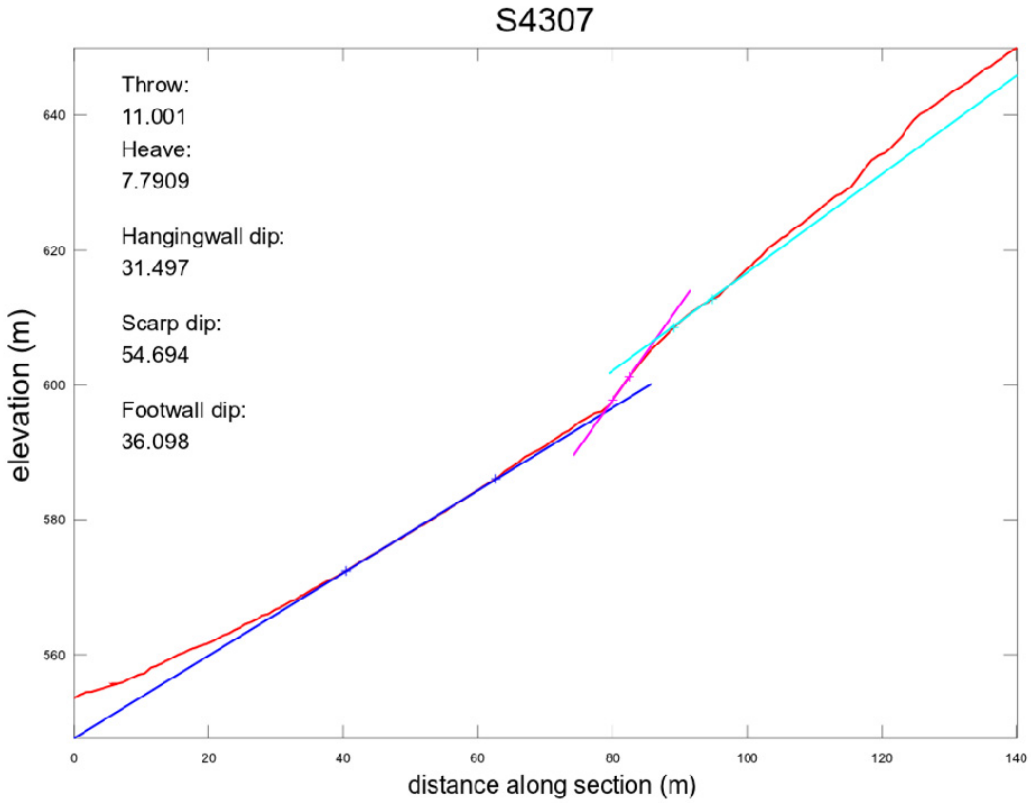

Figure 3.2.10: The output graphics file for the completed cross section interpretation, including the dip of the lower slope, fault plane and upper slope regression lines.

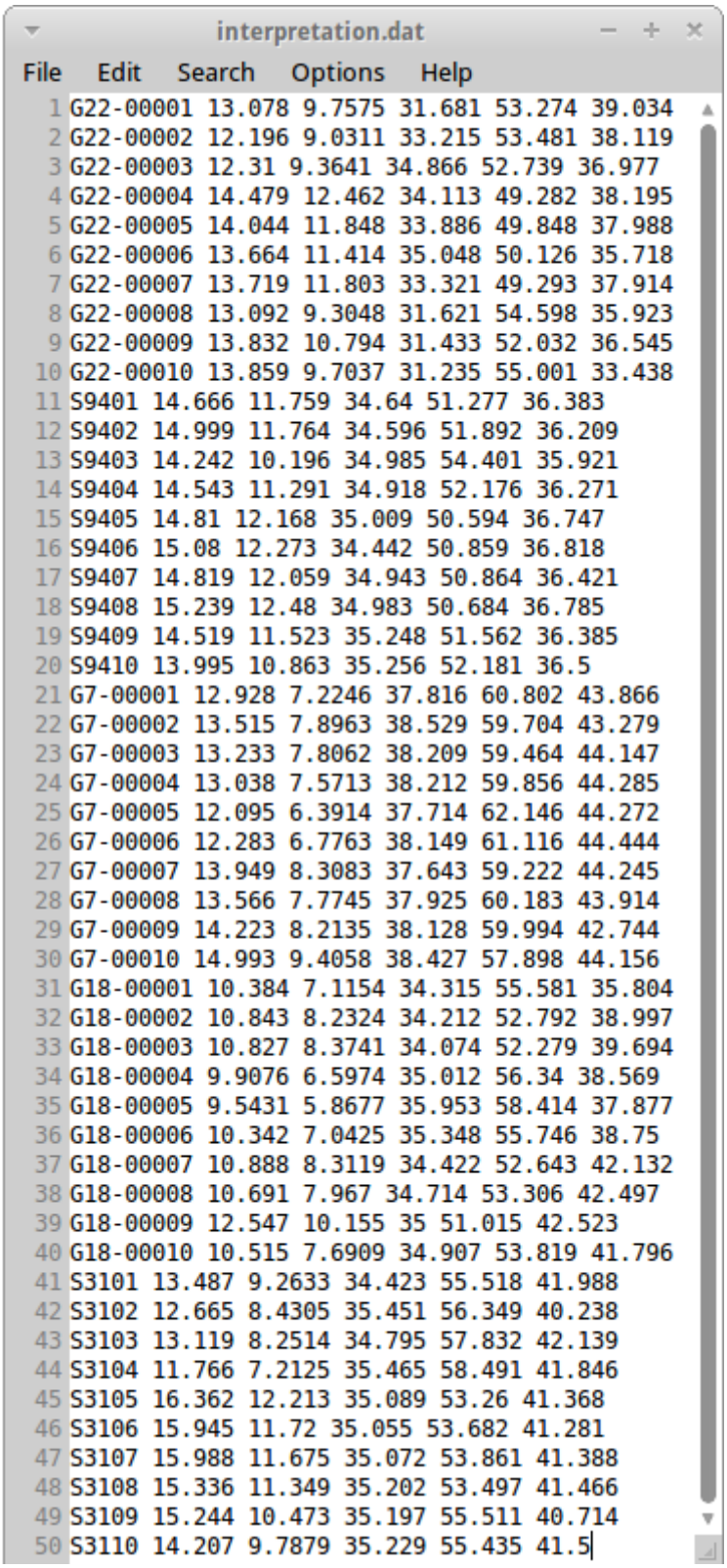

Figure 3.2.11: An example of a space delimited output file for multiple cross section interpretations. The data fields are: Name, throw, heave, hangingwall dip, scarp dip and footwall dip.

Data analysis

The mean and standard deviation for throw are calculated from the data from the ten profiles at each site. In order to plot the data as a fault length profile, the distance along the length of the fault to each cross section site is calculated by measuring from the tip of the fault to the left when viewing the fault from the hangingwall. A plot of the throw with distance along the fault is produced by plotting the mean throw for each cross section site against their corresponding distance along the fault. The corresponding calculated standard deviation is used to produce error bars ($\pm 1\sigma$) representing the uncertainty of the calculated mean at each site. The throw-rate T_R (mm/yr) for each site is calculated using the equation below, from the throw T (m) and the age of the offset upper slope in the footwall A (kyrs).

$$T_R = \frac{T}{A}$$

The calculated throw-rate at each site is used to produce an along-fault throw-rate profile (Fig. 3.2.13). The source of any variability in throw-rate along strike can be investigated by comparing the throw-rate profile with profiles of data gathered in the field, such as fault dip, strike and kinematic plunge direction (see Section 4.3). Throw is used as a variable, as opposed to heave, as measured throw is independent of the orientation of the cross section, whereas measured heave will vary as the angle of the cross section deviates from a dip-slip orientation (Fig. 3.2.14). The uncertainty and variability of throw-rate along strike provides an indication of the natural variability of throw along the fault, which in turn dictates the variability of any single measurement of throw along the fault and hence the weighting required when such data are used within models of regional hazard.

Strain-rate

Strain-rate can also be calculated across faults which have had throw-rate measured using this method. The advantage of describing deformation in terms of strain-rate instead of throw-rate is that strain-rate takes into account variations in fault geometry and of the direction of kinematic slip, as suggested by Faure Walker et al., (2009). Strain-rate is calculated for boxed shaped areas in map view using the equations below, as defined by Faure-Walker et al., (2009). The components of strain e_{11}, e_{12} and e_{22} and calculated for each sample box of width L and area a. T represents the average throw measured across the fault within the sample box and t is the time period of which that throw has formed (for instance 15 ±3 kyrs in the case of post glacial faulting in the central Apennines). The average values of kinematic plunge (*plunge*), kinematic slip direction (*slipdir*) and strike (*strike*) for field measurements within the sample box are also used (Fig. 3.2.12). The direction of principal strain for each box is then defined by θ. The strain-rate for each box (*strainrate*) is then calculated in the direction of the regional principal strain direction, defined by the average of the values of θ for each sample box along the fault. An example of a strain-rate profile for the Campo Felice fault using 250 m x 250 m sample boxes is shown in Figure 4.3.6 of Section 4.4.

$$e_{11} = \frac{1}{at} LT \cot(plunge) \sin(slipdir) \cos(strike)$$

$$e_{22} = \frac{-1}{at} LT \cot(plunge) \cos(slipdir) \sin(strike)$$

$$e_{12} = \frac{1}{2at} LT \cot(plunge) \cos(slipdir + strike)$$

$$\theta = \frac{\arctan(2\frac{e_{12}}{e_{11} - e_{22}})}{2}$$

$$strainrate = \frac{e_{11} + e_{22}}{2} - \frac{e_{11} - e_{22}}{2} \cos(2\theta_{ave}) - e_{12} \sin(2\theta_{ave})$$

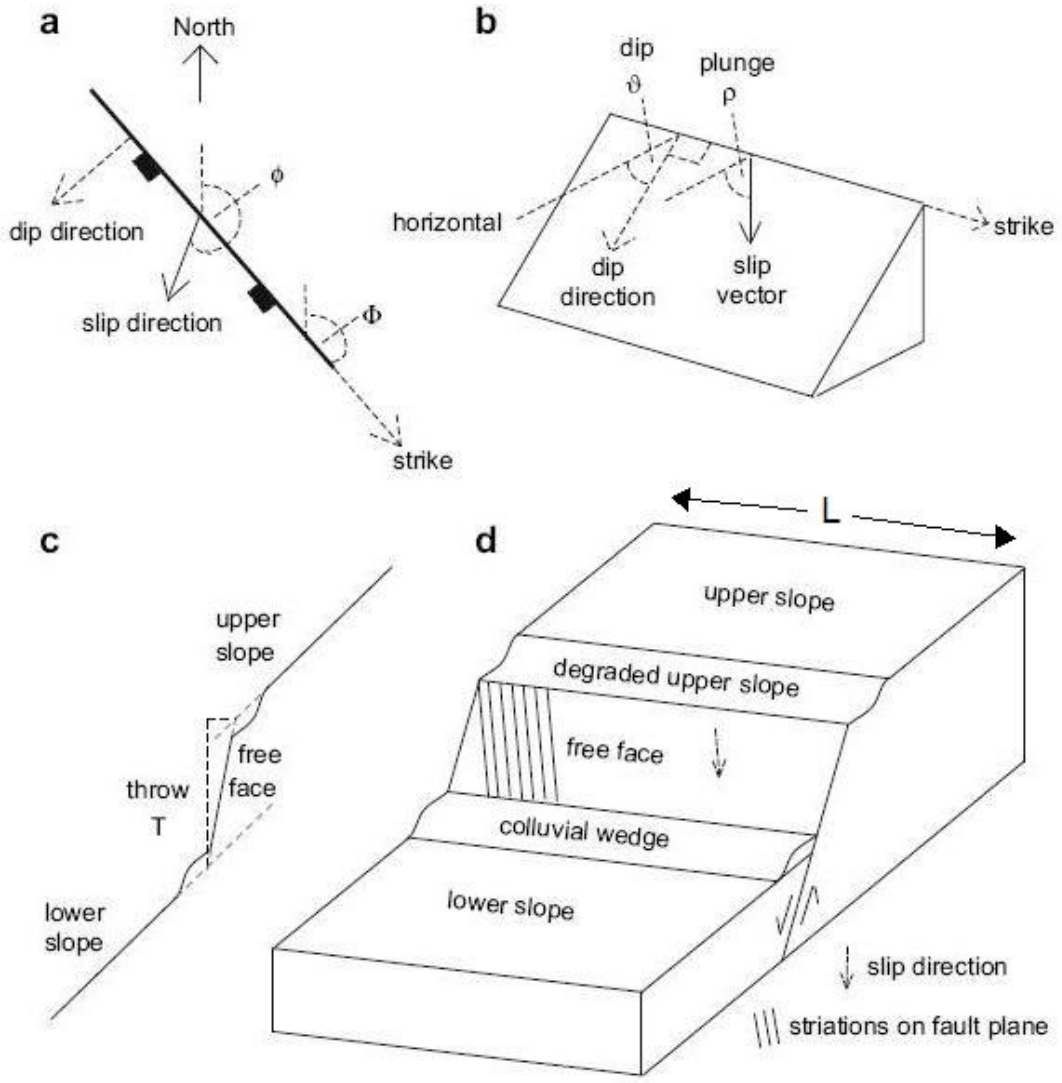

Figure 3.1.12: Schematic diagrams, explaining the origins of field measurements of *plunge*, *slip direction*, *strike*, *T (throw)* and *L (length)* as used in the equations to define strain rate in boxed regions of width *L* along normal faults (after. Faure-Walker et al., 2009).

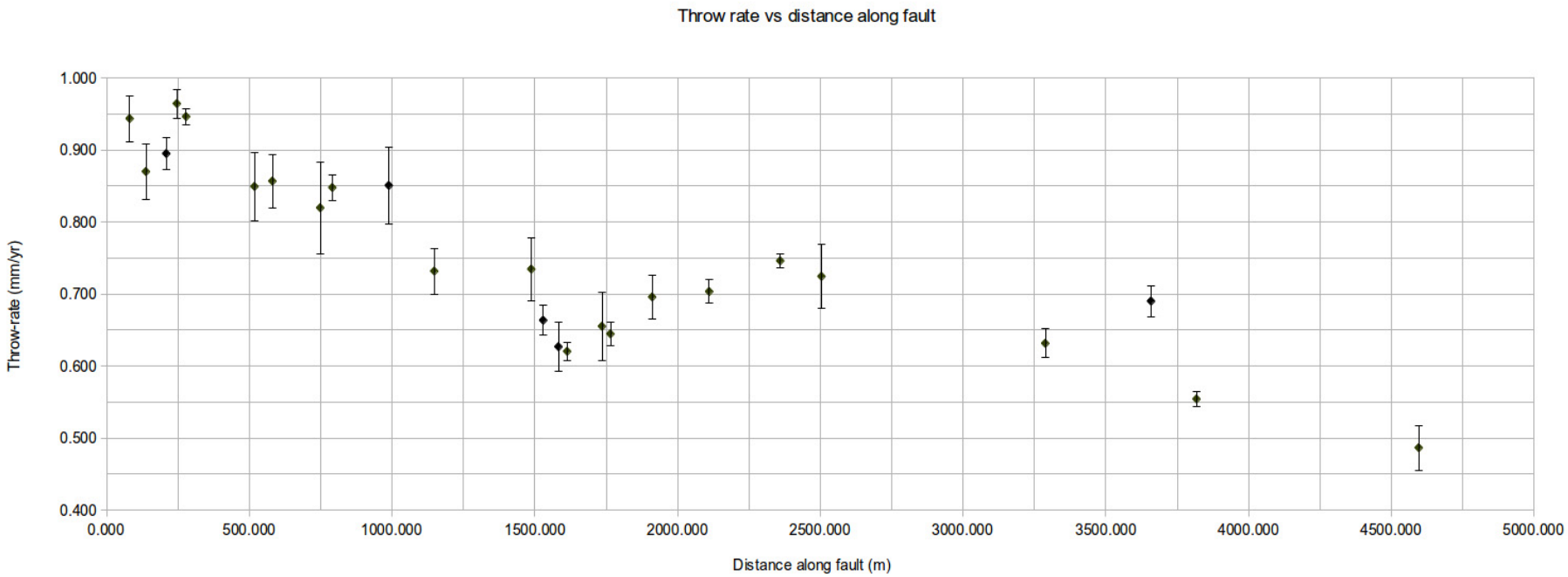

Figure 3.2.13: An example of a throw-rate profile, calculated from throw measurements using a 15 ka upper slope age.

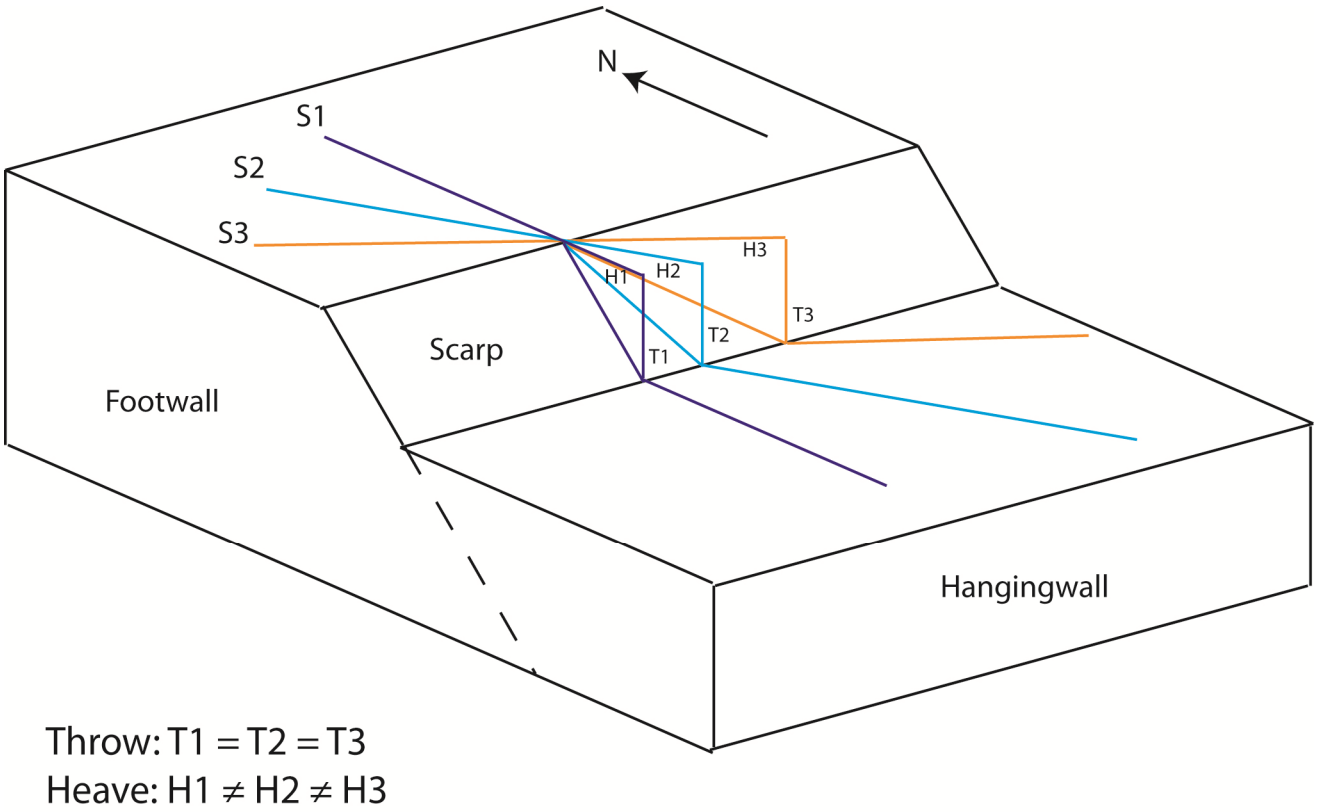

Figure 3.2.14: A schematic diagram demonstrating that for cross sections of varying bearing (oritentation) relative to north (S1, S2 & S3), the measurement of throw (T1, T2, T3) is consistent and independent of the bearing of the cross section, whereas heave (H1, H2, H3) is inconsistent and varies with the bearing of the cross section. The measurement of throw should be used when comparing cross sections with varing bearings / orientations relative to north.

3.2.3. Conclusions - Extracting normal fault throw-rate profiles from terrestrial laser scan datasets

The throw-rate and hence recurrence interval attributed to a particular fault, as well as its uncertainty is an important factor in probabilistic seismic hazard analysis. The method described in this chapter provides a means to extract a throw-rate profile from terrestrial laser scan datasets of active normal faults. Measuring strain-rate allows for the affects of fault geometry to be taken into account. Fault geometry can alter throw-rate values and so by calculating strain-rate this uncertainty is removed. These profiles are primary datasets with which to define the maximum throw-rate and strain-rate, as well as the natural and methodological variability attached to such values. Thus the application of *Crossint* provides a method to improve the accuracy and reduce uncertainty of seismic hazard analysis in the Apennines (see Section 4.4).

3.3. Modelling postseismic surface motion using repeat terrestrial laser scanning

3.3.1. Introduction and rationale

Terrestrial laser scanning provides a means of recording an accurate representation of a real world scene, through the generation of a 3D point cloud dataset. One step beyond this static approach is to acquire repeat datasets at specific time intervals from a scene that is actively deforming. By comparing each subsequently acquired point cloud to the first, it is possible to measure and model the magnitude of deformation which occurred over the survey time frame. One such scenario where this method can be applied is in the near-field of an earthquake surface rupture undergoing postseismic deformation (i.e. Wilkinson et al., 2010). Repeat terrestrial laser scanning of surface ruptures immediately following earthquakes provides a complimentary technique to other field methods commonly used to measure postseismic deformation, such as GPS (e.g. Cheloni et al., 2010) and differential interferometry (InSAR, e.g. Lanari et al., 2010). The advantages of repeat terrestrial laser scanning over GPS and InSAR methods include the ability to be deployed in the near-field of a surface rupture, and the ability to measure the deformation occurring simultaneously across many thousands of closely space points. The result is an exceptionally high resolution map of near-field postseismic deformation.

3.3.2. Methods

Site selection

In order to successfully measure surface deformation using repeat terrestrial laser scanning, it is important to choose a site with a surface which will provide a dataset with a minimal amount of noise. Examples of surfaces with high noise are a grassy field or a loose gravel road, which due to the roughness of the surface will generate large variability in the position of each laser return. Such variability can be enough to mask any subtle surface deformation. As a general rule (i.e. Wilkinson et al., 2012), the noise generated by the surface should not exceed half the magnitude of the deformation expected over the time interval, as two point cloud datasets are required to produce a measure of deformation. Examples of good sites are those with bare rock, smooth tarmac or concrete.

Another important consideration during site selection is the complexity of the surface over which the deformation is to be measured. If the scanner cannot be left in a fixed position for the duration of the entire survey campaign a later step in the method requires surface interpolation of each point cloud. It is therefore important to select a site surface whose point cloud can be meshed to a high degree of accuracy. The accuracy will depend on the interpolation and meshing methods used, of which there are many. Common pitfalls for meshing algorithms include surfaces with large, rapid changes in their surface normal, such as the 90-degree edges present in blocky, fractured outcrops or concrete structures. Many surface meshing algorithms tend to round off these edges to some degree [Wilkinson et al., 2012], creating inaccurate surface representations. The best approach is to choose sites with surfaces which are gently undulating or as planar as possible. A workaround for blocky outcrops is to subdivide the outcrop into a series of discrete planar surfaces.

Survey set up

To model deformation that occurs between an initial point cloud acquired at a site and all subsequently acquired point clouds, it is important that the point clouds are co-located in 3D space as accurately as possible. The most effective way of ensuring the acquired point clouds are accurately co-located is to leave the scanner in a fixed position for the duration of the survey campaign. In this case the x, y, z axis-origin of the point cloud, that is, the position of the scanner, does not change, and hence all point clouds have the same origin and are automatically co-located. In practice, there are few occasions where a laser scanner can be left in a fixed position for the duration of a survey campaign because the equipment is expensive and insurance usually does not cover unattended use in the field. If this method is used, it is important to have a means of surveying the stability of the scanner at its location, to ensure that it is in fact stable. In the situation where the scanner must be removed from the site after the acquisition of each point cloud, it is necessary to set up reflective markers at the survey site. The reflective markers remain in position for the entirety of the survey (or at least some other form of survey marker which allows the reflectors to reoccupy their positions ready for a new acquisition). The reflectors should be set up in a diamond pattern around the periphery of the survey site, at a range of different heights. Where possible the scanner should be located at the centre of the reflector network (Fig. 3.3.1). The reflectors are then used as static points to co-locate the point clouds. A diamond shaped reflector network over a range of heights ensures the point cloud can be co-located accurately in each of the x, y and z axes. A further consideration for reflector network design is to ensure that there are at least four reference reflectors placed within an area where deformation is considered to be minimal. In the case of an earthquake surface rupture with normal sense displacement,

the best place to locate reference reflectors is a significant distance into the footwall where deformation is likely to be less than in the hangingwall.

A final consideration for survey set up is to locate the scanner with a suitable view of the entire surface over which deformation is to be measured. This means that the scanner should be able to collect as close to a regularly spaced point cloud as possible over the entire surface. In the case of a level road surface, the point spacing in a point cloud collected from a scanner placed close to the ground will rapidly diverge with distance from the scanner, creating problems during interpolation at a later stage. In order to collect as close to a regularly spaced point cloud as possible, the scanner should be placed as high as practically possible, while not at the expense of stability. This is less of a consideration for surfaces perpendicular to the line of sight of the scanner, such as steeply dipping outcrop faces.

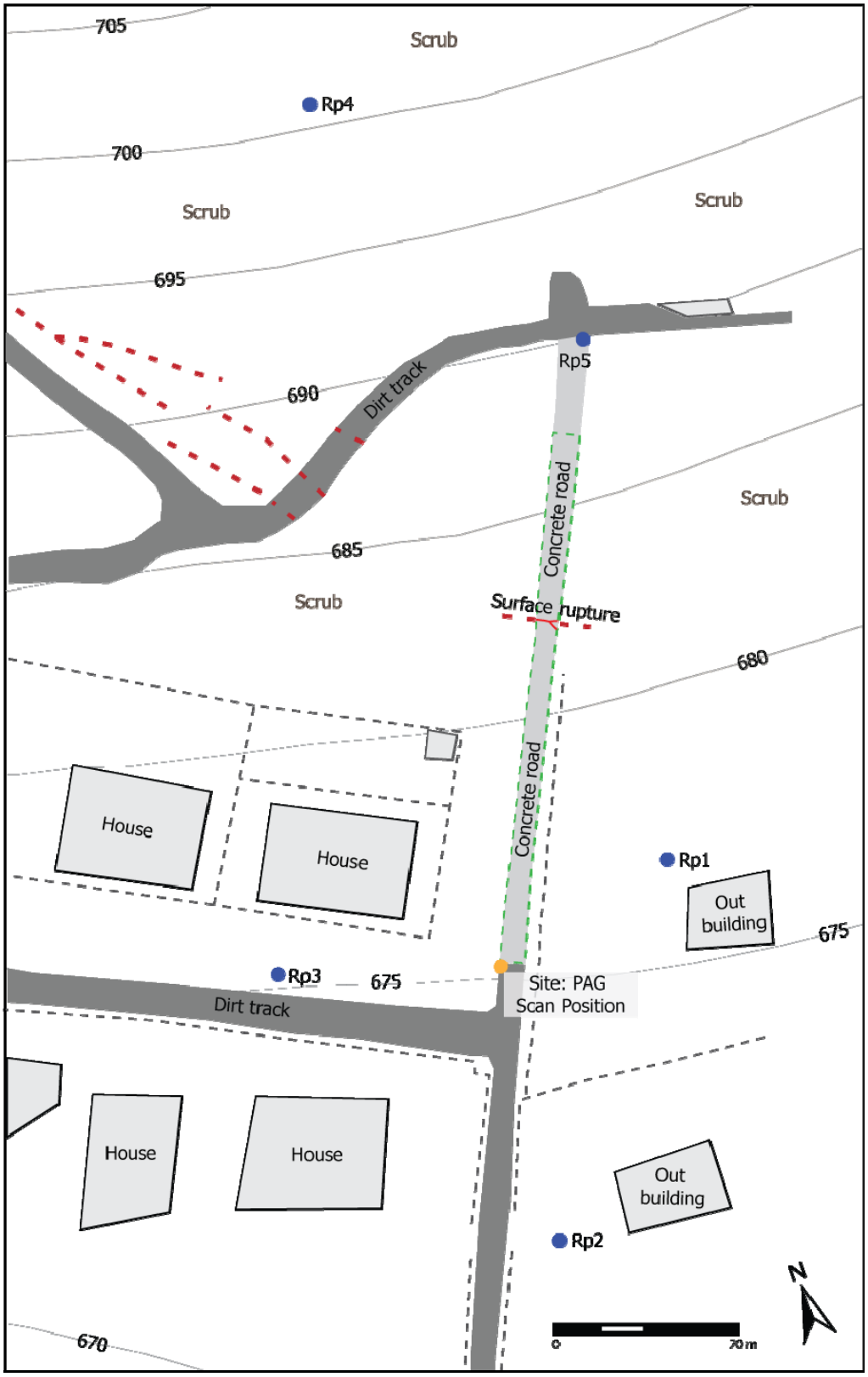

Figure 3.3.1: An example of a TLS survey set up, to measure active deformation across a surface rupture cross cutting a concrete road. The reflector positions are shown by blue dots (Rp1-Rp4). The topographic contour interval is 5 m.

Point cloud acquisition

Point clouds should be acquired at time intervals that correspond to when the deformation is expected to exceed twice the magnitude of the surface noise. When monitoring surface deformation, the higher the resolution of point cloud which can be acquired, the better, as closely spaced points can often be averaged over small areas to reduce noise. There are practical limitations on the point cloud resolution, such as time available at the survey site, as higher resolution point clouds take longer to acquire, which in turn uses more battery power, an issue when working in remote areas. A further consideration is the ability to work with the resultant data. It is important to ensure that the processing workflows are capable of working with large datasets. A common bottleneck in point cloud processing is the surface interpolation and meshing algorithms, which can require large amounts of CPU time and memory. In order to co-locate the point clouds, each of the reflectors in the reflector network should be scanned using the highest possible resolution. A closely spaced point cloud representing each reflector provides the most accurate measure of its position.

Initial point cloud processing

Each of the acquired point clouds are initially processed individually. The point clouds are cropped to remove any points from outside the surface of interest and any obvious sources of noise such as small clumps of vegetation, leaves and litter are manually removed as much as possible. The next step is to co-locate the scans within 3D space. The process of co-location (scan registration) is carried out within *RiSCAN*, by creating registration points in each of the point clouds from the reflector positions. The scan of each reflector is run through an internal reflector processing algorithm,

which uses knowledge of the shape and size of the reflector to produce an accurate centre point position (Fig. 3.3.2). Once the reflector registration points have been calculated for each point cloud, the point clouds are registered together. This process is carried out by rotating and translating each point cloud in 3D space, relative to the initially acquired point cloud until the reflector points coincide. The result co-locates the point clouds from each acquisition in 3D space (Fig. 3.3.3). As discussed in the previous section, in order to provide the best co-location possible, it is necessary to use reflectors with consistent positions, from a non-deforming part of the survey site, such as the footwall in the case of a surface rupture with normal sense displacement. Thus any surface deformation measured is in a footwall static reference frame and should the observed deformation be a combination of hangingwall subsidence and footwall uplift. The individual components of uplift and subsidence cannot be separated using this method.

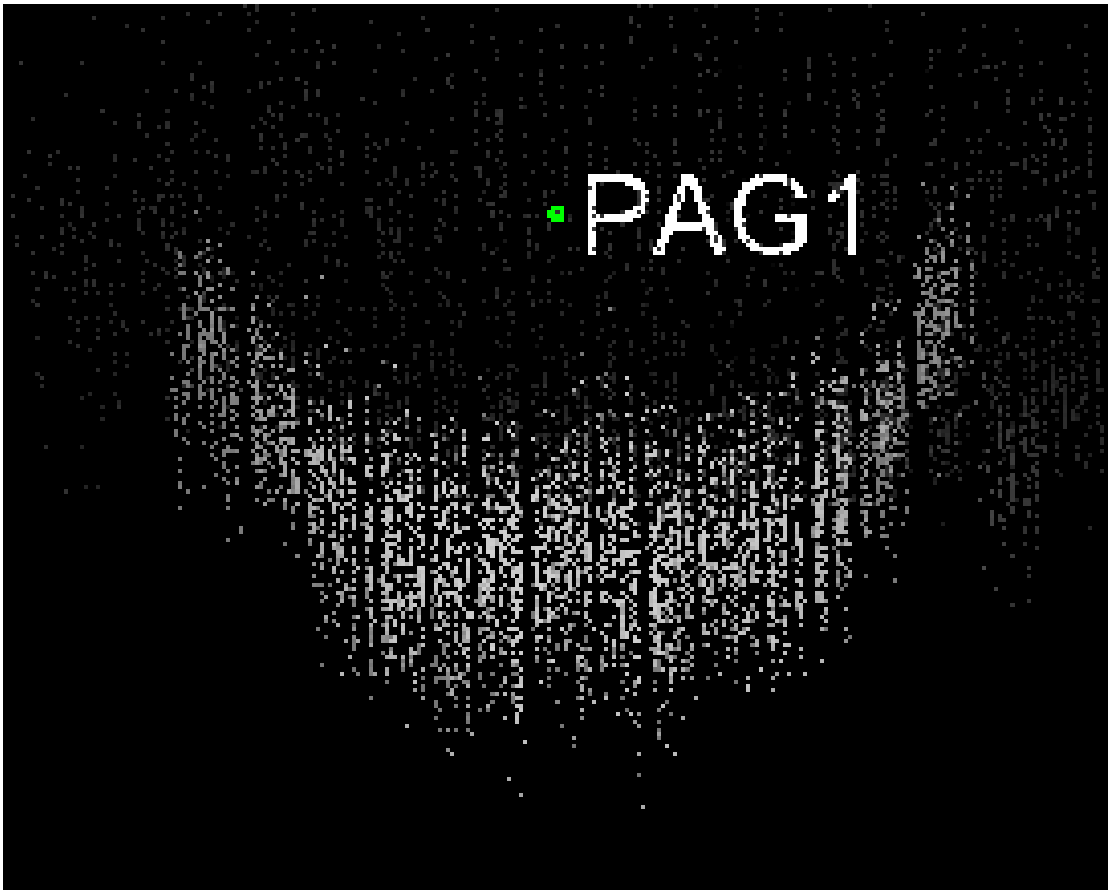

Figure 3.3.2: Oblique top-down view of a scan of a cylindrical reflector and the position (PAG1) of the centre of the reflector calculated using the reflector processing algorithm in *RiSCAN*.

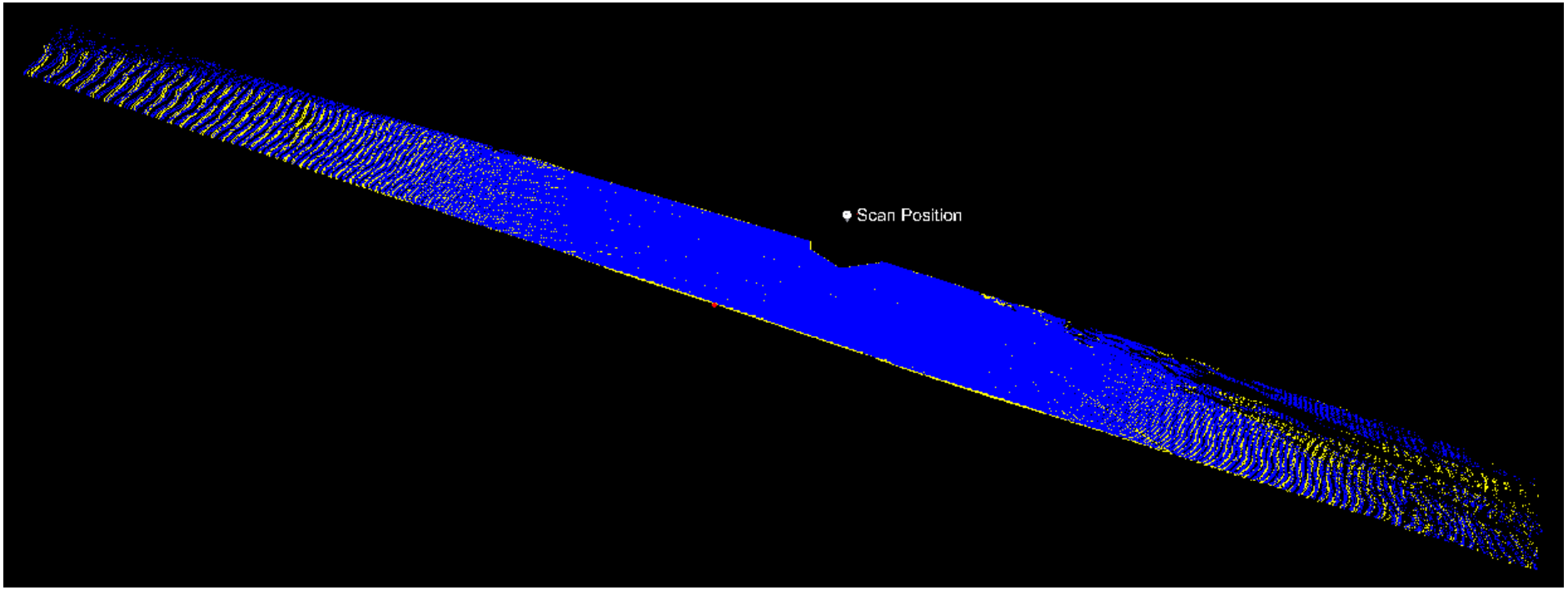

Figure 3.3.3: Oblique top-down view of the registration of two point clouds (blue & yellow) for Site SP (Chapter 5). The two point clouds are co-located in 3D space using the reflector positions in this survey.

Point cloud surface generation

Surface generation from each point cloud acts as a means to reduce the effect of noise and to provide like for like surfaces which can be used to measure surface deformation. Surfaces are generated individually from each point cloud using the discrete smooth interpolator (DSI, [Mallet, 1992]) algorithm in the program *goCAD*. The DSI algorithm aims to produce the smoothest surface possible from a point cloud while still honouring any inherent topography. A preliminary surface is first generated with a specified maximum spacing between triangle vertices (Fig. 3.3.4) which controls the resolution of the final output. The z-values of the preliminary surface are then modified using the DSI to honour the point cloud (Fig. 3.3.5). Individual surfaces are generated from each point cloud using copies of the preliminary surface and the DSI.

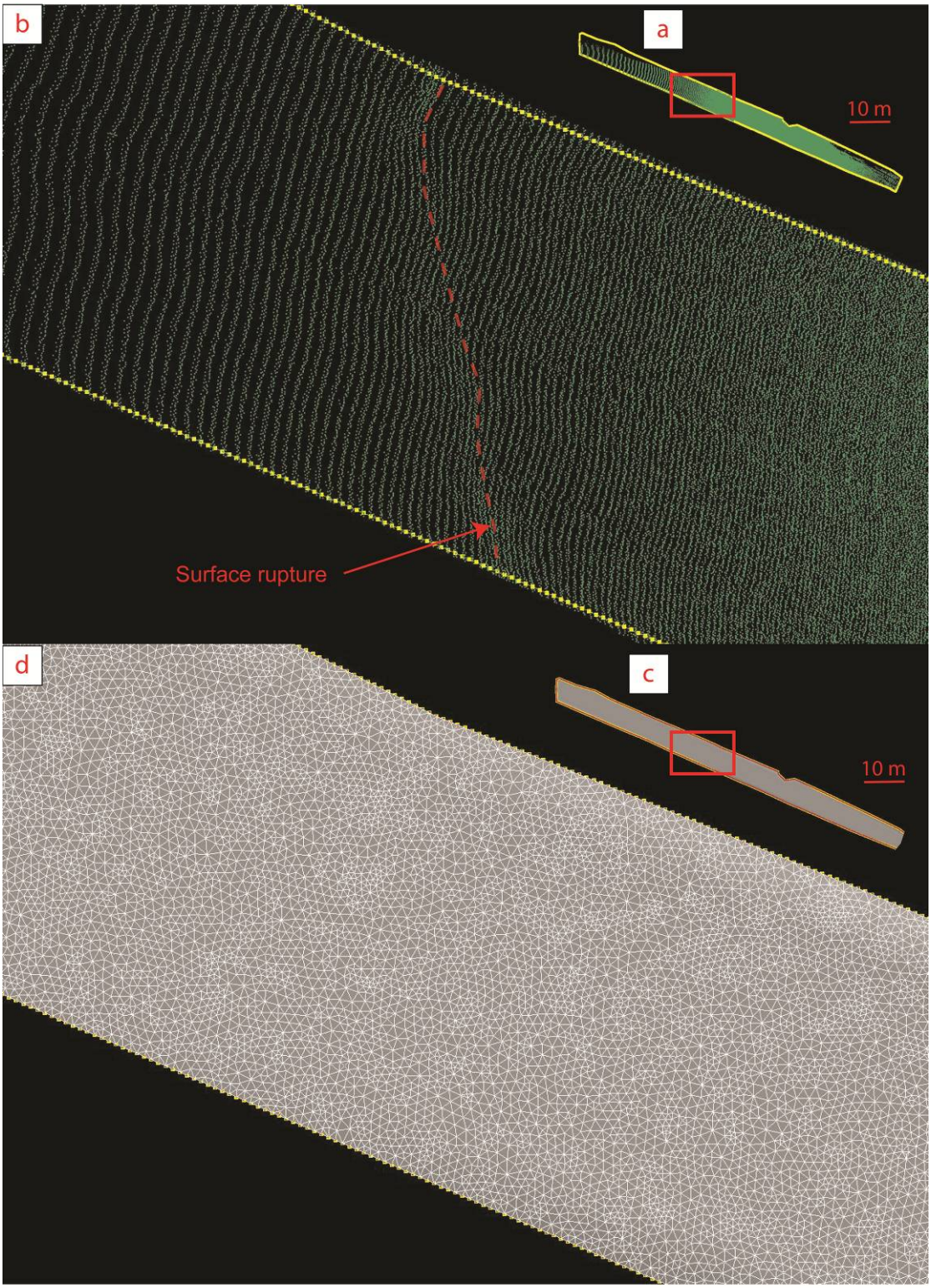

Figure 3.3.4: (a) Oblique top-down view of a point cloud dataset (green dots) of a tarmac road cross cut by a surface rupture (Site: SP, Chapter 5) and the surface boundary (yellow nodes). (b) A close up of the point set and the surface boundary from the red box in (a), note the trace of the surface rupture across the pointset. (c)

The preliminary surface, created from the surface boundary. The node spacing of the surface boundary (yellow nodes) is used to control the spacing between triangle vertices, shown by the white mesh (in this case ~10 cm).

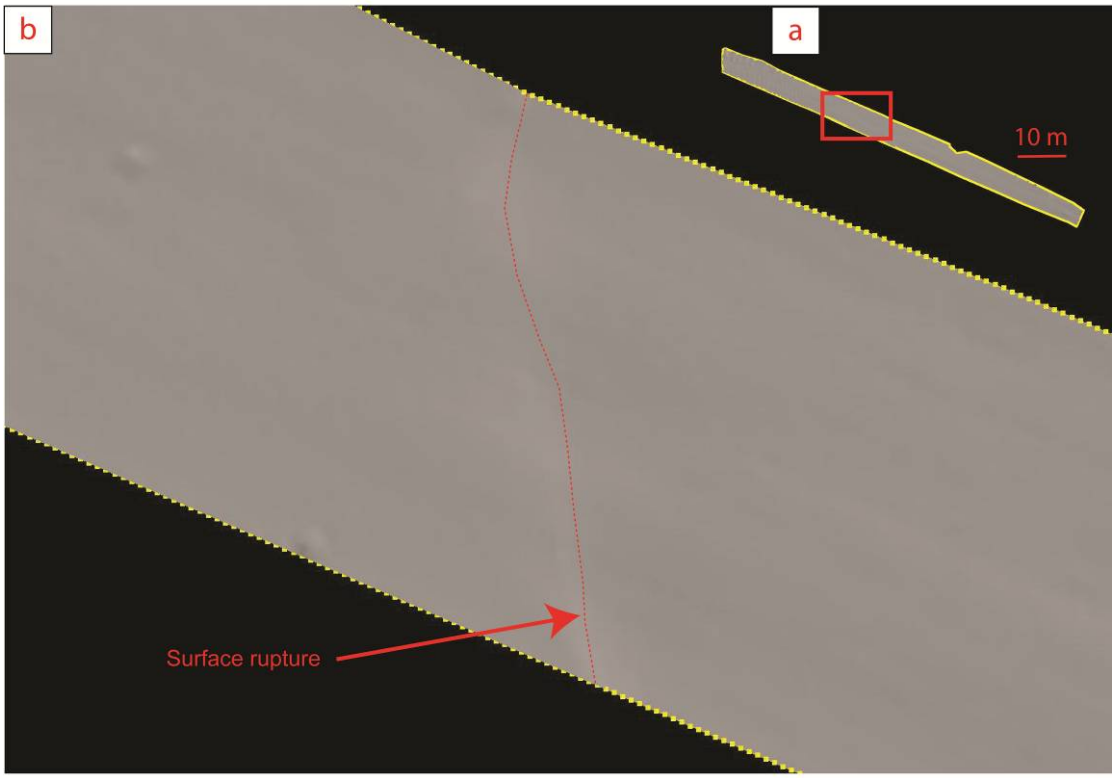

Figure 3.3.5: (a) Top-down oblique view of the initial DSI surface, created from the preliminary surface in Fig. 3.3.4.d by modifying the triangle vertices in the z-direction to honour the pointset. (b) Close up of the DSI surface from the red box in (a). Note the trace of the surface rupture and a subtle groove along the crown of the road where two strips of tarmac were butted together.

Calculating surface deformation using vertical differencing

Surface deformation is calculated between the surface generated from the initially acquired point cloud and any other surface generated from subsequently acquired point clouds. The vertical differencing tool in *goCAD* is used to measure the

deformation between the initial surface and any subsequent surface. The vertical differencing tool measures the deformation between two surfaces by calculating the vertical difference between pairs of corresponding triangle vertices. The vertices are corresponding as the interpolated surfaces are all generated from the same basic surface, during which the vertices are only shifted in a vertical sense to fit each point cloud. This creates a set of surfaces whose vertices are identical in map view. By calculating the vertical difference for all pairs of triangle vertices and then interpolating the result, the vertical component of deformation is computed across the entire surface. The resolution of the vertical differencing calculation is dependent on the spacing of triangle vertices chosen during the creation of the preliminary surface in the previous section. The result of the vertical differencing is displayed from a top-down map view perspective by applying a colourmap to the interpolated result (Fig. 3.3.6).

A cross sectional plot of the vertical difference result may be created by exporting the *x* position and calculated vertical difference data (*vd*) for all triangle vertices as an ascii text file. By calculating the bearing of the cross-sectional line which is to intersect the surface, as an angle relative to the x-axis (θ , Fig. 3.3.7), it is possible to resolve the *x* positions of the triangle vertices to distance along the cross section (*d*) using the following formula:

$$d = \frac{x}{\cos\theta}$$

A cross section of the calculated deformation between the two surfaces is created by plotting *d* against *vd* (Fig. 3.3.8). In order to reduce excessive noise in the plot it is

sometimes necessary to apply a moving point average to the data, allowing a smoother cross section to be created (Fig. 3.3.9).

Once a cross sectional plot has been created, a check of the accuracy of the point cloud co-location carried out in the earlier section 'initial point cloud processing' can be conducted. If reflector positions in the footwall were used to co-locate the point clouds, there should be close to zero vertical difference between the triangle vertices in the footwall. A linear shift with distance (divergence) of vertical difference in footwall vertices between the two surfaces signifies a less than ideal point cloud co-location (Fig. 3.3.9). The angle of divergence is obtained by applying a linear regression to the footwall vertical difference data in the cross section plot (Fig. 3.3.10). The angle of divergence (α) is the arctan of the gradient of the linear regression (m):

$$\alpha = \arctan(m)$$

The calculated angle of divergence (α) can be used to correct the co-location of the point clouds (and hence the DSI surfaces generated from them) by applying a rotation equal to that of the angle of divergence, about a horizontal axis of rotation perpendicular to the direction of the bearing of the cross-section (Fig. 3.3.7, yellow line). The axis of rotation must be specified as a unit vector (length = 1). The normalised x, y and z components of the axis of rotation *Ux*, *Uy* and *Uz* are calculated using the following formula, where θ is the angle between the x-axis and the bearing of the cross section.

$Ux = \sin\theta$
$Uy = \cos\theta$
$Uz = 0$

The rotation of angle α about the axis of rotation, defined by *Ux*, *Uy*, *Uz* is done using the 3x3 rotation matrix [*R*]:

$$[R] = \begin{bmatrix} (1-\cos\alpha)*Ux^2 + \cos\alpha & (1-\cos\alpha)*Ux*Uy + Uz*\sin\alpha & (1-\cos\alpha)*Ux*Uz - Uy*\sin\alpha \\ (1-\cos\alpha)*Ux*Uy - Uz*\sin\alpha & (1-\cos\alpha)*Uy^2 + \cos\alpha & (1-\cos\alpha)*Uy*Uz + Ux*\sin\alpha \\ (1-\cos\alpha)*Ux*Uz + Uy*\sin\alpha & (1-\cos\alpha)*Uy*Uz - Ux*\sin\alpha & (1-\cos\alpha)*Uz^2 + \cos\alpha \end{bmatrix}$$

(Adapted from the rotation matrix derivation at: www.euclideanspace.com/maths/geometry/rotations/conversions/angleToMatrix/index.html)

A corrected DSI surface is created by applying the rotation matrix [*R*] to the x, y, z co-ordinates of the DSI surface (*Sx*, *Sy*, *Sz*) created using the subsequently acquired point cloud in *goCAD* as follows:

$$\text{Corrected DSI surface} = [R] * \begin{bmatrix} Sx \\ Sy \\ Sz \end{bmatrix}$$

Following the correction of any inaccuracy in the co-location of the two point clouds, the vertical difference between the two DSI generated surfaces are again computed, interpolated across the surface and displayed as a colourmap (Fig. 3.3.11). The procedure to generate a cross section from the vertical difference calculation is repeated, with any divergence in the footwall due to non-optimal point cloud co-location now removed (Fig. 3.3.12).

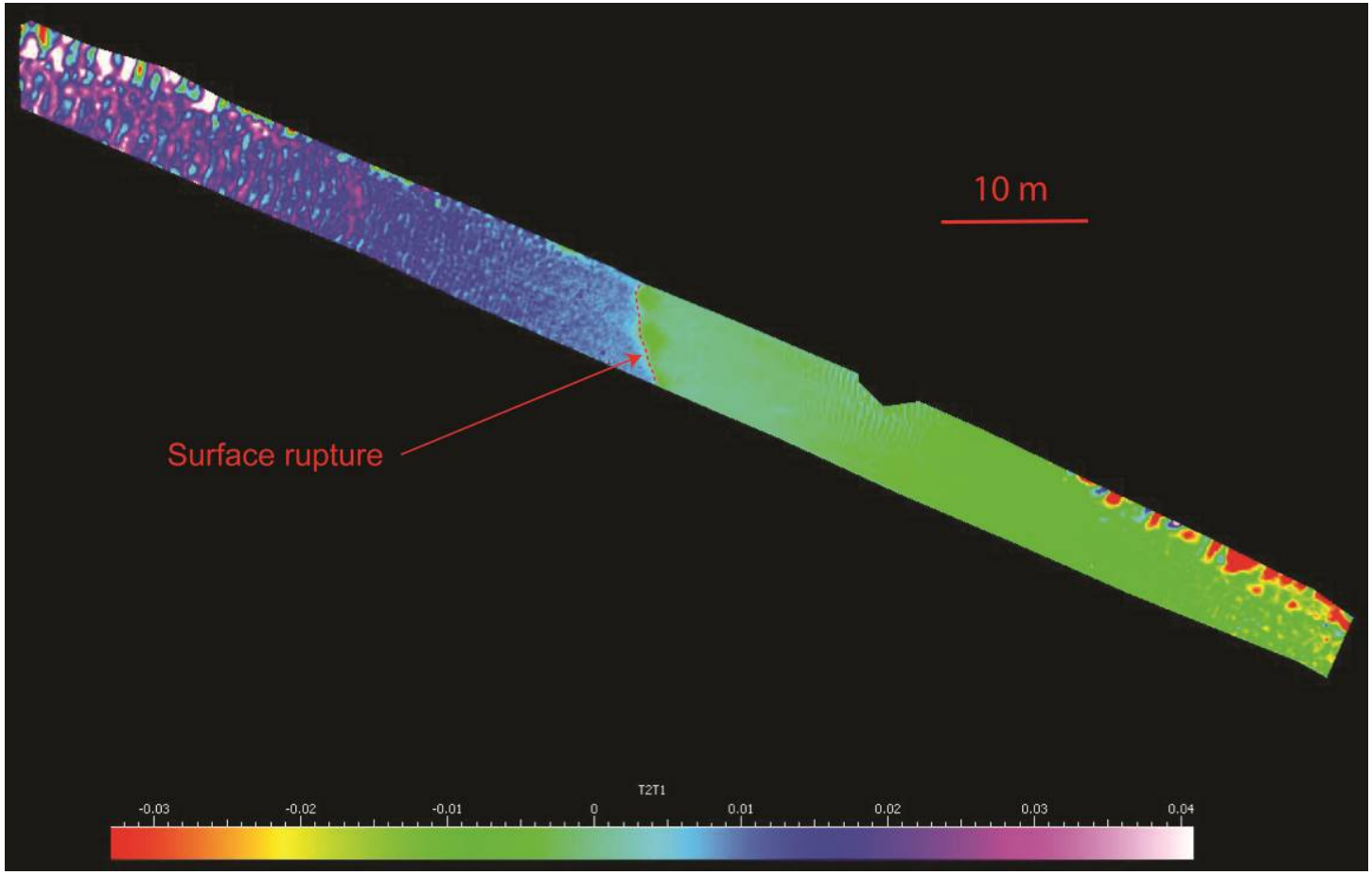

Figure 3.3.6: The result of vertical differencing of triangle vertices between the two surfaces, displayed on the surface as a colourmap. The colourmap scale (T2T1) is vertical difference in meters.

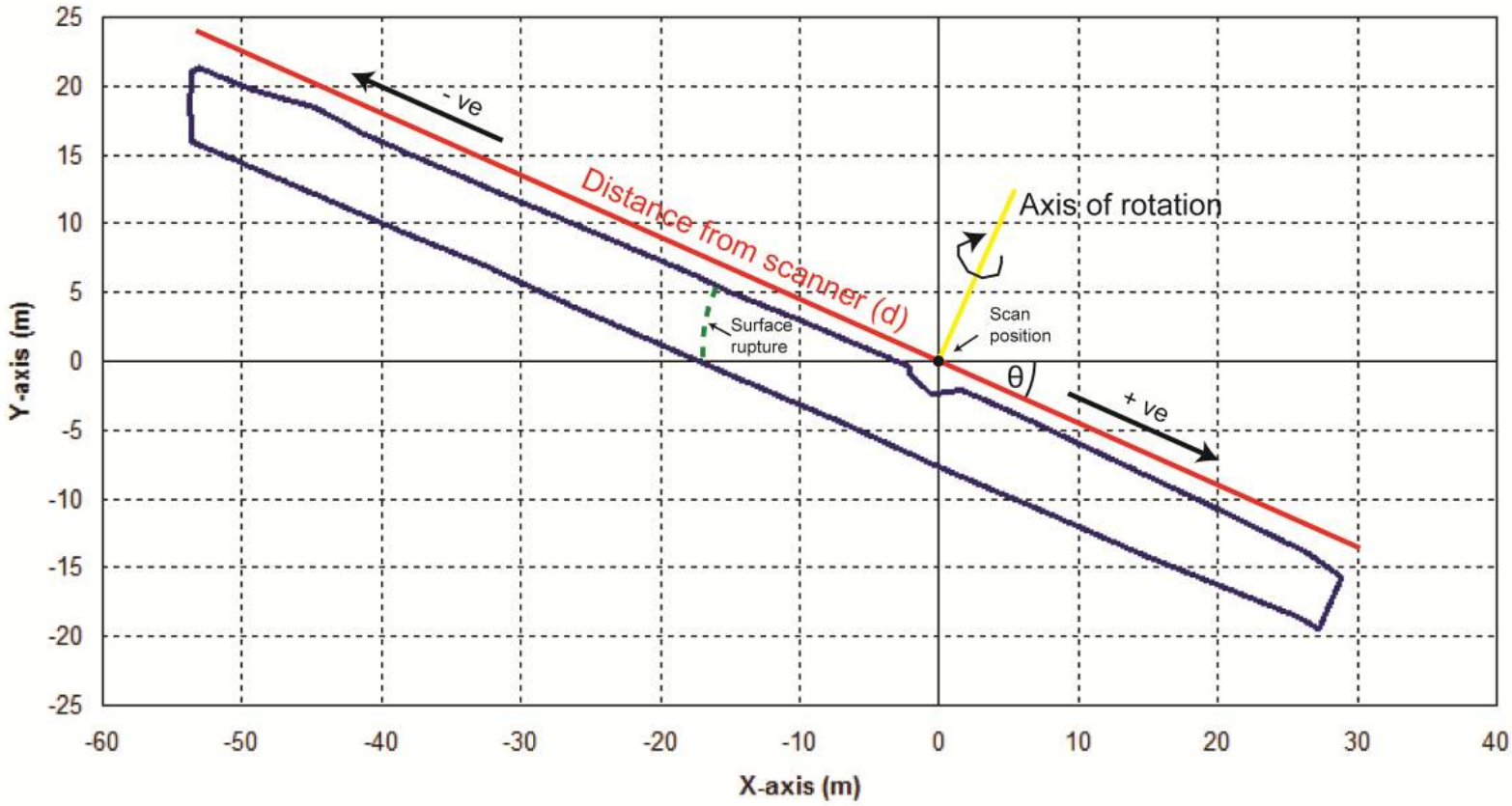

Figure 3.3.7: A map view of the surface boundary (blue) which contains the vertical difference data, and the line of the cross section (red line, 'distance from scanner' x-axis of Figs. 3.3.8 - 3.3.11) to be calculated. The scanner is located at the origin of the x – y axes. The axis of rotation, used to correct non-optimal point cloud co-location is shown by the yellow line.

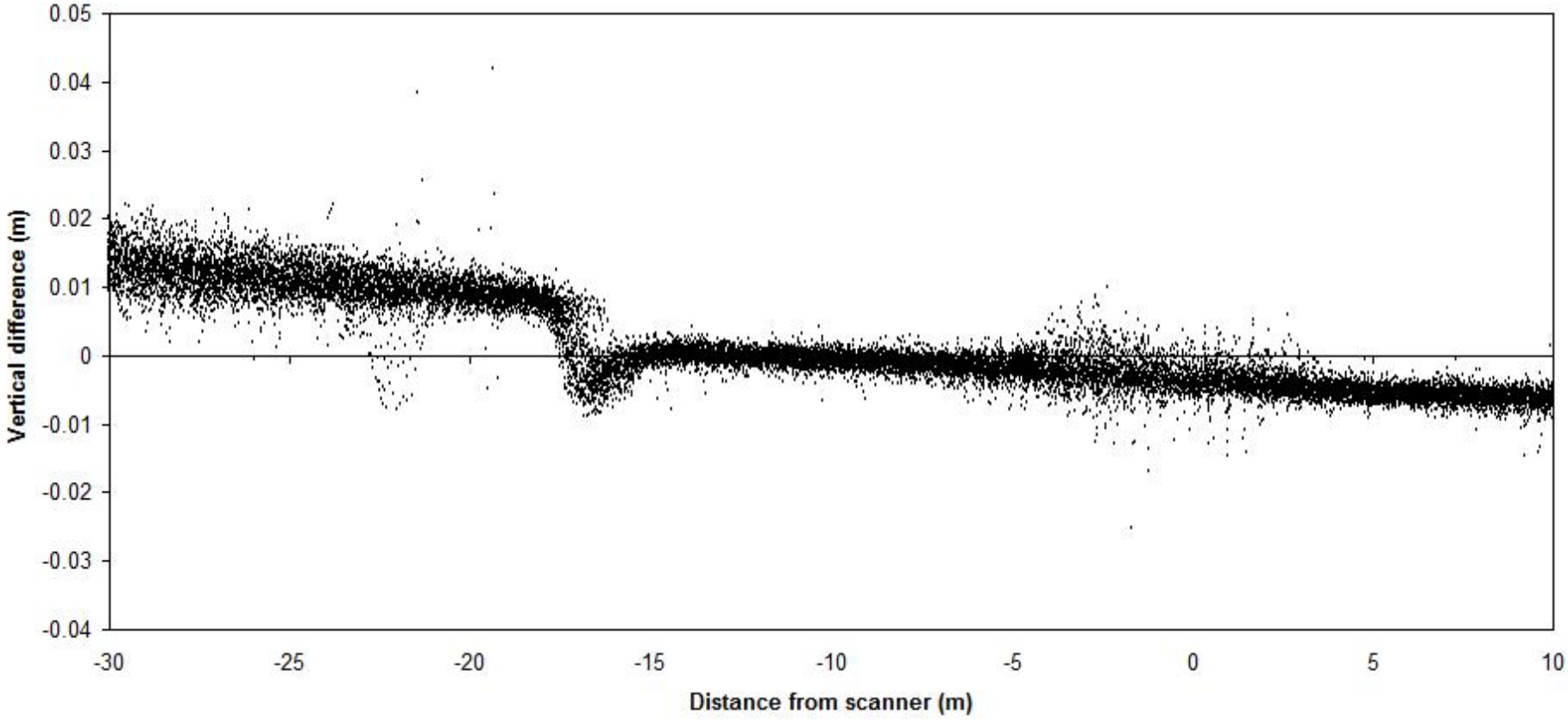

Figure 3.3.8: A cross sectional plot of the vertical difference data for each triangle vertex. Note the linear shift from the datum line with distance from the scanner.

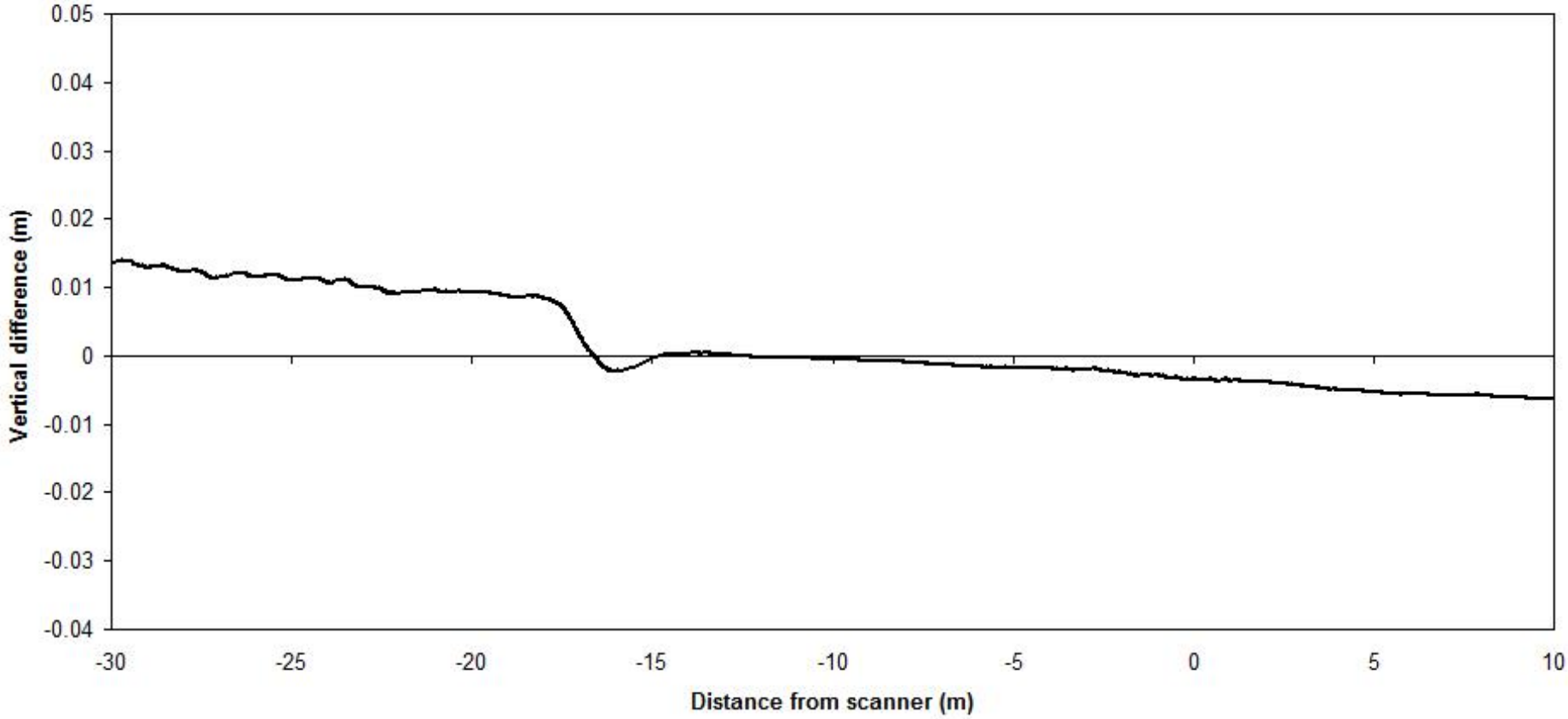

Figure 3.3.9: A cross sectional plot with a moving point average applied to smooth the data. Note the linear shift with distance (divergence) of the vertical difference values.

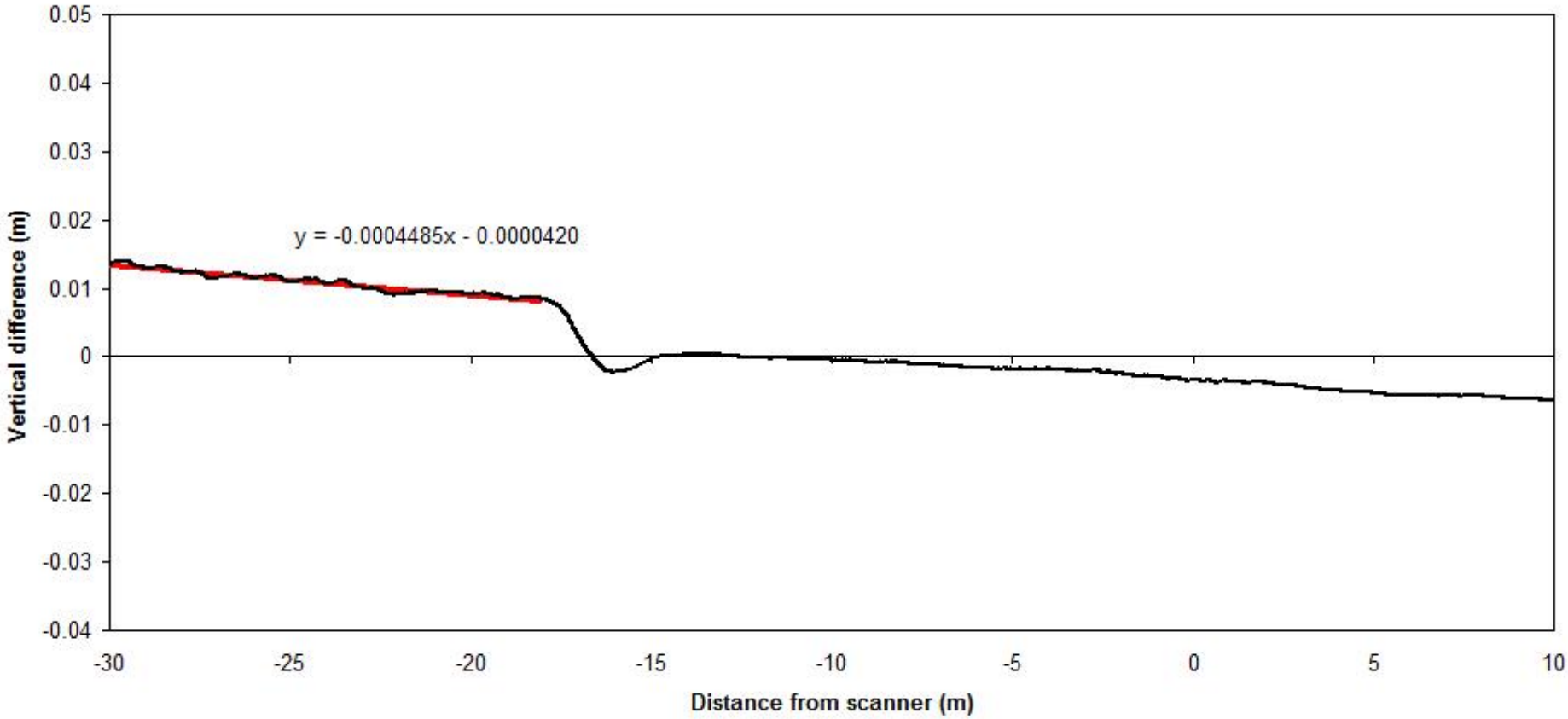

Figure 3.3.10: Linear regression (red line) of the vertical difference values in the footwall, used to define α and correct divergence.

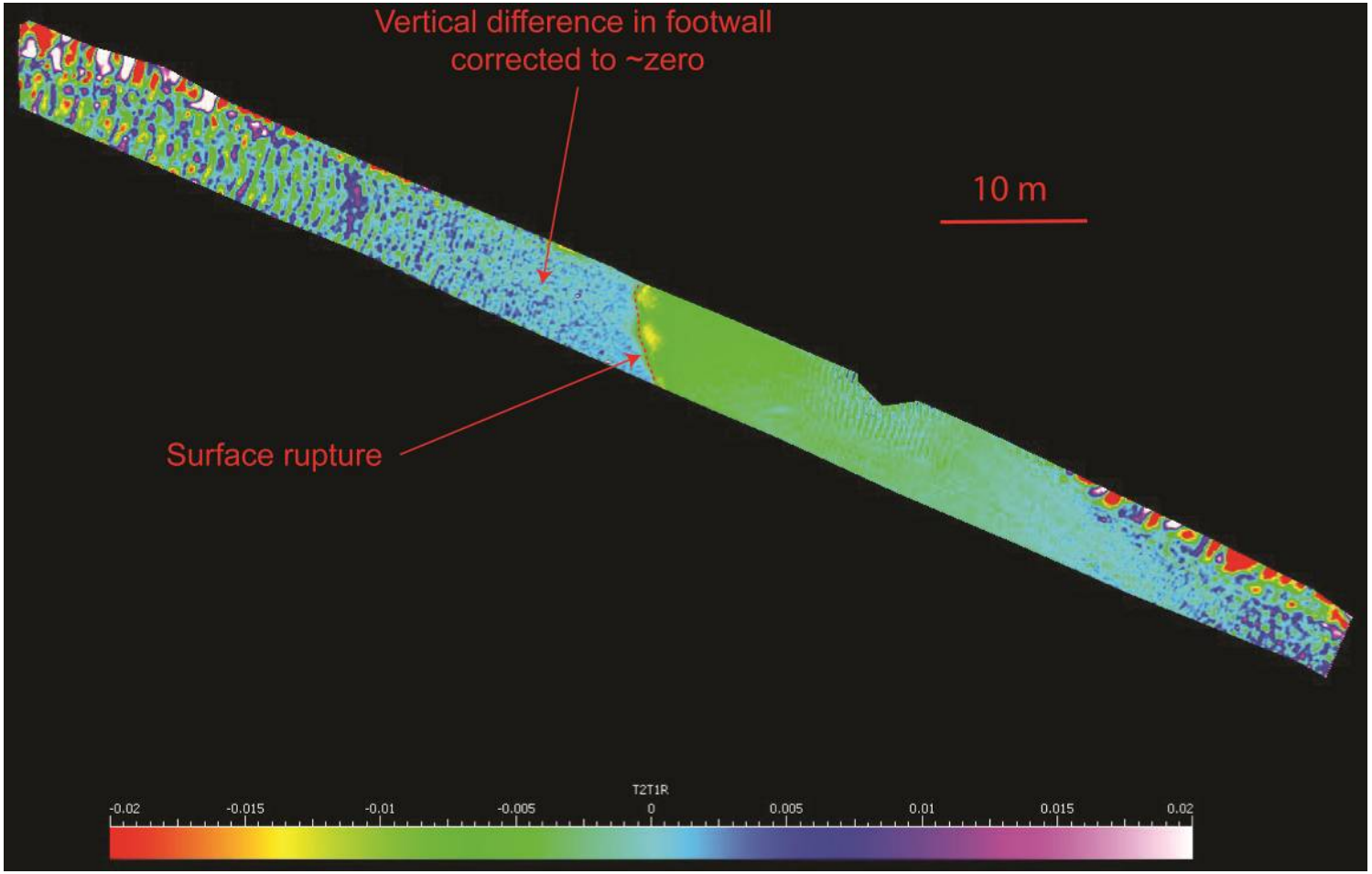

Figure 3.3.11: The corrected vertical difference colourmap for the two surfaces (T2T1R colourbar). Note the vertical difference in the footwall is corrected to zero compared to the linear shift in vertical difference with distance from the scanner shown in Fig. 3.3.6 & 3.3.9.

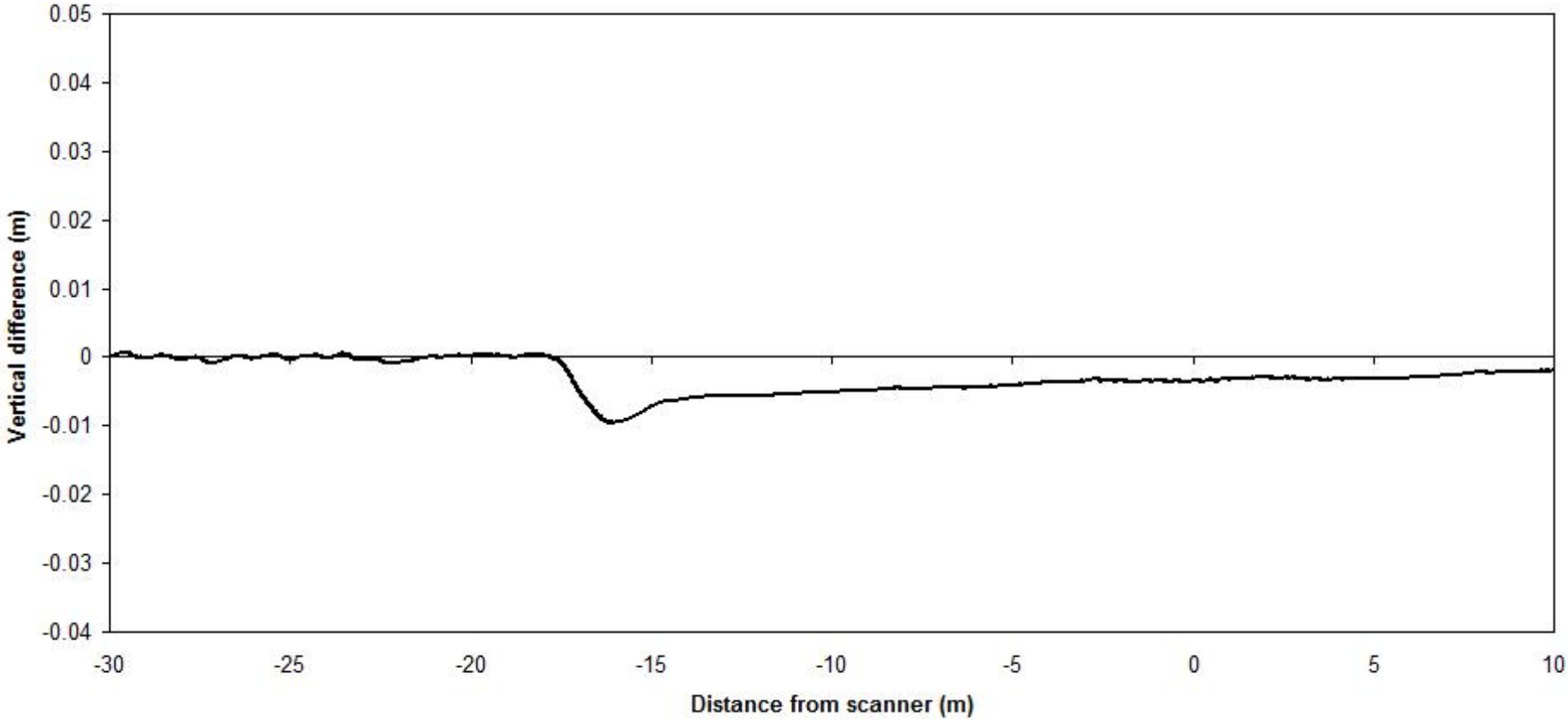

Figure 3.3.12: The corrected vertical difference cross sectional plot for the two DSI surfaces. Note the vertical difference in the footwall is corrected to zero, compared to the linear shift in vertical difference with distance from the scanner, as shown in Figure 3.3.9.

Calculating the horizontal component of deformation

Clearly the method above is only capable of calculating the vertical component of deformation in the case of a road surface. In order to gain an appreciation of the horizontal component of deformation across the surface, the reflector positions are used. The change in horizontal distance between reflectors paired across the surface rupture can be used to measure the horizontal deformation. The following equation is used to calculate the change in horizontal distance (H) between reflector A in the footwall and reflector B in the hangingwall. A_1 and B_1 represent the position of the two reflectors during the first acquired point cloud. A_2 and B_2 represent the position of the two reflectors during a subsequently acquired point cloud. Ax_1 represents the x co-ordinate of reflector A during the first acquired point cloud. Ay_1 represent the y co-ordinate of reflector A during the first acquired point cloud, and so on.

$$H = \sqrt{(Ax_2 - Bx_2)^2 + (Ay_2 - By_2)^2} - \sqrt{(Ax_1 - Bx_1)^2 + (Ay_1 - By_1)^2}$$

In order to provide an accurate measure of maximum horizontal deformation (H_{max}), the deformation measured (H) using the equation above is resolved in the direction of maximum deformation, using field measurements of the rupture kinematic slip direction. The operation is carried out using the following equation, where θ is the angle between the kinematic slip direction and the bearing of the line between reflectors A and B.

$$H_{\max} = \frac{H}{\cos\theta}$$

By using various combinations of reflector pairs, it is possible to calculate values for horizontal deformation, which can be used to complement the vertical difference maps describing vertical deformation.

3.3.3. Conclusions - Modelling postseismic surface motion using repeat terrestrial laser scanning

Repeat terrestrial laser scanning provides a new approach with which to measure active deformation. The method described provides calculation of surface deformation with unprecedented resolution and precision. This new approach allows subtle deformation, on the order of millimetres to decimetres to be measured and spatially mapped. The method is reliant on the selection of suitable study sites, primarily those with smooth, low noise surfaces, which can be accurately depicted as a meshed surface using the DSI algorithm. Repeat terrestrial laser scanning could be applied to a broad range of applications within the Earth Sciences, ranging from the measure of earthquake cycle related deformation (afterslip and postseismic deformation), surface deformations generated by volcanic activity (e.g. Pritchard, 2004), to coastal monitoring and geotechnical ground stability surveys. Chapter 5 provides an example of how the method can be applied to measure afterslip and postseismic deformation of the 2009 L'Aquila earthquake surface rupture.

Chapter 4: An analysis of variable throw-rate along the Campo Felice fault, using a high-resolution terrestrial laser scan dataset

4.1. Introduction

The earthquake recurrence interval of a fault, or the size of slip per event, and hence its seismic hazard is defined by its throw-rate [Roberts et al., 2004], because throw-rate is a direct measurement of cumulative fault slip events over a given time period. An increase in fault throw-rate will signify a decrease in the earthquake recurrence interval, or an increase in size of slip per event, producing an increase in seismic hazard. In order to calculate robust seismic hazard estimates it is important to properly characterise fault throw-rate over geological timescales. The central Italian Apennines have been undergoing extension since North-Eastward thrusting related to the convergence of Africa and Eurasia ceased during the Pliocene [Patacca et al., 1990]. An extensive array of North-West South-East trending normal faults have since formed in Mesozoic limestone bedrock (Fig. 4.1.2). Most faults are exposed at the surface as bedrock fault scarps which offset Late Pleistocene colluvial sediments deposited in basins within the hangingwall. The normal faults of the central Apennines which are presently seismically active have produced topographic offsets, through the process of fault slip during earthquakes. These faults offset a footwall upper slope surface formed during periglacial conditions during the last glacial maximum (Fig. 4.1.1, dated 15 ±3 Ka [Faure Walker et al., 2010]). The throw-rate of a fault over this 15 ±3 Ka interval can be calculated by measuring the vertical topographic offset of the footwall upper slope and the hangingwall lower slope in the field [Morewood & Roberts, 2000, Faure Walker et al. 2009]. Previous studies have

used traditional surveying methods such as total station to measure topographic offsets at a small number of sites along each fault.

The Campo Felice fault is a crustal scale (~5 km exposed scarp length) active normal fault in the central Italian Apennines exposed in Mesozoic-Cenozoic carbonates, with North-West – South-East strike (CF, Fig. 4.1.2). The fault is approximately 18 km in length and is split into two major segments, with a left stepping en-echelon geometry (Fig. 4.1.0). The North-Eastern fault segment is examined in this study (Red dashed line, Fig. 4.1.0). The fault has formed a small intra-montane basin in its hangingwall where a lake formed during the Pleistocene – Late Holocene. The surface expression of the fault is obscured by complex post-glacial geomorphology, including lacustrine sediments, outwash and alluvial fans (Fig. 4.1.0) as well as the creation of a periglacial upper slope surface in the footwall of the fault. There have been a number of studies on the timing of up to five glaciations identified within borehole cores from within the Campo Felice basin (i.e. Giraudi et al., 2011 and Giraudi & Frezzotti, 1997). A 20 m vertical offset of till was used to estimate a post-glacial slip-rate of 1.1 mm/yr for the fault (Galadini & Galli, 2000). A paleoseismic analysis of the bedrock fault scarp was conducted using image analysis which identified three horizontal bands. The three bands were used to identify two slip events on the fault scarp, dated between 860 – 1300 A.D. and ~1900 B.C. (Giaccio et al., 2002).

A new method has been developed to measure topographic offsets from a Terrestrial Laser Scan (TLS) point cloud dataset of the Campo Felice active normal fault. This method will increase the amount of measurements which can be acquired and will enable investigation into the effect fault geometry has on slip-rate. The method allows for the identification of suitable study sites, where the topographic

offset of the periglacial surface is created purely through the process of fault-slip during earthquakes. The TLS dataset is time-efficient to collect in the field, with throw-rate measurements carried out during post-fieldwork data processing. The result is that all suitable study sites are selected for throw-rate calculation, leading to an increase in throw-rate measurements between x3 – x10 over previous studies of similar faults using traditional field methods. In this study, the increased number of measurements for the Campo Felice fault allow for an along strike investigation into the factors controlling throw-rate variability and a revised maximum value for throw-rate with the uncertainty of this measurement.

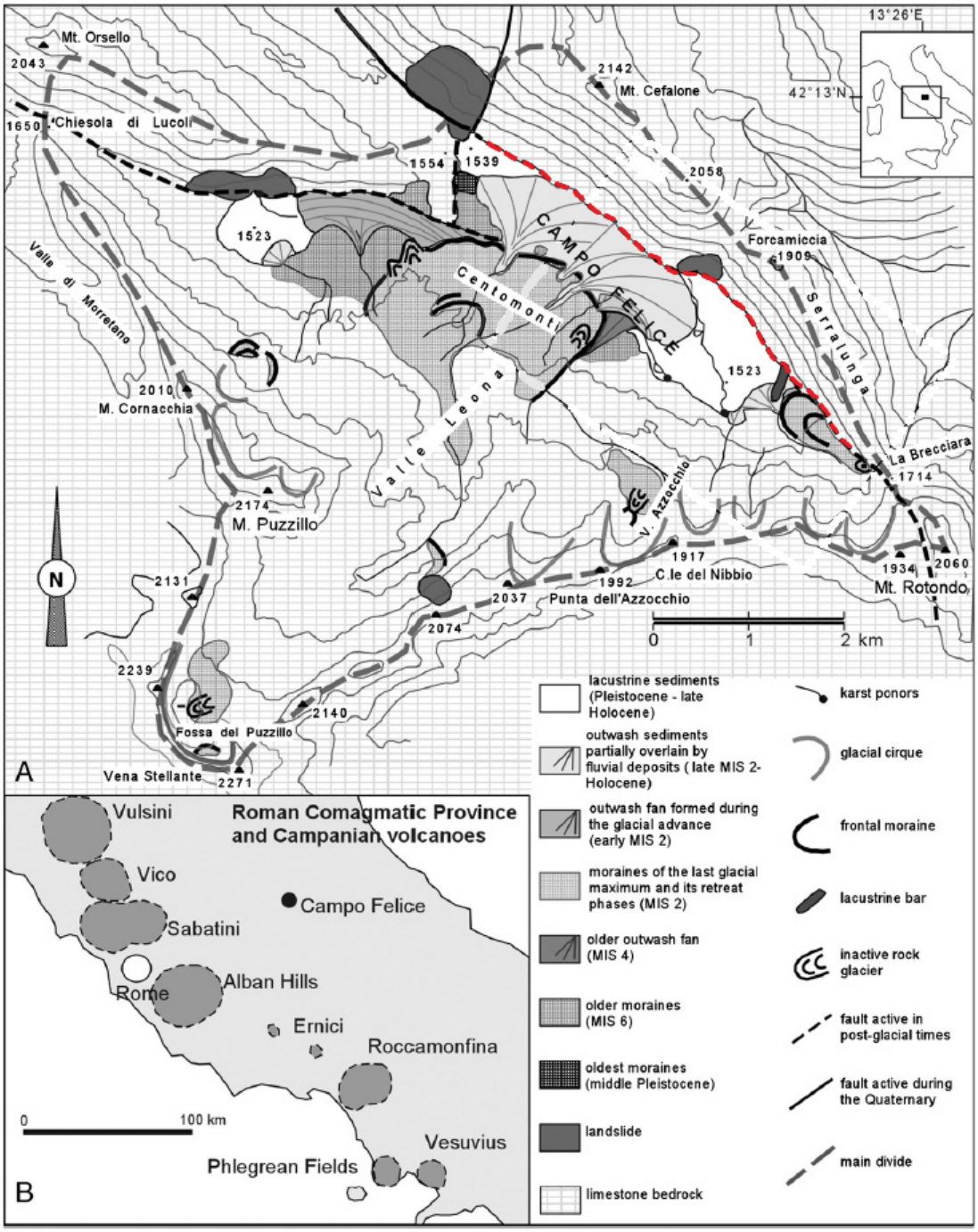

Figure 4.1.0: Map of the geomorphology of the Campo Felice fault (after Giraudi et al., 2011). Note the left stepping en echelon fault geometry. The North-Eastern segment of the fault (shown in red dashed line) was investigated in this study.

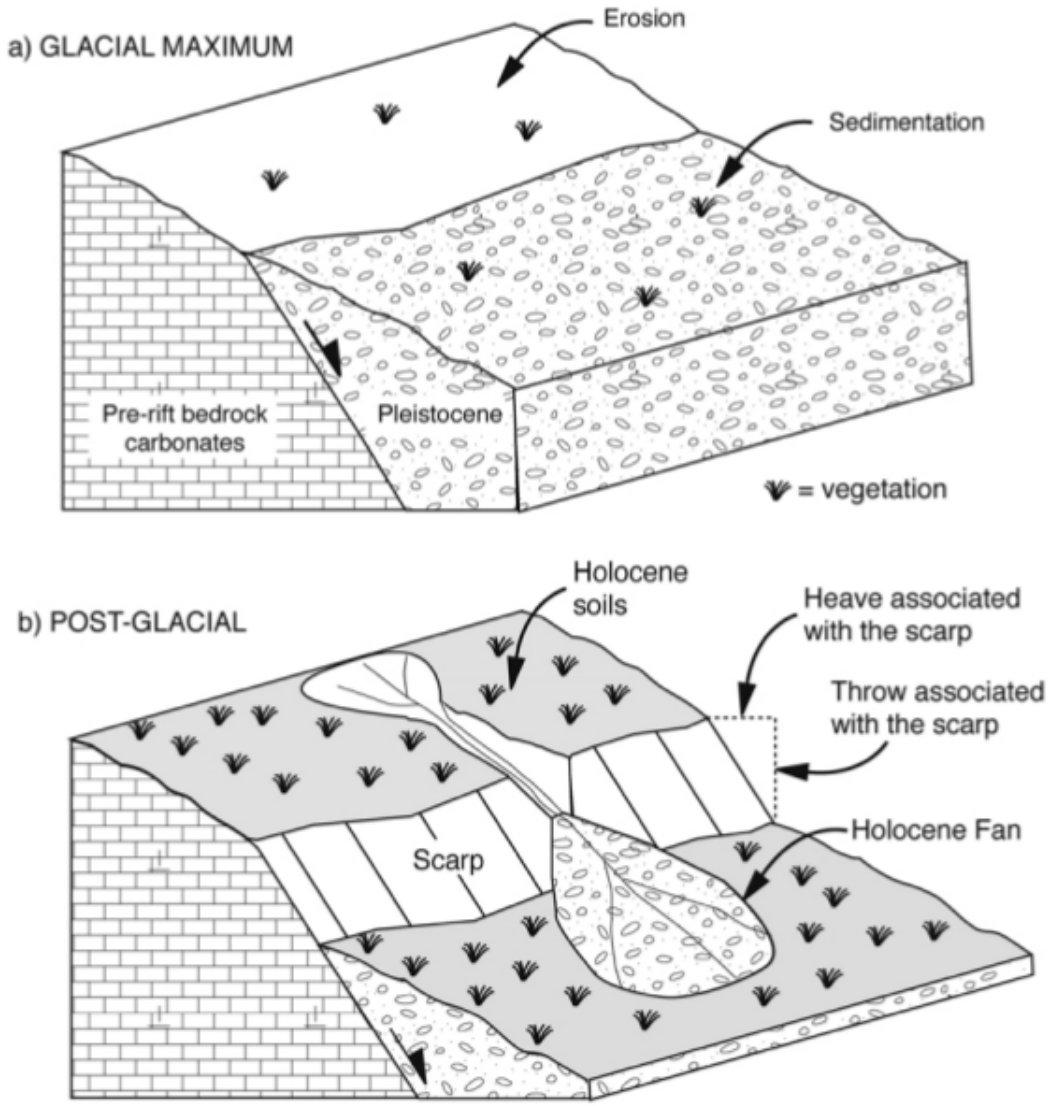

Figure 4.1.1: (a) Periglacial hangingwall sedimentation during the last glacial maximum outpaces the fault slip-rate, causing the fault to be buried in Pleistocene colluvium. A planar upper slope is formed in the footwall through erosion. (b) Blanket hangingwall sedimentation declines during post-glacial times. The fault slip-rate out paces localised hangingwall sedimentation. The fault is now exposed in the topography. The throw-rate of the fault since the last glacial maximum can be measured by the vertical offset between the footwall upper slope and the hangingwall lower slope. Figure adapted from Roberts and Michetti, (2004).

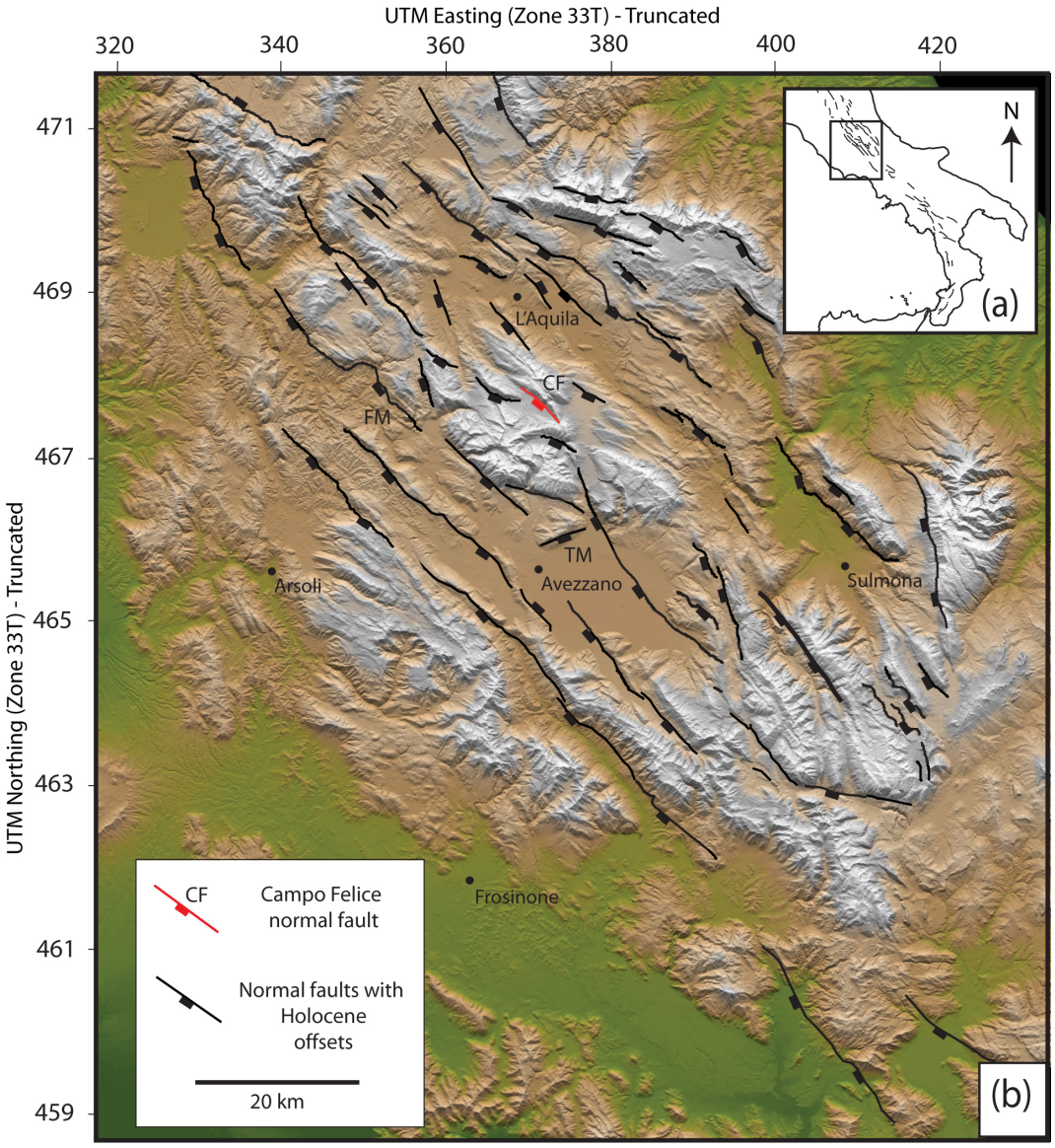

Figure 4.1.2: (a) Location map of the Italian peninsula. Active faults are shown as black lines. (b) Active normal fault map for the central Apennines. The surface trace of the Campo Felice normal fault is shown in red. Figure adapted from Roberts et al., 2010.

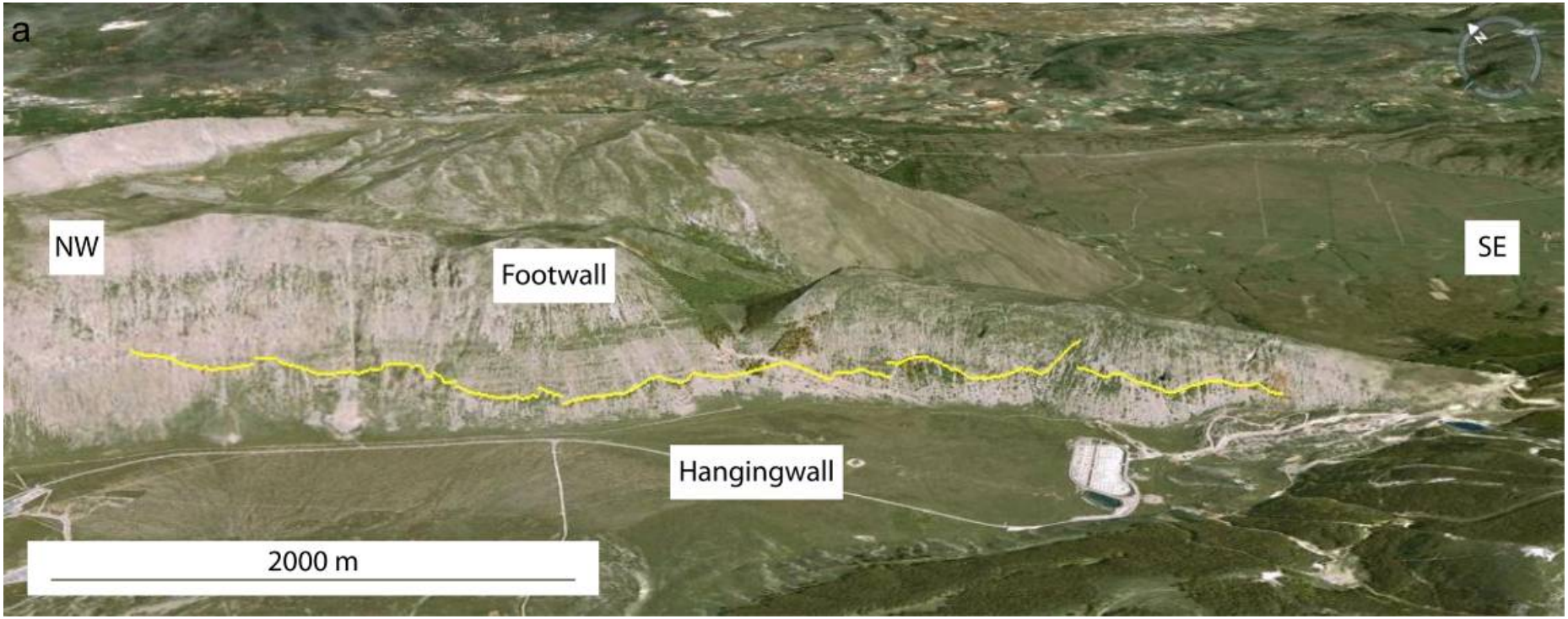

Figure 4.1.3: The Campo Felice fault as viewed in *Google Earth*. (a) Oblique view of the fault and the range front in its footwall.

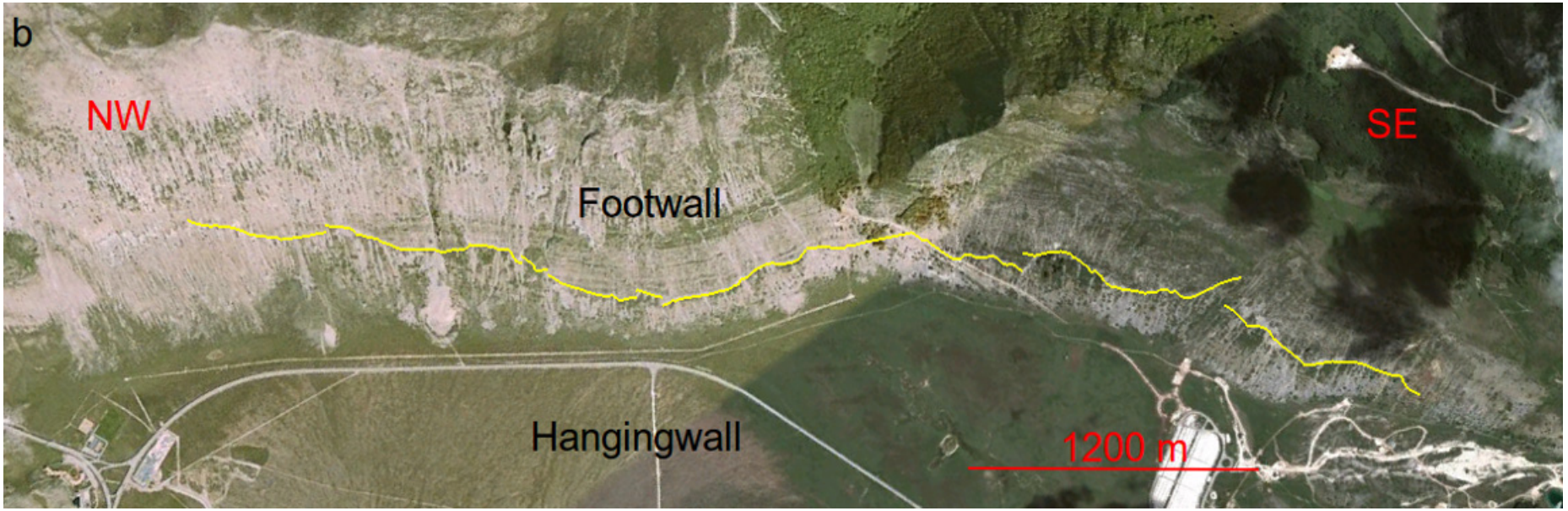

(b) Map view showing the variation in fault strike. Yellow lines represent the base of the exposed fault scarp.

4.2. Methods

4.2.1. Data collection

A terrestrial laser scan (TLS) point cloud dataset of the Campo Felice fault was acquired using a Riegl LMS-z420i laser scanner. The dataset consisted of six scan positions and 11 million points, covering the entire 5 km length of the Campo Felice fault (Fig. 4.2.1). The point clouds from each scan position were geo-referenced using the *RiSCAN* processing software. The UTM 33T co-ordinate system was chosen using the WGS84 datum. The geo-referencing (covered in Section 3.1.1) was carried out by surveying a network of cylindrical reflectors present within each point cloud using real time kinematic (RTK) GPS. This process correctly unites the point clouds from each scan position in 3D space.

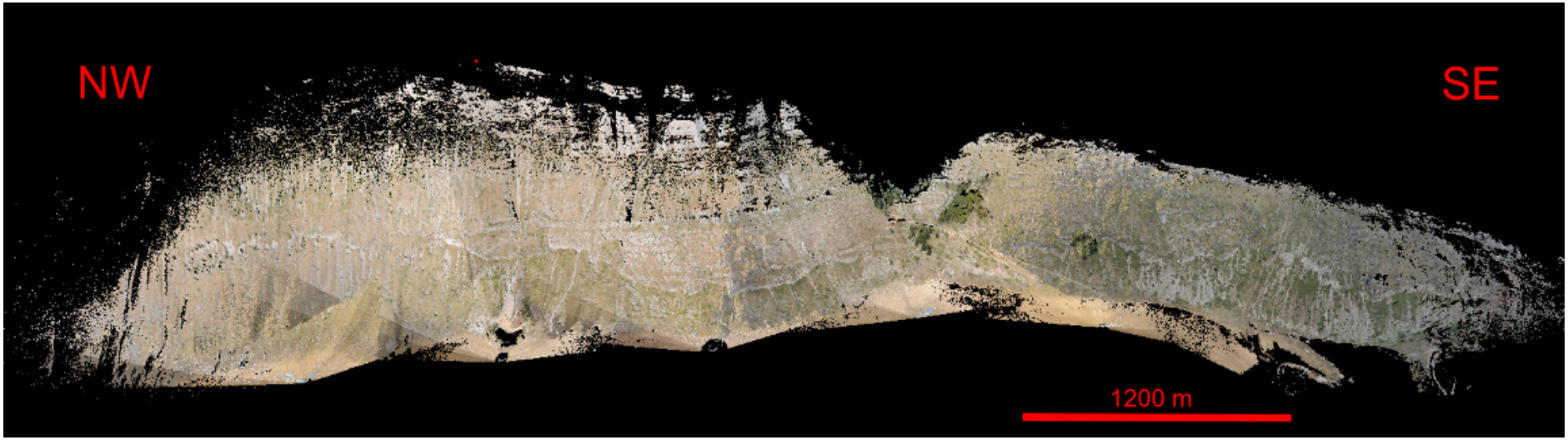

Figure 4.2.1: Terrestrial Laser Scan point cloud dataset of the Campo Felice fault. The point cloud is coloured using RBG data obtained from a digital camera mounted on top of the laser scanner. The location of the fault is denoted by the red line in Fig. 4.1.0 and 'CF', Fig 4.1.2.

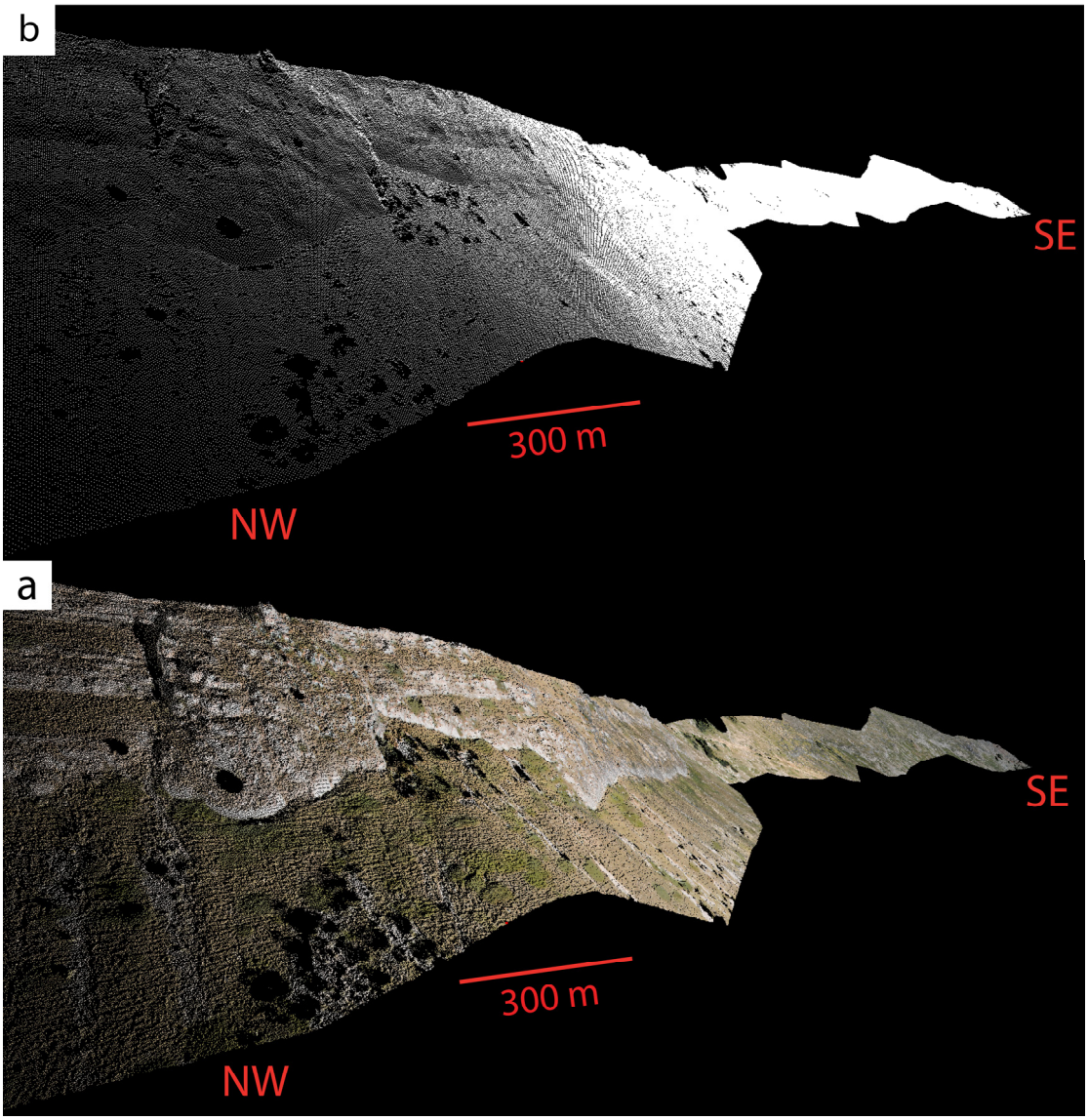

Figure 4.2.2: (a) Manual removal of vegetation from the point cloud dataset. (b) The product of the points2grid pseudo-vegetation filter, producing a dataset with regularly spaced points in map view. The method is described in more detail in Section 3.1.2.

4.2.2. Cross section site selection using geomorphic indicators

Geomorphic processes alter the perceived surface offset along active faults and are an important consideration for earthquake geologists. In order to study surface offsets produced solely by fault slip during earthquakes it is necessary to select study

sites which have not had their surface offset altered by geomorphic processes such as erosional gullying, colluvial and alluvial fan sedimentation or landslides. To aid the selection of suitable study sites, a series of derivative products highlighting the geomorphology of the Campo Felice fault were produced from the vegetation-filtered point cloud dataset and checked during fieldwork. The dataset was interpolated to produce a representative ground surface TIN and hillshade raster (Figs. 4.2.3 and 4.2.4) using the methods described in Section 3.1.2. The ground surface TIN and hillshade raster reveal several large gullies in the footwall of the fault, accompanied by large alluvial fans in the hangingwall (Figs. 4.2.4 & 4.2.6). There are also a series of erosive channels in the hangingwall. These features alter the perceived surface offset of the fault and therefore are unsuitable locations for study sites. A surface dip map (Fig. 4.2.5) and surface contour map with 10 m interval (Fig. 4.2.6) were also generated from the vegetation-filtered point cloud dataset using the methods described in Section 3.1.2. The surface dip map highlights regions of the ground surface which are low in dip (cool colours) or high in dip (warm colours). Rapid changes in colour in the footwall or hangingwall suggest these regions of the surface are degraded in relation to other regions where colour changes are more gradual. The generation of a surface contour map with 10 m interval reveals regions of the footwall and hangingwall which are degraded as curved, non-linear contours with changes in the distance between successive contours. Subtle erosive channels in the hangingwall are depicted as sharp kinks in the surface contours (Fig. 4.2.6).

4.2.3. Cross section interpretation using Crossint

The derivative products created from the point cloud dataset were used to select twenty five study sites deemed to be free from the effects of active geomorphic processes. Sites were selected on the basis of having a linear hangingwall or lower slope in cross section, free from alluvial fan sedimentation or erosive gulling, a fault scarp which is not degraded, as well as a distinct upper slope periglacial surface in the footwall created during the last glacial maximum (an example is shown in Section 3.2.2, Fig. 3.2.1). Cross sections were created at each of these sites from the surface TIN in *RiSCAN*, using the method described in Section 3.2.2. At each site ten cross sections were created in parallel, spaced at 1 m intervals (Fig. 4.2.7) producing two hundred and fifty in total. Each of the cross sections were interactively interpreted for throw using the program *Crossint* (Appendix ii) and the method described in Section 3.2.2.

4.2.4. Data analysis and generation of throw-rate and strain-rate profiles

The interpretation of batches of ten cross sections from each of the twenty five study sites using *Crossint* produced values for throw, heave, hangingwall dip, scarp dip and footwall dip (Appendix iii). From the set of ten cross section throw measurements at each site, up to five measurements deemed to be anomalous in relation to the mean for the set were eliminated from the following analysis (Appendix iii, column 4, red boxes). A value for throw-rate (mm/yr, Appendix iii, column 4) was calculated from the remaining throw measurements using the equation in Section 3.2.2, using an upper slope age of 15 ka. From these values the mean

throw-rate was calculated for each site (Appendix iii, column 6). The standard deviation for throw-rate was also calculated and used as a 1σ error bound for measurement precision (Appendix iii, column 5). A throw-rate profile for the Campo Felice fault (Fig. 4.3.1) was then produced by plotting the mean throw-rate at each site, against their distance along the fault (Appendix iii, column 2), with error bars from the standard deviation for throw-rate (Appendix iii, column 5). A profile for strain-rate was then generated from the measurements of throw, fault geometry and kinematics for 250 m x 250 m boxes along the fault using the 'Strain-rate' method described in Section 3.2.2 (Faure Walker et al., 2009, Fig. 4.3.6, Appendix v).

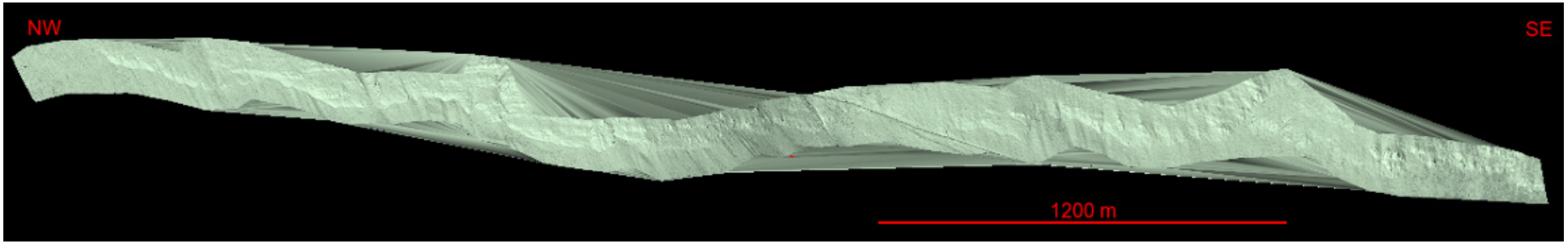

Figure 4.2.3: Triangular Irregular Network (TIN) interpolation of the vegetation-filtered point cloud dataset for the Campo Felice fault. The TIN allows for the identification of geomorphic features.

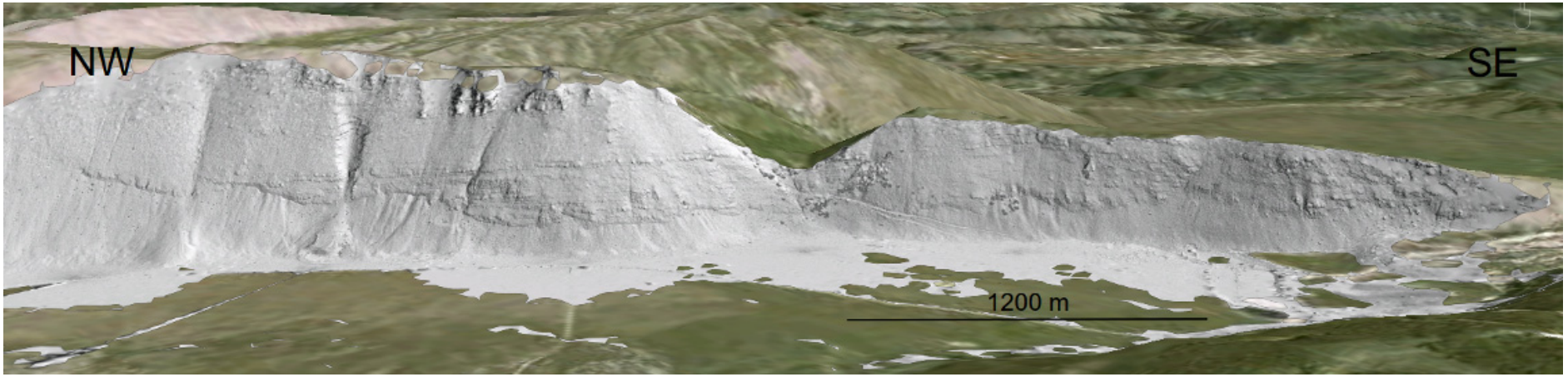

Figure 4.2.4: A hillshade raster of the vegetation-filtered point cloud dataset for the Campo Felice fault, viewed in *Google Earth*. The hillshade allows for the identification of geomorphic features.

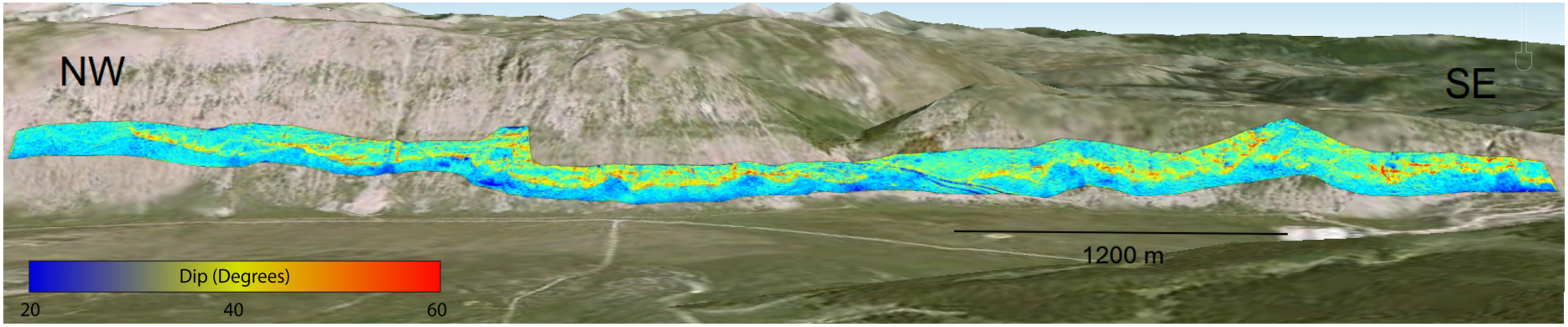

Figure 4.2.5: Surface dip map for the Campo Felice fault, viewed in *Google Earth*. Cool colours represent low surface dip ~20 degrees. Warm colours represent high surface dip ~60 degrees.

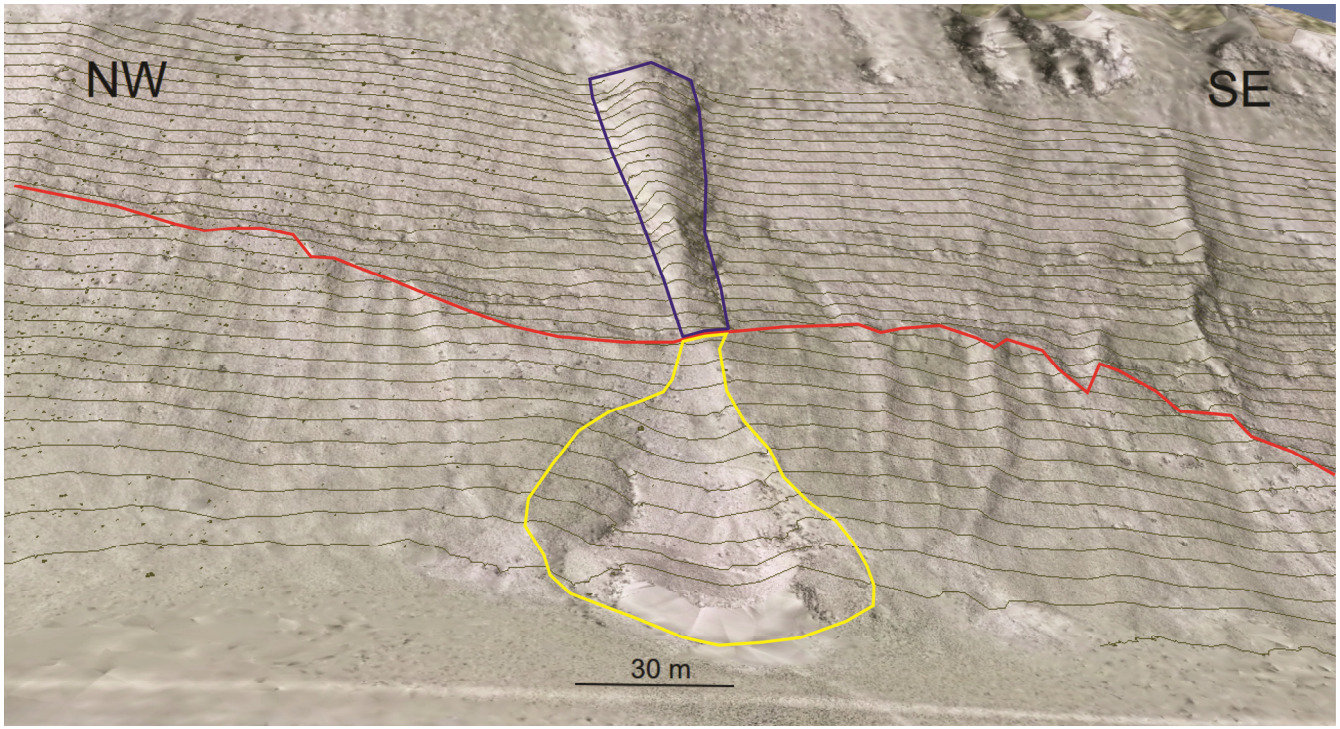

Figure 4.2.6: Surface contour map of 10 m interval imposed over the hillshade raster (see black box, fig. 3.1.5 for the location of this figure on the Campo Felice fault). None-linear contours highlight areas of gullying in the footwall and alluvial fan deposition in the hangingwall. Changes in the distance between successive contours indicate a change in surface dip. Subtle gullying in the hangingwall is depicted by kinks in the contours. The red line shows the base of the fault scarp. The blue polygon depicts the extent of a footwall gully, with the yellow polygon showing the extent of a hangingwall alluvial fan fed by this gully.

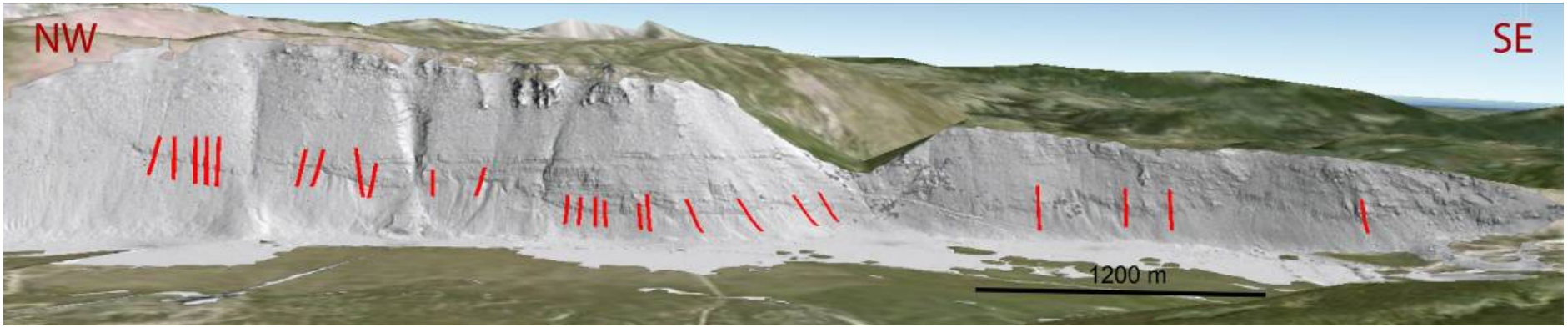

Figure 4.2.7: The locations of twenty five study sites selected for the generation of cross sections, displayed in *Google Earth*. The cross sections sites are shown in red, each site is a batch of ten cross-sections spaced at 1 m intervals, overlaying the hillshade raster.

4.2.5. Fault geometry and slip kinematic data

Two hundred and sixty eight field measurements were collected along the entire length of the Campo Felice fault at thirty four individual study sites. The collected measurements comprised of the strike and dip of the exposed fault scarp surface, and the slip direction measured from the plunge direction of fault striae, in cases where they could be seen (Appendix iv, Figs. 4.2.8 & 4.2.9). The field measurements were taken using a compass clinometer with locations provided by real time kinematic GPS with centimetre precision. In order to visualise the changing geometry and slip direction of the fault along its length, the measurements were averaged in the case where multiple measurements were taken at the same site and GPS locations were converted to distance along the fault, from the North-Western end of the studied segment, to be plotted on the x-axis against the various measurements (Figs. 4.3.3, 4.3.4 and 4.3.5. Appendix iv). The mean dip for the entire fault was 54° (1σ = 3.1°), the average strike was 129° (1σ = 16.5°) and the average slip direction was 216° (1σ = 11.5°).

Figure 4.2.8: An example of fault striae from the Campo Felice fault scarp, used to infer kinematic slip direction in the field. The slip direction is inferred by measuring the plunge direction of the striae with a compass clinometer.

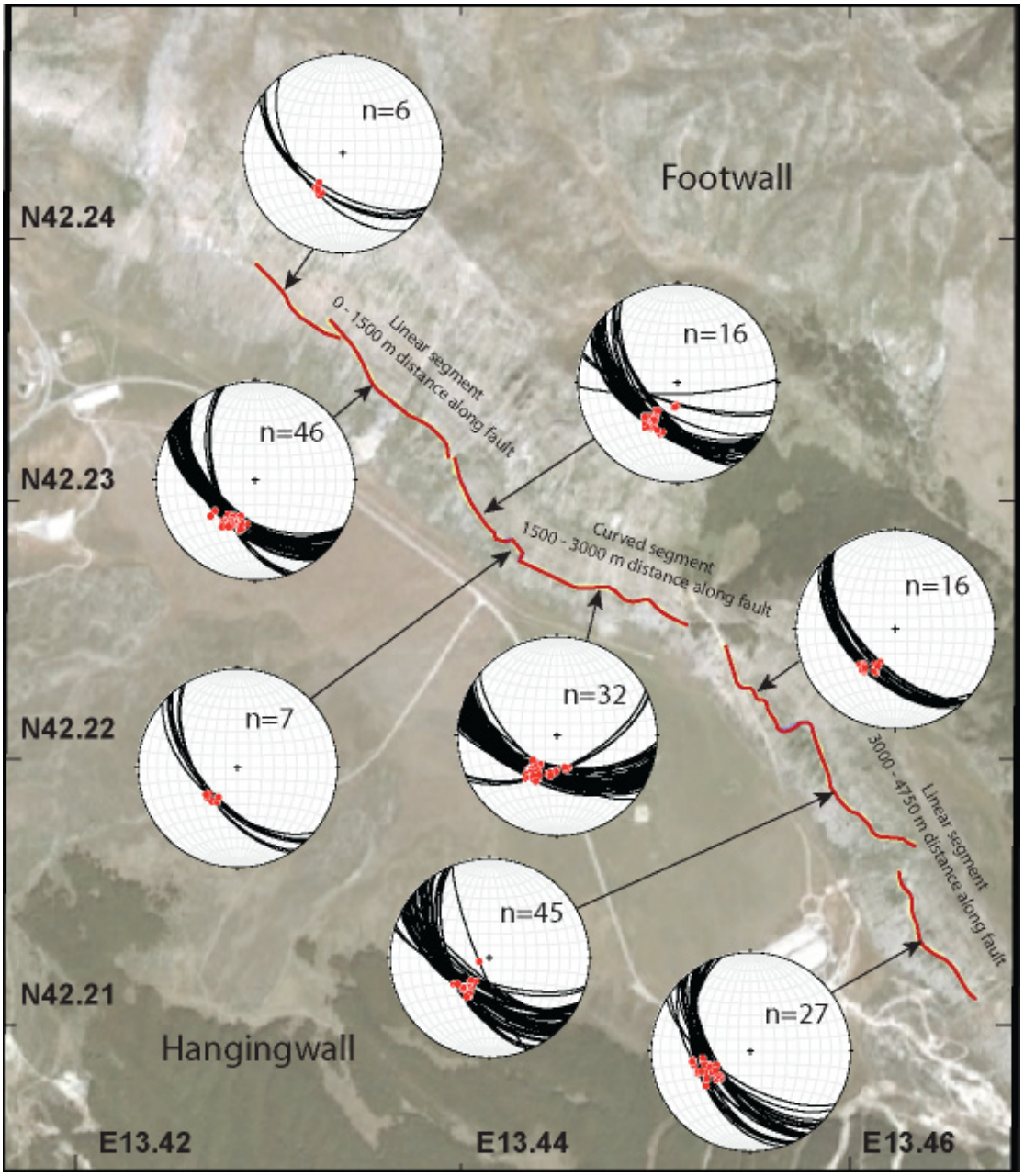

Figure 4.2.9: Lower hemisphere stereographic projection of the orientation of fault planes (great circles) and the kinematic slip-vector orientation defined by striated faults (red dots), showing how the slip-direction of faulting varies along the Campo Felice fault. The individual data is presented in Appendix iv. They have been grouped together by fault segment in order to create this figure.

4.3. Results

Data analysis of the interpretation of twenty five cross sections produced a throw-rate profile for the Campo Felice fault (Fig. 4.3.1). The throw-rate profile with calculated 1σ precisions describes a gradual increase in throw-rate along strike (Fig. 4.3.2) from a minimum of 0.487 ±0.031 mm/yr at the South-Eastern tip of the Campo Felice fault (Fig. 4.3.2, right hand side) to 0.964 ±0.020 mm/yr at the North-Western tip of the fault (Fig. 4.3.2, left hand side), where further along strike the fault becomes buried in scree with no discernable offset. The offset is interpreted as being relayed across strike on to the en echelon fault (Fig. 4.1.0). Superimposed on this general increase in throw-rate from South-East to North-West is a local increase in throw-rate between 1500 – 3500 m distance along the fault. The local increase reaches a maximum of 0.724 mm/yr at ~2600 m distance along the fault, representing a 17% increase from the value of 0.620 mm/yr depicted at the local minimum at ~1600 m distance (Fig. 4.3.2). The calculated 1σ precisions ranged from 0.010 – 0.063 mm/yr, with an average of 0.029 mm/yr for the entire dataset.

The field measurements of strike and dip, relating to fault geometry and the kinematic slip direction (Appendix iv) were plotted against distance along the Campo Felice fault. The measurements for fault strike (Figs. 4.3.3 & 4.2.9) describe two linear segments, located between 0 – 1500 m and 3000 – 4750 m distance along the fault. The two linear segments have strikes of ~126° ±10 (n = 70) and ~148° ±20 (n = 94) respectively. The section of the fault at 1500 – 3000 m (n = 104), between these two segments has a strike which describes a curved geometry from ~126° at 1500 m, to a low of 100° ±10 at 2175 m, increasing to ~140° at 3000 m. The field measurements of fault dip (Fig. 4.3.4) show fault dip to be consistent along the length of the fault, with little change in fault dip outside of the measurement precision of

±3°. The mean fault dip is 54° (±1σ = 3.1), the minimum and maximum measured dips are 48° and 61° respectively. The field measurements for the direction of slip (Fig. 4.3.5), collected from kinematic fault striae are consistent between 0 – 3000 m distance along the fault, with a mean slip direction of 211° (n = 151, ±1σ = 3.9). The slip direction becomes increasingly oblique towards the South-Eastern tip, in the direction of the centre of the fault (Red dots, Fig. 4.2.9). The direction of slip increases from ~211° at 3000 m distance along the fault to ~250° at the tip at 4750 m distance along the fault (Fig. 3.4.5).

The strain-rate profile (Fig. 4.3.6, green line), is calculated from data of throw, fault geometry and kinematic slip, using the method described by Faure Walker et al., 2009 (Section 3.2.2). The box size used to calculate strain was 250 x 250 m and was chosen as this allowed individual strain calculations for almost each of the twenty five cross section study sites. The strain-rate profile differs from the throw-rate profile (Fig. 4.3.6, red line) in that irregularities in throw are not replicated in the strain-rate profile. Strain decreases in a linear fashion from a maximum of ~3.51 ppm/yr at the North-Western exposed end of the Campo Felice fault to ~1.04 ppm/yr close to the tip at the South-Eastern end of the fault (Appendix v).

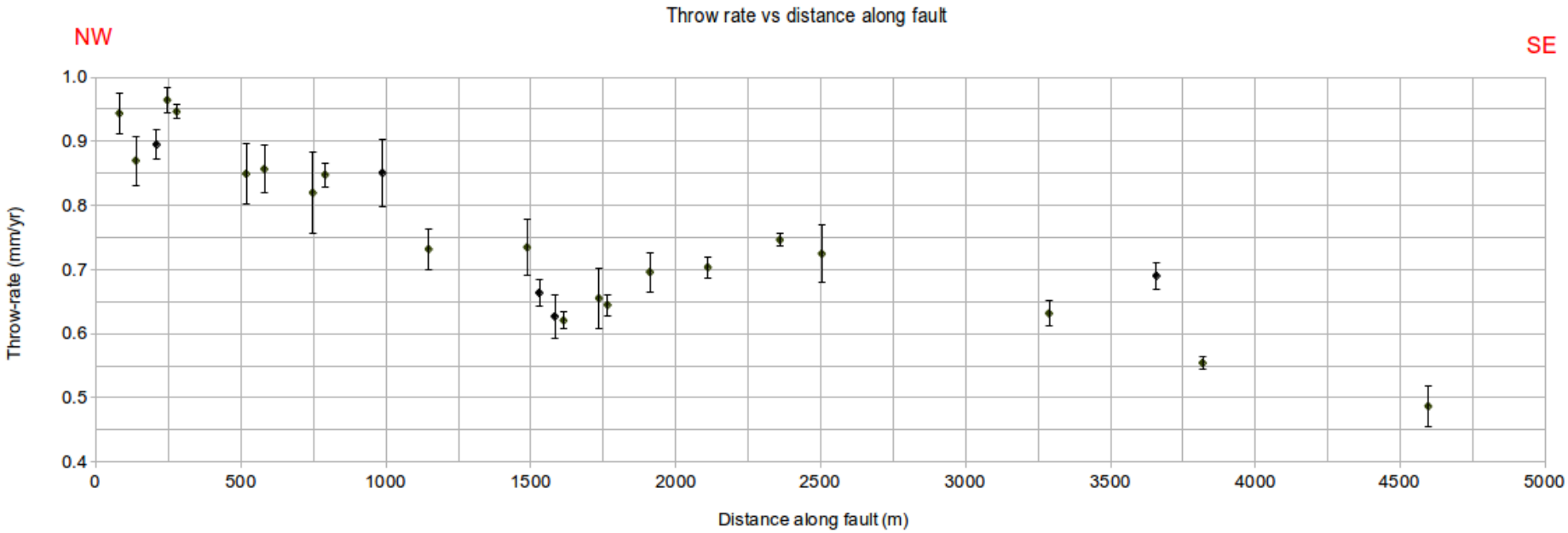

Figure 4.3.1: Throw-rate profile for the Campo Felice fault. Data points correlate with the red cross section lines in Figure 4.2.7.

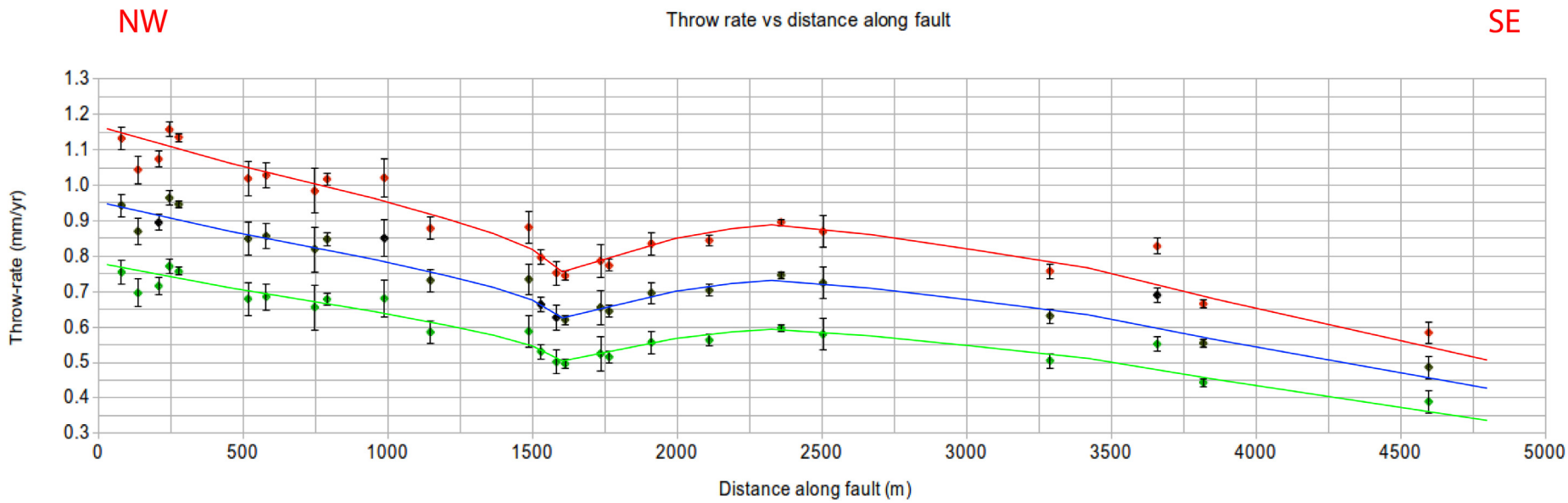

Figure 4.3.2: Annotated throw-rate profile for the Campo Felice fault. The blue line shows the throw-rate profile for the average case where the upper slope is of age 15 kyrs (black data points). The red line show the throw-rate profile for the maximum case where the upper slope age is 18 kyrs (red data points). The green line shows the throw-rate profile for the minimum case where the upper slope is of age 13 kyrs (green data points). The irregular shape of the throw-rate profile along strike, with a gradual increase in throw-rate from South-East to North-West with a local increase from this trend between 1500 – 3500 m distance along the fault.

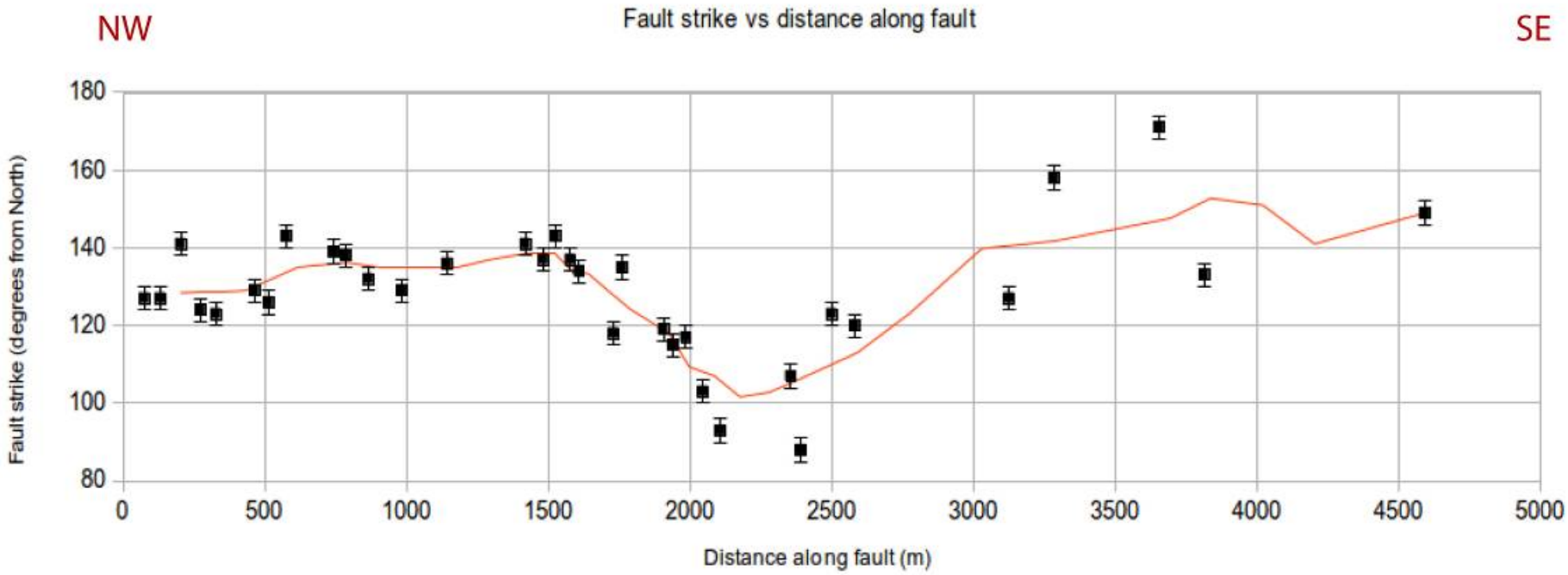

Figure 4.3.3: Field measurement data of fault scarp strike vs. distance along the fault. Error bars represent ±3° (The precision of a measurement taken using a compass by hand). The red line is a moving point average of five measurements.

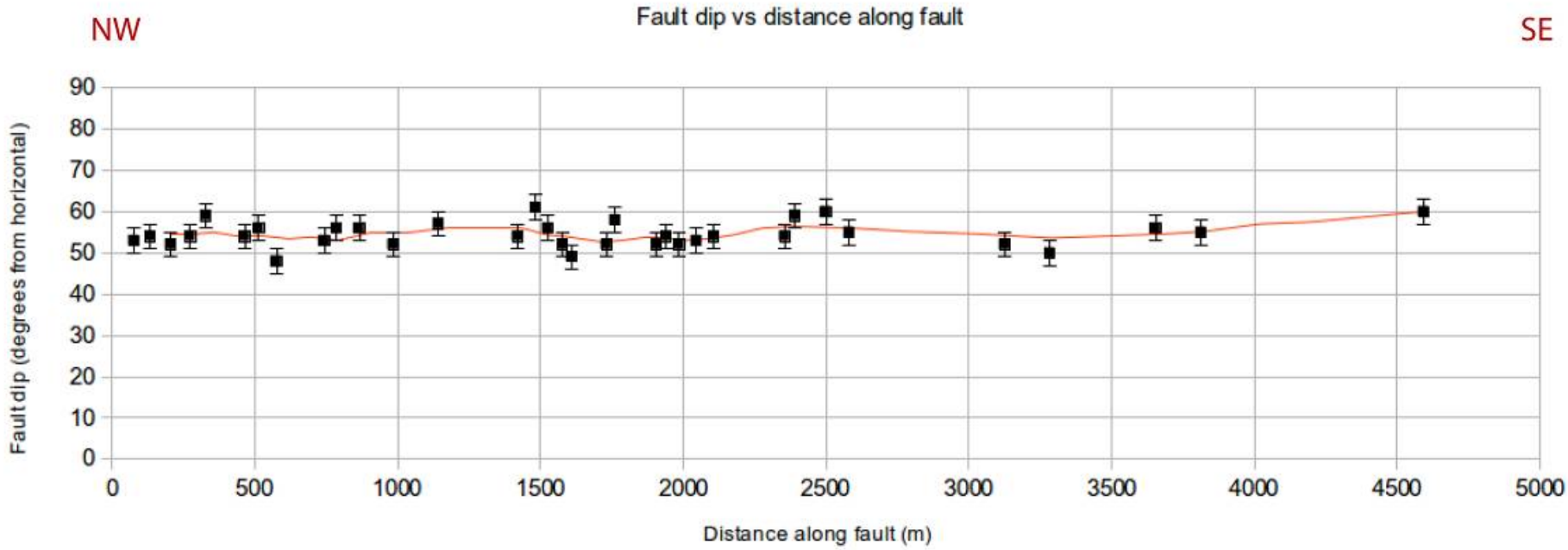

Figure 4.3.4: Field measurement data of fault dip vs. distance along the fault. Error bars represent ±3°. The red line is a moving point average of five measurements. Note the range in dip values is only 13° (min: 48°, max: 61°).

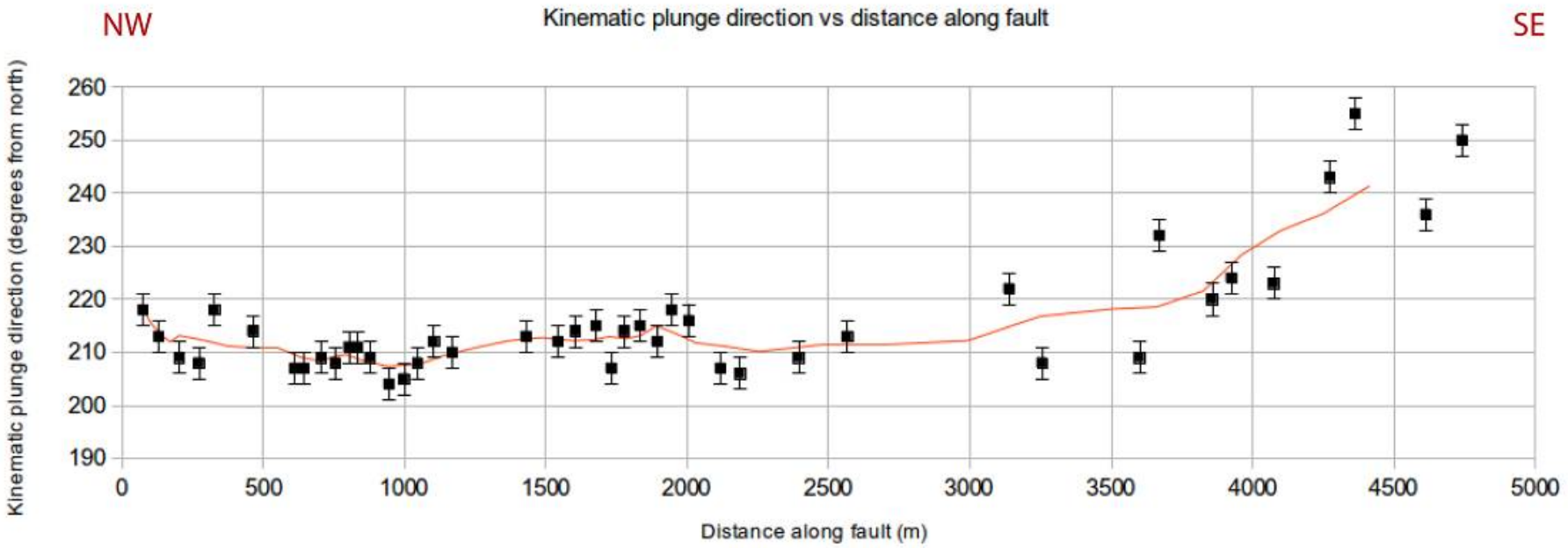

Figure 4.3.5: Field measurement data of kinematic slip vector plunge direction vs. distance along the fault. Error bars represent ±3°. The red line is a moving point average of five measurements. Note the plunge direction becomes more oblique toward the South-Eastern tip of the fault at 4700 m distance. The plunge direction does not vary significantly along the length of the rest of the fault.

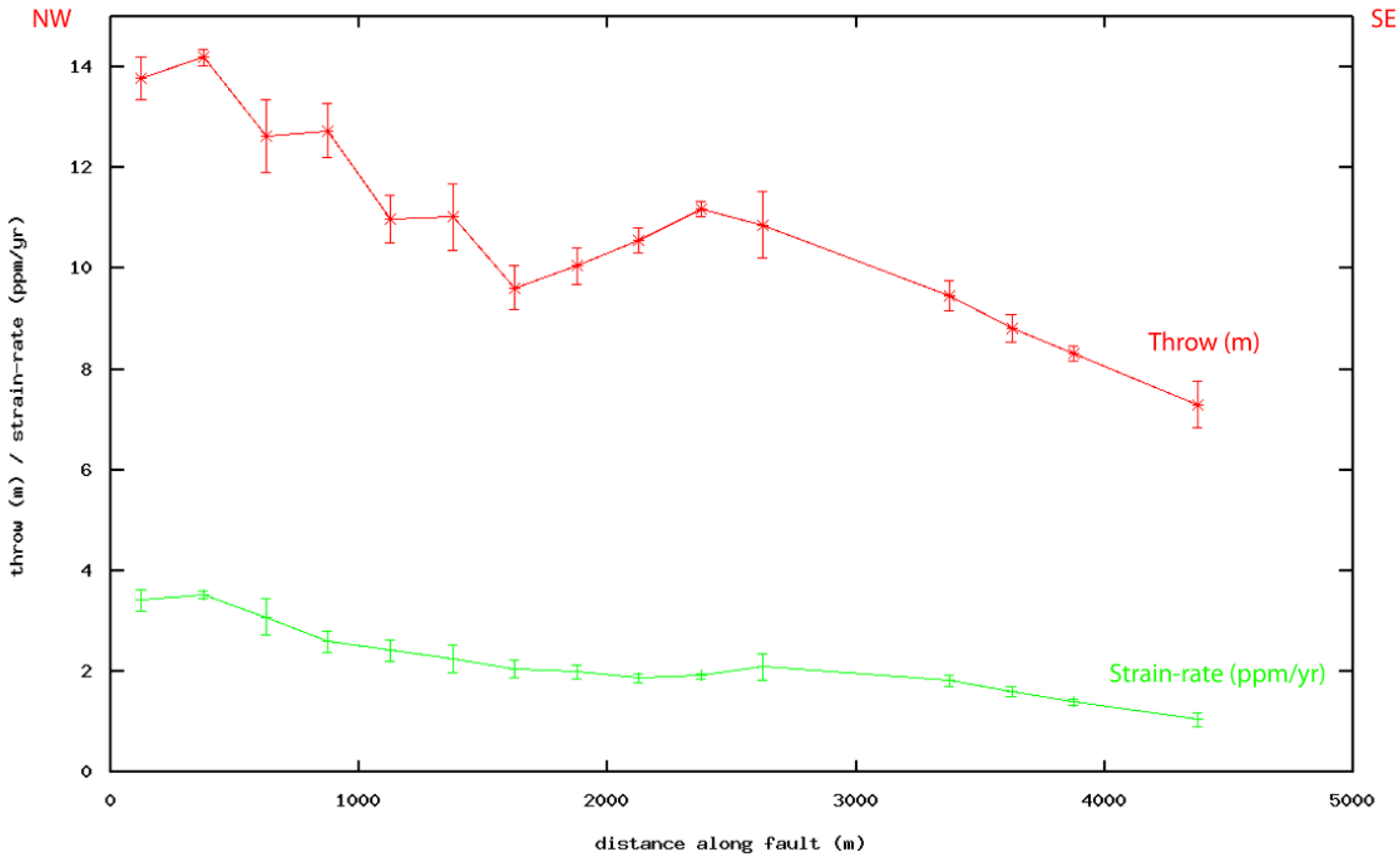

Figure 4.3.6: Profiles of throw (m, red line) and strain-rate (ppm/yr, green line) for the Campo Felice fault. Input data for the strain-rate calculation were binned to represent an average for 250 x 250 m boxed intervals along strike. The error bars in throw represent 1σ certainty. The error bars in strain-rate represent 2σ certainty. Data are shown for an upper slope age of 15 kyr.

4.4. Discussion

4.4.1. Interpretation of the throw-rate profile

The results of this study show that the Campo Felice fault has an irregular throw-rate profile (Figs. 4.3.1 & 4.3.2) with a significant local increase in throw-rate between 1500 – 3000 m distance along the fault. The observed throw-rate maximum for the studied segment of the Campo Felice fault (Red dashed line, Fig. 4.1.0) is at the North-Western tip of the this segment (Fig. 4.3.1, 0 m distance along the fault) suggesting that the North-Western tip of the segment as exposed in the field is not the true tip of the fault, indeed the fault continues to the North-West after stepping down on to an en-echelon segment. The North-Western tip of the studied segment has the highest throw-rate obtained through topographic analysis, which is not expected to be located at the fault tip. This section of the fault has the appearance of a tip in the field as the trace of the fault is buried by scree further to the North-West. This interpretation is supported by the field measurement of direction of slip (Fig. 4.3.5). The direction of slip becomes increasingly oblique to the strike of the fault towards the South-Eastern tip of the fault, suggesting that the local stress field is governed by the pinned nature of the fault tip, in which oblique slip becomes preferential (i.e. Roberts 1996a and Roberts 1996b). Conversely the slip direction does not become oblique at the apparent North-Western tip of the fault (Fig. 4.3.5, 0 m distance along the fault), suggesting that the fault does in fact continue beneath the scree. This interpretation has important implications for assessing the seismic hazard posed by this fault. The section of the fault with maximum throw-rate is most important as it is used as a proxy to define the maximum potential seismic hazard, as faults with higher throw-rates are expected to slip more frequently then those with lower throw-rates.

The maximum throw-rate expressed by the Campo Felice fault could be buried beneath the scree at the North-Western tip of the studied segment and so is unavailable for characterisation through topographic offset analysis. It is also possible that the throw may increase on to the en-echelon segment further West. Further investigation of both these possibilities is needed in order to determine the maximum throw-rate for the Campo Felice fault, however such investigation is beyond the scope of this study.

The local increase in throw-rate between 1500 – 3000 m, in relation to the overall North-West to South-East decline (Fig. 4.3.2) correlates with the change in the strike of the fault in the same location (Fig. 4.3.3). However the field measurements for fault dip and slip direction (Figs. 4.3.4 and 4.3.5) remain unchanged over this interval in relation to the rest of the fault. A study of changes in throw-rates across breached relay zones [Faure Walker et al., 2009], suggested that the throw-rate can change around a breached relay zone given a constant slip direction along the entire fault, under two scenarios. The first scenario involves a change in strike of the breached relay zone in relation to the main fault segments, assuming the strike of the main fault segments are close to dip-slip, as for the Campo Felice fault, an increase in throw-rate at the breached relay zone is required as the angle between the strike of the breached relay zone segment and the direction of slip deviates from 90° dip-slip (Fig. 4.4.1). The second scenario involves a change in dip of the breached relay zone in relation to the main fault segments while the strike of the segments remains static. An increase in dip of the breached relay zone segment in relation to the rest of the fault requires an increase in throw-rate of this segment in relation to the rest of the fault (Fig. 4.4.2), if the strain-rate is to remain constant. It is noted that variation in throw in both scenarios are modelled using changes in fault geometry within discrete, isolated

'boxed' regions, where there is no interaction or stress transfer between neighbouring boxes (see Figs. 4.4.1 and 4.4.2). In the real-world case where fault geometry changes along strike, the modelled variation in throw is expected to be accompanied by footwall deformation, often in the form of brittle facturing of the footwall bedrock.

The increase in local throw-rate observed for the Campo Felice fault between 1500 – 3000 m is not explained by a change in dip of the fault in this region, as shown by the field measurements for fault dip (Fig. 4.3.4). The local throw-rate increase can however be explained by the first scenario, in which the change in fault strike in this region, in relation to the rest of the fault, causes a change in throw-rate. The change in fault strike from ~126° to ~100° between 1500 – 2175 m (Fig. 4.3.3) represents a deviation from a 90° angle between strike and the slip direction (126° strike, ~211° slip direction, Fig. 4.3.5). The deviation between strike and slip direction reaches a maximum at 2175 m, where the strike decreases to ~100° and the slip direction remains unchanged at 211°. This decrease is accompanied by a local maximum in the increase in throw-rate at 2175 m (Fig. 4.3.2). The increase in throw-rate as the angle between strike and slip direction deviates from 90°, under conditions of static fault dip and slip direction, supports the prediction made in the first scenario by Faure Walker et al. (2009). The same study [Faure Walker et al., 2009] presented a method by which strain-rate could be calculated from field measurements of throw, throw-rate, fault geometry and kinematic slip (see Section 3.2.2). A throw profile for the Campo Felice fault was generated using this method (Fig. 4.3.6, Appendix v). The linear decrease in strain-rate with distance along the fault from the North-Western end of the fault to the South-Eastern tip shows that the irregularities in the throw-rate between 1500 – 3000 m are not irregularities in strain-rate. These irregularities in throw-rate

can be explained by a linear decrease strain-rate when also considering fault geometry and the kinematics of slip.

Furthermore, there is evidence to suggest that the last few earthquake slip events on the Campo Felice fault followed the long term pattern of variable throw-rate in relation to fault strike. The Campo Felice fault scarp displays a series of weathered bands, parallel to the base of the scarp. These bands have been investigated in a study by Giaccio et al., (2002), in which the authors propose the bands are related to successive coseismic slip events on the Campo Felice fault. The study identifies three bands exposed in processed photographs of the fault scarp, which are used to infer the last two slip events on the fault. The last slip event for the Campo Felice fault is visible at four separate sites (CH, CG, CL and CB) in the study by Giaccio et al., (2002). The size of the slip event at each site increases as the angle between the slip direction and fault strike deviates from 90°, in the same manner as the long term throw-rate measurements (Fig. 4.4.3). Given the correlation between the size of the slip event and the long term throw-rate, it is possible to suggest that the shape of the throw profile for past and future earthquakes on the Campo Felice fault may well show a similar increase in coseismic throw governed by the change in strike of the fault. This statement is only credible if it is assumed the entire Campo Felice fault ruptured in each earthquake, producing characteristic earthquakes of consistent slip size and that the direction of slip and fault geometry did not change over time.

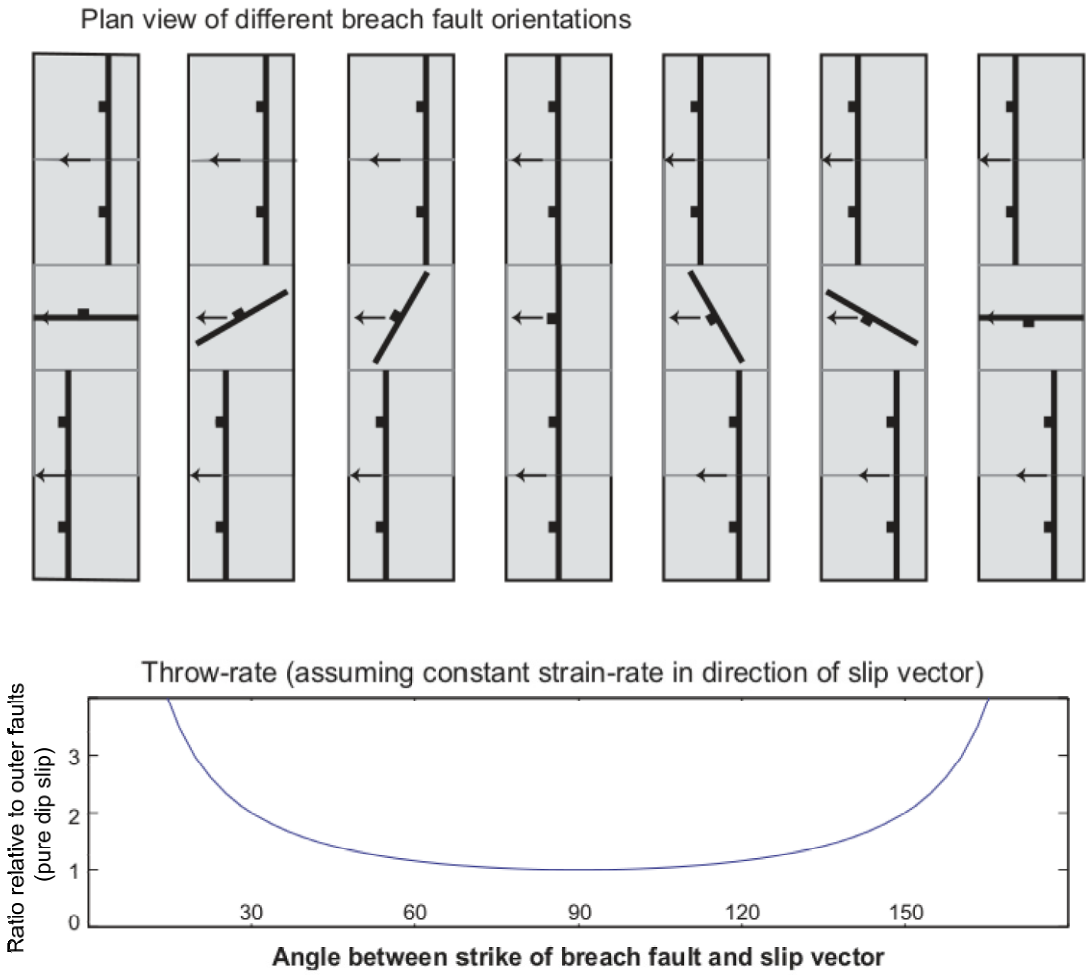

Figure 4.4.1: Scenario one: An increase in throw-rate for a breached relay segment is produced through deviation from a 90° angle between fault strike and slip direction, with a static slip direction (black arrows) and fault dip across all segments. Illustration taken from Faure Walker et al., (2009).

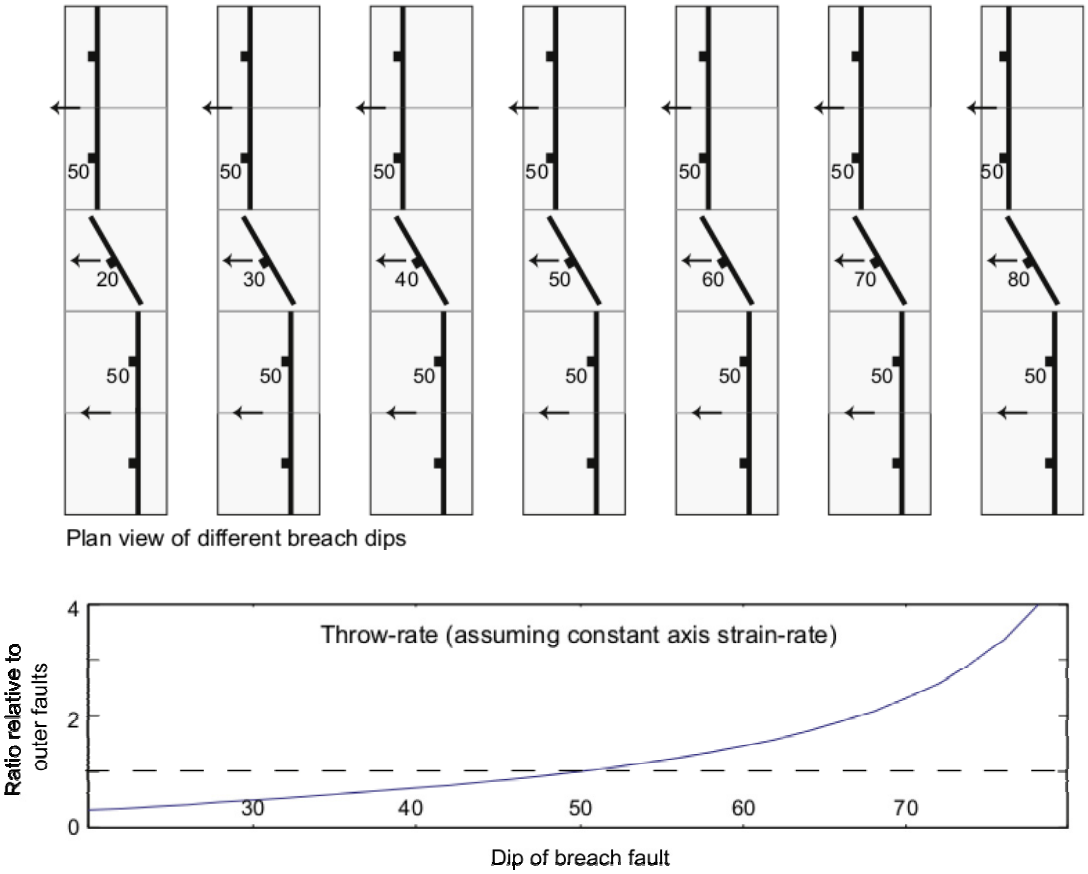

Figure 4.4.2: Scenario two: The relative change in throw-rate for a breached relay segment produced by a change in fault dip (numerical annotations) in relation to the surrounding segments, with static slip direction (black arrow) and fault strike geometry across all segments. Illustration taken from Faure Walker et al., (2009).

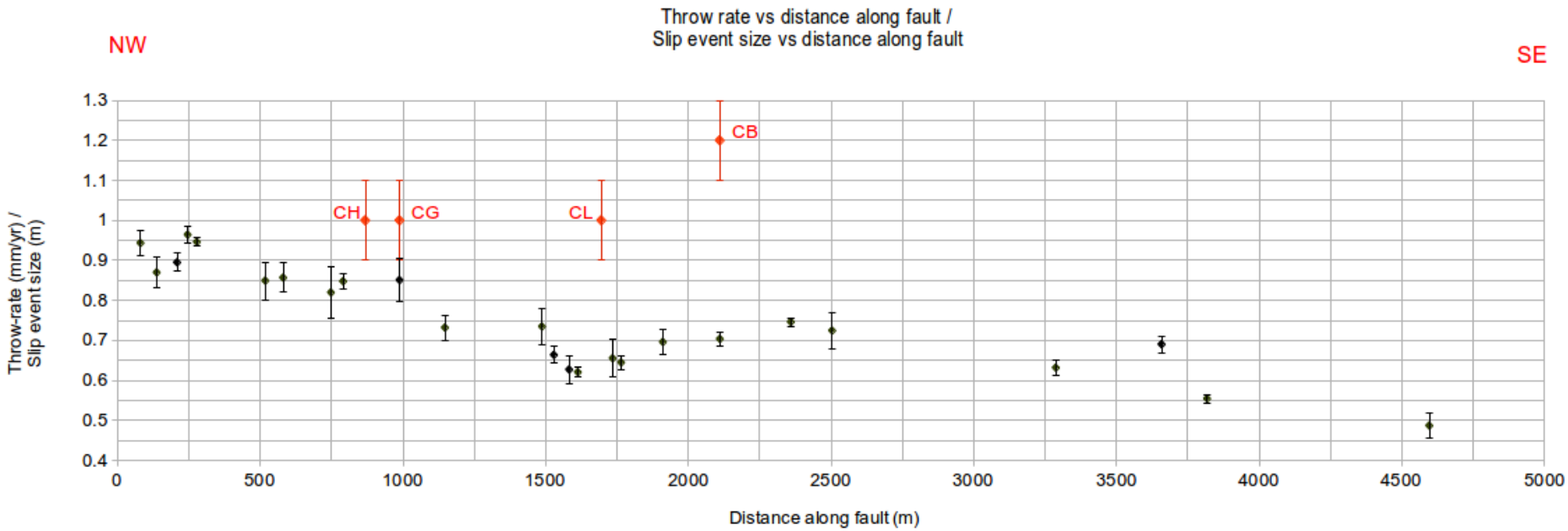

Figure 4.4.3: A comparison of long term slip-rate measurements and the size of the last slip event. Throw-rate measurements (mm/yr) over 15 ka are shown in black. Size of the last slip event (m) measured from Giaccio et al., (2002), for sites CH, CG, CL and CB shown in red.

4.4.2. Implications for the structural geology of the Campo Felice fault

The maximum throw-rate measured over the time period since the last glacial maximum represents the most robust throw-rate value with which to characterise the seismic hazard of the Campo Felice fault averaged over multiple seismic cycles. A previously published study of slip-rate for the Campo Felice fault [Galadini & Galli, 2000] identified *'a 20 m vertical offset of till related to the last glacial maximum; considering an age of 18,000 years, one obtains a vertical slip-rate of 1.1 mm/yr*'. This figure represents the most reliable slip-rate estimate for the Campo Felice fault obtained prior to this study; however the authors do not note the exact location of the site or the method used to calculate the offset. The maximum throw-rate calculated in this study is 0.964 ±0.020 mm/yr, obtained from an offset at the North-Western end of the exposed fault, using a revised upper slope age of 15 ka. This maximum throw-rate suggests the throw-rate of 1.1 mm/yr quoted for a single site by Galadini & Galli, 2002, represents an over-estimation of 14%. The difference between the two throw-rates is due to a difference in the measured offset (14.5 m for this study vs. 19.8 m by Galadini & Galli, 2002) and the age of the upper slope from the last glacial maximum (15 ka for this study vs. 18 ka used by Galadini & Galli, 2000). Slip-rates of 0.6 – 1.1 mm / yr were obtained from paleoseismological analysis of the surrounding Ovindoli-Pezza fault system [Pantosti et al., 1996] and are broadly comparable to those obtained from the Campo Felice fault in this study. It is worth noting however, that the quoted maximum throw-rate from this study can only be considered definitive once the offset of the en echelon continuation of the fault to the North-West is investigated.

The calculation of a strain-rate profile for the Campo Felice fault (Fig. 4.3.6, green line) shows that the strain decreases in a linear fashion from a maximum at the North-Western end of the studied part of the fault to a minimum near to the tip at the South-Eastern end. Linear displacement gradients have been observed along faults in previous studies [Cowie & Shipton, 1998, Manighetti et al., 2005] and support the result of a linear strain-rate profile for the Campo Felice fault. The strain-rate profile supports the idea that the region where the strain-rate is highest at the North-Western end of the fault must be studied in order to characterise the maximum seismic hazard of the Campo felice fault.

Using the terrestrial laser scan dataset to produce throw-rate and strain-rate profiles for the Campo Felice fault allowed the precision of each result to be reported by taking multiple closely spaced throw measurements at each study location. The uncertainty of each result is an important parameter if the data is to be used in seismic hazard analyses.

4.4.3. Implications for fault geometry on seismic hazard analysis

This study has shown that the local throw-rate for a normal fault is dependent on the angle between the strike of the fault and the slip direction, in the case where the dip of the fault remains static. This has implications for all studies which measure fault offsets to obtain throw-rates, such as paleoseismological trenching, geological surface offset, cosmogenic exposure dating of fault scarps or borehole stratigraphic studies. The location of the study site along the fault must be taken into account. If the study site is located on a segment where the strike of the fault deviates from the mean, then it is to be expected that throw-rates obtained from this site will be elevated or subdued depending on the deviation of the angle between strike and slip direction

towards or away from 90° to the slip direction. Field measurements of fault dip and kinematic slip direction should also be collected in order to ensure measured throw-rate values are not anomalous and are related to along strike variation of these parameters. This study has shown that it is possible to take these parameters which influence throw-rate (i.e. fault geometry and kinematic slip) into account by producing a value for strain-rate that is independent of the geometric parameters which influence throw-rate.

For example, considering the change in strike of 26°, from 126° to 100° along the Campo Felice fault between 1500 m and 2175 m (Fig. 4.3.3) produces an increase in throw-rate of 19%, or +0.114 mm/yr, from 0.61 mm/yr to 0.724 mm/yr (Fig. 4.3.2). If the latter throw-rate was extracted from a paleoseismic study of the Campo Felice fault, in which the anomalous increase in throw-rate due to strike at this site was not identified, the hazard posed by the Campo Felice fault at this site would be over estimated. If we assume that size of slip event scales linearly with long-term throw-rate and that the size of the last slip event of 1 m observed at site CL (Fig. 4.4.3) is correct for its location along the fault at 1500 m distance, a 19% increase in slip should occur between this site and site CB at 2110 m distance, due to the change in strike. The size of the last slip event at site CB is 1.2 m, representing a 20% increase in slip in relation to site CL. The correlation between increase in long-term throw-rate due to changes in fault strike and an increase in the size of the last slip event over the same transect may provide some evidence to suggest that variation in strike (or rather the angle between strike and the slip direction) is an important factor affecting throw-rate and size of slip event. The empirical relationship which relates size of slip event to moment magnitude (equation a, [Wells & Coppersmith, 1994]) can be used to calculate the over-estimation in moment magnitude which would occur if

paleoseismic data from inbetween the two sites was used whilst ignoring the change in fault strike. A 1 m offset produces a moment magnitude of 6.69 Mw, while a 1.2 m offset produces a moment magnitude of 6.75 Mw, representing an increase in moment magnitude of 1.15%. The moment magnitudes of the two sites can then be used to estimate the difference in predicted peak ground acceleration that would result (PGA, an important input for building design in areas of seismic hazard), under soil conditions at 10 km from the fault using SEA96 (equation b, [Spudich et al., 1997]). A moment magnitude of 6.69 Mw (calculated from 1 m slip event), produces a PGA of 0.2059 ms^{-2}, while a moment magnitude of 6.75 Mw (calculated from 1.2 m slip event) produces a PGA of 0.2125 ms^{-2}, representing an increase of 3.2% related to a change in fault strike of 26°. Such an increase in PGA, which would certainly affect engineering plans to design buildings to withstand earthquakes is sufficient to highlight the importance of conducting thorough investigation into throw-rate variability along seismically active faults. It would be possible to include the affects of fault geometry and kinematic slip which can produce unreliable estimates of hazard as they control local throw-rate, by instead calculating strain-rate. Unfortunately this cannot be achieved from the Wells and Coppersmith (1994) database, as fault orientations were not included. This is an area for future work, in order to revisit and updating this database with orientation data. Strain-rate has been shown to be independent of fault geometry and kinematic-slip, and so would provide a more reliable estimate of fault activity. This would require new regression relationships relating strain to maximum magnitude and for all studies to be able to estimate strain-rate from their field measurements.

$$Mw = 6.69 + 0.74 * \log(MD)$$

Equation a: Empirical relationship relating size of slip event (*MD*) to moment magnitude (*Mw*) from Wells & Coppersmith, 1994.

$$\log_{10} Y = 0.156 + 0.229 * (M - 6) - 0.945 * (\ln(R) / \ln(10))$$

$$R = \sqrt{r_{jb}^{\ 2} + 5.57}$$

Equation b: SEA96 [Spudich et al., 1997], used to estimate peak ground acceleration (*Y*) from moment magnitude (*M*), under soil conditions in extensional regimes, at distance (r_{jb}).

4.5. Conclusion

A throw-rate profile for the Campo Felice fault was generated from a terrestrial laser scan dataset using a newly developed method. The method allows the maximum number of suitable study sites for the measurement of throw to be utilised, through geomorphic mapping to identify sections of the fault suitable for study. The produced throw-rate profile increases from the South-Eastern tip of the fault to a maximum at the North-Western end of the studied part of the fault. The throw-rate profile is also irregular with a local increase between 1500 – 3000 m distance along the fault. This irregularity is controlled by changes in fault strike. The throw-rate increases as the angle between strike and the slip direction deviates from 90°. The influence of fault geometry on the perceived throw-rate at individual sites should be an important consideration for paleoseismic and geological offset studies. This study has shown that the adverse affects of fault geometry and kinematic slip direction in estimating throw-rate can be negated by instead reporting strain-rate. Strain-rate takes into account fault geometry and kinematic slip direction and so is a more robust value for assessment fault activity. The strain-rate profile for the Campo Felice fault shows a linear decrease from the North-Western exposed end of the studied section of the fault to the South-Eastern fault tip, whereas the throw-rate was found to decrease from the North-West to South-East in an irregular fashion, controlled by fault geometry.

The maximum measured throw-rate of the Campo Felice fault is 0.964 ±0.020 mm/yr, which represents a minor refinement of estimates from previous studies. However, this figure now includes an attached precision and is shown in context to the rates along the rest of the fault. The throw-rate may increase past the North-Western end of the studied fault on to the en echelon fault segment to the North West.

Therefore the maximum throw-rate obtained from this study can only be considered definitive once the remained of the fault has been investigated.

Chapter 5: A study of postseismic deformation of the 2009 L'Aquila earthquake surface rupture

5.1. Introduction

Earthquakes produce coseismic displacement along faults that may then accumulate further movements during the weeks after the main shock. This study reports the novel use of repeat Terrestrial Laser Scanning (TLS) to monitor postseismic ground surface deformation following the 6th April 2009, 6.3 Mw earthquake, which struck the city of L'Aquila in the Abruzzo region, central Italy. The seismicity was identified to originate from a ~0.6 – 0.8 m normal sense displacement within a fault zone dipping 54° to the South-West [Walters et al., 2009, Vittori et al., 2011] from a hypocenter at ~6 km depth [Cheloni et al., 2010]. The Paganica fault, with normal displacement, striking ~130° N, 6 km East-North-East of the city of L'Aquila was identified as the source of the seismicity (location denoted by 'PG', Fig. 1.1). A discontinuous surface rupture was mapped for 2.6 km along the base of the Paganica fault [Vittori et al., 2011] (Figs. 5.1.1 & 5.1.2), although other studies [Boncio et al., 2010, Galli et al., 2009] suggest the rupture was longer, up to 13 – 19 km. The sharp increase in topographic gradient North-Eastwards, across contour 680 m in Figure 5.1.2, between sites PA and SP is the geomorphic expression of the Paganica fault. Each rupture segment displayed a consistent kinematic slip direction of 218° ± 5° [Wilkinson et al., 2010]. The coseismic offset along these rupture segments was of normal-sense displacement and ranged from hairline cracks with little or no offset to up to 10 cm vertical offset towards the centre of the surface rupture, close to the town of Paganica [Boncio et al., 2010, Vittori et al., 2011].

This study investigates the along-strike distribution and magnitude of postseismic deformation using repeat Terrestrial Laser Scan (TLS) datasets at four sites (Figs. 5.1.1, 5.1.2 & 5.1.3: TM, PAG, SP & EP) spanning the 2.6 km extent of the surface rupture of the Paganica fault, as defined by Vittori et al., (2011). Suitable surface rupture study sites outside of this range could not be reliably identified due to the confusion between surface rupturing and secondary effects. Each of the four study sites chosen were verified as primary surface ruptures as their offsets were reasonable for a 6.3 Mw earthquake and the rupture opening directions were consistent with the L'Aquila earthquake focal mechanism. The data from the four study sites are complemented by that of across-rupture total station measurements from a fifth site (Figs. 5.1.1, 5.1.2 & 5.1.3: PA). This multi-site approach provides an insight into the along-rupture magnitude and distribution of postseismic deformation. The measurements are confined to surface deformation in the near-field within a few tens of meters of the surface rupture.

In order to provide evidence that the measured surface motions can be attributed to postseismic deformation, the surface motions observed at site PAG, in the centre of the rupture are compared to theoretical and empirical models which describe rupture postseismic deformation for previous earthquakes. Measurements of near-field on-rupture postseismic deformation are used to investigate the hypothesis that postseismic deformation within the fault zone occurs in specific regions as a response to increased shear stresses due to large gradients in coseismic slip. The magnitude of postseismic deformation measured in the near-field is compared to far-field values measured from studies of GPS [Cheloni et al., 2010] and differential interferometry (DInSAR) [Lanari et al., 2011] to suggest that postseismic deformation on all scales is driven by afterslip within a discrete fault zone. The work in this

chapter has been published as two papers, Wilkinson et al., 2010 (Appendix vi) and Wilkinson et al., 2012 (Appendix vii).

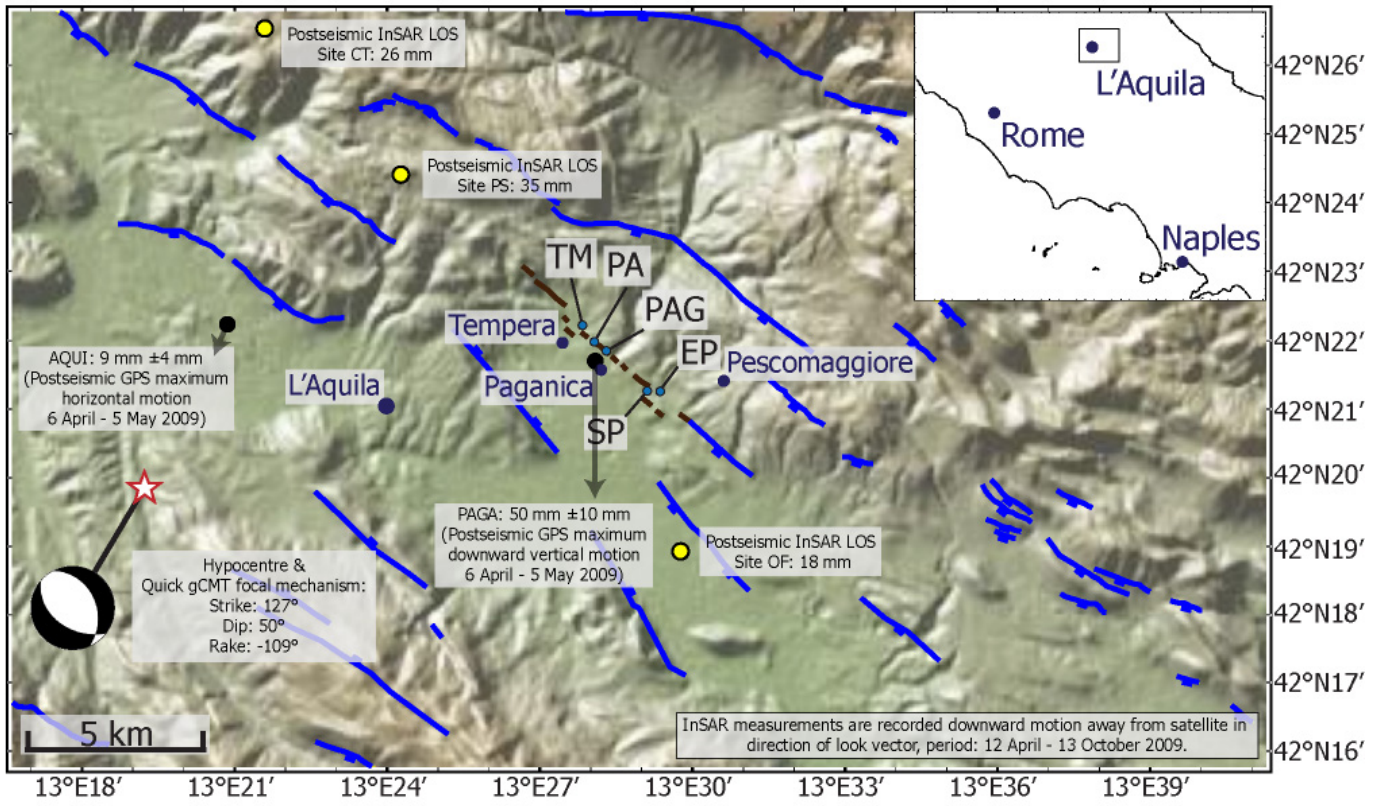

Figure 5.1.1: Map of the interpreted active normal faults of the L'Aquila region, and the five study sites PAG, SP, EP, TM and PA. The L'Aquila earthquake surface ruptures are shown in brown (adapted from Roberts, 2008, Falcucci et al., 2009, Michetti et al., 2000, Vittori et al., 2011). Additional postseismic data in the far-field from D-InSAR is obtained from Lanari et al., 2010. The postseismic GPS data is from Cheloni et al., 2010.

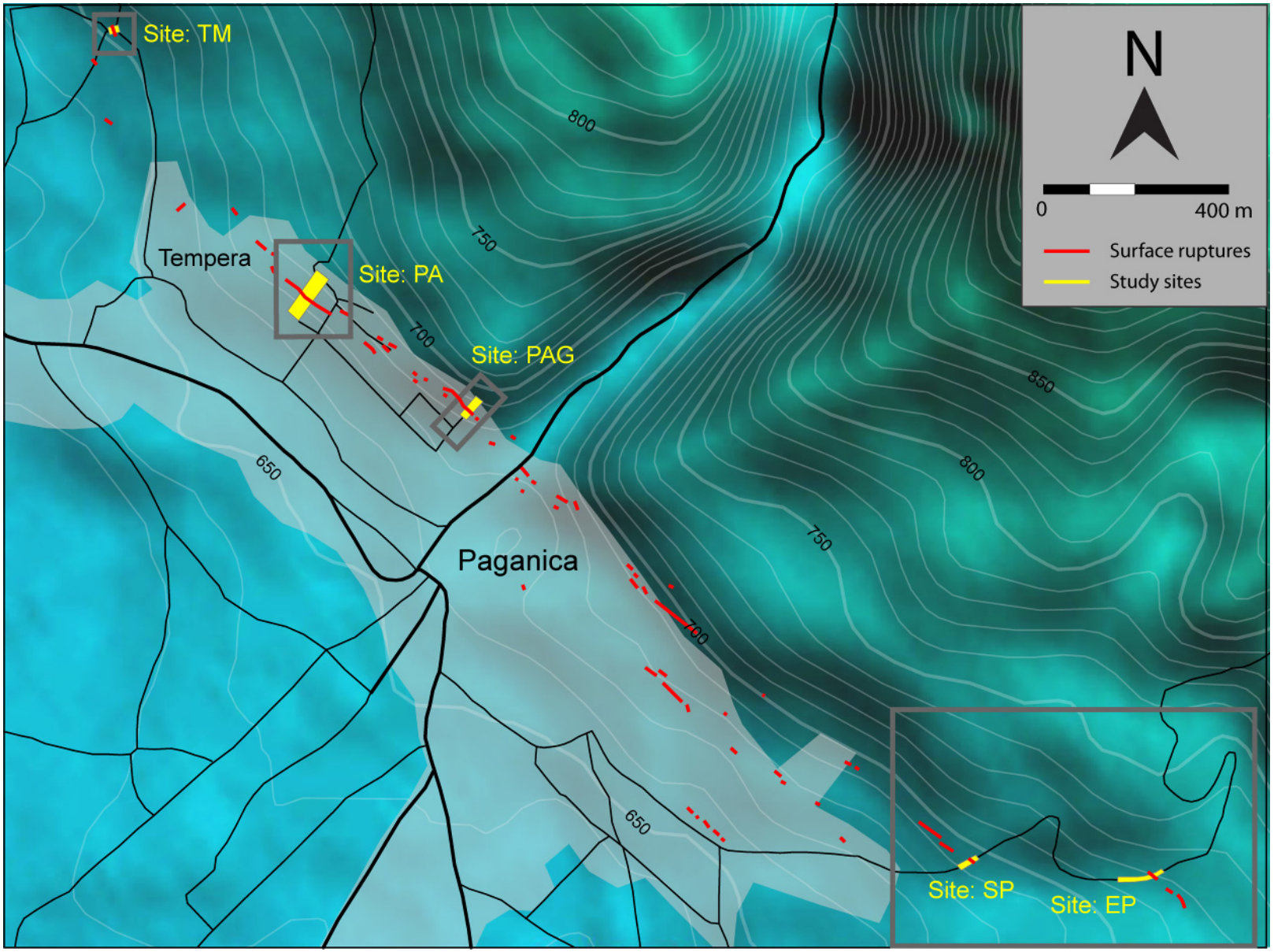

Figure 5.1.2: Regional ASTER GDEM* derived topographic map, detailing the location of the five study sites and the mapped surface ruptures shown in red after Vittori et al., 2011. *ASTER GDEM is a product of METI and NASA.

Figure 5.1.3: Field photos of the five L'Aquila earthquake surface rupture study sites where postseismic deformation was measured.

5.2. Data collection and processing

Twenty three terrestrial laser scan point cloud datasets were acquired between 8 and 126 days after the L'Aquila earthquake (Table 5.3.1), spread across four road sites (Fig. 5.1.1. PAG, SP, EP and TM) where surface ruptures of the Paganica fault were observed. A network of reflectors was set up at each study site to allow scan co-registration and to measure line of sight horizontal deformation (see Section 3.3.2 for method). The relatively short range from the position of the laser scanner to the areas studied (up to 70 m) allowed point cloud datasets to be collected with very high spatial density (point spacing of 4 – 10 mm). The point cloud datasets for each site were processed to measure postseismic deformation using the vertical differencing and horizontal extension between reflector pairs methods as described in Section 3.3.2. Error bounds presented after calculated magnitudes of vertical motion represent $\pm 2\sigma$ range of certainty and are calculated from the local set of measured magnitudes around the area of interest. The error bounds vary between datasets and locations within each dataset due to variations in the smoothness of the road surfaces.

5.3. Results

5.3.1. Site PAG

Site PAG (13.471450°E 42.362631°N), lies towards the centre of the surface rupture (Fig. 5.1.1) and is situated on a rough concrete road on the outskirts of Paganica (Fig. 5.3.1). The surface rupture cross cuts the concrete road with a North-West – South-East strike and an initial vertical displacement of ~7.5 cm was observed eight days after the earthquake. The TLS data acquired at the site consists of seven repeat scans acquired at 8, 11, 35, 39, 43, 48 and 124 days after the earthquake (Table 5.3.1.). The scan data were cropped to cover a 3 m x 65 m section of the road which spans the hangingwall, rupture and footwall of the Paganica surface rupture. The results of the surface generation and vertical difference measurements describe surface deformation which is partitioned between afterslip on the rupture and the progressive development of a growing hangingwall syncline (Fig. 5.3.2). The boxed zone in Figure 5.3.2.b highlights an area of damage (breaking off of the footwall) to the surface rupture received between days 11 and 35 attributed to a vehicle being driven over it. The similarity of the deformation observed along the rest of the road before and after the vehicle damage shows that the immediate 2 - 3 m of footwall was the only part of the road which was damaged. Both the rupture afterslip and the hangingwall syncline continued to move with a decaying rate until the end of our survey (Fig. 5.3.6.a). The maximum rupture afterslip totalled 13.4 ± 2.6 mm. The maximum observed subsidence in the hangingwall syncline was 14.3 ± 2.3 mm. Thus, the maximum vertical postseismic deformation observed was 27.7 ± 2.3 mm, from the combined rupture afterslip and hangingwall syncline subsidence. The network of five reflector positions at the site (Rp1-Rp5, Fig. 5.3.1.c) were used to calculate the

horizontal component of postseismic deformation, which totalled 21.8 ± 5.0 mm for the 8 – 124 day period after the earthquake.

5.3.2. Site SP

Site SP (13.484543°E 42.354447°N) is situated towards the South-Eastern end of the surface rupture (Fig. 5.1.1), on the tarmac road from Paganica to Pescomaggiore (Fig. 5.1.2). The rupture is defined by a 5 – 50 cm wide zone of small cracks, striking North-West – South-East. The cracks were 2 – 5 mm wide with no apparent vertical displacement when first observed eleven days after the earthquake. Five scans were acquired at the site between 11, 38, 42, 45 and 126 days after the earthquake, spanning an area 6 x 49 m encompassing the hangingwall, surface rupture and footwall. Surface fitting and vertical differencing show progressive hangingwall subsidence indicative of rupture afterslip, accompanied by the initial development of a syncline in the immediate hangingwall of the rupture (Fig. 5.3.3). Rupture afterslip was measured with respect to the first scan datum and inferred by projecting the hangingwall surface of each dataset into the rupture zone. The maximum afterslip 126 days after the earthquake was 13.1 ± 4.1 mm, calculated from the difference between scan SP1 and SP5. The hangingwall syncline developed between datasets SP1 and SP2 (11 – 38 days), representing 2.7 ± 2.2 mm of vertical subsidence. Further significant growth of the syncline was not observed after 38 days. The maximum vertical postseismic deformation is 16.0 ± 2.2 mm. This figure represents the sum of the afterslip observed between the first and last data acquisitions (13.1 mm), plus the observed subsidence of the hangingwall syncline (2.7 mm) over the same period. A network of four reflectors (Rs1 - Rs4, Fig. 5.3.1.a) paired across the rupture moved 27.6 ± 5.0 mm horizontally in the direction of the coseismic slip vector (218°)

between SP1 and SP5. The components of postseismic deformation of each surface relative to the first are shown in Figure 5.3.6.b; they describe deformation increasing at a decaying rate, indicative of afterslip and near-field postseismic deformation.

5.3.3. Site EP

Site EP (13.489044°E 42.354056°N) is located 370 m due East of site SP on the road from Paganica to Pescomaggiore (Figs. 5.1.1 and 5.1.2). The appearance of the rupture is very similar to that at SP, defined by a narrow zone of cracks crossing the road. The cracks had horizontal displacements of 2 – 5 mm when first observed ten days after the earthquake, but with no observable vertical displacement. Five scans were acquired, at 10, 38, 42, 46 and 125 days after the earthquake, of a 9 x 84 m area comprising the hangingwall, rupture and footwall. Surface generation and vertical differencing show a syncline located within the first 4 m of the hangingwall (Fig. 5.3.4: -18 m to -22 m distance from the scanner) that developed between scans EP1 - EP2, along with tilting of the hangingwall towards the rupture between 4 - 50 m from the rupture (-18 m to -50 m distance from the scanner). Hangingwall tilting was contemporaneous with uplift of up to 20 mm at 72 m from the rupture (50 m distance from the scanner). A period of quiescence followed, with little or no change in the surface between EP2 – EP4, except for 2 mm subsidence of the hangingwall from its tilted position. The final scan EP5, acquired 125 days after the earthquake shows significant downthrow of the entire hangingwall by 10.8 ± 3.8 mm relative to EP1, with additional subsidence of 4.6 mm, creating a hangingwall syncline 48 m from the rupture (5 m – 50 m distance from the scanner (Fig. 5.3.4.b). 10.8 ± 3.8 mm of afterslip was observed between 10 and 125 days by projecting the tilted hangingwall into the rupture. The combined magnitude of vertical postseismic deformation

between 10 and 125 days is 15.4 ± 3.1 mm, representing the sum of the maximum afterslip observed (10.8 ± 3.8 mm) combined with the observed subsidence of the hangingwall syncline (4.6 ± 3.1 mm) over the same period. A network of five reflectors (Re1 – Re5, Fig. 5.3.1.a) paired across the rupture were used to measure a horizontal deformation of 20.3 ± 5.0 mm, between 10 – 125 days, resolved in the direction of the coseismic slip vector. The components of postseismic deformation of each surface relative to the first are shown in Figure 5.3.6.c. They describe deformation increasing at a decaying rate, indicative of afterslip and near-field postseismic deformation.

5.3.4. Site TM

Site TM (13.462563°E 42.370022°N) is located towards the North-West end of the surface rupture, on the outskirts of the village of Tempera (Fig. 5.1.1). The study site is a rough tarmac road (Fig. 5.3.1.b), 4 m x 51 m, comprising the Paganica surface rupture, hangingwall and footwall. The surface rupture consists of a single crack cross cutting the tarmac road. The scanner was positioned 33 m into the footwall (Fig. 5.3.1.b), as the road was too narrow to position the scanner in the hangingwall at this site. As observed twelve days after the earthquake, the crack had a horizontal displacement of 8 – 12 mm, with no observable vertical offset. The site was scanned six times, (12, 37, 41, 44, 47 and 124 days) after the earthquake (TM1 – TM6, Table 5.3.1). Surface fitting and vertical differencing revealed vertical deformations mostly below the precision of the method (Fig 5.3.5: -2.8 mm < $\pm 2\sigma$ < 2.8 mm), suggesting that minimal vertical postseismic deformation occurred at the site. Most of the vertical deformations are however downward and appear to create a subtle depression in the hangingwall between 33 m (the rupture) – 63 m (the rest of

the hangingwall) distance from the scanner. Values for rupture afterslip were calculated using the vertical deformation of the road in the immediate hangingwall of the rupture. The maximum observed afterslip was 2.4 ± 2.8 mm, occurring between 12 and 124 days after the earthquake. A network of five reflectors paired across the rupture was used to calculate the horizontal component of postseismic deformation. The horizontal postseismic deformation observed between 12 and 124 days was 3.2 ± 5.0 mm. The components of postseismic deformation over the survey period (Fig. 5.3.6.d) describe deformations below the precision of the method, suggesting little or no postseismic deformation occurred at this site.

5.3.5. Site PA

Site PA (13.467295°E 42.364682°N) is located 400 m North-West of site PAG (Fig. 5.1.2). A 40 bar water pipe serving the town of Paganica crosses the Paganica fault at this site and ruptured during the 6th April earthquake and also subsequently, following repair, at 06:00 on the 19th April. The immediate area of the water pipe was heavily excavated by water leaking from the pipe at high pressure following rupture during the April 6th earthquake. Although those sediments which may have been ruptured were washed away, surface ruptures remain in the immediate area a few tens of meters along strike with coseismic displacements of 10 – 15 cm [Vittori et al., 2011]. At this site, we summarize data (with permission) from the Geological Survey of Trentino [Degasperi, 2010]. The Geological Survey installed a Leica TCA2003 automatic total station 63 m in the hangingwall of the rupture (Fig. 5.3.1.d: point A0). The total station was paired with a staked prism 40 m in the footwall (Fig. 5.3.1.d: point A1) and set to record the distance to the prism at regular intervals with a precision ± 1.1 mm (1.0 mm +1ppm over ~100 m distance). The

vertical and horizontal components of postseismic deformation between 17 – 330 days after the earthquake were calculated by comparing subsequent vertical and horizontal distances to the initial measurement. We use the six measurements from 17, 31, 44, 65, 85 and 114 days (Table 5.3.1, PA1 – PA6), as they span the same time period as the TLS surveys. The data following day 114 show little or no additional postseismic deformation. The vertical postseismic deformation observed between 17 – 114 days was 13.8 ± 1.1 mm. The maximum horizontal postseismic deformation observed was 10.1 ± 1.1 mm over the same period. The measurements of vertical and horizontal deformation increase with a decreasing rate over the study period, indicative of afterslip and near-field postseismic deformation. Due to the nature of these data, we were unable to assess whether or not a hangingwall syncline developed at this site.

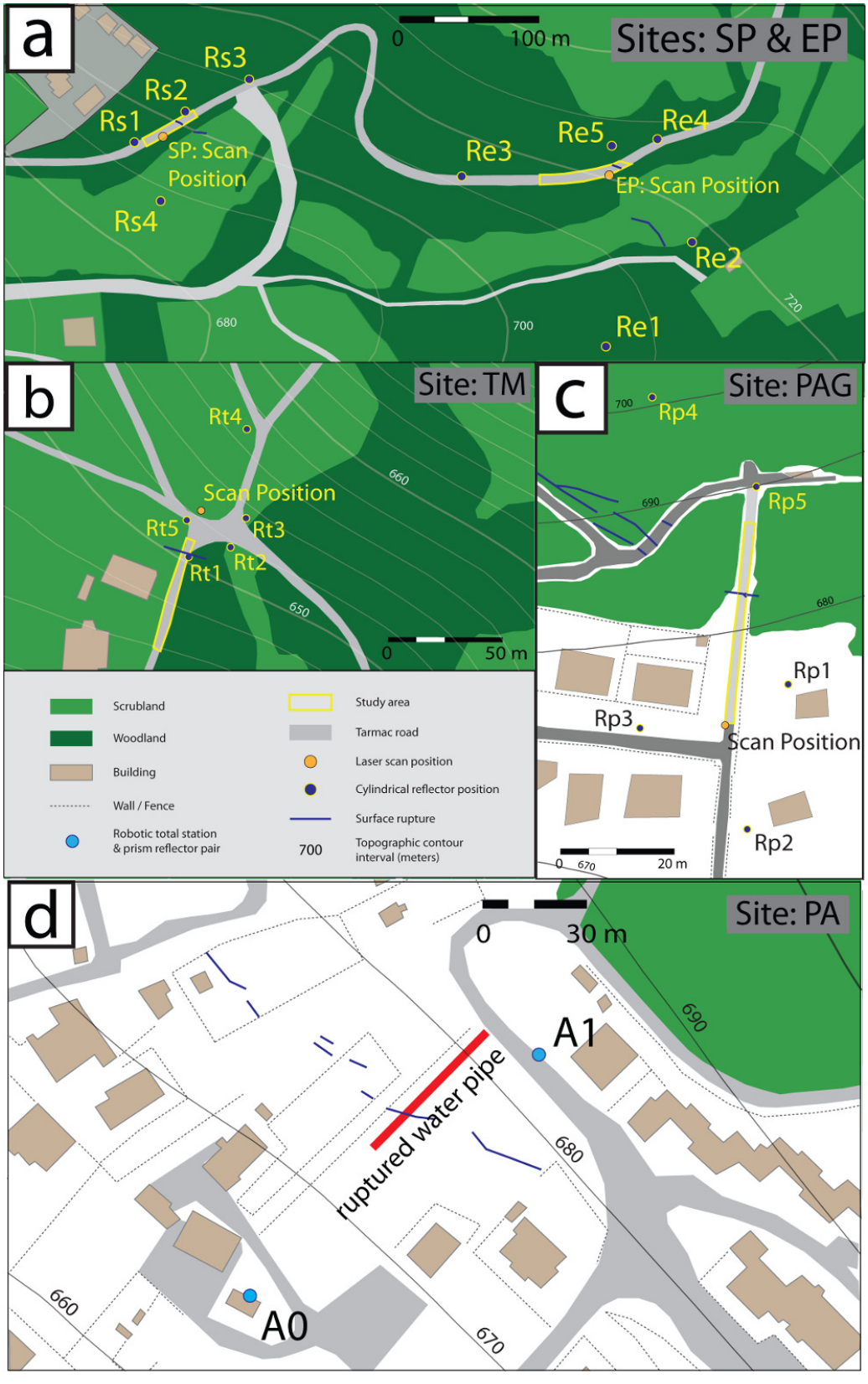

Figure 5.3.1: (a - d) Local maps for sites SP & EP, TM, PAG and PA. Land use depicts line of sight restrictions on the reflector network and the extent of the study areas.

Survey dates and measurements of rupture throw, hangingwall syncline subsidence, combined rupture throw and hangingwall syncline subsidence, and horizontal line of sight extension between reflectors for each of the five datasets, relative to the first measurement acquired at each site							
Date	**Dataset ID**	**Location (lat/long)**	**Days since earthquake**	**Rupture throw since first dataset (mm)**	**Hangingwall syncline subsidence since first dataset (mm)**	**Combined rupture throw and hangingwall syncline subsidence since first dataset (mm) / Site PA: Total vertical deformation (mm)**	**Horizontal line of sight extension between reflectors since first dataset (mm)**
14/04/09	PAG 1	13.471450°E 42.362631°N	8	-	-	-	-
17/04/09	PAG 2		11	2.2 ±0.7	11.6 ±2.3	13.8 ±2.3	11.4 ±5
11/05/09	PAG 3		35	3.9 ±2.4	19.5 ±1.8	23.4 ±1.8	15.9 ±5
15/05/09	PAG 4		39	4.1 ±2.2	19.4 ±1.2	23.5 ±1.2	9.3 ±5
19/05/09	PAG 5		43	5.2 ±2.2	17.3 ±1.5	22.5 ±1.5	16.4 ±5
24/05/09	PAG 6		48	8.3 ±2.0	16.2 ±2.8	24.5 ±2.8	17.2 ±5
08/08/09	PAG 7		124	13.4 ±2.6	14.3 ±2.3	27.7 ±2.3	21.8 ±5
17/04/09	SP1	13.484543°E 42.354447°N	11	-	-	-	-
14/05/09	SP2		38	6.8 ±1.3	2.7 ±2.2	9.5 ±2.2	7.2 ±5
18/05/09	SP3		42	7.3 ±3.45	3.3 ±2.5	10.6 ±2.5	16.5 ±5
21/05/09	SP4		45	8.0 ±3.2	3.3 ±2.4	11.3 ±2.4	19.7 ±5
10/08/09	SP5		126	13.1 ±4.1	2.9 ±2.2	16.0 ±2.2	27.6 ±5
16/04/09	EP1	13.489044°E 42.354056°N	10	-	-	-	-
14/05/09	EP2		38	3.3 ±3.6	-3.1 ±2.1	0.2 ±2.1	14.3 ±5
18/05/09	EP3		42	3.4 ±2.6	-2.2 ±2.0	1.2 ±2.0	15.9 ±5
22/05/09	EP4		46	4.5 ±2.9	-2.2 ±2.25	2.3 ±2.25	10.5 ±5
09/08/09	EP5		125	10.8 ±3.8	4.6 ±3.1	15.4 ±3.1	20.3 ±5
18/04/09	TM1	13.462563°E 42.370022°N	12	-	-	-	-
13/05/09	TM2		37	0.6 ±2.8	-	-	-4.8 ±5
17/05/09	TM3		41	0.9 ±2.8	-	-	4.2 ±5
20/05/09	TM4		44	1.7 ±2.8	-	-	2.9 ±5
23/05/09	TM5		47	1.9 ±2.8	-	-	1.4 ±5
08/08/09	TM6		124	2.4 ±2.8	-	-	3.2 ±5
23/04/09	PA1	13.467295°E 42.364682°N	17	-	-	-	-
07/05/09	PA2		31	-	-	3.1 ±1.1	5 ±1.1
20/05/09	PA3		44	-	-	7.8 ±1.1	6.3 ±1.1
10/06/09	PA4		65	-	-	10.8 ±1.1	6.8 ±1.1
30/06/09	PA5		85	-	-	11.7 ±1.1	12.5 ±1.1
29/07/09	PA6		114	-	-	13.8 ±1.1	10.1 ±1.1

Table 5.3.1: TLS Survey dates and measurements of postseismic deformation. Error bounds represent ±2σ.

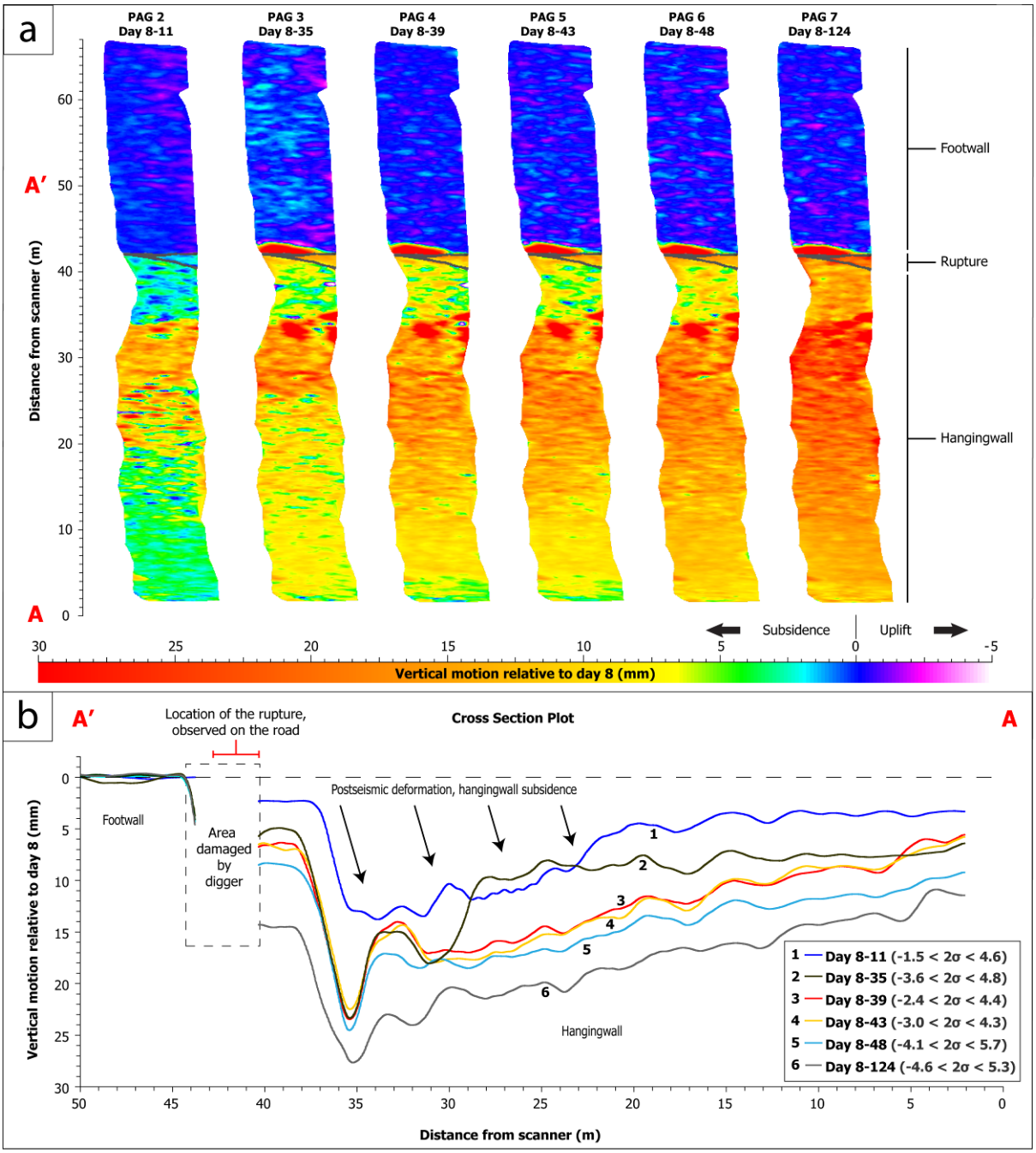

Figure 5.3.2: Postseismic deformation results for site PAG. (a) Color map plot of vertical deformation (mm) in a footwall static reference frame for subsequent TLS datasets, relative to the initially acquired dataset. (b) Cross sectional plots of the surface deformation between A – A' in (a).

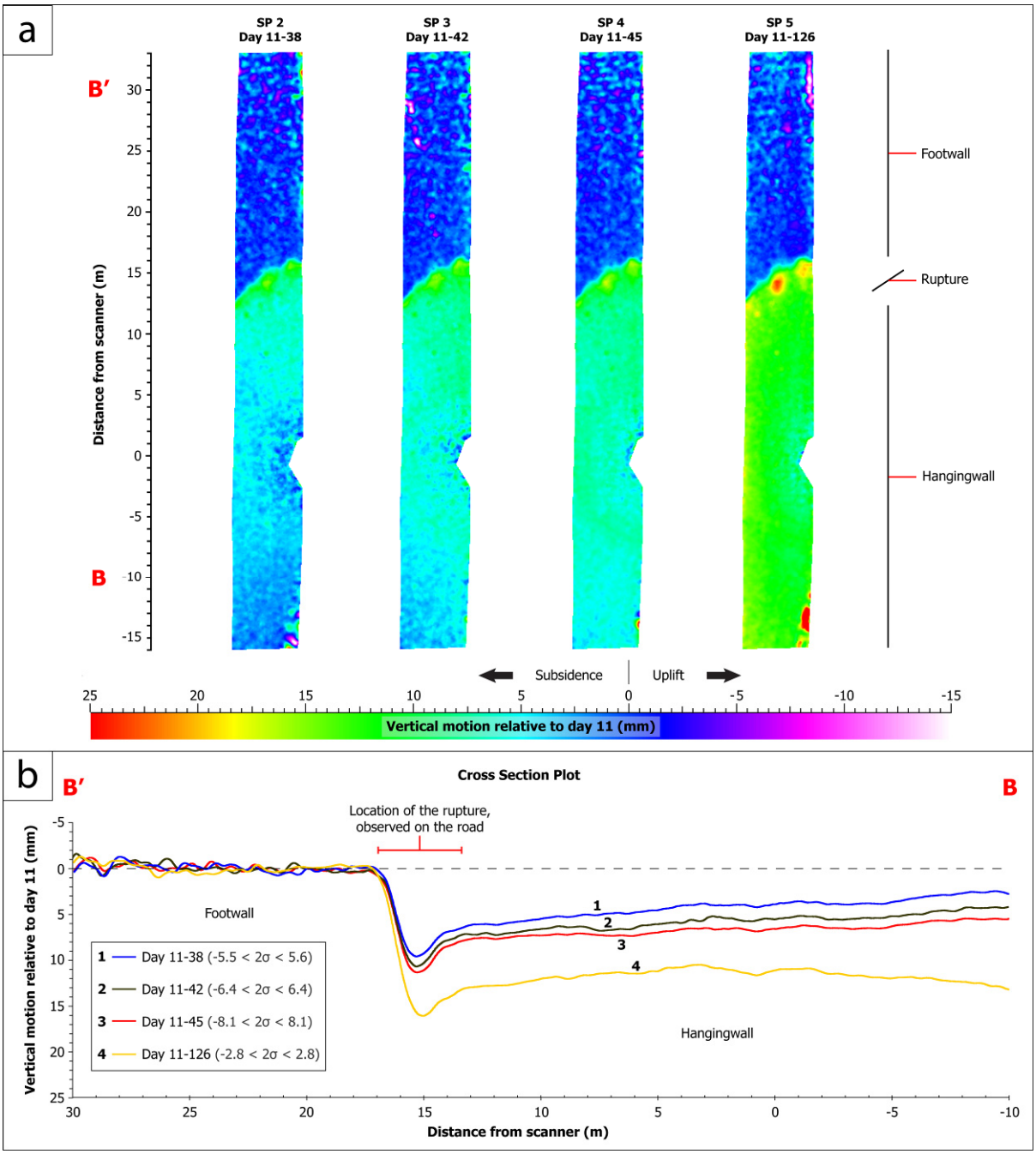

Figure 5.3.3: Postseismic deformation results for site SP. (a) Color map plot of vertical deformation (mm) in a footwall static reference frame for subsequent TLS datasets, relative to the initially acquired dataset. (b) Cross sectional plots of the surface deformation between B – B' in (a).

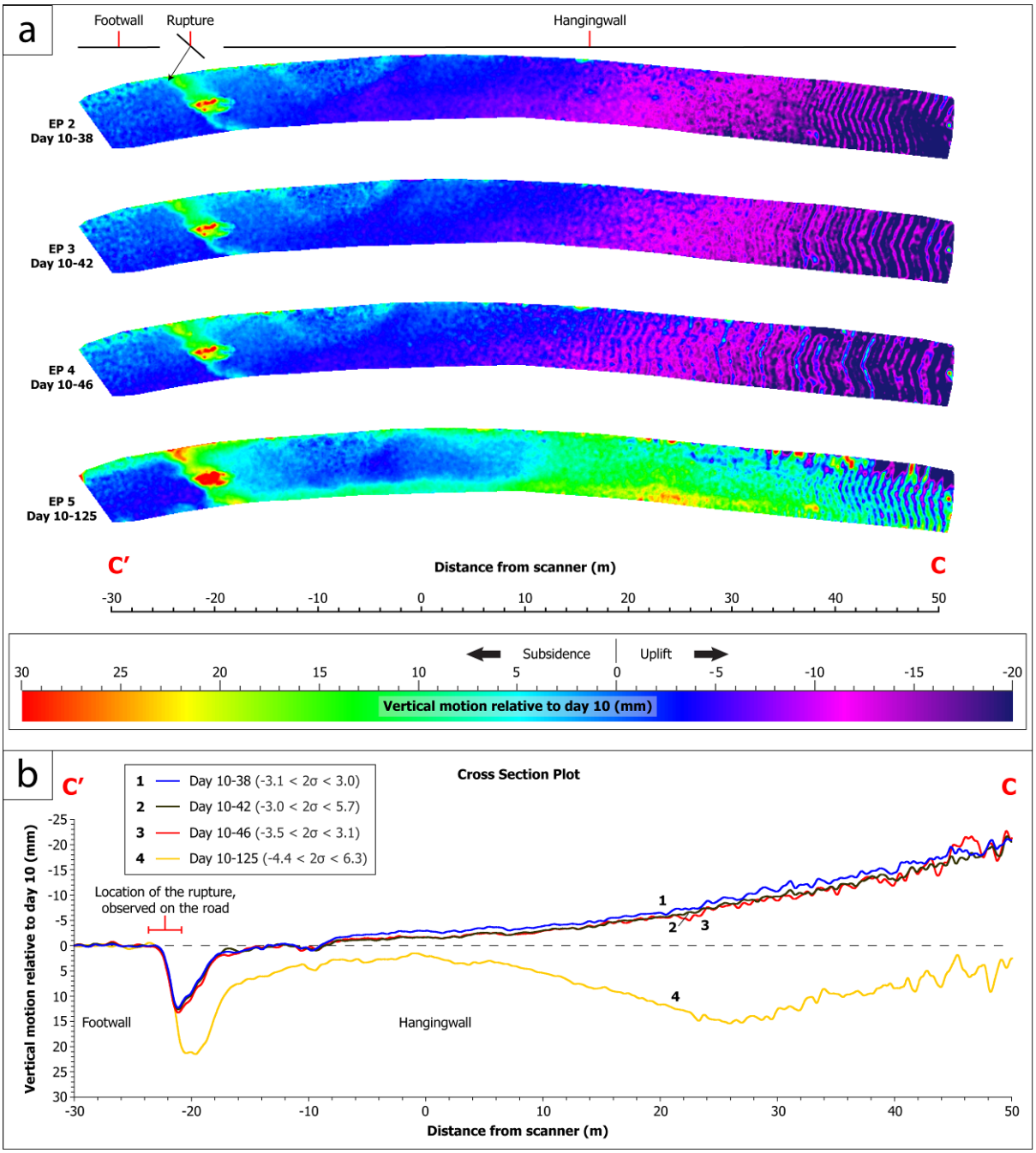

Figure 5.3.4: Postseismic deformation results for site EP. (a) Color map plot of vertical deformation (mm) in a footwall static reference frame for subsequent TLS datasets, relative to the initially acquired dataset. (b) Cross sectional plots of the surface deformation between C – C' in (a).

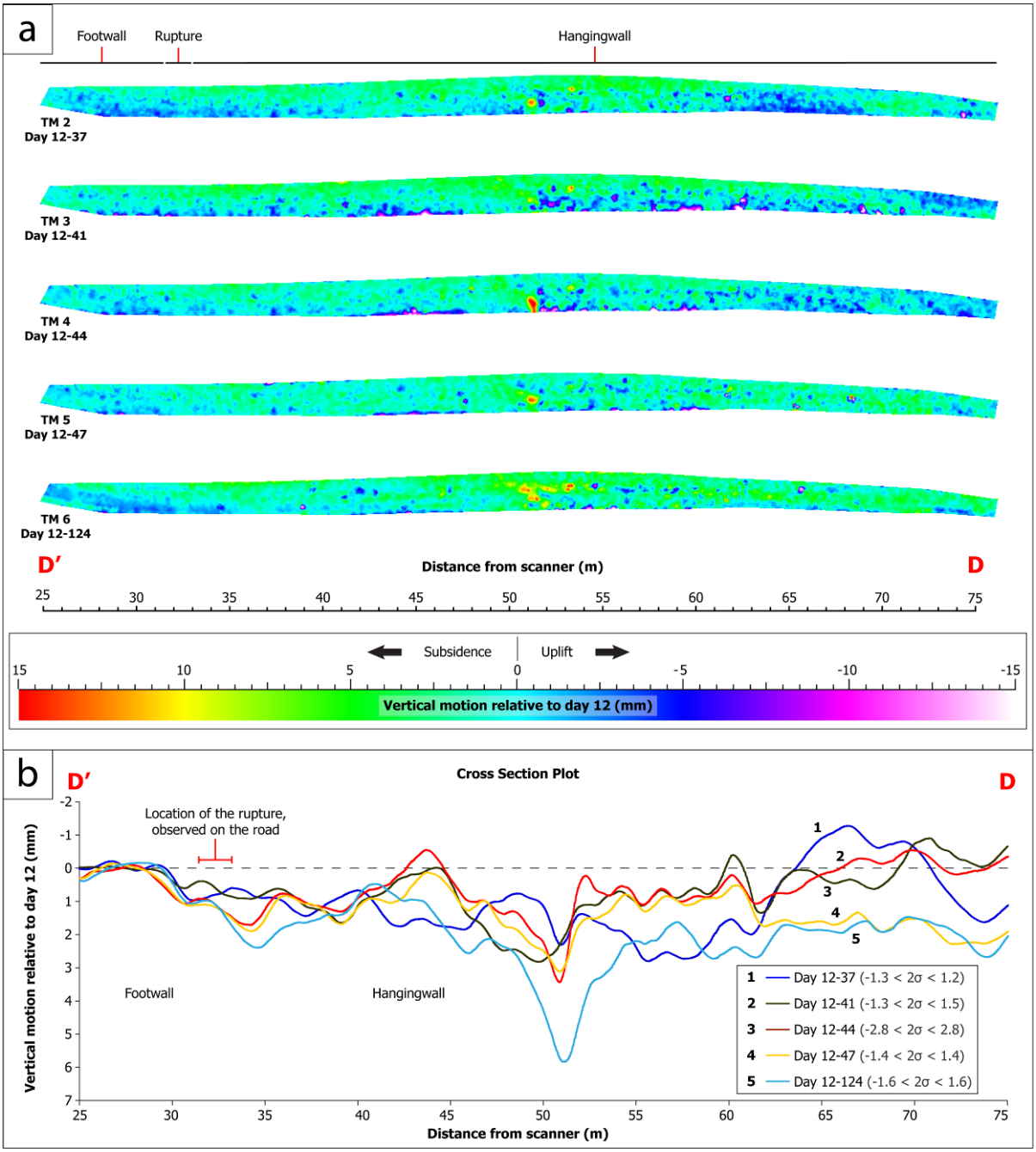

Figure 5.3.5: Postseismic deformation results for site TM. (a) Color map plot of vertical deformation (mm) in a footwall static reference frame for subsequent TLS datasets, relative to the initially acquired dataset. (b) Cross sectional plots of the surface deformation between D – D' in (a).

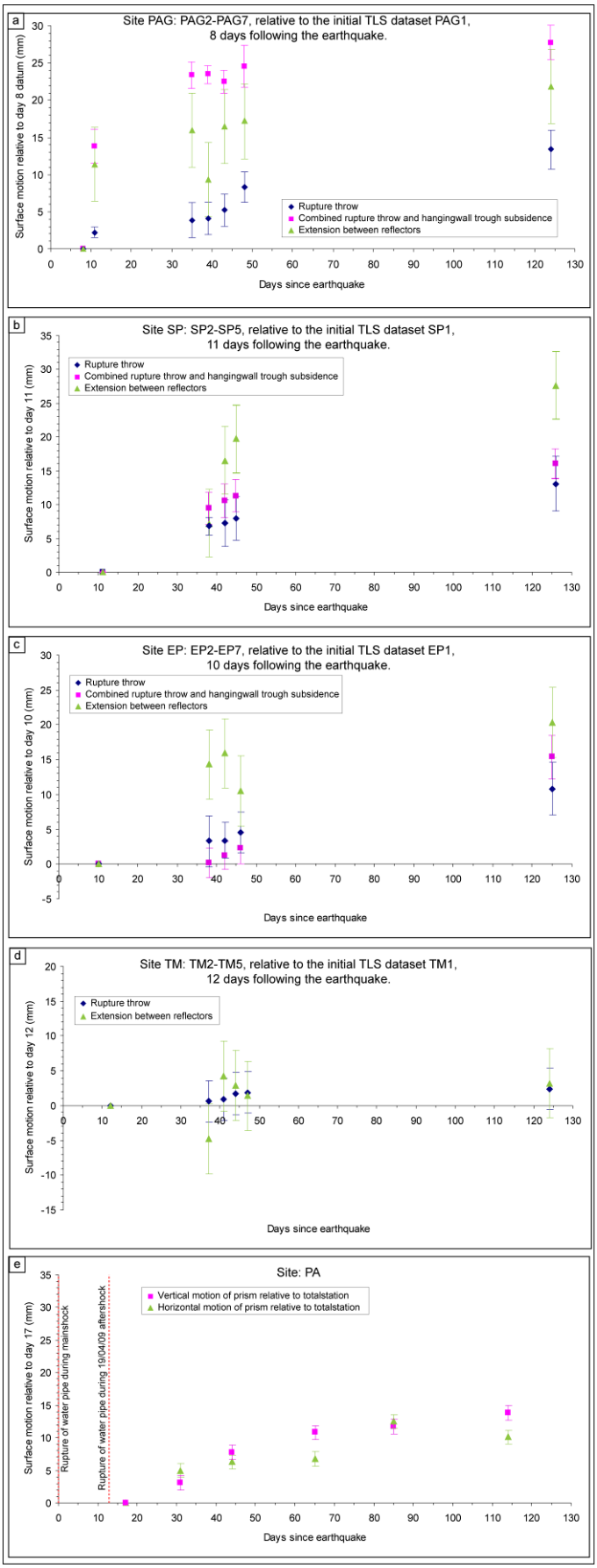
a
Site PAG: PAG2-PAG7, relative to the initial TLS dataset PAG1,
8 days following the earthquake.
Surface motion relative to day 8 datum (mm)
Rupture throw
Combined rupture throw and hangingwall trough subsidence
Extension between reflectors
Days since earthquake
b
Site SP: SP2-SP5, relative to the initial TLS dataset SP1,
11 days following the earthquake.
Surface motion relative to day 11 (mm)
Rupture throw
Combined rupture throw and hangingwall trough subsidence
Extension between reflectors
Days since earthquake
c
Site EP: EP2-EP7, relative to the initial TLS dataset EP1,
10 days following the earthquake.
Surface motion relative to day 10 (mm)
Rupture throw
Combined rupture throw and hangingwall trough subsidence
Extension between reflectors
Days since earthquake
d
Site TM: TM2-TM5, relative to the initial TLS dataset TM1,
12 days following the earthquake.
Surface motion relative to day 12 (mm)
Rupture throw
Extension between reflectors
Days since earthquake
e
Site: PA
Surface motion relative to day 17 (mm)
Rupture of water pipe during mainshock
Rupture of water pipe during 19/04/09 aftershock
Vertical motion of prism relative to totalstation
Horizontal motion of prism relative to totalstation
Days since earthquake

Figure 5.3.6: (a - d) Postseismic deformation measurements for each TLS dataset relative to the initial dataset, plotted against time since the earthquake. Error bars represent 2σ certainty. (e) Site PA: Horizontal and vertical components of the change in distance between points A0 and A1 (Fig. 5.3.1.d), relative to the first measurement at day 17.

5.4. Discussion

5.4.1. Comparison of data to afterslip models

The measured dataset of postseismic deformation from site PAG, located close to mid way along the surface rupture, was compared with previously published theoretical and empirical models that describe measured postseismic deformation (afterslip) from rupture studies following previous earthquakes [Bucknam et al., 1978, Williams & Magistrale, 1989, Marone et al., 1991] (Figs. 5.4.1 & 5.4.2). These models have not been optimised to fit the data from site PAG; they have been plotted relative to day 8, the first observation for site PAG, using published parameters defined from measured afterslip following previous earthquakes [Bucknam et al., 1978, Sharp et al., 1989, Williams & Magistrale, 1989]. The data for rupture throw, not including hangingwall syncline subsidence, are indicative of afterslip, showing broad agreement with previously published afterslip models with correlation coefficients ranging from 0.9149–0.9318 (Fig. 5.4.1). Field observations 500 m – 1500 m SE of site PAG, by Boncio et al., (2010), were used to estimate how much afterslip occurred on the rupture at site PAG before the first laser scan was acquired. The observations document the widening of a ground fracture by 30–50 mm between the 6th and 25th April and the vertical development of a hangingwall flexure by 25 mm between the 6th April and 19th May. It is estimated ~15 mm of this vertical motion developed between the 6th and 14th April as most of the afterslip is known to occur in the first few days following the earthquake. If the observations of Boncio et al., (2010), apply to site PAG, then it is estimated that of the 75 mm of vertical offset measured across the rupture at site PAG on the 14th April, ~15 mm of this measurement was produced by postseismic deformation on the rupture between 6th

and 14th April and 50 mm by coseismic offset. By adding 15 mm to the observation of 13.4 mm of rupture throw observed between 14th April and 8th August, it is estimated that the total measured afterslip on the rupture since 6th April is ~28.4 mm. This figure is in broad agreement with what the previously published models for afterslip predict for the magnitude of afterslip between day 0 and day 124 (6^{th} April – 8^{th} August) at this site (Fig. 5.4.1.b). Given that it is estimated at the coseismic offset at this site was 50 mm (75 – 15 mm) and that the postseismic deformation is ~28.4 mm (~15 mm estimated + 13.4 mm observed), the ratio of coseismic to postseismic deformation at this site is 1.67:1 (the postseismic deformation is 60% that of the coseismic).

If the postseismic deformation associated with the growth of the hangingwall syncline is added to that formed by rupture throw, the previously published afterslip models describe such combined motions with lower certainty (correlation coefficients 0.8863–0.9073). This increase in mismatch is largely because of the relatively rapid syncline subsidence between days 8–11. Between days 8–124, the rate and magnitude of subsidence of the hangingwall syncline were comparable to and at times exceeded that of the rupture afterslip, with the combined rupture afterslip and subsidence of the hangingwall syncline approximately twice that of the rupture afterslip at day 124. The similarity in magnitude of the combined rupture throw and subsidence of the hangingwall syncline in relation to the data for horizontal extension suggests that hangingwall deformation driven by afterslip within the fault zone is responsible for the growth of the syncline and formed a major component of the postseismic extension at PAG.

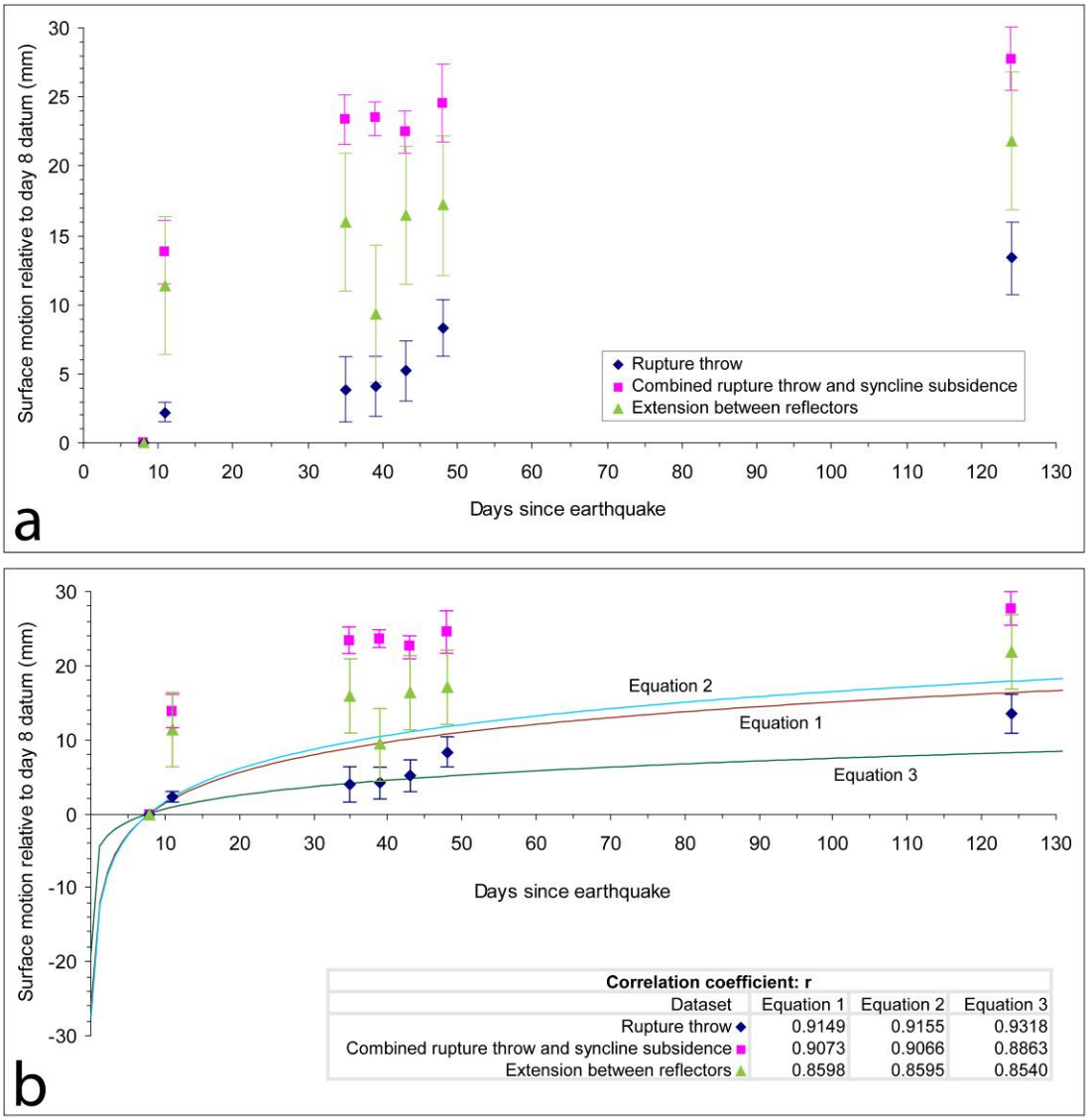

Figure 5.4.1: (a) Surface motions for the six TLS datasets (PAG2–PAG7), relative to the initial TLS dataset PAG1, 8 days following the earthquake (Table 5.3.1) plotted against time since the earthquake. Error bars represent 2s (95%) certainty. (b) Graphical comparison of published theoretical and empirical models for afterslip (Equations 1, 2 and 3 in figure 5.4.2) to our datasets, together with their correlation coefficients.

$D = a + b\log T$ (1)[1]		$U^P = U_C^S + \alpha' \ln\left[\left(\frac{\beta'}{\alpha'}\right)t + 1\right]$ (2)[2]			$D = at^b$ (3)[3]	
[1]Model 1: Equation defined by least-squares regression of observed displacement data on logarithm of time from the 1976 Guatemala earthquake [*Buckham et al.*, 1978]. D = modeled displacement (mm) a = coseismic rupture offset (mm) b = gradient of best fit line through the data plotted as logarithm of time T = time since earthquake (days)		[2]Model 2: Two variable version of a closed-form solution for afterslip [*Marone et al.*, 1991, after *Scholtz*, 1990] modified to accommodate coseismic measurements, and used to model 1987 Superstition Hills afterslip data [*Sharp et al.*, 1989]. U_p = modeled displacement (mm) U^S_c = coseismic rupture offset (mm) α' = a parameter (mm) defining the friction rate parameter divided by spring stiffness, analogous to the thickness of the velocity strengthening region, the former obtained from best fit to data plotted as logarithm of time β' = coseismic slip velocity in the velocity strengthening region (mm/day)			[3]Model 3: Slip decay model [*Williams and Magistrale*, 1989] describing displacement data from the 1987 Superstition Hills earthquake sites 2M, 2T and 2U. D = modeled displacement (mm) a = coseismic rupture offset (mm) b = decay rate parameter t = time since earthquake (days)	
a (mm)	***b***	***U^S_c (mm)***	***α'***	***β'***	***a (mm)***	***b***
0 (replacement of 50.9 as there is no coseismic component to be compared in our dataset)	13.9	0 (replacement of 237.1 as there is no coseismic component to be compared in our dataset)	65.69	518.1	14.6	0.131
Parameters calculated from data of the 1976 Guatemala earthquake, Zacapa site.		Parameters calculated from data of the 1987 Superstition Hills Earthquake site 2T [*Sharp et al.*, 1989].			Parameters calculated from data of the 1987 Superstition Hills Earthquake, Site 2T.	

Figure 5.4.2: Theoretical and empirical afterslip models with parameters obtained from afterslip datasets of previous earthquakes.

5.4.2. Spatial distribution of postseismic deformation and comparison to fault zone regions of high coseismic slip gradient

The location of the five study sites along the Paganica surface rupture (Fig. 5.1.1) enables an analysis of the spatial distribution of postseismic deformation following the L'Aquila earthquake. The surface expression of rupture afterslip and near-field postseismic deformation is not constant along the surface rupture and is highly variable over short distances. The magnitude of the vertical and horizontal components of postseismic deformation between 8 and 44 days (or the closest measurement dates available at each site) is shown for the five sites in Figure 5.4.3.a. The greatest vertical and horizontal postseismic deformation over this period occurred at site PAG (22.5 mm ± 3.3 mm and 16.4 mm ± 5 mm respectively), towards the

centre of the surface rupture. The observed vertical and horizontal components of postseismic deformation decrease from site PAG towards sites TM and EP at the North-Westrn and South-Eastern ends of the rupture respectively. The vertical and horizontal components of postseismic deformation between days 8 and 126 (or the closest measurement dates available at each site) are shown for the five sites in Figure 5.4.3.b. The maximum observed vertical and horizontal components of postseismic deformation are still observed at PAG, with the exception of the horizontal deformation observed at SP. The relative change in the components of postseismic deformation between days 44 and 126 is shown in Figure 5.4.3.c. There is a significant increase in deformation over this time period towards the South-Eastern end of the rupture, observed at sites SP and EP, while deformation at TM to the North-West remains low. The vertical and horizontal components of deformation observed at SP increase by 5.4 ± 2.5 mm and 11.1 ± 5 mm between days 42 and 126, while the vertical and horizontal components of deformation observed at EP increase by 14.2 ± 3.1 mm and 4.4 ± 5 mm between days 42 and 126. In comparison, the vertical and horizontal components of postseismic deformation at PAG, towards the centre of the rupture increased by 5.2 ± 2.3 mm and 5.4 ± 5 mm respectively.

To illustrate this relative increase in postseismic deformation at the South-Eastern end of the rupture, the maximum observed postseismic deformation at each site was plotted alongside published estimates for the coseismic slip within the fault zone (Fig. 5.4.4). The postseismic deformation is expected to decrease from a maximum at sites PAG and PA at the centre of the surface rupture, to site TM at the North-West tip and sites EP and SP in the South-East tip. Sites SP and EP have relatively high magnitudes of postseismic deformation, even though they are at the tip of the rupture. This is due to these sites being situated above a region of high

coseismic slip gradient, as shown by the blue and green lines in Figure 5.4.4.(a). The theory of afterslip [Marone et al., 1991] dictates that afterslip is driven by coseismic slip deficits (high gradients in coseismic slip) within the fault zone at depth. The unconsolidated material within the fault zone is thought to respond to equilibrate differential shear stresses in the fault zone by the process of gradual creep over time. This behaviour is thought to be responsible for the characteristic decaying rate of afterslip motion observed on surface ruptures. This theory explains the decaying rate of postseismic deformation observed at sites PAG, PA, SP and EP. The theory also accounts for the fact that the magnitude of postseismic deformation is greatest at sites PAG and PA at the centre of the rupture, while the magnitude of deformation at sites SP and EP are higher than would be expected at the South-Eastern tip of the rupture, as they are situated above a region of high coseismic slip gradient within the fault zone.

In order to explain the variation in postseismic deformation observed at the different study sites along the surface rupture, it is nessecairy to study the coseismic slip pattern within the fault zone beneath these study sites. A study by Cheloni et al., (2010), compared coseismic and postseismic fault slip maps for the L'Aquila earthquake produced by inverting far-field GPS data. By correlating the regions of postseismic slip to those on the periphery of the regions of coseismic slip they suggested that postseismic deformation is greatest in regions where shear stresses, produced by large gradients in coseismic slip, are highest. In order to test this correlation against the postseismic measurements from this study, coseismic slip within the fault zone was plotted by sampling horizontal transects at 1.5 km and 3.5 km depth along the length of the fault using values from the modelled coseismic fault slip map inferred from coseismic GPS motions [Cheloni et al., 2010], (Figs. 5.4.4.a &

b). The mean of the horizontal and vertical components of the maximum observed postseismic deformation for each of the five study sites was plotted against the values of coseismic slip (Fig. 5.4.4.b). In order to directly compare the postseismic surface measurements to the modelled coseismic slip within the fault plane, these magnitudes are resolved onto a modelled 54° dipping fault plane, (Table 5.4.1, columns 5, 6 & 7, Figure 5.4.4.b, yellow circles). Sites SP and EP at the South-Eastern end of the rupture, where significant increases in postseismic deformation were observed between 44 – 126 days are located above a region in the fault zone where the gradient of coseismic slip is high at 3.5 km depth (estimated from the blue line in Fig. 5.4.4.b as ~28 cm change in coseismic slip per km distance along the fault). Sites PA and TM, which experienced relatively lower values of postseismic deformation are located above a region where the coseismic slip gradient is of a lesser value at 3.5 km depth (estimated from the blue line in Fig. 5.4.4.b as ~10 cm change in coseismic slip per km distance along the fault). The correlation between the coseismic slip gradient and the increased magnitude of on-rupture postseismic deformation between 44 – 126 days provides near-field evidence to support the suggestion by Cheloni et al. (2010), that postseismic deformation is driven by high gradients in coseismic slip within the fault zone. A coseismic slip map produced by Atzori et al., (2009), from a coseismic interferogram also shows a similar signal of high coseismic slip gradient within the fault zone, supporting the above. Their slip map was not used in this comparative analysis as the cell size is slightly greater than the spacing between the study sites. The difference in postseismic deformation between the study sites suggests postseismic deformation occurs as a response to a complex pattern of coseismic slip, which produces varying stresses within the fault zone.

Site	Survey Timeframe (Days after earthquake)	Maximum observed vertical postseismic deformation (mm)	Maximum observed horizontal postseismic deformation (mm)	Maximum observed vertical postseismic deformation, resolved down dip (mm)	Maximum observed horizontal postseismic deformation, resolved down dip (mm)	Mean of resolved vertical and horizontal components (mm)
PAG	8 – 124	27.7	21.8	47.1	26.9	37.0
SP	11 – 126	16.0	27.6	27.2	34.1	30.7
EP	10 – 125	15.4	20.3	26.2	25.1	25.7
TM	12 – 124	2.4	4.2	4.1	5.2	4.7
PA	17 - 114	13.8	10.1	23.5	12.5	18.0

Table 5.4.1: The maximum vertical and horizontal components of postseismic deformation, as observed and resolved as slip in a 54° dipping fault zone.

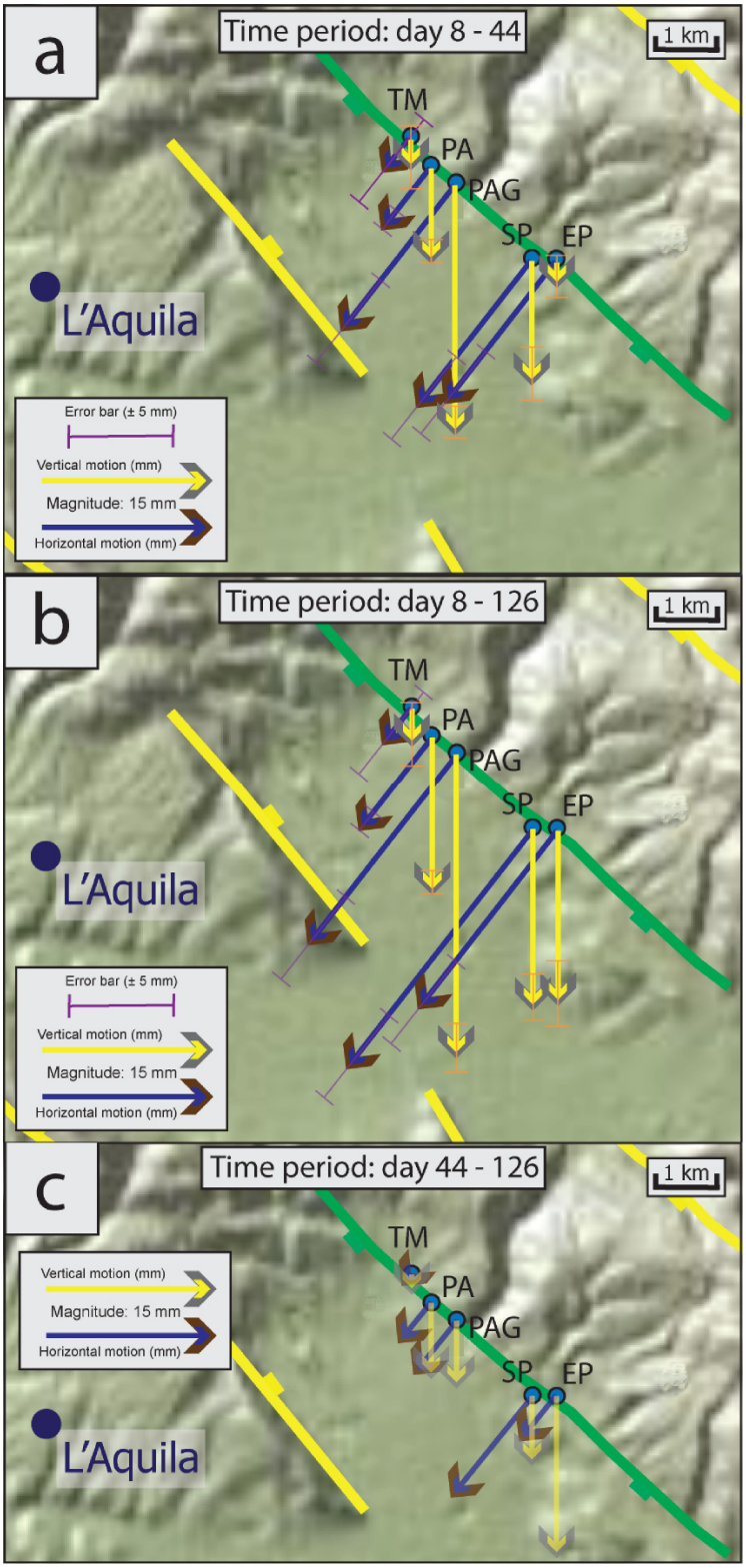

Figure 5.4.3: Map distribution of the horizontal and vertical components of postseismic deformation observed at the five study sites over the period: (a) 8 – 44 days, (b) 8 – 126 days, (c) 44 – 126 days. Arrow lengths and error bars for each

measurement scaled from those shown in the legend. The green line represents the inferred subsurface trace of the Paganica fault.

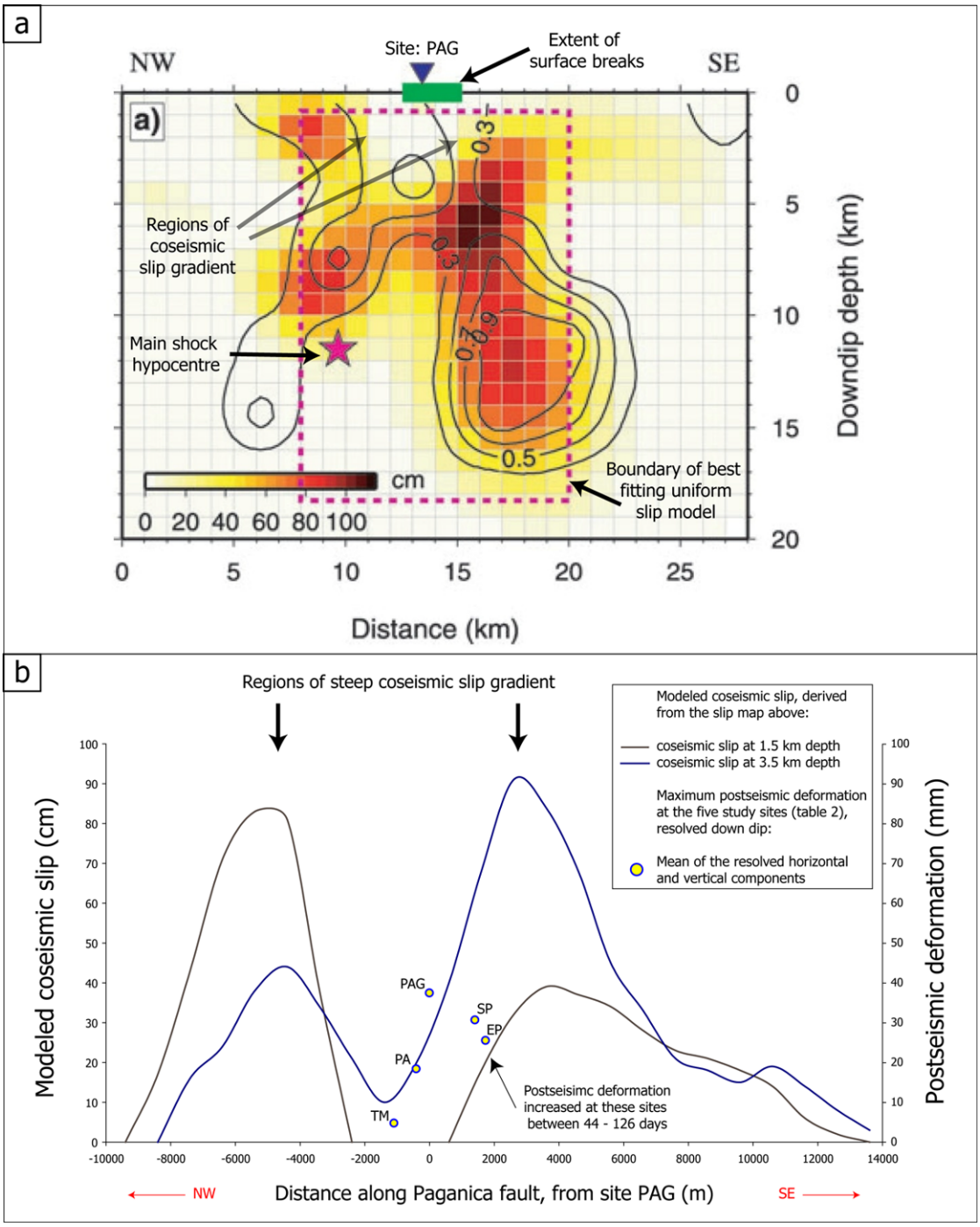

Figure 5.4.4: (a) Modelled coseismic fault slip map from Cheloni et al., 2010. The contours represent coseismic slip in meters. (b) Plot of the coseismic slip at 1.5 km and 3.5 km depth within the fault zone and the maximum observed postseismic

deformation at each study site. The precise positions of peaks in coseismic slip will be affected by the errors estimated through Monte Carlo simulation (see Cheloni et al., 2010, their supplementary material).

5.4.3. Comparison with far-field datasets

The maximum horizontal and vertical components of postseismic deformation observed in the far-field using GPS [Cheloni et al., 2010] are 9 mm towards the South-South-West (site: AQUI) and 50 mm downward (site: PAGA) respectively (Fig 5.1.1, black arrows). The three areas of maximum line of sight postseismic displacement (PS, CT & OF) identified by Lanari et al., 2010 using SBAS-DInSAR are downward 35 mm, 26 mm and 18 mm respectively (Fig. 5.1.1, yellow dots, PS, CT & OF). These far-field postseismic measurements are not significantly greater than the near-field deformation measured at sites PAG, PA, SP and EP. This comparison suggests that the source of far-field postseismic deformation can be attributed to near-field postseismic deformation of similar magnitude. Modelling the propagation of near-field postseismic deformations into the far-field is required in order to rigorously test this hypothesis. This further work is beyond the scope of this thesis.

5.4.4. Implications for palaeoearthquake magnitudes

The localised nature of postseismic surface motions measured at sites PAG, SP and EP produced several millimetres of slip across the rupture that was visible with the naked eye. Vertical motions associated with the growth of a hangingwall syncline (interpreted as a signal of shallow afterslip at depth within the fault zone) at these sites would have been missed without the use of TLS, as they were too subtle to

observe with the naked eye alone, and no pre-earthquake datum existed in the form of a precise topographic map. This is important because such subtle subsidence associated with hangingwall folding accounts for up to 52% of the total vertical postseismic deformation (site PAG). Postseismic deformation associated with hangingwall folding may be unaccounted for within empirical slip‐magnitude relationships, especially for smaller earthquakes [e.g., Wells & Coppersmith, 1994]. If this is the case, the inclusion of hangingwall deformation measured in this study would have doubled the actual coseismic offset for the given earthquake magnitude, if the total subsidence had not been attributed to a combination of postseismic and coseismic deformation. In palaeoseismic studies such slip‐magnitude datasets are used to estimate palaeoearthquake magnitudes from measured offsets [Bakun et al., 2005; Vigny et al., 2005; Ryder et al., 2007]. Uncertainty in the coseismic surface offset for a given magnitude within the slip‐magnitude datasets introducted by unresolved postseismic deformation will lead to uncertainty in the paleoearthquake magnitude for a given offset.

Hangingwall synclines are observed at many paleoseismic sites within the Italian Apennines [D'Addezio et al., 1996, Pantosti et al., 1996, Galli et al., 2002, Galli et al., 2008]. Also, surface motions described as '*uplift of the footwall and a warp‐like hangingwall subsidence (folding)*' were recorded during a study of afterslip on the surface rupture of the 1995 Egion earthquake [Koukouvelas & Doutsos, 1996]. The observed postseismic development of hangingwall synclines of significant magnitude at sites PAG, SP and EP, suggest such features are persistent along normal faulted surface ruptures of earthquakes of >6 Mw. The persistence of synclines of significant magnitude along surface ruptures suggest that they represent an important signal of the magnitude of afterslip in the shallow regions of the fault

zone and an attempt to resolve such motions should be attempted for empirical slip-magnitude datasets.

5.5. Conclusion

The use of repeat TLS at four sites along the L'Aquila earthquake surface rupture enabled postseismic deformation on the order of ~3 mm to be observed at distances of up to 50 m from the laser scanner. The measurements of postseismic deformation from sites PAG, SP, EP and PA show an increase over time with decreasing rate, indicative of afterslip within the fault zone. Surface deformation observed at site TM is below the precision of the method and deemed insignificant. The rate and magnitude of postseismic deformation observed at site PAG was found to be comparable to theoretical and empirical equations that describe rupture postseismic slip for previous earthquakes. A relative increase in postseismic deformation was observed between 44 – 126 days at sites SP and EP towards the South-Eastern end of the rupture. This increase is attributed to a high gradient of coseismic slip within the fault zone beneath these sites and suggests the increase in deformation is driven by increased shear stresses in this part of the fault zone. The magnitude of far-field postseismic deformation, measured using GPS and InSAR is not significantly greater that the near-field deformation measured at distances up to 50 m of the rupture. For this earthquake it is suggested that localized afterslip within the fault zone, driven by increased shear stresses in regions of high coseismic slip gradient is responsible for the majority of postseismic deformation on all scales. Hangingwall synclines were observed developing postseismically at sites PAG, SP and EP, which are thought to represent a signal of shallow afterslip within the fault zone. The vertical deformation associated with these features accounts for up to 52% of the total vertical deformation observed, which the total postseismic deformation observed was up to 60% of the coseismic. The identification of hangingwall synclines

in several paleoseismic studies suggest that they are an important common feature of normal faulting surface ruptures for earthquakes of >6 Mw. The inclusion of such features in field studies and slip-magnitude relationships will reduce uncertainty in the magnitude of paleoearthquake estimates.

Chapter 6: Discussion – The role of quantitative spatially and temporally constrained field studies to refine paleoearthquake magnitudes for use in seismic hazard analyses

6.1. Introduction

Field studies play an important role in the identification of seismically active faults and their potential hazard and are a fundamental step towards assessing regional seismic hazard [Pace et al., 2006]. An assessment of the uncertainty in the results of such studies is important for the correct weighting in their contribution within the process of defining seismic hazard for a region based on numerous multidisciplinary studies [Peruzza et al., 2010]. Parameters required for seismic hazard analysis which are not reported directly from field studies are often estimated or are deemed entirely 'fictitious' [Peruzza et al., 2010]. For example, unknown elapsed times (time since last earthquake) default to 9,999 years within the database of individual seismogenic sources for central Italy (DISS) [Basili et al., 2008]. Field studies which aim to identify fault activity over timescales on the order of numerous, recent seismic cycles provide a means to improve estimates of elapsed times within such databases [Roberts et al., 2004]. The uncertainty inherent to these field studies can be reduced through the process of refining working practices based on the methods described in this thesis. Specifically, this thesis has demonstrated that: 1) the incorporation of the effect of fault geometry (i.e. changes in strike) on the size of paleoearthquake offsets is potentially important and 2) a large proportion of paleoseismic offsets measured in moderate magnitude earthquakes may be due to postseismic deformation, rather than coseismic slip alone. The incorporation of both these effects will allow for an

improvement in the estimation of paleoearthquake magnitudes and hence hazard analysis.

6.2. Discussion

6.2.1. The effect of fault geometry on throw-rates and coseismic fault offsets

The study of fault throw-rate along the Campo Felice fault in Chapter 4 of this thesis has shown using TLS that fault geometry can control local throw-rates and that a continuous strain-rate profile is unaffected by changes in fault geometry. Fault geometry is also expected to control coseismic slip, as suggested by the correlation between throw-rate and the magnitude of coseismic slip bands on the base of the Campo Felice fault scarp [Giaccio et al., 2002] (Fig. 4.4.3). Paleoseismic studies which aim to assess earthquake magnitude based on coseismic offsets in trenching studies must therefore consider and correct for the potential effect of fault geometry on any measured coseismic offset. In particular the fault chosen for paleoseismic study must be carefully mapped in its entirety to determine if the fault geometry at the trench location is representative of that of the rest of the fault. The kinematic slip direction for the studied fault must be obtained through field study of fault striations or offset landforms to correct for the affect of fault geometry, as the correction relies on the deviation of fault strike towards or away from a dip-slip configuration (Fig. 4.4.1). Once the slip direction and fault geometry are known a measurement of coseismic offset from a trench study can be revised for the effect of fault geometry in order to provide a more reliable estimate of the true coseismic slip and hence earthquake magnitude (Fig. 6.2.1, box a).

For instance, of the twenty studied faults detailed within a review of twenty years of paleoseismology in Italy [Galli et al., 2008], none of the studies attempt to factor in the affect of fault geometry on their magnitude estimations. In most cases the general strike of the studied fault is described, but paleoseismic sites are often chosen

in areas where oblique fault geometry exists, for example close to fault tips (i.e. the Northern Matese fault system, Galli et al., 2008) and within splays which deviate from the overall strike of the fault system (i.e. the Piano di Pezza and the Norcia faults, Galli et al., 2008). Such site selection, with disregard to the effect of fault geometry on paleoseismic offsets, can lead to uncharacteristic magnitude estimates for the fault being studied. By incorporating the outcomes from this thesis regarding the effects of fault geometry on paleoearthquake offsets, paleoearthquake magnitudes will be estimated with reduced uncertainty. The concerns of the effect of fault geometry also apply to studies of fault scarp exposure dating using ^{36}Cl techniques [Palumbo et al., 2004, Schlagenhauf et al., 2010] as changes in geometry are expected to affect throw-rates, which in turn will increase or decrease the amount of slip at a specific study site during each earthquake. ^{36}Cl exposure dating techniques require slip events (earthquakes) to be as large as possible for a fault in question, to enable changes in ^{36}Cl concentration to be detected on the fault scarp and identification of every successive slip event. In a case where the local fault geometry may suppress slip event size, that particular site may not be a good place to sample the scarp and detect a complete earthquake history. Where representative slip size and earthquake magnitude are also of concern, the outcomes of this study suggest that a ^{36}Cl sample site must be chosen in a place where the fault geometry is representative of the majority of the fault so that any slip events detected are considered representative (i.e. not local maxima, due to peculiarities in local fault geometry).

Field studies of coseismic surface ruptures from present and historical earthquakes where magnitude is known provide key empirical relationships that relate the parameters of coseismic slip and surface rupture length to moment magnitude [Wells & Coppersmith, 1994]. The effect that fault geometry has on the coseismic

offset is therefore also an important parameter that should be accounted for in these field studies (Fig. 6.2.1, box e).

Chapter 4 of this thesis has shown that strain-rate can be calculated for boxed regions at regular intervals along a fault (Fig. 4.3.6), providing the throw-rate, fault geometry and kinematic slip direction is known (see section 3.2.2 for method, after Faure Walker et al., 2009). The strain-rate profile for the Campo Felice fault showed a linear decrease in strain-rate from the centre of the fault to the South-Eastern tip, whereas the throw-rate profile was irregular due to changes in fault geometry. It is therefore suggested that strain-rate is a superior measure of fault activity, as it provides a more robust estimate which is unaffected by changes in fault geometry or kinematic slip direction. Indeed, calculation of strain-rate at various locations along strike for fault systems which have irregular throw-rate profiles (i.e. Bull et al., 2006) may help to explain if these irregularities are related to changes in fault geometry and kinematic slip or if they are related to true changes in local and regional strain-rates. The calculation of strain-rates may also explain anomalously high fault throw-rates and slip per event values measured at locations along faults where the strike of the fault changes from that of the rest of the fault, or the regional trend. For example, the throw-rate of 0.9 – 2.0 mm/yr and slip per event of 2 – 3 m measured from paleoseismic investigation on the Piano di Pezza [Pantosti et al., 1996] may be anomalously high due to a change in fault strike from NW to WNW – ESE at the study site. The Magnola fault in the central Apennines near the village of Forme has a strike of WNW – ESE, whereas the regional trend of faults in the Apennines is NW – SE. A paleoseismic study by Schlagenhauf et al., (2011) revealed slip events of 2.6 - 3.6 m, which exceed those seen on any other faults in the Apennines. The reason for

these large slip events could be partly due to the peculiar orientation of the Magnola fault within the Apennine array.

Studies that are able to generate a profile of throw-rate along strike (Chapter 4, Fig. 4.3.1) provide information on active fault length. For instance, the study of throw-rate along the Campo Felice fault in Chapter 4 of this thesis revealed that the Campo Felice fault is greater in length than the segment studied, as the throw-rate is greatest at the North-Western exposed tip of the fault. The study suggests that the North-Western tip of the Campo Felice fault is draped in scree, thus producing the appearance of a fault tip. The throw-rate maximum measured at this location means that it is likely that the fault continues for some distance beneath the scree to the North-West and that the active slip is transferred from this segment on to the en echelon segment to the West. The ability to generate throw-rate and strain-rate profiles for exposed faults enables the identification of true fault tips, by the characteristic tapering of throw-rate into the tip. Only once the surface expression of an exposed fault or surface rupture is shown to tip out at both its lateral extremities can the exposed length of the fault be considered a reliable measurement of fault or surface rupture length. Such validated measurements for fault length and rupture length (assuming characteristic earthquakes occur in which the entire fault length ruptures) can then be used to estimate maximum magnitude from the appropriate regression relationships (Fig. 6.2.1, box c). In cases where the magnitude of the earthquake is known, for instance in the case of the 2009 L'Aquila earthquake, validated rupture length and observed earthquake magnitude can be included in empirical databases to revise and improve the current regression relationships to take into account validated rupture length vs. magnitude. This approach represents an improvement of the content of the databases, rather than simply relying on an estimate

of rupture length from field studies where the distribution of throw has not been mapped to properly constrain the surface rupture length.

6.2.2. Assessing and correcting for near-field postseismic deformation in moderate magnitude paleoseismic offsets

The study of postseismic deformation along the L'Aquila surface rupture in Chapter 5 of this thesis has shown that significant surface deformation may occur postseismically in the near-field of a normal faulted surface rupture. This near-field postseismic deformation has not been routinely measured when normal faulted surface ruptures of recent and historical earthquakes are studied in the field. Paleoseismic studies measure normal fault offsets from earthquakes of unknown magnitude that are considered to be produced solely by coseismic slip; it is uncommon for a postseismic component of deformation to be considered. Earthquake magnitudes for those paleo-earthquakes are then estimated using the empirical relationships between coseismic slip and earthquake magnitude. These datasets in turn are defined from field studies of recent and historical earthquakes of known magnitude. However the effect may be assessed sometime after the earthquake once postseismic deformation has played out and it is not possible to separate it from the coseismic component of slip. Therefore there is a discrepancy in how field data has been used to define the empirical relationships and how field data is collected to measure coseismic paleoearthquake offsets. In the case of moderate magnitude normal faulting earthquakes (<M 6.5), where coseismic slip is mostly dissipated within the unconsolidated part of the fault zone, there exists potential for the ratio of near-field postseismic to coseismic deformation to be significant [Marone et al., 1991]. Hence it is suggested here that the disparity between measured coseismic offsets from recent

earthquakes and measurements of assumed coseismic-only fault offsets measured from paleoseismic investigations is likely to be greatest for moderate magnitude normal faulting earthquakes. Thus paleoseismic offsets for earthquakes of unknown, moderate magnitude are likely to be overestimated, through the unintentional inclusion of significant postseismic deformation, especially where assumed coseismic-only offsets may include off-fault deformation in the form of graben-type features. For example the paleoseismic study of the Ovindoli-Pazza fault in Central Italy [D'Addezio et al., 1996] revealed a complex morphology of offset sediments related to earthquake slip events which included significant off-fault deformation close to the main fault (Fig. 6.2.4). This off-fault deformation, in the form of graben features made the identification of coseismic offsets (and hence slip-rates) difficult, which increased the uncertainty of the slip-rate quoted in this study.

The over-estimation of coseismic offsets in paleoseismic studies could lead to an overestimation of paleoearthquake magnitudes that do not factor in significant postseismic deformation, in the case of moderate magnitude earthquakes (Fig. 6.2.2). The surveying of newly formed normal faulting surface ruptures using terrestrial laser scanning, as carried out in Chapter 5 of this thesis, allows near-field postseismic deformation to be quantified for moderate magnitude earthquakes. If a precise pre-earthquake datum existed for the rupture study site (i.e. a pre-earthquake TLS or large-scale airborne LiDAR dataset, or another form of topographic survey – GPS, total station etc.), the coseismic deformation could also be distinguished from the postseismic component, both in terms of magnitude of deformation, but also spatially in terms of distance from the surface rupture. Empirical relationships relating coseismic slip, near-field postseismic deformation and combined near-field coseismic and postseismic deformation for a given magnitude could be improved (Fig. 6.2.1,

box d). Once the ratio and spatial distribution of near-field coseismic to postseismic deformation is known for moderate magnitude events it will be possible to apply this knowledge to the measurement of suspected moderate magnitude paleoseismic slip events (Fig. 6.2.1, box b). The correct regression relationship can then be used to estimate earthquake magnitude dependant on whether the paleoseismic offset represents coseismic slip (i.e. use the current regression relationships, assumed to be based on measurement of coseismic offsets), or a suspected combination of coseismic slip and near-field postseismic deformation, based on paleo-offset morphology (i.e. use a revised version of the regression relationship, where postseismic deformation is combined with coseismic slip). In the case of the L'Aquila earthquake, it is estimated that the ratio of postseismic to coseismic deformation at study site PAG was ~60% (see Section 5.4.1). An example of the revised regression relationship for combined coseismic and postseismic offsets (i.e. the original coseismic offset measurements x1.67 to factor in the estimated postseismic component) is shown in figure 6.2.3. Using this revised regression, a paleoseismic offset measured at 0.5 m (Fig. 6.2.3, pink line) would have been produced by an earthquake of 6.45 Mw (Fig. 6.2.3, green line), whereas the original regression relationship would over predict the earthquake magnitude as 6.56 Mw (Fig. 6.2.3, orange line). Accounting for the presence of significant postseismic deformation in both paleoseismic trench offsets and regression relationships will reduce the uncertainty of magnitude estimation for moderate magnitude events.

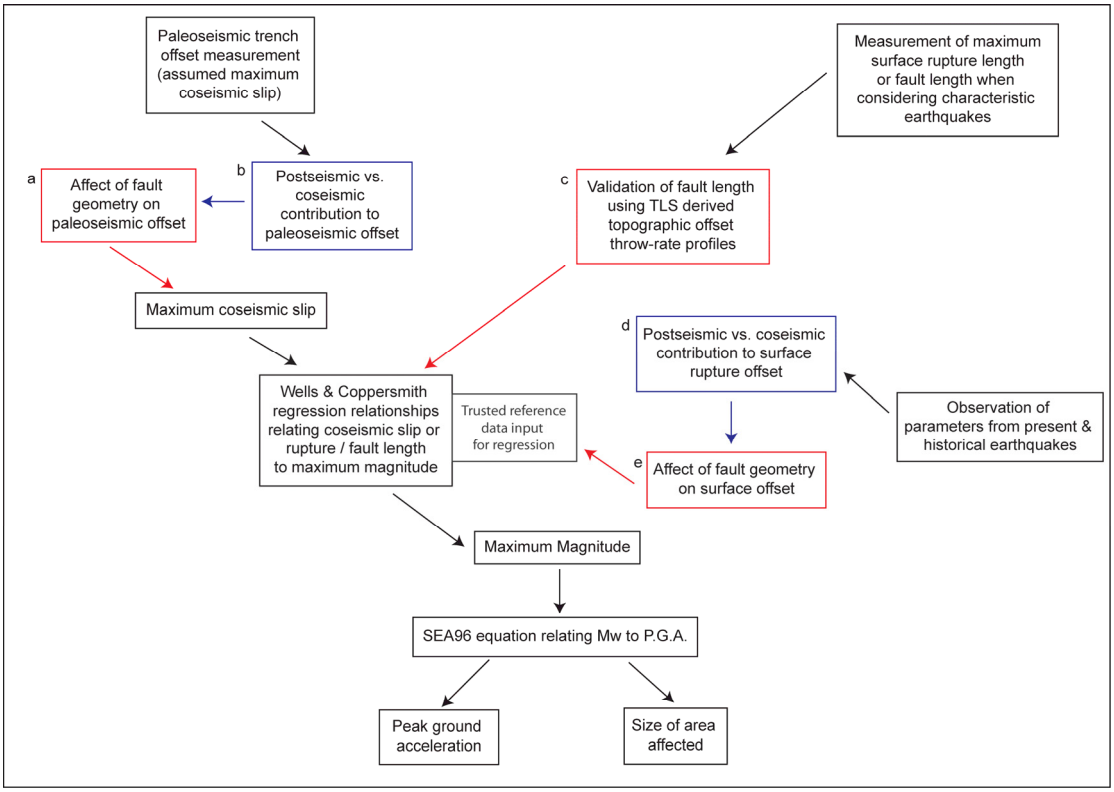

Figure 6.2.1: A flow chart summarising the process of obtaining peak ground acceleration and size of the affected area from a paleoseismic trench offset, a mapped surface rupture or the length of an exposed active fault. The red boxes are stages in the process which can be refined using the outcomes from Chapter 4 of this thesis. The blue boxes are stages in the process which can be refined using the outcomes from Chapter 5 of this thesis. The Wells & Coppersmith regression relationships refer to Wells & Coppersmith, 1994. SEA96 is an equation which relates earthquake moment magnitude to peak ground acceleration at distance from the fault, for normal faulting earthquakes [Spudich et al., 1997].

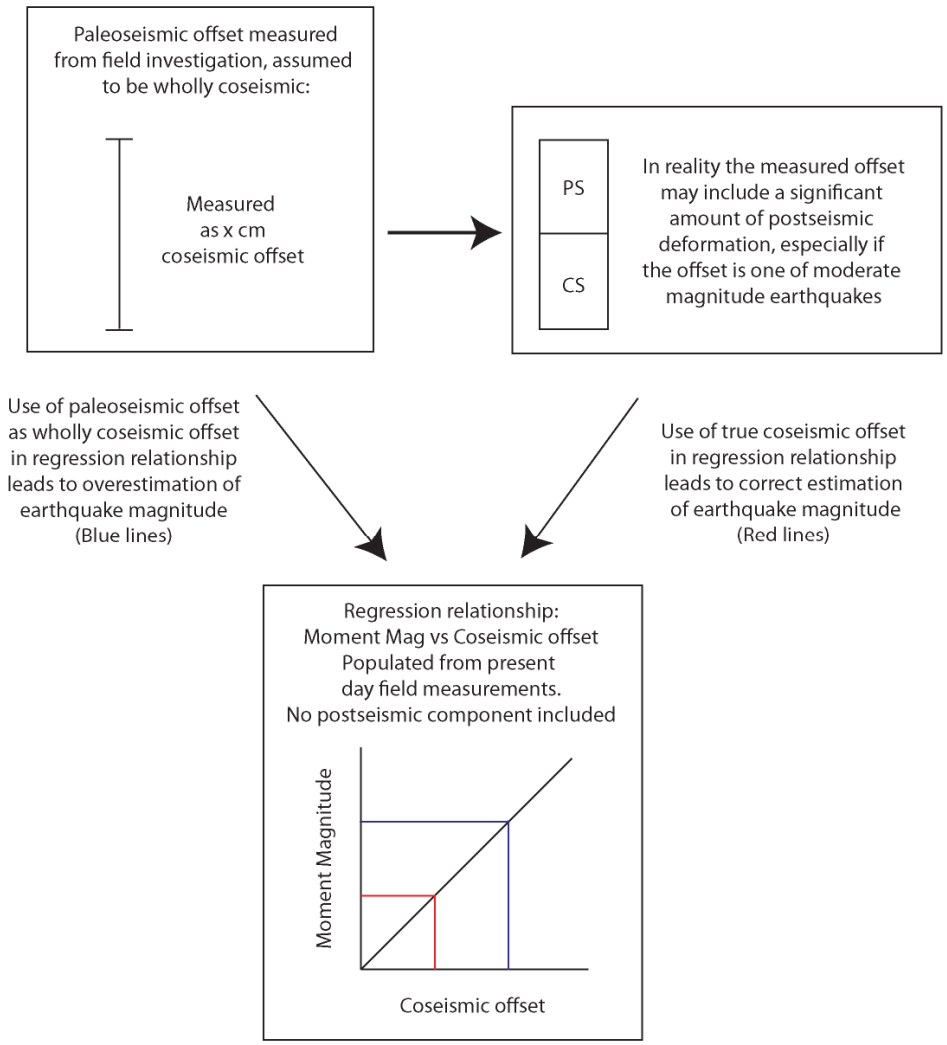

Figure 6.2.2: An illustration of the process leading to overestimation of paleoearthquake magnitudes from paleoseismic offsets which are assumed to be wholly coseismic.

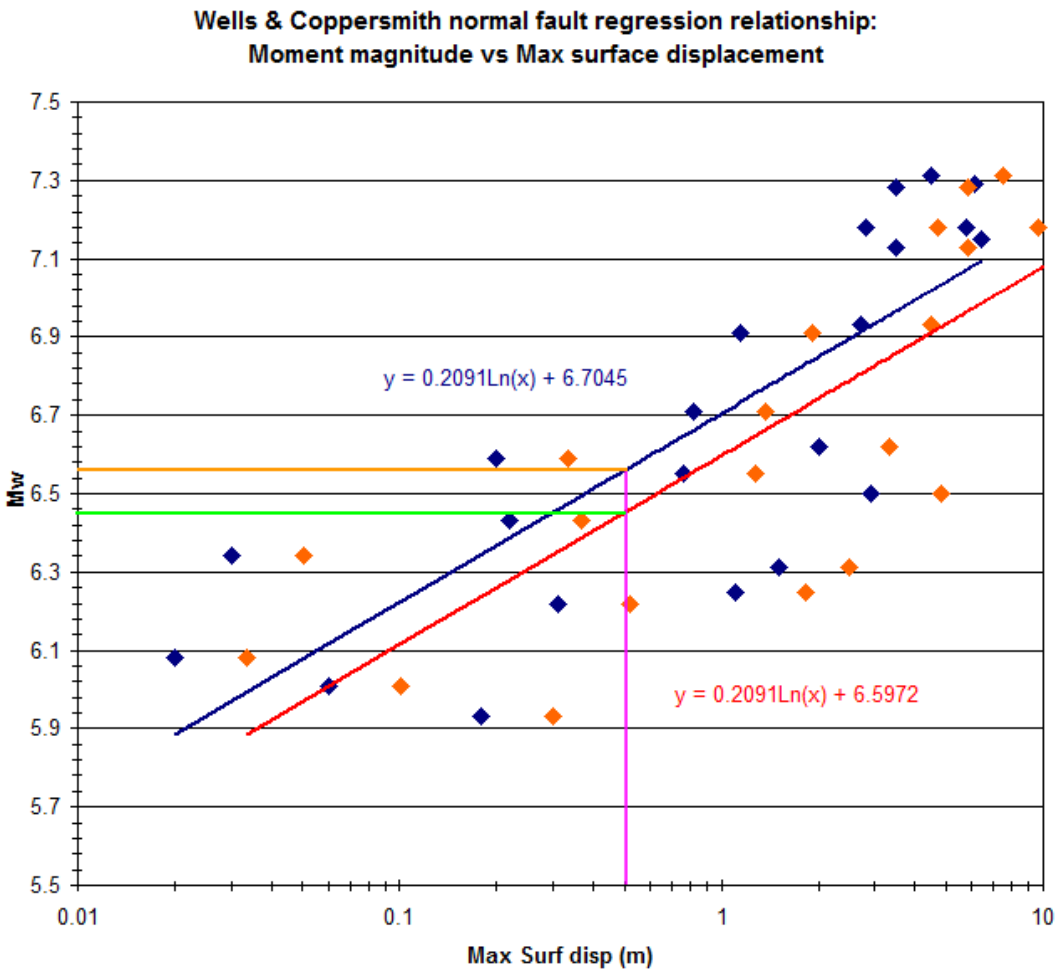

Figure 6.2.3: The Wells & Coppersmith (1994) regression relationship database used to estimate Moment magnitude from maximum suface offset, for earthquake of magnitude 5.5 – 7.5 Mw. The data and regression in blue represents the original data in the database, which is assumed to be field measurements of coseismic–only offsets. The data and regression in red represents an estimation of the combined coseismic and postseismic offset that would be observed for moderate magnitude earthquakes, using a coseismic – postseismic ratio of 1.67:1 (~60%). The regression in red would be more appropriate to estimate moment magnitude from paleoseismic offsets, where the components of coseismic and postseismic deformation cannot be distinguished. The pink line represents a paleoseismic offset measurement of 0.5 m. The original regression estimates the moment magnitude as 6.56 (orange line), whereas the revised

combined coseismic-postseismic regression reduces the moment magnitude to 6.45 (green line).

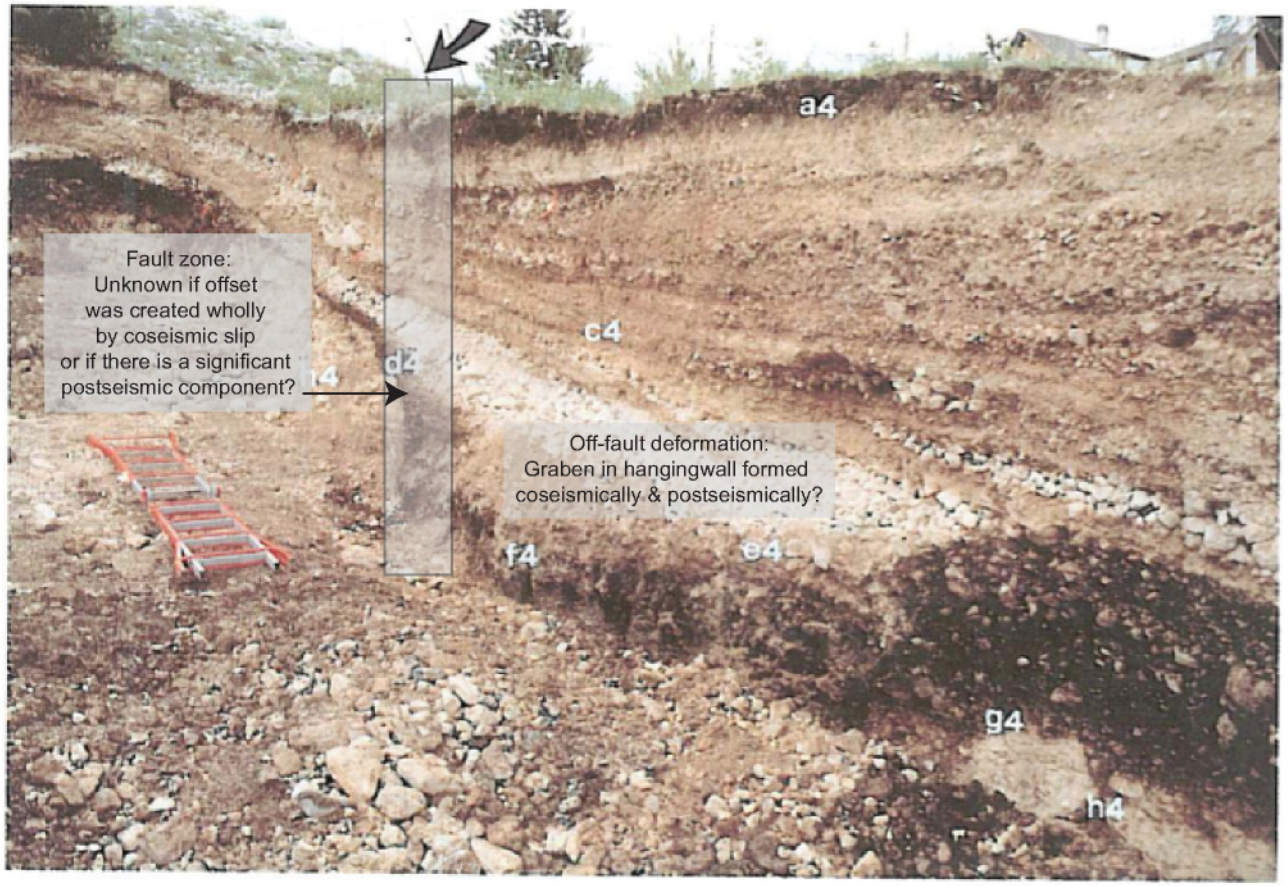

Figure 6.2.4: The trench wall of a paleoseismic study of the Ovindoli-Pezza normal fault in the central Apennines [D'Addezio et al., 1996]. The fault zone is denoted by the arrow. Note the graben which has formed in the hangingwall. The proximity of the graben, off-fault deformation to the fault zone makes it difficult to precisely distinguish on-fault coseismic offsets from off-fault postseismic deformation in such studies.

6.2.3. Future Work

The studies in the thesis demonstrate how fault geometry and postseismic slip may affect paleoearthquake offsets, however further work is needed to establish a robust set of relationships that can be applied to paleoseismic offsets that are created from a range of different earthquake magnitudes and in different field locations.

1. Further study of surface ruptures from present and future earthquakes with a focus on the ratio of coseismic to postseismic deformation, as well as the effect of changes in surface rupture / fault geometry on the magnitude of coseismic and postseismic deformation is required. The study of present and future earthquakes with this focus will eventually allow a new set of regression equations relating combined coseismic and postseismic deformation expected for various magnitudes. The investigation of changes in surface rupture and fault geometry would eventually allow a quantitative relationship between geometry (or deviation from mean strike) vs. expected surface rupture offset (coseismic and postseismic combined) to be defined. Only once these relationships are defined from a dataset consisting of many field studies spanning the range of earthquake magnitudes can they be considered robust enough to reduce uncertainty in the estimation of paleoearthquake magnitudes from the measurement of paleoseismic offsets.

2. The continued study of bedrock fault scarps, with offsets created over recent, multiple seismic cycles. Study of successive offsets is important for the definition of the characteristic behaviour of multiple earthquakes at the same

location on the same fault, as opposed to the study of single earthquakes, which may not be representative. Further work can be carried out to link fault geometry to smaller scale surface roughness of the fault and kinematics, for example fault asperities and corrugations. TLS can be used to analyse surface roughness and fault geometry on several scales. The further study of the effect of fault geometry on fault scarp offsets will allow for increased understanding of the effect of changes in fault geometry on size of single and multiple slip events. As well as how best to measure and define 'changes' in fault geometry. For instance, would it be best to compare local fault geometry at a study site to the mean geometry of the studied fault as a whole, or should the regional geometry of many faults be considered as the baseline from which to measure deviations in fault geometry? The use of ^{36}Cl exposure dating of fault scarps would also allow for increased understanding of the effect of fault geometry on the size of individual earthquake slip events by studing a single fault at multiple sites. Once the effect of fault geometry on size of slip event is known for a range of earthquake magnitudes / sizes of slip events, then a regression relationship can be refined which relates changes in fault geometry to the expected size of slip event. The study of changes in size of slip event with changing fault geometry will also provide information on how best to choose a paleoseismic study site on a fault that is likely to provide paleoearthquake offsets which best describe the overall activity of the entire fault. In contrast, poor site selection in a location with unusual or unrepresentative fault geometry would yield a distorted impression of the fault activity.

3. The observation that significant postseismic deformation occurs following moderate magnitude earthqukes is an important consideration for civil engineers and property insurers. Further work should be carried out to assess the impact of postseismic deformation on buildings and other infrastructure. It is an important concern that postseismic deformation is wrongly considered to be insignificant in magnitude. Such deformation occurs in a subtle manner over extended periods of time and so is likely to be overlooked or disreguarded in connection with the earthquake. It is suggested that significant effects on buildings and infrastucture from postseismic deformation should be expected and monitored over an extended period in order that any remedial work conducted by civil engineers or the assessment of claims against property insurers are appropriate.

6.3. Conclusion

The outcomes of field studies of recent and historical earthquakes, and studies of fault throw-rates over recent multiple seismic cycles can be used to improve our understanding of earthquake processes. In particular, the magnitude and distribution of coseismic and postseismic near-field earthquake surface deformation can be obtained from the study of recently formed surface ruptures. The effect that fault geometry may have on these deformations can be investigated through the measurement of throw-rates along faults over multiple seismic cycles. The creation of throw-rate profiles for normal faults also allow for the validation of maximum fault length (a proxy for maximum earthquake magnitude), through the identification of tapered throw at fault tips. The ability to investigate surface deformation of recent earthquakes provides important data for the refinement of empirical relationships for moderate magnitude events. This process in turn reduces the variability of maximum magnitude estimates from paleoseismic offsets through refined relationships between surface offset and earthquake magnitude and through an increased understanding of the spatial and temporal formation of the coseismic and postseismic components of surface deformation. The calculation of strain-rate profiles provide a more robust estimate of fault activity when compared with throw-rate, as throw-rate can be irregular and is affected by changes in fault geometry and direction of kinematic slip. By accounting for fault geometry in measurements of throw-rate, paleoseismic offsets and surface deformation following recent earthquakes, or by preferentially calculating strain-rate, it is possible to reduce the uncertainty of inferred maximum magnitudes. A reduction in the uncertainty of maximum magnitudes will in turn lead to improved seismic hazard analyses.

Chapter 7: Conclusions

1) Terrestrial laser scanning (TLS), combined with traditional field observations provides an extremely powerful and versatile tool for the earthquake geologist.

2) The ease of acquisition, spatial resolution and precision of TLS datasets enable the investigation of surface faulting to an unprecedented degree. The methods described within this thesis provide a basis for further studies.

   Specifically:

   (a) The analysis of topographic offsets, throw-rates and strain-rates over multiple seismic cycles and the effect of fault geometry on measurements of throw, for crustal scale normal faults, through the interpretation of TLS-derived cross sections.

   (b) The mapping of geomorphic features along active normal faults, such as landslips, footwall and hangingwall gullies and alluvial fans. Geomorphology of fault scarps provides important site characterisation for the selection of study sites for the interpretation of topographic offsets and paleoseismic study.

   (c) The measurement and monitoring of the magnitude, spatial and temporal distribution of near-field postseismic deformation using repeat collection of TLS datasets.

   (d) Traditional field observations, including the mapping of active faults and surface ruptures, and the collection of fault geometry and kinematic slip data. Such observations are essential prior to the collection of TLS data, as they provide irreplaceable direct observations and enable the proper planning required in order to design and implement successful TLS field surveys.

3) The study of Late Pleistocene fault offsets from a TLS dataset at twenty five geomorphically suitable study sites along the Campo Felice fault enabled the

creation of profiles of throw-rate and strain-rate. The collection of field data for kinematic slip direction and fault geometry enabled an investigation into the effect of fault geometry (deviation in strike from a dip-slip configuration) on throw-rates. The study found that a deviation in strike away from a dip-slip configuration increased the throw-rate at this section of the fault in relation to the rest of the fault. The dip of the fault and kinematic slip direction were shown to be consistent along the fault and so were ruled out as possible contributors to the changes in throw-rate. The study found that while throw-rate was irregular and affected by fault geometry, strain-rate was linear and decreased from the fault centre to the South-Eastern tip. A study of weathered bands, exposed on the fault scarp, that also increase in the section of the fault where the fault geometry changed significantly, was used to show that individual coseismic offsets and not just cumulative throw on the Campo Felice fault is also likely to be controlled by fault geometry.

4) The study of postseismic deformation using repeat terrestrial laser scanning following the 2009 L'Aquila earthquake revealed the rate, magnitude and distribution of near-field postseismic deformation at four sites along the surface rupture. The magnitude of postseismic deformation was found to be on the order of 60% that of the coseismic, for a site at the centre of the surface rupture. The postseismic deformation was mostly manifested as the formation of a broad depression in the hangingwall, which would not have been observed without the use of TLS. The study highlighted the need to consider postseismic deformation as a significant contributor to paleoseismic offsets for moderate magnitude events. The rate of decay of postseismic deformation was found to be comparable to theoretical and empirical models for afterslip, based

on parameters from previous earthquakes. The along fault distribution of postseismic deformation was found to correlate with regions of high coseismic slip gradient within the fault zone, suggesting that afterslip within the fault zone at the periphery of patches of coseismic slip were the driving mechanism for the postseismic deformations at the surface.

5) The outcome of the studies within this thesis were shown to directly affect the estimation of maximum magnitude of paleoseismic offsets, due to the effect fault geometry was shown to have on throw-rate and coseismic slip, as well as the observation that postseismic deformation for moderate magnitude earthquakes can form a significant proportion of the near-field offset observed and often assumed as coseismic slip in paleoseismic studies.

6) The uncertainty in paleoearthquake magnitude estimates can be reduced as follows:

(a) By reporting strain-rate instead of throw-rate.

(b) By correcting regression relationships used to estimate magnitude for a given offset.

(c) By accounting for the effects of fault geometry on paleoseismic offsets.

(d) By accounting for the significant amount of postseismic deformation present in surface deformation for moderate magnitude events.

7) The observation that significant postseismic deformation occurs following moderate magnitude earthqukes is an important consideration for civil engineers and property insurers. The work in this thesis has shown that postseismic deformation is a significant, but subtle and gradual process which is of sufficient magnitude to effect buildings and other infratructure. It is suggested that significant effects on buildings and infrastucture from

postseismic deformation should be expected and monitored over an extended period in order that any remedial work and the assessment of insurance claims are appropriate.

References

Amoruso, A. & Crescentini, L., 2009. Slow diffusive fault slip propagation following the 6 April 2009 L'Aquila earthquake, Italy, *Geophys. Res. Lett.*, 36, L24306.

Arrowsmith, R., Haddad, D. E., Akciz, S. O., Oldow, J. S., Mauer, J. & Rhodes, D. D., 2009. Terrestrial Laser Scanning Applications in Paleoseismology (Invited). *American Geophysical Union, Fall Meeting 2009*, abstract #G53E-08

Atzori, S., Hunstad, I., Chini, M., Salvi, S., Tolomei, C., Bignami., Stramondo, S., Trasatti, E., Antonioli, A. & Boschi, E., 2009. Finite fault inversion of DInSAR coseismic displacement of the 2009 L'Aquila earthquake (central Italy). *Geophys. Res. Lett.*, 36, L15305.

Bakun, W. H., Aagaard, B., Dost, B., Ellsworth, W. L., Hardebeck, J. L., Harris, R. A., Ji, C., Johnston, M. J. S., Langbein, J., Lienkaemper, J. J., Michael, A. J., Murray, J. R., Nadeau, R. M., Reasenberg, P. A., Reichle, M. S., Roeloffs, E. A., Shakal, A., Simpson, R. W. & Waldhauser, F., 2005. Implications for prediction and hazard assessment from the 2004 Parkfield earthquake, *Nature*, 437, 969–974.

Basili, R., Valensise, G., Vannoli, P.., Burrato, P., Fracassi, U., Mariano, S., Tiberti, M. M. & Boschi, E., 2008. The Database of Individual Seismogenic Sources (DISS), version 3: Summarizing 20 years of research on Italy's earthquake geology. *Tectonophysics*, 453, 20-43.

Beauprêtre, S., Garambois, S., Manighetti, I., Malavieille, J., Sénéchal, G., Chatton, M., Davies, T., Larroque, C., Rousset, D., Cotte, N. & Romano, C, 2012. Finding the buried record of past earthquakes with GPR-based palaeoseismology: a case study on the Hope fault, New Zealand. *Geophys. J. Int.*, 189, 2012.

Bell, R., McNeill, L. C., Henstock, T. J. & Bull, J. M., 2011. Comparing extension on multiple time and depth scales in the Corinth Rift, Central Greece. Bell, R, *Geophys. J. Int.*, 186, 463-470.

Boncio, P., Pizzi, A., Brozzetti, F., Pomposo, G., Lavecchia, G., Di Naccio, D. & Ferrarini, F., 2010. Coseismic ground deformation of the 6 April 2009 L'Aquila earthquake (central Italy, Mw6.3). *Geophys. Res. Lett.*, 37, L06308.

Bubeck, A., 2009. A study of Subsurface Geology of the Tre Monti and Fiamignano Fault Using Ground Penetrating Radar and Seismic Refraction Surveying Techniques. *MSci thesis, University College London.*

Bubeck, A, Vsemirnova, K., Jones, R. & Wilkinson, M. Combining Ground Penetrating Radar and Terrestrial LiDAR to produce 3D Virtual Outcrop Models. In prep. (a).

Bubeck, A., Wilkinson, M., Roberts, G. P., McCaffrey, K. J. W., Phillips, R., Cowie, P. A. & Sammonds, P., submitted. The tectonic geomorphology of bedrock scarps on active normal faults in the Italian Apennines mapped using combined ground

penetrating radar and terrestrial laser scanning. *Geomorphology special issue 'Geomorphology of Active faults'*.

Bucknam, R. C., Plafker, G. & Sharp, R. V., 1978. Fault movement (afterslip) following the Guatemala earthquake of February 4, 1976, *Geology*, 6, 170–173.

Bull, J. M., Barnes, P. M., Lamarche, G., Sanderson, D. J., Cowie, P. A., Taylor, S. K. & Dix, J. K., 2006. High-resolution record of displacement accumulation on an active normal fault: implications for models of slip accumulation during repeated earthquakes. *J. Struct. Geol.*, 28 (7), 1146-1166.

Cheloni, D. D'Agostino, N., D'Anastasio, E., Avallone, A., Mantenuto, S., Giuliani, R., Mattone, M., Calcaterra, S., Gambino, P., Dominici, D., Radicioni, F. & Fastellini, G., 2010. Coseismic and initial post-seismic slip of the 2009 M-w 6.3 L'Aquila earthquake, Italy, from GPS measurements. *Geophys. J. Int.,* 181 (3)*,* 1539-1546.

Childs, C., Watterson, J. & Walsh, J. J., 1995. Fault overlap zones within developing normal fault systems. *J Geol Soc London*, 152, 535-549.

Childs, C., Nicol, A., Walsh, J. J. & Watterson, J., 2003. The growth and propagation of synsedimentary faults. *J. Struct, Geol.*, 25, 633-648.

Cinti, F. R., Pantosti, D., De Martini, P. M., Pucci, S., Civico, R., Pierdominici, S., Cucci, L., Brunori, C. A., Pinzi, S. & Patera A., 2011. Evidence for surface faulting

events along the Paganica fault prior to the 6 April 2009 L'Aquila earthquake (central Italy). *J. Geophys. Res.*, 116, B07308.

Cowie, P. A. & Shipton, Z. K., 1998. Fault tip displacement gradients and process zone dimensions. *J. Struct. Geol.*, 20, 983 – 997.

CPTI Working Group, 2004. Catalogo Parametrico dei Terremoti Italiani, vers. 2004 (CPTI04). INGV, Bologna. Available at http://emidius.mi.ingv.it/CPTI/home.html

Crosby, C. J., Krishnan, S., Arrowsmith, J. R., Kim, H. S., Colunga, J., Alex, N. & Baru, B, in review. Points2Grid: An Efficient Local Gridding Method for DEM Generation from Lidar Point Cloud Data. *Geosphere special issue on Applications of Lidar in the Earth Sciences.*

D'Addezio, G., Pantosti, D. & De Martini, P. M., 1996. Palaeoseismologic and geomorphic investigations along the middle portion of the Ovindoli ‐ Pezza Fault (Central Italy), *Ann. Geofis.*, 39, 663–675.

D'Agostino, N., Mantenuto, S., D'Anastasio, E., Giuliani, R., Mattone, M., Calcaterra, S., Gambino, P. & Bonci, L., 2011. Evidence for localized active extension in the central Apennines (Italy) from global positioning system observations. *Geology*, 39, 291-294.

Dawers, N. H., Anders, M. H. & Scholz, C. H., 1993. Growth of normal faults: Displacement-length scaling. *Geology,* 21, 1107-1110.

Degasperi, M., 2010. Relazione sui monitoraggi nella zona di Paganica. Provincia Autonoma di Trento, Servizio Geologico, Report Marzo 2010. http://www.protezionecivile.tn.it/geologico/images/Notizie2010/abruzzo/report_03_2010+ALL.pdf

Delaunay, B., 1934. Sur la sphère vide, Izvestia Akademii Nauk SSSR, Otdelenie Matematicheskikh i Estestvennykh Nauk, 7, 793–800.

Densmore, A. L., Dawers, N. H., Gupta, S., Allen, P. A. & Gilpin, R., 2003. Landscape evolution at extensional relay zones. *J. Geophys. Res.*, 108, B5, 2273.

Emergeo Working Group, 2010. Evidence for surface rupture associated with the Mw 6.3 L'Aquila earthquake sequence of April 2009 (central Italy), *Terra Nova*, 22, 43–51.

Falcucci, E., Gori, S., Peronace, E., Fubelli, G., Moro, M., Saroli, M., Giaccio, B., Messina, P., Naso, G., Scardia, G., Sposato, A., Voltaggio, M., Galli, P. & Galadini, F., 2009. The Paganica Fault and Surface Coseismic Ruptures Caused by the 6 April 2009 Earthquake (L'Aquila, Central Italy). *Seismol. Res. Lett., 80 (6),* 940-950.

Faure Walker, J. P., Roberts, G. P., Cowie, P. A., Papanikolaou, I., Sammonds, P. R., Michetti, A. M. & Phillips, R. J., 2009. Horizontal strain-rates and throw-rates across breached relay zones, central Italy: Implications for the preservations of throw deficits at points of normal fault linkage. *J. Struct. Geol.*, 31, 1145-1160.

Faure Walker, J. P., Roberts, P. A., Sammonds, P. R. & Cowie, P., 2010. Comparison of earthquake strains over 10^2 and 10^4 year timescales: Insights into variability in the seismic cycle in the central Apennines, Italy. *J. Geophys. Res.*, 115, B10418.

Faure Walker, J. P., Roberts, G. P., Cowie, P. A., Papanikolaou, I., Michetti, A. M., Sammonds, P., Wilkinson, M., McCaffrey, K. J. W. & Phillips, R., 2012. Relationship between topography, rates of extension and mantle dynamics in the actively-extending Italian Apennines. *Earth Planet. Sc. Lett*., 325-326, 76-84.

Ferry, M., Meghraoui, M., Girard, J. F., Rockwell, T. K., Kozaci, O., Akyuz, S. & Barka, A., 2004. Ground-penetrating radar investigations along the North Anatolian fault near Izmit, Turkey: Constraints on the right-lateral movement and slip history. *Geology,* 32, 85-88.

Freed, A. M., 2007. Afterslip (and only afterslip) following the 2004 Parkfield, California, earthquake. *Geophys. Res. Lett.*, 34, L06312.

Galadini, F. & Galli, P., 2000. Active Tectonics in the Central Apennines (Italy) – Input Data for Seismic Hazard Assessment, *Nat. Hazards*, 22, 225-270.

Galli, P., Galadini, F., Moro, M. & Giraudi, C., 2002. New palaeoseismological data from the Gran Sasso d'Italia area (cental Apennines), *Geophys. Res. Lett.*, 29(7), 1134.

Galli, P., Galadini, F. & Pantosti, D., 2008. Twenty years of Palaeoseismology in Italy, *Earth Sci. Rev.*, 88, 89–117.

Galli, P., Giaccio, B. & Messina, P., 2010. The 2009 central Italy earthquake seen through 0.5 Myr-long tectonic history of the L'Aquila faults system. *Quaternary Sci. Rev.*, 29, 3768-3789.

Giaccio, B., Galadini, F., Sposato, A., Messina, P., Moro, M., Zreda, M., Cittadini, A., Salvi, S. & Todero, A., 2002. Image processing and roughness analysis of exposed bedrock fault planes as a tool for paleoseismological analysis: results from the Campo Felice fault (central Apennines, Italy), *Geomorphology*, 49, 281-301.

Giraudi, C. & Frezzotti, M., 1997. Late Pleistocene Glacial Events in the Central Apennines, Italy. *Quaternary Res.*, 48, 280-290.

Giraudi, C., Bodrato, G., Lucchi, M. R., Cipriani, N., Villa, I. M., Giaccio, B. & Zuppi, G. M., 2011. Middle and late Pleistocene glaciations in the Campo Felice Basin (central Apennines, Italy). *Quaternary Res.,* 75, 219-230.

Gold, P. O., Cowgill, E., Kreylos, O. & Gold, R. D., 2012. A terrestrial lidar-based workflow for determining three–dimensional slip vectors and associated uncertainties. *Geosphere*, 8, 431-442.

Hunstad, I., Selvaggi, G., D'Agostino, N., England, P., Clarke, P. & Pierozzi, M., 2003. Geodetic strain in peninsular Italy between 1875 and 2001. *Geophys. Res. Lett.*, 30, 1181.

Imber, J., Childs, C., Nell, P. A. R., Walsh, J. J., Hodgetts, D. & Flint, S., 2003. Hanging wall fault kinematics and footwall collapse in listric growth fault systems. *J. Struct. Geol.*, 25, 197-208.

Isenberg, M. & Shewchuk, J. LAStools: converting, viewing, and compressing LIDAR data in LAS format. http://www.cs.unc.edu/~isenburg/lastool

Kirby, E., Whipple, K. X., Tang, W. & Chen, Z., 2003. Distribution of active rock uplift along the eastern margin of the Tibetan Plateau: Inferences from bedrock channel longitudinal profiles. *J. Geophys. Res.*, 108, B4, 2217.

Koukouvelas, I. K. & Doutsos, T. T., 1996. Implications of structural segmentation during earthquakes: the 1995 Egion Earthquake, Gulf of Corinth, Greece, *J. Struct. Geol.*, 18, 1381–1388.

Lanari, R., Berardino, P., Bonano, M., Casu, F., Manconi, A., Manunta, M., Manzo, M., Pepe, A., Pepe, S., Sansosti, E., Solaro, G., Tizzani, P. & Zeni, G., 2010. Surface displacements associated with the L'Aquila 2009 Mw 6.3 earthquake (central Italy): New evidence from SBAS-DInSAR time series analysis. *Geophys. Res. Lett.*, 37, L20309.

Langbein, J., Murray, J. R. & Snyder, H. A., 2006. Coseismic and Initial Postseismic Deformation from the 2004 Parkfield, California, Earthquake, Observed by Global Positioning System, Electronic Distance Meter, Creepmeters, and Borehole Strainmeters. *B. Seis. Soc. Am.*, 96, 304-320.

Lee, J., Rubin, C. M. & Calvert, A., 2001. Quaternary faulting history along the Deep springs fault, California. *Geol. Soc. Am. Bull.*, 113, 855-869.

Lee, J. C., Chu, H. T., Angelier, J., Hu, J. C., Chen, H. Y. & Yu, S. B., 2006. Quantitative analysis of surface coseismic faulting and postseismic creep accompanying the 2003, M_w = 6.5, Chengkung earthquake in eastern Taiwan. *J. Geophys. Res.*, 111, B02405.

Maerten, L., Pollard, D. D. & Maerten, F., 2001. Digital mapping of three-dimensional structures of the Chimney Rock fault system, central Utah. *J. Struct. Geol.*, 23, 585-592.

Mallet, J. L., 1992. *GOCAD*: A computer aided design program for geological applications, in Three Dimensional Modeling With Geoscientific Information Systems, edited by A. K. Turner, pp. 123–141, Kluwer, Netherlands.

Manighetti, I., Campillo, M., Sammis, C., Mai, P. M. & King, G., 2005. Evidence for self-similar, triangular slip distributions on earthquakes: Implications for earthquake and fault mechanics. *J. Geophys. Res.*, 110, B05302.

Mansfield, C. S. & Cartwright, J. A., 1996. High resolution fault displacement mapping from three-dimensional seismic data: evidence for dip linkage during fault growth. *J. Struct. Geol.*, 18, 249-263.

Marone, C., 1998. Laboratory-Derived Friction Laws and Their Application to Seismic Faulting. *Annu. Rev. Earth Planet. Sci.* 26, 643–96.

Marone, C. J., Scholtz, S. H. & Bilham, R., 1991. On the mechanics of Earthquake Afterslip. *J. Geophys. Res. B: Solid Earth*, 96, 8441-8452.

McCaffrey, K. J. W., Jones, R. R., Holdsworth, R. E., Wilson, R. W., Clegg, P., Imber, J., Holliman, N. & Trinks, I., 2005. Unlocking the spatial dimension: digital technologies and the future of geoscience fieldwork. *J Geol Soc London,* 162(6): 927-938.

McLoed, A. E., Dawers, N. H. & Underhill, J. R., 2000. The propagation and linkage of normal faults: insights from the Strathspey-Brent-Statfjord fault array, northern North Sea. *Basin Research,* 12, 263-284.

Michetti, A. M., Brunamonte, F., Serva, L. & Vittori, E., 1996. Trench investigations of the 1915 Fucino earthquake fault scarps (Abruzzo, central Italy): Geological evidence of large historical events. *J. Geosphys. Res.*, 101, 5921-5936.

Michetti, A. M., Serva, L. & Vittori, E., 2000. Italy hazard from Capable Faulting, a database of active capable faults of the Italian onshore territory [CD - ROM], report, Agenzia Nazionale Protezione Ambiente, Rome.

Moretti, I., Sakellariou, D., Lykousis, V. & Micarelli, L., 2003. The Gulf of Corinth: an active half graben? *J. Geodyn.*, 36, 323-340.

Morewood, N. C. & Roberts, G. P., 2000. The geometry, kinematics and rates of deformation within an en echelon normal fault segment boundary, central Italy. *J. Struct. Geol.*, 22, 1027-1047.

Mouslopoulou, V., Walsh, J. J. & Nicol, A., 2009. Fault displacement rates on a range of timescales. *Earth Planet. Sc. Lett.*, 278, 186-197.

Muraoka, H. & Kamata, H., 1983. Displacement distribution along minor fault traces. *J. Struct. Geol.,* 5, 483-495.

O'Callaghan, J. F. & Mark, D. M., 1984. The Extraction of Drainage Networks From Digital Elevation Data. *Computer Vision, Graphics and Image Processing*, 28, 328-344.

Oldow, J. S. & Singleton, E. S., 2008. Application of Terrestrial Laser Scanning in determining the pattern of late Pleistocene and Holocene fault displacement from the offset of pluvial lake shorelines in the Alvord extensional basin, northern Great Basin, USA. *Geosphere*, 4, 536-563.

Oskin, M. E., Arrowsmith, J. R., Corona, A. H., Elliott, A. J., Fletcher, J. M., Fielding, E. J., Gold, P. O., Garcia, J. J. G., Hudnut, K. W., Lui-Zeng, J. & Teran, O., 2012. Near-Field Deformation from the El Mayor–Cucapah Earthquake Revealed by Differential LIDAR. *Science*, 335, 702-705.

Pace, B., Peruzza, L., Lavecchia, G. & Boncio, P., 2006. Layered Seismogenic Source Model and Probabilistic Seismic-Hazard Analyses in Central Italy. *B. Seis. Soc. Am.*, 96, 107-132.

Palumbo, L., Benedetti, L., Bourles, D., Cinque, A. & Finkel, R., 2004. Slip history of the Magnola fault (Apennines, Central Italy) from 36Cl surface exposure dating: evidence for strong earthquake over the Holocene. *Earth Planet. Sc. Lett.*, 225, 163–176.

Pantosti, D., D'Addezio, G. & Cinti, F. R., 1996. Palaeoseismicity of the Ovindoli‐Pezza fault, central Apennines, Italy: A history including a large, previously unrecorded earthquake in the Middle Ages (860–1300 A.D.), *J. Geophys. Res.*, 101, 5937–5959.

Papanikolaou, I. D. & Roberts, G. P., 2007. Geometry, kinematics and deformation rates along the active normal fault system in the Southern Apennines: Implications for fault growth. *J. Struct. Geol.*, 29, 166–188.

Papanikolaou, I., Roberts, G. P. & Michetti, A. M., 2005. Fault scarps and deformation rates in Lazio–Abruzzo, Central Italy: Comparison between geological fault slip-rate and GPS data. *Tectonophysics,* 408, 147-176.

Papanikolaou, I. D., Foumelis, M., Parcharidis, I., Lekkas, E. L. & Fountoulis, I. G., 2010. Deformation pattern of the 6 and 7 April 2009, MW=6.3 and MW=5.6 earthquakes in L'Aquila (Central Italy) revealed by ground and space based observations, *Nat. Hazards Earth Syst. Sci.*, 10, 73-87.

Patacca, E., Sartori, R. & Scandone, P., 1990. Tyrrhenian Basin and Apenninic Arcs: kinematic relations since late Tortonian times. *Mem. Soc. Geol. It*. 45, 425–451.

Peacock, D. C. P. & Sanderson, D. J. 1991. Displacements, segment linkage and relay ramps in normal fault zones. *J. Struct. Geol.*, 13, 721-733.

Peruzza, L., Pace, B. & Cavallini, F., 2010. Error propagation in time-dependent probability of occurrence for characteristic earthquakes in Italy. *J. Seismol.*, 14, 119-141.

Pritchard, M. E. & Simons, M., 2004. An InSAR-based survey of volcanic deformation in the central Andes, *Geochem. Geophys. Geosyst.,* 5, Q02002.

Reicherter, K., Kaiser, A. & Stackebrandt, W., 2005. The post-glacial landscape evolution of the North German Basin: morphology, neotectonics and crustal deformation. *Int. J. Earth. Sci.* 94, 1083-1093.

Roberts, G. P., 1996a. Variation in slip directions along normal fault systems. *J. Struct. Geol.*, 18, 835 – 845.

Roberts, G. P., 1996b. Noncharacteristic normal faulting surface ruptures from the Gulf of Corinth, Greece. *J. Geophys. Res.*, 101, 25255 – 25267.

Roberts, G. P., Cowie, C., Papanikolaou, I. & Michetti, A. M., 2004. Fault scaling relationships, deformation rates and seismic hazards: an example from the Lazio–Abruzzo Apennines, central Italy. *J. Struct. Geol.*, 26, 377-398.

Roberts, G. P. & Michetti, A. M., 2004. Spatial and temporal variations in growth rates along active normal fault systems: an example from The Lazio-Abruzzo Apennines, central Italy. *J. Struct. Geol.*, 26, 339-376.

Roberts, G. P., 2006. Multi-seismic cycle velocity and strain fields for an active normal fault system, central Italy. *Earth Planet. Sc. Lett.*, 251, 44-51.

Roberts, G. P., 2008. Vizualisation of active normal fault scarps in the Apennines, Italy: A key to assessment of tectonic strain release and earthquake rupture, in *Google Earth Science*, edited by D. DePaor, *J. Virtual Explorer,* 30(4).

Roberts, G. P., Raithatha, B., Sileo, G., Pizzi, A., Pucci, S., Faure Walker, J., Wilkinson, M., McCaffrey, K., Phillips, R. J., Michetti, A. M., Guerrieri, L., Blumetti, A. M., Vittori, E., Cowie, P., Sammonds, P., Galli, P., Boncio, P., Bristow, P. &

Walters., R., 2010. Shallow subsurface structure of the 2009 April 6 M w 6.3 L'Aquila earthquake surface rupture at Paganica, investigated with ground-penetrating radar, *Geophys. J. Int.*, 183, 774-790.

Rockwell, T., Ragona, D., Seitz, G., Langridge, R., Aksoy, M. E., Ucarkus, G., Ferry, M., Meltzner, A. J., Klinger, Y., Meghraoui, M., Satir, D., Barka, A. & Akbalik, B., 2009. Palaeoseismology of the North Anatolian Fault near the Marmara Sea: implications for fault segmentation and seismic hazard. From: Reicherter, K., Michetti, A. M. & Silva P. G. (eds) Palaeoseismology: Historical and Prehistorical Records of Earthquake Ground Effects for Seismic Hazard Assessment. *The Geological Society, London, Special Publications*, 316, 31–54.

Ryder, I., Parsons, B., Wright, T. J. & Funning, G. J., 2007. Postseismic motion following the 1997 Manyi (Tibet) earthquake: InSAR observations and modeling, *Geophys. J. Int.*, 169, 1009–1027.

Schlagenhauf, A., Gaudemer, Y., Benedetti, L., Manighetti, I., Palumbo, L., Schimmelpfennig, I., Finkel, R. & Pou, K., 2010. Using in situ Chlorine-36 cosmonuclide to recover past earthquake histories on limestone normal fault scarps: a reappraisal of methodology and interpretations. *Geophys. J. Int.*, 182, 36-72.

Schlagenhauf, A., Manighetti, I., Benedetti, L., Gaudemer, Y., Finkel, R., Malavieille, J. & Pou, K. 2011. Earthquake supercycles in Central Italy, inferred from ^{36}Cl exposure dating. *Earth Planet. Sc. Lett.*, 307, 487-500.

Scholz, C. H., 1990. The Mechanics of Earthquakes and Faulting, Cambridge Univ. Press, New York.

Serpelloni, E., Anzidei, M., Baldi, P., Casula, G. & Galvani, A., 2005. Crustal velocity and strain-rate fields in Italy and surrounding regions: new results from the analysis of permanent and non-permanent GPS networks. *Geophys. J. Int.*, 161, 861-880.

Sharp, R. V., Budding, K. E., Boatwright, J., Ader, M. J., Bonilla, M. G., Clark, M. M., Fumal, T. E., Harms, K. K., Lienkaimper, J. J., Morton, D. M., O'Neill, B. J., Ostergren, C. L., Ponti, D. J., Rymer, M. J., Saxton, J. L. & Sims, J. D., 1989. Surface faulting along the Superstition Hills fault zone and nearby faults associated with the earthquakes of 24 November 1987, *B. Seismol. Soc. Am.*, 79, 252–281.

Smith, S. W. & Wyss, M. 1968. Displacement on the San Andreas fault initiated by the 1966 Parkfield earthquake. *B. Seismol. Soc. Am.,* 58, 1955-74.

Spudich, P., Fletcher, J. B., Hellweg, M., Boatwright, J., Sullivan, C., Joyner, W. B., Hanks, T. C., Boore, D. M., McGarr, A., Baker, L. M. & Lindh, A. G., 1997. SEA96--A New Predictive Relation for Earthquake Ground Motions in Extensional Tectonic Regimes, *Seis. Res. Let.*, 68, 190-198.

Sylvester, A. G., 1993. Investigation of the nearfield postseismic slip following the Mw 7.3 Landers earthquake sequence of 28 June 1992, California. *Geophys. Res. Lett.*, 20, 1079-1082.

Tucker, G. E., McCoy, S. W., Whittaker, A. C., Roberts, G. P., Lancaster, S. T. & Phillips, R., 2011. Geomorphic significance of postglacial bedrock scarps on normal-fault footwalls. *J. Geophys. Res.*, 116, F01022.

Vigny, C., Simons, W. J. F., Abu, S., Bamphenyu, R., Satirapod, C., Choosakul, N., Subarya, C., Socquet, A., Omar, K., Abidin, H. Z. & Ambrosius, B. A. C., 2005. Insight into the 2004 Sumatra–Andaman earthquake from GPS measurements in southeast Asia, *Nature*, 436, 201–206.

Vittori, E., Di Manna, P., Blumetti, A. M., Comerci, V., Guerrieri, L., Esposito, E., Michetti, A. M., Porfido, S., Piccardi, L., Roberts, G. P., Berlusconi, A., Livio, F., Sileo, G., Wilkinson, M., McCaffrey, K. J. W., Phillips, R. J. & Cowie, P. A., 2011. Surface faulting of the April 6th 2009 Mw 6.3 L'Aquila earthquake in central Italy. *B. Seismol. Soc. Am.,* 101, 1507-1530.

Walsh, J. J. & Watterson, J., 1987. Distributions of cumulative displacement and seismic slip on a single normal fault surface. *J. Struct. Geol.*, 9, 1039-1046.

Walters, R. J., Elliott, J. R., D'Agostino, N., England, P. C., Hunstad, P. C., Jackson, J. A., Parsons, B., Phillips, R. J. & Roberts, G., 2009. The 2009 L'Aquila earthquake (central Italy): A source mechanism and implications for seismic hazard. *Geophys. Res. Lett*., 36, L17312.

Wells, D. L. & Coppersmith, K. J., 1994. New empirical relationships among magnitude, rupture length, rupture width, rupture area and surface displacement, *B. Seismol. Soc. Am.*, 84, 974–1002.

Wilkinson, M., McCaffrey, K. J. W., Roberts, G., Cowie, P. A., Phillips, R. J., Michetti, A. M., Vittori, E., Guerrieri, L., Blumetti, A. M., Bubeck, A., Yates, A. & Sileo, G., 2010. Partitioned postseismic deformation associated with the 2009 Mw 6.3 L'Aquila earthquake surface rupture measured using a terrestrial laser scanner, *Geophys. Res. Lett.*, 37*,* L10309.

Wilkinson, M. W., McCaffrey, K. J. W., Roberts, G. P., Cowie, P. A., Phillips, R. J., Degasperi, M., Vittori, E. & Michetti, A. M., 2012. Distribution and Magnitude of Postseismic Deformation of the 2009 L'Aquila Earthquake (M6.3) Surface Rupture Measured Using Repeat Terrestrial Laser Scanning, *Geophys. J. Int.*, 189, 911-922.

Williams, P. L. & Magistrale, H. W., 1989. Slip along the Superstition Hills fault associated with the 24 November 1987 Superstition Hills, California, Earthquake, *B. Seismol. Soc. Am.*, 79, 390–410.

Young, M. J., Gawthorpe, R. L. & Hardy, S, 2001. Growth and linkage of a segmented normal fault zone: the Late Jurassic Murchison-Statfjord North Fault, northern North Sea. *J. Struct. Geol.*, 23, 1933-1952.

Zielke, O., Arrowsmith, J. R., Ludwig, L. G. & Akçiz, S. O., 2010. Slip in the 1987 and Earlier Large Earthquakes Along the Carrizo Plain, San Andreas Fault. *Science*, 327, 1119-1122.

Appendixes

Appendix (i)

img2points code, written for GNU/octave

```
function img2points()

clc

disp("------------------------------------------------------------------------")
disp("|                          img2points v1.0                             |")
disp("|    A program to convert GPR trace images to XYZRGB pointsets        |")
disp("| written by Max Wilkinson - Dept. Earth Sciences, Durham University |")
disp("|               email: maxwell.wilkinson@durham.ac.uk                 |")
disp("------------------------------------------------------------------------")
disp("\n")

disp("-------------------------------------------------------------------------------")
input_file = input("Please enter the name of the input GPR trace image, including the
file extension: \n", "");
disp("-------------------------------------------------------------------------------\n")

I = imread(input_file); % Read in the image file as a 3D matrix (2D based on image
pixels + R,G,B channels)

v_scale = input("Please enter the vertical pixel spacing from the input image, as a
distance in meters.\nFor example if 100 pixels occupy 10 meters on your vertical
scale, enter 0.1 as the pixel spacing': \n", "");
disp("-------------------------------------------------------------------------\n")

v_scale = str2num(v_scale); % Convert keybaord input string to a number

h_scale = input("Please enter the horizontal pixel spacing from the input image, as a
distance in meters.\nFor example if 100 pixels occupy 10 meters on your horizontal
scale, enter 0.1 as the pixel spacing': \n", "");
disp("-------------------------------------------------------------------------\n")

h_scale = str2num(h_scale); % Convert keyboard input string to a number
```

```
x_pos = input("Please enter the easting coordinate (x) in UTM meters which corresponds to the position of the GPR at the far left of the input image:\n", "");
disp("--------------------------------------------------------------------------\n")

y_pos = input("Please enter the northing coordinate (y) in UTM meters which corresponds to the position of the GPR at the far left of the input image:\n", "");
disp("--------------------------------------------------------------------------\n")

bearing = input("Please enter the bearing in degrees relative to geographic north, of the direction of the GPR trace from the far left of the input image to the far right:\n", "");
disp("--------------------------------------------------------------------------\n")

z_pos = input("Please enter the elevation (z) in meters which corresponds to the top left position of in the input image. Note that this may be above the topography:\n", "");
disp("--------------------------------------------------------------------------\n")

x_pos = str2num(x_pos); % Convert keyboard input string to a number
y_pos = str2num(y_pos); % Convert keyboard input string to a number
bearing = str2num(bearing); % Convert keyboard input string to a number
z_pos = str2num(z_pos); % Convert keyboard input string to a number

image_width = columns(I); % Get number of pixels in image width
image_height = rows(I); % Get number of pixels in image height

z_pos_end = z_pos - (v_scale*image_height); % Calculate the elevation of the bottom of the trace image
d_pos_end = h_scale*image_width; % Calculate the position of the far right of the image, relative to the far left

R = I(:,:,1); % Read the first dimension of matrix I into matrix R
G = I(:,:,2); % Read the second dimension of matrix I into matrix G
B = I(:,:,3); % Read the thrid dimension of matrix I into matrix B

I = 0; % Clear the memory by setting I to a scalar

v_scale = v_scale*-1;
```

```
Z = ([z_pos:v_scale:z_pos_end]'); % Create Z (depth) column vector, spanning the elevation of the GPR trace, using the top left elevation, the pixel spacing and the number of pixels in the height of the image
Z2 = Z; % set Z2 to Z

while (columns(Z) < image_width) % Build matrix Z from multiples of column vector Z
Z = [Z,Z2]; % Create a matrix Z from multiples of column vector Z with the number of columns equal to the pixels in the width of the input image
endwhile

D = [0:h_scale:d_pos_end]; % Create a row vector D (distance along the section), using the pixel spacing and number of pixels
D2 = D; % set D2 to D

while (rows(D) < image_height) % Build matrix D from multiples of row vector Z
D = [D;D2]; % Create a matrix D from multiples of row vector D with the number of rows equal to the pixel in the height of the input image
endwhile

output_file = input("Please enter the name of the output file, including the file extension, for example 'output.txt': \n", ""); % Prompt user to specify the output file

f_id = fopen(output_file,'w'); % Open the output file for writing

Dc = 1; % Initialize Dc (Distance column counter) before entering while loop

while (Dc <= image_width) % Do for column conter up to number of pixels in width of image

Dr = 1; % Initialize Dr (Distance row counter) before entering while loop

while (Dr <= image_height) % Do for row counter up to number of pixels in height of image

x = x_pos + (D(Dr,Dc)*sin(bearing*(pi/180))); % Take initial x position and add Dr,Dc position from D matrix combined with the bearing of the GPR line
```

```
y = y_pos + (D(Dr,Dc)*cos(bearing*(pi/180))); % Take initial y position and add Dr,Dc
position from D matrix combined with the bearing of the GPR line
z = Z(Dr,Dc); % Take Dr,Dc position from Z matrix and use as z
r = R(Dr,Dc); % Take Dr,Dc position from R matrix and use as r
g = G(Dr,Dc); % Take Dr,Dc position from G matrix and use as g
b = B(Dr,Dc); % Take Dr,Dc position from B matrix and use as b

fprintf(f_id, '%f %f %f %f %f %f\n', x,y,z,r,g,b) % Output a line of the current
x,y,z,r,g,b parameters to the output file

Dr = Dr + 1; % Add one to Dr counter
endwhile

Dc = Dc + 1; % Add one to Dc counter
endwhile

fclose(f_id); % close the output file
disp("\nDone.\n")

end
```

Appendix (ii)

Crossint code, written for GNU/octave

```
function crossint()


clc
more off

disp("--------------------------------------------------------------------------------")
disp("                                  crossint v0.5                                 ")
disp("       A cross-section interpretation program, written by Max Wilkinson       ")
disp("                          email: maxwell.wilkinson@durham.ac.uk                 ")
disp("--------------------------------------------------------------------------------")

input_file = input("(1)Please enter the name of the cross section data file, including
the file extension:\n","");

topo_data = dlmread(input_file);
topo_x = topo_data(1:end,1);
topo_y = topo_data(1:end,2);
topo_z = topo_data(1:end,3);
clear topo_data;

% make elevation relative to start of section
topo_z = topo_z - min(topo_z);

% calculate distance along section from x and y values
topo_h = ((topo_x.*topo_x)+(topo_y.*topo_y)).^(1/2);
topo_h = topo_h - min(topo_h);

% set initial parameters for while loops
confirm_hw = 1;
confirm_hw1 = 1;
confirm_hw2 = 1;

% begin hangingwall while loops
while (confirm_hw == 1)
```

```
% begin first hangingwall point loop
while (confirm_hw1 == 1)

% prompt to pick first hangingwall point
disp("--------------------------------------------------------------------------------")
disp("(2)Please pick your first point in the hangingwall")

% draw the inital cross section plot
% position figure for large monitor usage: [left,bottom,xsize,ysize]
figure("position",[0,800,1620,1050])
plot(topo_h,topo_z,'.1')
set(gca(),"fontsize",10)
xlabel('distance along section (m)')
ylabel('elevation (m)')
title(input_file)
axis("tight","equal");

% pick first hw point
[hw1_x,hw1_y] = ginput(1);

% find closest point in topo data to the pick
absolute = abs(topo_h-hw1_x);
index = find(min(absolute)==(absolute));
hw1_x = topo_h(index(1));
hw1_y = topo_z(index(1));

close

% plot cross section with first picked hw point
figure("position",[0,800,1620,1050])
plot(topo_h,topo_z,'.1',hw1_x,hw1_y,'+')
set(gca(),"fontsize",10)
xlabel('distance along section (m)')
ylabel('elevation (m)')
title(input_file)
axis("tight","equal");

% prompt for confirmation
```

```
disp("--------------------------------------------------------------------------------")
disp("(3)Are you happy with your first hangingwall pick?")
disp("Press right mouse button to confirm, or left mouse button to retry the pick")

% use mouse input as confirmation
[x1,y1,buttons] = ginput(1);
confirm_hw1 = buttons;

close

% if lmb pressed, go back to start
endwhile
% end first hangingwall point loop

% start second hangingwall point loop
while (confirm_hw2 == 1)

disp("--------------------------------------------------------------------------------")
disp("(4)Please pick your second point in the hangingwall")

% plot the cross section and the confirmed first picked hw point
figure("position",[0,800,1620,1050])
plot(topo_h,topo_z,'.1',hw1_x,hw1_y,'+')
set(gca(),"fontsize",10)
xlabel('distance along section (m)')
ylabel('elevation (m)')
title(input_file)
axis("tight","equal");

% pick second hw point
[hw2_x,hw2_y] = ginput(1);

% find closest point in topo data to the pick
absolute = abs(topo_h-hw2_x);
index = find(min(absolute)==(absolute));
hw2_x = topo_h(index(1));
hw2_y = topo_z(index(1));
close
```

```
% plot cross section with two hw picked points
figure("position",[0,800,1620,1050])
plot(topo_h,topo_z,'.1',hw1_x,hw1_y,'+3',hw2_x,hw2_y,'+3')
set(gca(),"fontsize",10)
xlabel('distance along section (m)')
ylabel('elevation (m)')
title(input_file)
axis("tight","equal");

% prompt for confirmation
disp("------------------------------------------------------------------------------")
disp("(5)Are you happy with your second hangingwall pick?")
disp("Press right mouse button to confirm, or left mouse button to retry the pick")

% use mouse input as confirmation
[x1,y1,buttons] = ginput(1);
confirm_hw2 = buttons;
close

% if lmb pressed, go back to start
if (confirm_hw2 == 1)
endif
endwhile
% end second hangingwall point loop

% calculate the range of topo data vaules for x and y which lie between the picked
points
hw_x_index = find(hw1_x == topo_h);
hw_x_index2 = find(hw2_x == topo_h);
if (hw_x_index < hw_x_index2)
hw_x = topo_h(hw_x_index:hw_x_index2);
hw_y = topo_z(hw_x_index:hw_x_index2);
else
hw_x = topo_h(hw_x_index2:hw_x_index);
hw_y = topo_z(hw_x_index2:hw_x_index);
endif

% return regression through the selected topo data
hw_fit = polyfit(hw_x,hw_y,1);
```

```
hw_pick_m = hw_fit(1:end,1);
hw_pick_c = hw_fit(1:end,2);

% calculate dip of regression line
hw_dip = num2str(atand(hw_pick_m));

% extend the regression line the length of the section
hw_y_topo = (hw_pick_m.*topo_h)+hw_pick_c;

% plot cross section and two hw picked points and line through them for length of the
section
figure("position",[0,800,1620,1050])
plot(topo_h,topo_z,'.1',hw1_x,hw1_y,'+3',hw2_x,hw2_y,'+3',topo_h,hw_y_topo,'-3')
set(gca(),"fontsize",10)
xlabel('distance along section (m)')
ylabel('elevation (m)')
title(input_file)
axis("tight","equal");

% prompt for confirmation of regression
disp("--------------------------------------------------------------------------------")
disp("(6)The dip of the hangingwall interpretation line you have picked is:")
disp(hw_dip)
%disp("The correlation coefficient of the line to the data between the pick points
is:")
%disp(R_hw_2)
disp("Are you happy with this hangingwall interpretation line?")
disp("Press right mouse button to confirm, or left mouse button to retry the
hangingwall pick process")

% use mouse input to confirm
[x1,y1,buttons] = ginput(1);
confirm_hw = buttons;
close

% if lmb pressed repeat the entire loop
if (confirm_hw == 1)
confirm_hw1 = 1;
confirm_hw2 = 1;
```

```
else
endif
endwhile
% end hangingwall while loops

% set inital parameters for scarp while loops
confirm_s = 1;
confirm_s1 = 1;
confirm_s2 = 1;

% start scarp while loops
while (confirm_s == 1)

% start first scarp point while loop
while (confirm_s1 == 1)

% prompt to pick first point on scarp
disp("--------------------------------------------------------------------------------")
disp("(7)Please pick your first point on the scarp")

% plot cross section and two hw picked points and line through them
figure("position",[0,800,1620,1050])
plot(topo_h,topo_z,'.1',hw1_x,hw1_y,'+3',hw2_x,hw2_y,'+3',topo_h,hw_y_topo,'-3')
set(gca(),"fontsize",10)
xlabel('distance along section (m)')
ylabel('elevation (m)')
title(input_file)
axis("tight","equal");

% pick first scarp point
[s1_x,s1_y] = ginput(1);

% find closest point in topo data to the pick
absolute = abs(topo_h-s1_x);
index = find(min(absolute)==(absolute));
s1_x = topo_h(index(1));
s1_y = topo_z(index(1));
close
```

```
% plot cross section and scarp pick
figure("position",[0,800,1620,1050])
plot(topo_h,topo_z,'.1',hw1_x,hw1_y,'+3',hw2_x,hw2_y,'+3',topo_h,hw_y_topo,'-
3',s1_x,s1_y,'+4')
set(gca(),"fontsize",10)
xlabel('distance along section (m)')
ylabel('elevation (m)')
title(input_file)
axis("tight","equal");

% prompt for confirmation
disp("--------------------------------------------------------------------------------")
disp("(8)Are you happy with your first scarp pick?")
disp("Press right mouse button to confirm, or left mouse button to retry the pick")

% use mouse button as confirmation
[x1,y1,buttons] = ginput(1);
confirm_s1 = buttons;

close

% if lmb pressed go back to start of loop
if (confirm_s1 == 1)
endif
endwhile
% end first scarp point loop

% start second scarp point while loop
while (confirm_s2 == 1)

% prompt to pick second scarp point
disp("--------------------------------------------------------------------------------")
disp("(9)Please pick your second point on the scarp")

% plot cross section and scarp pick
figure("position",[0,800,1620,1050])
plot(topo_h,topo_z,'.1',hw1_x,hw1_y,'+3',hw2_x,hw2_y,'+3',topo_h,hw_y_topo,'-
3',s1_x,s1_y,'+4')
set(gca(),"fontsize",10)
```

```
xlabel('distance along section (m)')
ylabel('elevation (m)')
title(input_file)
axis("tight","equal");

% pick second scarp point
[s2_x,s2_y] = ginput(1);

% find closest point in topo data to the pick
absolute = abs(topo_h-s2_x);
index = find(min(absolute)==(absolute));
s2_x = topo_h(index(1));
s2_y = topo_z(index(1));
close

% plot cross section and two scarp picks
figure("position",[0,800,1620,1050])
plot(topo_h,topo_z,'.1',hw1_x,hw1_y,'+3',hw2_x,hw2_y,'+3',topo_h,hw_y_topo,'-
3',s1_x,s1_y,'+4',s2_x,s2_y,'+4')
set(gca(),"fontsize",10)
xlabel('distance along section (m)')
ylabel('elevation (m)')
title(input_file)
axis("tight","equal");

% prompt for confirmation
disp("------------------------------------------------------------------------------")
disp("(10)Are you happy with your second scarp pick?")
disp("Press right mouse button to confirm, or left mouse button to retry the pick")

% use mouse button as confirmation
[x1,y1,buttons] = ginput(1);
confirm_s2 = buttons;
close
endwhile
% end second scarp point while loop

% calculate the range of topo data values for x and y which lie between the picked
points
```

```
s_x_index = find(s1_x == topo_h);
s_x_index2 = find(s2_x == topo_h);
if (s_x_index < s_x_index2)
s_x = topo_h(s_x_index:s_x_index2);
s_y = topo_z(s_x_index:s_x_index2);
else
s_x = topo_h(s_x_index2:s_x_index);
s_y = topo_z(s_x_index2:s_x_index);
endif

% return regression through picked points
s_fit = polyfit(s_x,s_y,1);
s_pick_m = s_fit(1:end,1);
s_pick_c = s_fit(1:end,2);

% calculate dip of regression line
s_dip = num2str(atand(s_pick_m));

% extend scarp regression line to min and max topo_z
s_x_topo_1 = ((min(topo_z))-s_pick_c)./s_pick_m;
s_y_topo_1 = min(topo_z);
s_x_topo_2 = ((max(topo_z))-s_pick_c)./s_pick_m;
s_y_topo_2 = max(topo_z);

s_x_topo = [s_x_topo_1;s_x_topo_2];
s_y_topo = [s_y_topo_1;s_y_topo_2];

% plot cross section and two scarp picks
figure("position",[0,800,1620,1050])
plot(topo_h,topo_z,'.1',hw1_x,hw1_y,'+3',hw2_x,hw2_y,'+3',topo_h,hw_y_topo,'-
3',s1_x,s1_y,'+4',s2_x,s2_y,'+4',s_x_topo,s_y_topo,'-4')
set(gca(),"fontsize",10)
xlabel('distance along section (m)')
ylabel('elevation (m)')
title(input_file)
axis("tight","equal");

% prompt for confirmation of scarp regression line
disp("--------------------------------------------------------------------------------")
```

```
disp("(11)The dip of the scarp interpretation line you have picked is:")
disp(s_dip)
disp("Are you happy with this scarp interpretation line?")
disp("Press right mouse button to confirm, or left mouse button to retry the scarp
pick process")

% use mouse buttons to confirm
[x1,y1,buttons] = ginput(1);
confirm_s = buttons;
close

% if lmb pressed repeat the loop
if (confirm_s == 1)
confirm_s1 = 1;
confirm_s2 = 1;
else
endif
endwhile
% end scarp while loop

% get paramaters to correctly shortern the length of the picked lines, take the
beginning of the hw line - hw_x1 to be minimum topo_h, work out corresponding hw_y1
hw_x1 = min(topo_h);
hw_y1 = (hw_pick_m.*hw_x1)+hw_pick_c;

% take maximum sn_x value and use this as the vaule for the end of the hw line -
hw_x2, work out the corresponding hw_y2
if (s1_x > s2_x)
hw_x2 = s1_x;
hw_y2 = (hw_pick_m.*s1_x)+hw_pick_c;
else
hw_x2 = s2_x;
hw_y2 = (hw_pick_m.*s2_x)+hw_pick_c;
endif

% read min and max x and y coordinates for the hw line into column vectors for
plotting
hw_x_l = [hw_x1;hw_x2];
hw_y_l = [hw_y1;hw_y2];
```

```
% take maximum hwn_x value and use this as the value for the start of the scarp line -
s_x1, work out the corresponding s_y1
if (hw1_x > hw2_x)
s_x1 = hw1_x;
s_y1 = (s_pick_m.*hw1_x)+s_pick_c;
else
s_x1 = hw2_x;
s_y1 = (s_pick_m.*hw2_x)+s_pick_c;
endif

% take the end of the scarp line - s_x2 to be maximum topo_h, work out corresponding
s_y1
s_y2 = max(topo_z);
s_x2 = (s_y2-s_pick_c)./s_pick_m;

% read min and max x and y coordinates for the scarp line into column vectors for
plotting
s_x_l = [s_x1;s_x2];
s_y_l = [s_y1;s_y2];

% initial parameters for footwall while loops
confirm_fw = 1;
confirm_fw1 = 1;
confirm_fw2 = 1;

% start footwall while loops
while (confirm_fw == 1)

% start first footwall point loop
while (confirm_fw1 == 1)

% prompt to pick for footwall point
disp("--------------------------------------------------------------------------------")
disp("(12)Please pick your first point in the footwall")

% plot cross section and two footwall picks
figure("position",[0,800,1620,1050])
```

```
plot(topo_h,topo_z,'.1',hw1_x,hw1_y,'+3',hw2_x,hw2_y,'+3',hw_x_l,hw_y_l,'-
3',s1_x,s1_y,'+4',s2_x,s2_y,'+4',s_x_l,s_y_l,'-4')
set(gca(),"fontsize",10)
xlabel('distance along section (m)')
ylabel('elevation (m)')
title(input_file)
axis("tight","equal");

% pick first footwall point
[fw1_x,fw1_y] = ginput(1);

% find closest point in topo data to the pick
absolute = abs(topo_h-fw1_x);
index = find(min(absolute)==(absolute));
fw1_x = topo_h(index(1));
fw1_y = topo_z(index(1));
close

% plot cross section and two footwall picks
figure("position",[0,800,1620,1050])
plot(topo_h,topo_z,'.1',hw1_x,hw1_y,'+3',hw2_x,hw2_y,'+3',hw_x_l,hw_y_l,'-
3',s1_x,s1_y,'+4',s2_x,s2_y,'+4',s_x_l,s_y_l,'-4',fw1_x,fw1_y,'+5')
set(gca(),"fontsize",10)
xlabel('distance along section (m)')
ylabel('elevation (m)')
title(input_file)
axis("tight","equal");

% prompt for confirmation of first footwall pick
disp("--------------------------------------------------------------------------------")
disp("(13)Are you happy with your first footwall pick?")
disp("Press right mouse button to confirm, or left mouse button to retry the pick")

% if lmb pressed, repeat the loop
[x1,y1,buttons] = ginput(1);
confirm_fw1 = buttons;

close
endwhile
```

```
% end first footwall point loop

% start second footwall point loop
while (confirm_fw2 == 1)

% prompt to pick the second footwall point
disp("--------------------------------------------------------------------------------")
disp("(14)Please pick your second point in the footwall")

% plot cross section and two scarp picks
figure("position",[0,800,1620,1050])
plot(topo_h,topo_z,'.1',hw1_x,hw1_y,'+3',hw2_x,hw2_y,'+3',hw_x_l,hw_y_l,'-
3',s1_x,s1_y,'+4',s2_x,s2_y,'+4',s_x_l,s_y_l,'-4',fw1_x,fw1_y,'+5')
set(gca(),"fontsize",10)
xlabel('distance along section (m)')
ylabel('elevation (m)')
title(input_file)
axis("tight","equal");

% pick second scarp point
[fw2_x,fw2_y] = ginput(1);

% find closest point in topo data to the pick
absolute = abs(topo_h-fw2_x);
index = find(min(absolute)==(absolute));
fw2_x = topo_h(index(1));
fw2_y = topo_z(index(1));
close

% plot cross section and two scarp picks
figure("position",[0,800,1620,1050])
plot(topo_h,topo_z,'.1',hw1_x,hw1_y,'+3',hw2_x,hw2_y,'+3',hw_x_l,hw_y_l,'-
3',s1_x,s1_y,'+4',s2_x,s2_y,'+4',s_x_l,s_y_l,'-4',fw1_x,fw1_y,'+5',fw2_x,fw2_y,'+5')
set(gca(),"fontsize",10)
xlabel('distance along section (m)')
ylabel('elevation (m)')
title(input_file)
axis("tight","equal");
```

```
% prompt to confirm the pick
disp("-------------------------------------------------------------------------------")
disp("(15)Are you happy with your second footwall pick?")
disp("Press right mouse button to confirm, or left mouse button to retry the pick")

% use mounse button to confirm
[x1,y1,buttons] = ginput(1);
confirm_fw2 = buttons;

close

endwhile
% end second footwall point loop

% calculate the range of topo data vaules for x and y which lie between the picked
points
fw_x_index = find(fw1_x == topo_h);
fw_x_index2 = find(fw2_x == topo_h);
if (fw_x_index < fw_x_index2)
fw_x = topo_h(fw_x_index:fw_x_index2);
fw_y = topo_z(fw_x_index:fw_x_index2);
else
fw_x = topo_h(fw_x_index2:fw_x_index);
fw_y = topo_z(fw_x_index2:fw_x_index);
endif

% return regression through picked points
fw_fit = polyfit(fw_x,fw_y,1);
fw_pick_m = fw_fit(1:end,1);
fw_pick_c = fw_fit(1:end,2);

% calculate the dip of the regression line
fw_dip = num2str(atand(fw_pick_m));

% calculate the extent of the footwall regression line for the section
fw_x1 = s_x1;
fw_y1 = (fw_pick_m.*fw_x1)+fw_pick_c;
fw_x2 = max(topo_h);
fw_y2 = (fw_pick_m.*fw_x2)+fw_pick_c;
```

```
% read min and max x and y coordinates for the footwall line into column vectors for
plotting
fw_x_l = [fw_x1;fw_x2];
fw_y_l = [fw_y1;fw_y2];

% calculate the new extent of the scarp regression line for the section using max_z
from fw picks
if (fw1_y > fw2_y)
s_y2 = fw1_y;
else
s_y2 = fw2_y;
endif
s_x2 = (s_y2-s_pick_c)./s_pick_m;

% re-read min and max x and y coordinates for the scarp line into column vectors for
plotting
s_x_l = [s_x1;s_x2];
s_y_l = [s_y1;s_y2];

% plot cross section and two scarp picks
figure("position",[0,800,1620,1050])
plot(topo_h,topo_z,'.1',hw1_x,hw1_y,'+3',hw2_x,hw2_y,'+3',hw_x_l,hw_y_l,'-
3',s1_x,s1_y,'+4',s2_x,s2_y,'+4',s_x_l,s_y_l,'-
4',fw1_x,fw1_y,'+5',fw2_x,fw2_y,'+5',fw_x_l,fw_y_l,'-5')
set(gca(),"fontsize",10)
xlabel('distance along section (m)')
ylabel('elevation (m)')
title(input_file)
axis("tight","equal");

% calculate the intersection of the hw and scarp regression lines
x_hw_s = (s_pick_c-hw_pick_c)./(hw_pick_m-s_pick_m);
y_hw_s = (x_hw_s.*hw_pick_m)+hw_pick_c;

% calculate the intersection of the scarp and fw regression lines
x_s_fw = (fw_pick_c-s_pick_c)./(s_pick_m-fw_pick_m);
y_s_fw = (x_s_fw.*s_pick_m)+s_pick_c;
```

```
% calculate the throw and heave
throw = y_s_fw-y_hw_s;
heave = x_s_fw-x_hw_s;

% prompt for confirmation
disp("--------------------------------------------------------------------------------")
disp(sprintf("(16) The dip of the footwall interpretation line you have picked is:
%s",fw_dip))
disp(sprintf("     The throw for your interpretation is: %f",throw))
disp(sprintf("     The heave for your interpretation is: %f",heave))
disp("     Are you happy with this footwall interpretation line?")
disp("     Press right mouse button to confirm, or left mouse button to retry the
footwall pick process")

% use mouse buttons to confirm
[x1,y1,buttons] = ginput(1);
confirm_fw = buttons;

% if lmb pressed repeat the entire loop
if (confirm_fw == 1)
close
confirm_fw1 = 1;
confirm_fw2 = 1;
else
endif
endwhile
% end footwall loops

close

% plot cross section with title for printing
figure("position",[0,800,1620,1050])
plot(topo_h,topo_z,'.1',hw1_x,hw1_y,'+3',hw2_x,hw2_y,'+3',hw_x_l,hw_y_l,'-
3',s1_x,s1_y,'+4',s2_x,s2_y,'+4',s_x_l,s_y_l,'-
4',fw1_x,fw1_y,'+5',fw2_x,fw2_y,'+5',fw_x_l,fw_y_l,'-5')
title(input_file);
info =
sprintf('%s\n%s\n%s\n%s\n%s\n%s\n%s\n%s\n%s\n%s\n%s\n','Throw:',num2str(throw),'Heave:',nu
```

```
m2str(heave),"\n","Hangingwall dip:",num2str(hw_dip),"\n","Scarp
dip:",num2str(s_dip),"\n","Footwall dip:",num2str(fw_dip));
text((min(topo_h)+((max(topo_h)-min(topo_h))/20)),(max(topo_z)-((max(topo_z)-
min(topo_z))/20)),info);
set(gca(),"fontsize",10)
xlabel('distance along section (m)')
ylabel('elevation (m)')
title(input_file)
axis("tight","equal");

% create output directory to store output
mkdir("output");
mkdir("./output/images/");

output_file = strcat(pwd,"/output/images/",input_file,".svg");
print(output_file,"-dsvg","-color","-S1280,800")
disp("--------------------------------------------------------------------------------")
disp(sprintf("Interpreted cross-section saved as: %s",output_file))
close

% open the output file for writing
f_id = fopen("./output/interpretation.dat",'a');

% output a line of the current parameters to the output file
throw = num2str(throw);
heave = num2str(heave);
hw_dip = num2str(hw_dip);
s_dip = num2str(s_dip);
fw_dip = num2str(fw_dip);
data_output = sprintf('%s %s %s %s %s %s',input_file,throw,heave,hw_dip,s_dip,fw_dip);

fprintf(f_id, '%s %s %s %s %s %s\n', input_file,throw,heave,hw_dip,s_dip,fw_dip);

% close the output file
fclose(f_id);
disp("--------------------------------------------------------------------------------")
disp(sprintf("Data output line: %s",data_output))
disp(sprintf("Appended to the file: %s%s",pwd,'/output/interpretation.dat'))
```

```
% create & move input file to directory './interpreted'
mkdir("interpreted");
interpreted = strcat(pwd,"/interpreted/",input_file);
movefile(input_file, interpreted);
disp("--------------------------------------------------------------------------------")
disp(sprintf("Input file: %s",input_file))
disp(sprintf("Moved to directory: %s%s",pwd,'/interpreted/'))
disp("--------------------------------------------------------------------------------")
disp("Process complete, exiting to prompt.")
disp("--------------------------------------------------------------------------------")

end
```

Appendix (iii)

Crossint cross section interpretation output for the Campo Felice fault

Name	Dist (m)	Throw (m)	Throw Rate (mm/yr)	Stdev Throw rate	Mean Throw rate	Heave (m)	Hwall dip (degrees)	Scarp dip (degrees)	Fwall dip (degrees)
N91-01	71.45	15.215				9.403	36.22	58.28	37.95
N91-02	72.45	14.953	0.997			8.830	36.08	59.44	37.70
N91-03	73.45	14.291	0.953			8.163	35.90	60.26	38.13
N91-04	74.45	15.138				8.910	35.76	59.52	36.66
N91-05	75.45	13.312				6.914	35.62	62.55	37.83
N91-06	76.45	13.533	0.902			7.518	35.37	60.95	39.12
N91-07	77.45	13.820	0.921			7.970	35.23	60.03	39.32
N91-08	78.45	14.184	0.946			8.258	35.27	59.79	38.77
N91-09	79.45	14.126	0.942			8.419	35.26	59.21	38.98
N91-10	80.45	13.299		0.032	0.943	7.676	35.34	60.01	39.44
S9301	128.34	11.753				8.347	33.88	54.62	37.17
S9302	129.34	12.305	0.820			8.515	34.10	55.32	36.80
S9303	130.34	12.198				8.294	34.16	55.79	36.72
S9304	131.34	12.299	0.820			8.988	34.07	53.84	37.36
S9305	132.34	13.414	0.894			9.952	34.00	53.43	36.91
S9306	133.34	13.901				10.409	33.76	53.18	37.09
S9307	134.34	13.495	0.900			9.705	33.64	54.28	37.14
S9308	135.34	14.580				10.582	33.79	54.03	36.40
S9309	136.34	13.437	0.896			9.397	33.87	55.03	36.70
S9310	137.34	13.333	0.889	0.039	0.870	9.408	34.00	54.79	36.76
S9311	199.89	13.414	0.894			10.408	34.92	52.19	36.57
S9312	200.89	13.067	0.871			10.215	35.09	51.99	36.60
S9313	201.89	13.374	0.892			10.772	34.79	51.15	36.85
S9314	202.89	13.224	0.882			10.582	34.45	51.33	36.80
S9315	203.89	12.797				9.488	35.24	53.45	36.40
S9316	204.89	13.826	0.922			10.968	34.40	51.58	36.63
S9317	205.89	14.428				10.749	35.56	53.31	35.66
S9318	206.89	14.887				11.515	35.45	52.28	35.78
S9319	207.89	13.934	0.929			10.885	34.82	52.00	36.35
S9320	208.89	13.114	0.874	0.023	0.895	9.827	35.14	53.16	36.28
S9401	236.78	14.666	0.978			11.759	34.64	51.28	36.38

		14.99				11.76			
S9402	237.78	9				4	34.60	51.89	36.21
		14.24				10.19			
S9403	238.78	2	0.949			6	34.99	54.40	35.92
		14.54				11.29			
S9404	239.78	3	0.970			1	34.92	52.18	36.27
		14.81				12.16			
S9405	240.78	0	0.987			8	35.01	50.59	36.75
		15.08				12.27			
S9406	241.78	0				3	34.44	50.86	36.82
		14.81				12.05			
S9407	242.78	9				9	34.94	50.86	36.42
		15.23				12.48			
S9408	243.78	9				0	34.98	50.68	36.79
		14.51				11.52			
S9409	244.78	9	0.968			3	35.25	51.56	36.39
		13.99		0.02	0.96	10.86			
S9410	245.78	5	0.933	0	4	3	35.26	52.18	36.50
		14.08				10.08			
G4-01	269.18	7	0.939			0	34.55	54.41	38.28
		14.28							
G4-02	270.18	9	0.953			9.982	34.43	55.06	37.96
		14.76				10.54			
G4-03	271.18	2				8	34.70	54.45	37.53
		15.64				12.13			
G4-04	272.18	9				3	34.49	52.21	38.49
		14.40				10.53			
G4-05	273.18	8	0.961			4	34.96	53.83	38.11
		14.10				10.64			
G4-06	274.18	8	0.941			3	34.95	52.97	38.82
		14.18				10.73			
G4-07	275.18	3	0.946			9	34.96	52.87	38.86
		14.33				10.76			
G4-08	276.18	6	0.956			3	34.83	53.10	38.81
		13.93				10.45			
G4-09	277.18	8	0.929			0	35.34	53.14	38.55
		14.93		0.01	0.94	11.23			
G4-10	278.18	6		1	6	6	35.19	53.05	38.26
		10.59							
G5-01	508.86	7				5.792	38.36	61.34	39.61
		12.26							
G5-02	509.86	2	0.817			6.398	37.50	62.45	39.44
		10.75							
G5-03	510.86	2				6.416	38.73	59.17	39.38
		11.38							
G5-04	511.86	4				6.107	37.85	61.79	39.56
		11.71							
G5-05	512.86	3	0.781			6.162	37.56	62.25	39.91
		12.94							
G5-06	513.86	1	0.863			7.658	37.66	59.38	39.59
		12.54							
G5-07	514.86	3	0.836			6.816	37.32	61.48	40.24
		13.57							
G5-08	515.86	4	0.905			7.526	37.10	60.99	39.30
		15.86				10.36			
G5-09	516.86	8				6	37.10	56.84	39.34
		13.38		0.04	0.84				
G5-10	517.86	9	0.893	7	9	6.826	36.97	62.99	39.26
		12.92							
G7-01	571.46	8	0.862			9.220	37.87	59.01	39.54
		13.51				10.04			
G7-02	572.46	5	0.901			2	37.21	58.15	40.48
		13.23							
G7-03	573.46	3	0.882			9.545	36.98	59.49	39.46
		13.03							
G7-04	574.46	8	0.869			8.658	37.17	59.86	42.46
		12.09							
G7-05	575.46	5	0.806			8.603	37.37	60.07	42.07
		12.28							
G7-06	576.46	3	0.819			8.205	37.27	61.25	40.95
		13.94							
G7-07	577.46	9				9.926	37.03	58.94	41.35
		13.56				10.36			
G7-08	578.46	6				8	37.29	58.22	41.52
		14.22				10.49			
G7-09	579.46	3				3	37.30	58.25	40.97

		14.993		0.037	0.857				
G7-10	580.46					9.783	37.23	58.48	43.27
		16.798				12.618			
S8501	738.97		1.120				31.37	53.09	43.66
		11.343							
S8502	739.97		0.756			8.533	33.27	53.05	40.81
		12.299							
S8503	740.97		0.820			9.085	34.05	53.55	35.72
		12.244							
S8504	741.97		0.816			9.101	34.17	53.38	39.02
		13.365				10.389			
S8505	742.97		0.891				34.85	52.14	39.76
		17.735				13.977			
S8506	743.97						31.03	51.76	44.83
		14.840				11.256			
S8507	744.97						34.13	52.82	42.95
		15.619				11.438			
S8508	745.97						34.41	53.78	41.34
		11.153							
S8509	746.97		0.744			8.782	33.02	51.78	45.63
		13.358		0.063	0.820	10.233			
S8510	747.97		0.891				33.76	52.55	35.43
		12.931							
G8-01	781.47		0.862			7.312	35.35	60.52	39.51
		13.283							
G8-02	782.47					7.412	35.63	60.85	38.65
		13.312							
G8-03	783.47					7.828	36.01	59.54	40.39
		12.652							
G8-04	784.47		0.843			6.940	36.51	61.26	39.88
		12.987							
G8-05	785.47		0.866			7.450	36.13	60.16	41.44
		12.912							
G8-06	786.47		0.861			7.179	34.87	60.93	42.41
		12.402							
G8-07	787.47		0.827			6.591	35.49	62.01	42.33
		12.402							
G8-08	788.47		0.827			6.718	35.23	61.30	43.23
		12.271							
G8-09	789.47					8.278	35.64	59.35	40.06
		13.364		0.018	0.848				
G8-10	790.47					7.948	36.04	59.26	41.69
G10-01	979.31	11.900	0.793			7.430	32.99	58.02	41.47
G10-02	980.31	11.739				7.666	33.24	56.85	41.64
G10-03	981.31	11.724				7.077	33.52	58.89	40.40
G10-04	982.31	13.498	0.900			9.720	33.85	54.24	40.80
G10-05	983.31	12.072	0.805			8.681	34.24	54.28	41.54
G10-06	984.31	12.143	0.810			7.394	34.53	58.66	38.50
G10-07	985.31	13.667				9.641	34.39	54.80	39.26
G10-08	986.31	13.615				9.521	34.76	55.04	38.52
G10-09	987.31	13.463	0.898			9.043	34.46	56.11	38.44
G10-10	988.31	13.479	0.899	0.053	0.851	9.146	34.33	55.84	38.61
G11-01	1138.51	11.950				6.504	37.59	61.44	44.30
G11-02	1139.51	10.926	0.728			5.543	38.03	63.10	43.81
G11-03	1140.51	11.433	0.762			5.857	37.02	62.87	44.42
G11-04	1141.51	12.021				6.590	37.25	61.27	44.15
G11-05	1142.51	10.297	0.686			5.115	37.27	63.58	44.10
G11-06	1143.51	11.936				6.510	36.87	61.39	44.21
G11-07	1144.51	11.082	0.739			5.924	37.50	61.87	42.78

G11-08	1145.51	11.537	0.769			5.973	36.73	62.63	43.31
G11-09	1146.51	10.579	0.705			5.609	37.02	62.07	43.58
G11-10	1147.51	9.3042		0.032	0.732	4.698	36.79	63.21	44.93
G12-01	1478.33	9.5183				5.450	36.26	60.20	43.25
G12-02	1479.33	9.880	0.659			5.621	36.09	60.37	43.78
G12-03	1480.33	11.177	0.745			6.704	36.05	59.04	39.75
G12-04	1481.33	10.826	0.722			5.990	35.80	61.05	42.19
G12-05	1482.33	11.370	0.758			6.736	35.67	59.35	46.60
G12-06	1483.33	11.835	0.789			6.594	35.31	60.87	44.35
G12-07	1484.33	11.016	0.734			6.205	34.97	60.61	50.13
G12-08	1485.33	13.221				7.247	34.27	61.27	44.94
G12-09	1486.33	13.022				7.444	34.24	60.25	48.18
G12-10	1487.33	14.736		0.044	0.734	9.080	34.48	58.36	45.42
G13-01	1520.13	10.192	0.679			5.244	35.18	62.77	45.33
G13-02	1521.13	9.449	0.630			4.603	37.54	64.03	38.17
G13-03	1522.13	10.068	0.671			5.344	35.14	62.04	47.75
G13-04	1523.13	8.376				4.417	38.27	62.19	44.22
G13-05	1524.13	13.620				9.023	35.74	56.48	47.22
G13-06	1525.13	9.870	0.658			5.966	39.45	58.85	43.08
G13-07	1526.13	13.397				7.844	37.75	59.65	35.64
G13-08	1527.13	10.186	0.679			5.201	37.05	62.95	44.51
G13-09	1528.13	12.742				7.667	36.32	58.97	45.25
G13-10	1529.13	14.252		0.021	0.664	9.671	36.60	55.84	47.16
G14-01	1573.62	9.402	0.627			5.253	36.00	60.81	38.39
G14-02	1574.62	7.616				4.082	37.35	61.81	42.04
G14-03	1575.62	9.925	0.662			5.879	36.02	59.36	39.65
G14-04	1576.62	8.449				4.451	36.99	62.22	38.20
G14-05	1577.62	8.776	0.585			5.294	36.19	58.90	42.70
G14-06	1578.62	8.512				4.397	35.82	62.68	40.30
G14-07	1579.62	8.318				4.117	35.43	63.67	40.99
G14-08	1580.62	8.789	0.586			5.071	36.19	60.02	39.04
G14-09	1581.62	9.734	0.649			5.753	35.56	59.42	39.10
G14-10	1582.62	9.787	0.652	0.034	0.627	5.801	35.19	59.34	38.43
S74-01	1604.09	9.264	0.618			5.748	35.23	58.18	40.84
S74-02	1605.09	9.431	0.629			6.111	35.21	57.06	40.54
S74-03	1606.09	9.558	0.637			6.162	35.11	57.19	40.30
S74-04	1607.09	10.177				6.433	35.22	57.70	32.98
S74-05	1608.09	9.343	0.623			5.959	35.29	57.47	40.34

S74-06	1609.09	9.258	0.617			6.100	35.53	56.62	38.45
S74-07	1610.09	8.345				5.108	35.51	58.53	40.65
S74-08	1611.09	8.405				5.454	35.50	57.02	42.12
S74-09	1612.09	8.988	0.599			5.933	35.89	56.57	40.50
S74-10	1613.09	8.269		0.013	0.620	5.297	35.78	57.36	41.11
S75-01	1725.93	8.045				5.516	35.31	55.56	46.23
S75-02	1726.93	7.902				4.855	34.81	58.44	45.73
S75-03	1727.93	9.394	0.626			5.852	35.41	58.08	47.20
S75-04	1728.93	8.955	0.597			5.990	34.51	56.22	43.88
S75-05	1729.93	7.828				4.949	34.34	57.70	46.45
S75-06	1730.93	9.261	0.617			6.156	34.42	56.39	43.38
S75-07	1731.93	10.439	0.696			7.369	34.19	54.78	44.62
S75-08	1732.93	10.251	0.683			6.965	33.96	55.81	45.25
S75-09	1733.93	10.659	0.711			7.644	34.47	54.35	43.89
S75-10	1734.93	6.439		0.047	0.655	3.951	34.57	58.47	47.54
S5101	1755.74	9.270	0.618			5.572	33.08	58.99	39.22
S5102	1756.74	9.585	0.639			5.558	32.96	59.89	37.30
S5103	1757.74	9.421	0.628			5.296	32.45	60.66	38.35
S5104	1758.74	9.978	0.665			5.722	32.48	60.17	38.79
S5105	1759.74	9.833	0.656			5.410	32.81	61.18	40.70
S5106	1760.74	10.738				6.357	33.01	59.37	42.23
S5107	1761.74	9.893	0.660			6.084	34.49	58.41	44.62
S5108	1762.74	9.838	0.656			5.689	33.41	59.96	45.96
S5109	1763.74	9.540	0.636			5.682	34.84	59.22	47.72
S5110	1764.74	7.926		0.017	0.645	4.721	32.33	59.22	44.46
G18-01	1901.90	10.384	0.692			7.115	34.32	55.58	35.80
G18-02	1902.90	10.843	0.723			8.232	34.21	52.79	39.00
G18-03	1903.90	10.827	0.722			8.374	34.07	52.28	39.69
G18-04	1904.90	9.908	0.661			6.597	35.01	56.34	38.57
G18-05	1905.90	9.543	0.636			5.868	35.95	58.41	37.88
G18-06	1906.90	10.342	0.689			7.043	35.35	55.75	38.75
G18-07	1907.90	10.888	0.726			8.312	34.42	52.64	42.13
G18-08	1908.90	10.691	0.713			7.967	34.71	53.31	42.50
G18-09	1909.90	12.547				10.155	35.00	51.02	42.52
G18-10	1910.90	10.515	0.701	0.031	0.696	7.691	34.91	53.82	41.80
S4301	2101.74	11.054				8.021	31.25	54.04	38.96
S4302	2102.74	11.143				7.309	31.35	56.74	38.88
S4303	2103.74	10.358	0.691			7.302	31.76	54.82	37.98

	2104.74	10.747				7.808	32.76	54.00	35.25
S4304			0.716						
	2105.74	10.287				7.236	33.29	54.88	33.74
S4305			0.686						
	2106.74	10.868				7.771	32.46	54.43	34.42
S4306			0.725						
	2107.74	10.812				7.717	32.09	54.48	35.26
S4307			0.721						
	2108.74	10.405				7.703	31.91	53.49	38.23
S4308			0.694						
	2109.74	11.587				8.373	32.46	54.15	37.73
S4309									
	2110.74	10.384		0.016	0.703	7.932	32.43	52.63	36.81
S4310			0.692						
	2350.31	11.180				8.272	32.09	53.50	35.85
S4401			0.745						
	2351.31	11.371				8.021	31.41	54.80	35.89
S4402			0.758						
	2352.31	11.128				8.339	31.71	53.15	37.96
S4403			0.742						
	2353.31	10.816				7.139	32.35	56.57	35.57
S4404									
	2354.31	11.226				8.184	32.34	53.91	36.92
S4405			0.748						
	2355.31	10.952				7.809	33.45	54.51	35.45
S4406			0.730						
	2356.31	11.106				7.982	33.67	54.29	35.36
S4407			0.740						
	2357.31	11.510				7.986	32.56	55.25	36.18
S4408									
	2358.31	10.662				7.641	32.50	54.37	37.10
S4409									
	2359.31	11.372		0.010	0.746	8.191	32.68	54.24	36.29
S4410			0.758						
G23-01	2495.00	9.5661				4.465	29.38	64.98	36.92
G23-02	2496.00	9.5261				4.219	29.48	66.11	36.81
G23-03	2497.00	10.793	0.720			5.883	29.31	61.41	36.89
G23-04	2498.00	10.198	0.680			4.630	29.46	65.58	36.64
G23-05	2499.00	9.9430	0.663			4.301	29.25	66.61	35.09
G23-06	2500.00	11.560	0.771			6.389	29.59	61.07	36.69
G23-07	2501.00	11.993				6.913	29.67	60.04	36.59
G23-08	2502.00	12.772				8.399	29.81	56.67	36.71
G23-09	2503.00	11.345	0.756			6.131	29.81	61.62	36.63
G23-10	2504.00	11.360	0.757	0.045	0.724	6.219	29.91	61.30	36.58
	3278.87	9.0251				6.735	36.82	53.27	39.06
S3201			0.602						
	3279.87	8.8551				6.758	36.72	52.65	42.99
S3202									
	3280.87	9.8580	0.657			8.054	37.96	50.75	40.15
S3203									
	3281.87	10.254				7.994	37.01	52.06	39.50
S3204									
	3282.87	9.3187	0.621			6.337	37.37	55.78	39.36
S3205									
	3283.87	9.6690	0.645			8.017	38.16	50.34	39.91
S3206									
	3284.87	9.0521				6.888	38.05	52.73	38.81
S3207									
	3285.87	9.6240	0.642			8.317	38.65	49.17	38.98
S3208									
	3286.87	8.4591				7.049	38.42	50.20	39.42
S3209									
	3287.87	9.3400	0.623	0.020	0.631	7.797	38.19	50.14	39.07
S3210									
	3649.31	10.770	0.718			7.187	36.40	56.28	43.68
S2101									

	3650.3	11.05							
S2102	1	7				7.703	36.09	55.14	44.81
	3651.3	10.69							
S2103	1	4	0.713			7.221	36.44	55.97	44.92
	3652.3								
S2104	1	8.838				4.739	36.38	61.80	43.88
	3653.3	10.83							
S2105	1	3				7.159	36.65	56.54	43.13
	3654.3	10.27							
S2106	1	0	0.685			6.491	36.94	57.71	41.60
	3655.3	10.31							
S2107	1	6	0.688			6.784	37.28	56.67	41.51
	3656.3	11.15							
S2108	1	4				7.456	36.92	56.24	41.16
	3657.3	10.09							
S2109	1	8	0.673			6.508	37.34	57.20	40.17
	3658.3			0.02	0.69				
S2110	1	9.961	0.664	1	0	6.784	36.97	55.74	41.86
	3808.7								
S2201	3	7.552				4.906	35.69	56.99	42.90
	3809.7								
S2202	3	8.168	0.545			5.592	35.91	55.61	43.41
	3810.7								
S2203	3	8.772				5.927	35.85	55.95	43.35
	3811.7								
S2204	3	7.542				4.777	36.15	57.65	39.59
	3812.7								
S2205	3	8.122	0.541			5.315	36.35	56.80	43.85
	3813.7								
S2206	3	8.385	0.559			5.456	36.47	56.95	43.84
	3814.7								
S2207	3	8.266	0.551			5.204	36.43	57.81	44.53
	3815.7								
S2208	3	8.688				5.786	36.54	56.34	45.50
	3816.7								
S2209	3	8.474	0.565			5.241	36.61	58.26	45.31
	3817.7			0.01	0.55				
S2210	3	8.470	0.565	0	4	6.022	36.57	54.59	44.70
G37-	4587.2								
01	2	8.736				3.484	48.61	68.26	45.47
G37-	4588.2								
02	2	9.927				4.552	48.55	65.37	47.19
G37-	4589.2								
03	2	9.952				4.464	48.41	65.84	47.33
G37-	4590.2								
04	2	9.279				3.723	47.27	68.14	51.79
G37-	4591.2								
05	2	7.380	0.492			3.028	47.65	67.69	55.05
G37-	4592.2								
06	2	7.102	0.473			2.811	48.17	68.40	51.04
G37-	4593.2								
07	2	7.928	0.529			3.019	48.17	69.15	47.30
G37-	4594.2								
08	2	6.906	0.460			2.514	47.86	70.00	45.38
G37-	4595.2								
09	2	6.749	0.450			2.617	49.25	68.81	44.08
G37-	4596.2			0.03	0.48				
10	2	7.740	0.516	1	7	3.035	50.70	68.59	52.01

Appendix (iv)

Field data for the Campo Felice fault

Measurement name	Dip (degrees from horizontal)	Strike (degrees from North)	Plunge direction (Degrees from North)	Distance along fault (m)
N91	53	127	218	75.446
S93	54	127	228	132.342
S93_2	52	141	239	203.888
G4	54	124	258	273.18
S95	59	123	268	328.125
S96	54	129	264	463.745
G5	56	126	no data	512.856
G7	48	143	no data	575.456
K234	52	138	196	588.856
K233	49	136	197	612.686
K232	53	134	196	636.516
K231	51	133	198	643.284
K230	51	136	210	650.051
K229	56	132	207	690.629
K228	57	134	210	708.901
K227	54	130	209	727.172
S85	53	139	no data	742.972
K226	56	136	208	743.149
K225	58	135	207	751.137
K224	56	136	209	774.365
G8	56	138	no data	785.465
K223	53	134	211	789.604
K222	58	126	210	820.748
K221	56	129	212	826.998
N86	56	132	no data	865.218
K219	59	131	211	865.866
K220	57	132	206	865.866
K218	58	129	210	892.802
K216	57	118	209	919.738
K217	53	123	207	919.738
K214	54	120	202	946.673
K215	56	121	204	946.673
K212	54	125	195	973.609
K213	53	119	206	973.609
K211	56	124	198	980.930
G10	52	129	no data	983.309
K210	54	121	197	995.571
K208	53	121	198	1002.891
K209	56	123	199	1002.891
K207	54	128	207	1014.072
K206	56	129	206	1025.252
K205	56	121	210	1069.527
K204	53	118	209	1076.042
K203	57	129	211	1114.127
K202	56	158	218	1120.729

K201	59	161		213	1133.933
K199	58	160		216	1140.535
K200	57	162		214	1140.535
G11	57	136	no data		1142.509
K198	57	132		191	1156.963
K197	60	135		203	1173.391
K194	49	132		233	1180.187
K195	48	133		231	1180.187
K196	61	132		201	1186.984
K190	50	141		218	1193.780
K191	51	143		216	1193.780
K192	51	142		212	1193.780
K193	48	139		215	1193.780
K188	63	142		210	1389.876
K189	62	146		212	1389.876
K187	65	140		209	1401.217
K182	50	128		208	1412.559
K183	52	126		202	1412.559
K184	58	146		221	1412.559
K185	56	143		224	1412.559
K186	55	141		223	1412.559
S73	54	141	no data		1418.933
K180	66	140		214	1454.600
K181	64	142		212	1454.600
G12	61	137	no data		1482.33
K178	64	120		217	1513.662
K179	61	122		214	1513.662
G13	56	143	no data		1524.129
K177	58	134		211	1546.708
G14	52	137	no data		1577.617
K176	49	131		212	1597.635
K175	58	131		214	1602.078
S74	49	134	no data		1608.085
K172	54	128		214	1608.742
K173	56	126		213	1608.742
K174	57	130		216	1608.742
K170	47	131		198	1659.710
K171	49	135		196	1659.710
K169	54	133		218	1668.512
K165	57	128		216	1677.314
K166	56	121		219	1677.314
K167	53	126		212	1677.314
K168	55	124		219	1677.314
K163	48	126		215	1685.909
K164	53	124		217	1685.909
K161	48	120		210	1710.208
K162	49	121		212	1710.208
S75	52	118	no data		1729.9295
K159	73	108		188	1731.533
K160	74	106		185	1731.533
K157	58	138		229	1754.744
K158	81	88		182	1754.744
S51	58	135	no data		1759.744
K155	57	131		210	1767.712

K156	61	137		212	1767.712
K153	59	136		214	1780.679
K154	61	139		216	1780.679
K151	58	148		226	1808.813
K152	58	146		224	1808.813
K146	53	110		206	1858.716
K147	56	112		208	1858.716
K148	54	108		210	1858.716
K149	56	114		204	1858.716
K150	51	108		205	1858.716
K144	52	106		205	1877.591
K145	54	108		208	1877.591
K143 (S.S.)	52	115		214	1883.882
K142	51	114		212	1897.411
G18	52	119	no data		1905.9
K141	51	104		216	1919.139
K140	53	103		217	1923.239
S41	54	115	no data		1939.537
K139	64	119		224	1956.002
S42	52	117	no data		1984.797
K136	58	114		209	2001.179
K137	59	112		207	2001.179
K138	60	117		208	2001.179
K133	49	118		218	2014.061
K134	48	117		216	2014.061
K135	52	120		218	2014.061
G19	53	103	no data		2044.999
K131	56	118		218	2072.095
K132	57	119		217	2072.095
K129	62	129		220	2080.566
K130	61	128		218	2080.566
K125	52	109		204	2098.432
K126	54	108		208	2098.432
K127	52	110		210	2098.432
K128	51	112		208	2098.432
S43	54	93	no data		2105.736
K122	54	110		210	2107.827
K123	52	106		209	2107.827
K124	51	109		212	2107.827
K119	58	109		210	2138.082
K120	59	110		212	2138.082
K121	56	112		209	2138.082
K117	59	106		190	2158.942
K118	56	102		189	2158.942
K116	59	104		193	2179.801
K112	62	94		182	2193.756
K113	63	99		185	2193.756
K114	61	98		181	2193.756
K115	63	106		182	2193.756
S44	54	107	no data		2354.337
K108	58	105		216	2359.700
K109	59	100		218	2359.700
K110	52	105		219	2359.700
K111	54	108		220	2359.700

K104	64	96		209	2376.609
K105	65	99		211	2376.609
K106	66	105		210	2376.609
K107	62	97		212	2376.609
K102	63	67		166	2385.087
K103	62	94		210	2385.087
G22	59	88	no data		2389.829
K100	64	63		160	2411.201
K101	62	66		165	2411.201
G23	60	123	no data		2499.001
K097	52	116		206	2544.410
K098	56	119		208	2544.410
K099	57	114		210	2544.410
K095	58	118		208	2564.153
K096	56	117		207	2564.153
K090	58	119		216	2571.064
K091	59	121		217	2571.064
K092	57	120		219	2571.064
K093	58	124		212	2571.064
K094	59	121		213	2571.064
S45	55	120	no data		2579.953
K086	49	138		219	3104.101
K087	50	139		216	3104.101
K088	50	142		217	3104.101
K089	51	138		218	3104.101
S31	52	127	no data		3124.632
K083	50	138		225	3143.435
K084	52	139		223	3143.435
K085	53	142		220	3143.435
K080	49	131		221	3241.996
K081	47	135		220	3241.996
K082	48	136		221	3241.996
K074	54	138		204	3257.042
K075	58	139		206	3257.042
K076	57	142		207	3257.042
K077	59	138		210	3257.042
K078	62	136		204	3257.042
K079	61	137		205	3257.042
S32	50	158	no data		3282.865
K069	59	136		209	3599.878
K070	60	139		210	3599.878
K071	62	137		207	3599.878
K072	60	138		208	3599.878
K073	61	139		210	3599.878
S21	56	171	no data		3653.306
K065	57	153		231	3669.238
K066	59	155		233	3669.238
K067	58	157		232	3669.238
K068	56	154		230	3669.238
S22	55	133	no data		3812.732
K062	59	132		221	3819.732
K063	57	133		220	3819.732
K064	62	135		221	3819.732
K061	81	158		248	3838.337

K058	70	128	210	3840.663
K059	71	127	212	3840.663
K060	74	129	218	3840.663
K055	66	121	216	3852.685
K056	68	125	212	3852.685
K057	67	126	214	3852.685
K052	58	130	202	3855.208
K053	57	132	206	3855.208
K054	59	131	205	3855.208
K048	58	142	230	3870.343
K049	59	147	225	3870.343
K050	58	146	227	3870.343
K051	56	147	226	3870.343
K047	57	140	228	3874.126
K043	53	141	224	3924.641
K044	54	145	220	3924.641
K045	52	142	224	3924.641
K046	53	146	227	3924.641
K039	55	121	210	3997.670
K040	56	125	209	3997.670
K041	57	122	207	3997.670
K042	59	127	202	3997.670
K034	59	118	193	4015.120
K035	59	119	197	4015.120
K036	60	117	194	4015.120
K037	61	121	196	4015.120
K038	60	119	191	4015.120
K033	59	125	219	4033.806
K031	70	107	223	4039.660
K032	67	109	220	4039.660
K028	65	123	227	4045.513
K029	62	126	231	4045.513
K030	61	131	229	4045.513
K026	50	158	248	4273.897
K027	47	158	238	4273.897
K021	46	155	247	4362.695
K022	44	163	249	4362.695
K023	44	156	257	4362.695
K024	44	158	262	4362.695
K025	43	157	260	4362.695
K017	56	150	248	4569.488
K018	51	148	245	4569.488
K019	56	145	241	4569.488
K020	57	149	242	4569.488
K014	62	146	248	4586.223
K015	58	146	238	4586.223
K016	59	148	242	4586.223
G37	60	149	no data	4591.222
K010	62	146	258	4592.938
K011	60	133	234	4592.938
K012	59	150	253	4592.938
K013	58	147	262	4592.938
K008	60	136	236	4599.652
K009	61	137	234	4599.652

K007	64	122	231	4622.365
K006	60	126	229	4638.363
K005	47	135	232	4727.959
K004	62	147	252	4743.064
K003	58	139	227	4801.977
K001	59	137	231	4822.889
K002	59	141	229	4822.889

Field data for the Campo Felice fault (averaged by site)

Dip (degrees from horizontal)	Strike (degrees from north)	Distance along fault (m)	Kinematic slip vector plunge direction (degrees from north)	Distance along fault (m)
53	127	75.45	218	75.45
54	127	132.34	213	132.34
52	141	203.89	209	203.89
54	124	273.18	208	273.18
59	123	328.13	218	328.13
54	129	463.75	214	463.75
56	126	512.86	207	612.69
48	143	575.46	207	644.68
53	139	742.97	209	706.85
56	138	785.47	208	756.16
56	132	865.22	211	804.05
52	129	983.31	211	835.15
57	136	1142.51	209	877.84
54	141	1418.93	204	945.04
61	137	1482.33	205	998.61
56	143	1524.13	208	1046.81
52	137	1577.62	212	1104.19
49	134	1608.09	210	1169.53
52	118	1729.93	213	1430.04
58	135	1759.74	212	1542.58
52	119	1905.9	214	1606.15
54	115	1939.54	215	1678.54
52	117	1984.8	207	1731.22
53	103	2045	214	1776.09
54	93	2105.74	215	1832.61
54	107	2354.34	212	1893.58
59	88	2389.83	218	1944.76
60	123	2499	216	2006
55	120	2579.95	207	2117.39
52	127	3124.63	206	2187.37
50	158	3282.87	209	2394.97
56	171	3653.31	213	2567.12
55	133	3812.73	222	3138.52
60	149	4591.22	208	3255.16
			209	3599.88
			232	3669.24
			220	3857.26
			224	3924.64
			223	4074.86
			243	4273.9
			255	4362.69
			236	4612.29
			250	4741.18

Appendix (v)

Data used to calculate strain-rate in 250 m bins along strike

Plunge of kinematic slip (degrees from horizontal)	Strike (degrees from north)	Kinematic slip direction (degrees from north)	Throw (m)	Distance along strike (m)	Strain-rate (ppm/yr)
47	128	213	13.77	125	3.41
47	129	213	14.19	375	3.52
47	134	208	12.63	625	3.08
52	136	208	12.74	875	2.59
50	135	210	10.98	1125	2.42
52	138	213	11.02	1375	2.25
51	134	212	9.62	1625	2.05
53	118	215	10.05	1875	1.99
54	104	210	10.55	2125	1.86
55	105	209	11.19	2375	1.91
53	113	209	10.87	2625	2.09
53	142	208	9.47	3375	1.82
54	148	221	8.80	3625	1.60
55	153	222	8.31	3875	1.39
55	153	249	7.30	4375	1.04

Appendix (vi)

‘Partitioned postseismic deformation associated with the 2009 Mw 6.3 L’Aquila earthquake surface rupture measured using a terrestrial laser scanner’ – Published manuscript based on Chapter 5 of this thesis

GEOPHYSICAL RESEARCH LETTERS, VOL. 37, L10309, doi:10.1029/2010GL043099, 2010

Partitioned postseismic deformation associated with the 2009 Mw 6.3 L'Aquila earthquake surface rupture measured using a terrestrial laser scanner

M. Wilkinson,[1] K. J. W. McCaffrey,[1] G. Roberts,[2] P. A. Cowie,[3] R. J. Phillips,[4] Alessandro Maria Michetti,[5] E. Vittori,[6] L. Guerrieri,[6] A. M. Blumetti,[6] A. Bubeck,[7] A. Yates,[8] and G. Sileo[5]

Received 3 March 2010; revised 7 April 2010; accepted 16 April 2010; published 25 May 2010.

[1] Using 3D terrestrial laser scan (TLS) technology, we have recorded postseismic deformation on and adjacent to the surface rupture formed during the 6th April 2009 L'Aquila normal faulting earthquake (Mw 6.3). Using surface modeling techniques and repeated surveys 8–124 days after the earthquake, we have produced a 4D dataset of postseismic deformation across a 3 × 65 m area at high horizontal spatial resolution. We detected millimetre-scale movements partitioned between discrete surface rupture slip and development of a hangingwall syncline over 10's of meters. We interpret the results as the signal of shallow afterslip in the fault zone. We find 52% of the total postseismic hangingwall vertical motion occurs as deformation within 30 m of the surface rupture. The total postseismic vertical motions are approximately 50% that of the coseismic. We highlight the importance of quantifying partitioned postseismic contributions when applying empirical slip-magnitude datasets to infer palaeoearthquake magnitudes. **Citation:** Wilkinson, M., et al. (2010), Partitioned postseismic deformation associated with the 2009 Mw 6.3 L'Aquila earthquake surface rupture measured using a terrestrial laser scanner, *Geophys. Res. Lett.*, *37*, L10309, doi:10.1029/2010GL043099.

1. Introduction

[2] Earthquakes produce coseismic motions that may amplify during the weeks after the mainshock. We report the novel use of a Terrestrial Laser Scanner (TLS) to monitor postseismic ground surface deformation following the 6th April 2009, M_w 6.3 earthquake, which struck L'Aquila in the Abruzzo region, Italy. Field observations [*Falcucci et al.*, 2009] in the days after the earthquake identified a discontinuous surface rupture ~12 km in length, with discontinuous ruptures over a distance of 2 km along the Paganica fault, situated northeast of Paganica (Figure 1). InSAR and body-wave seismology studies identified the earthquake slip plane as a SW-dipping normal fault with ~0.6–0.8 m coseismic slip at depth, propagating to the surface on the Paganica fault [*Atzori et al.*, 2009; *Walters et al.*, 2009]. The Paganica rupture, as observed in the field has normal sense displacement with a consistent downthrow along its length towards 218° ± 5° constrained by opening directions across ground cracks. Observed coseismic throw across localised cracks and ruptures ranged from 0.7 15.0 cm [*Galli et al.*, 2009; *Falcucci et al.*, 2009; *Emergeo Working Group*, 2010]. Observations with InSAR on Envisat tracks predicted "surface ruptures of ~10 cm" [*Walters et al.*, 2009]. Postseismic afterslip for the L'Aquila event has been inferred using a laser strain meter system located 20 km NE of the epicentre [*Amoruso and Crescentini*, 2009]. Also field observations documented the widening of ground cracks and increased surface offsets along the surface rupture observed over two months after the earthquake [*Galli et al.*, 2009; *Boncio et al.*, 2010]. Our study monitored the postseismic ground surface deformation of a concrete road (Site ID. PAG, 13.471450°E 42.362631°N). The road is perpendicular to the strike of the Paganica fault, across which a sharp surface rupture had formed. This section of the surface rupture is close to the centre of the overall trace with measured vertical offset of ~7.5 cm when we first visited the site on the 14th April, 8 days after the earthquake (Figure 1).

2. Method

[3] Terrestrial laser scanning is a relatively new form of ground based remote sensing. The time of flight of an emitted laser and its reflected returning counterpart are used to calculate the range between a tripod-mounted laser scanner and the ground surface. By incrementally adjusting the direction in vertical and horizontal steps, the scanner is able to sample reflections from regularly spaced areas of the ground surface within the line of sight of the scanner. For each ground reflection a unique point in 3D space is calculated, with many ground reflections populating a point cloud dataset. At study site PAG, using a Riegl LMS-z420i laser scanner with single point precision of 8 mm at 50 m range (Riegl LMS-420i datasheet, available at http://riegl.com/uploads/tx_pxpriegldownloads/10_DataSheet_Z420i_18-03-2010.pdf), point clouds of ~2.5 million individual points spaced between 4–10 mm apart were acquired, defining 195 m^2 of the road surface. A network of five reflector positions was

[1]Department of Earth Sciences, Durham University, Durham, U.K.
[2]School of Earth Sciences, Birkbeck College, University of London, London, U.K.
[3]School of Geosciences, University of Edinburgh, Edinburgh, U.K.
[4]Institute of Geophysics and Tectonics, University of Leeds, Leeds, U.K.
[5]Dipartmento di Scienze Chimiche e Ambientale, Università dell'Insubria, Como, Italy.
[6]Geological Survey of Italy, High Institute for the Environmental Protection and Research, Rome, Italy.
[7]Geospatial Research Ltd., Department of Earth Sciences, Durham University, Durham, U.K.
[8]Department of Earth Sciences, Uppsala University, Uppsala, Sweden.

0094-8276/10/2010GL043099

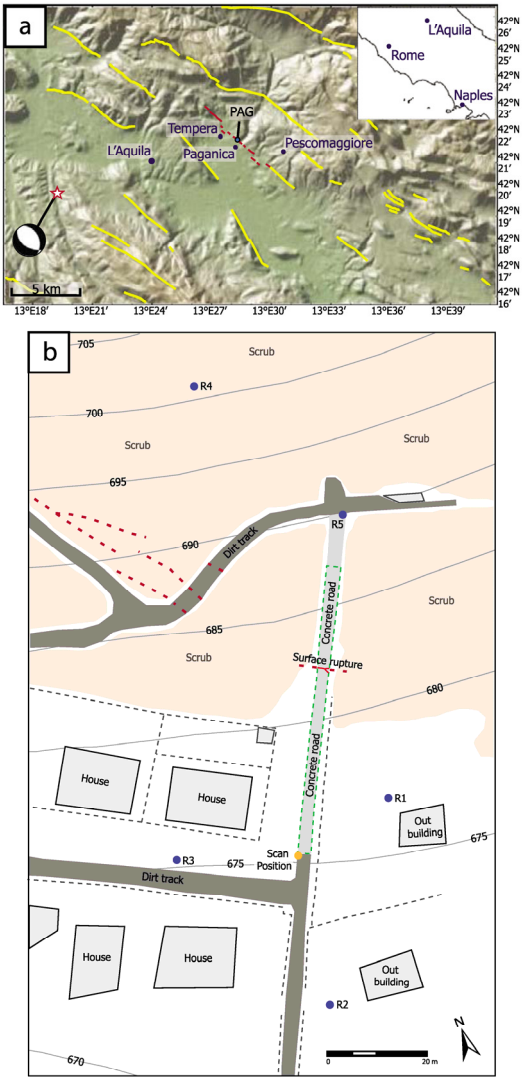

Figure 1. (a) Interpreted active normal faults of the Abruzzo region with the L'Aquila earthquake surface ruptures along the Paganica fault shown in red (adapted from *Roberts* [2008], *Falcucci et al.* [2009], *Michetti et al.* [2000], and ISPRA (Geological effects induced by the L'Aquila earthquake (6 April 2009, MI = 5.8) on the natural environment: Preliminary report, 2009, available at http://www.apat.gov.it/site/en-GB/Projects/INQUA_Scale/Documents/). The star south west of L'Aquila marks the hypocentre of the 2009 main shock with Quick gCMT focal mechanism attached (Strike 127°, Dip 50°, Rake −109°). (b) Site map of PAG showing the modeled dataset boundary inside the green dashed line and the location of the scan position and five reflectors. The discontinuous nature of the surface rupture outside the dataset boundary is shown by red dashed lines.

Table 1. Survey dates and measurements of rupture throw, syncline subsidence, combined rupture throw and syncline subsidence and line of sight extension between reflectors for each of the TLS datasets (PAG2-PAG7), relative to the first PAG1 datum

Date	Dataset ID	Days since earthquake	Rupture throw since 14/04/09 (mm)	Syncline subsidence since 14/04/09 (mm)	Combined rupture throw and syncline subsidence since 14/04/09 (mm)	Line of sight extension between reflectors since 14/04/09 (mm)
14/04/09	PAG 1	8	-	-	-	-
17/04/09	PAG 2	11	2.2	11.6	13.8	11.4
11/05/09	PAG 3	35	3.9	19.5	23.4	15.9
15/05/09	PAG 4	39	4.1	19.4	23.5	9.3
19/05/09	PAG 5	43	5.2	17.3	22.5	16.4
24/05/09	PAG 6	48	8.3	16.2	24.5	17.2
08/08/09	PAG 7	124	13.4	14.3	27.7	21.8

created, including sites 20 m into the footwall and 40 m into the hangingwall (Figure 1). Repeat datasets were obtained on seven occasions between 8 and 124 days after the main earthquake (Table 1). The reflectors were used as control points to position the point cloud datasets into a footwall-static reference frame relative to the day 8 dataset. A point cloud acquired for any scanned surface shows a Gaussian distribution of errors about the mean, which represents a close approximation to the real surface. A representative road surface for each of the seven TLS datasets for PAG was created using the discrete smooth interpolation (DSI) method [*Mallet*, 1992]. The DSI operates by creating a preliminary meshed surface with triangle vertices spaced 10 × 10 cm. Each of the triangle vertices are then translated to a location which represents the mean of the local surrounding points within the point cloud dataset (see Figure S1 for a workflow of the method).[1] The high density of our point clouds allowed us to detect minimum vertical differences between modeled surfaces of 1.5–5.7 mm, dependent on the part of the surface being compared, with 95% confidence (based on the 2σ variation in the moving point average for triangle vertices, window size 250 points, used to create the cross sectional plots in Figure 2b). Comparison of the vertical difference between the initial hangingwall surface and each subsequent surface allowed quantification of the near field postseismic hangingwall deformation relative to day 8 (Figure 2). The 5-point reflector network also enabled us to measure horizontal extension by comparing the average change in horizontal distance between reflectors paired across the fault relative to their horizontal distance at day 8.

3. Data and Comparison With Existing Afterslip Models

[4] Our datasets allowed us to precisely measure the relative vertical movement for points on the 65 × 3 m road surface (Figure 2). Two discrete styles of surface motion were observed. Firstly, throw on the rupture increased by 13.4 mm ± 2.6 mm between day 8 and day 124. Secondly, in addition to throw on the rupture, a further 14.3 mm ± 2.3 mm of vertical offset was measured, associated with growth of a warp or hangingwall syncline between day 8 and 124, originating from 7 m into the hangingwall. The syncline increased in width from 20 metres between days 8 and 15, to >30 m by day 124. The maximum vertical offset which developed between 8 and 124 days after the earthquake for the combined rupture and syncline was 27.7 mm ± 2.3 mm. We note that 14.3 mm of this value (52%) would have been missed if the syncline had not been recognised and measured. Horizontal extension measured by averaging the change in distance between reflectors paired across the rupture totalled 21.8 mm ± 5.0 mm. Measurements of extension over intermediate time periods are similar to the equivalent combined rupture and syncline vertical motions (Figure 3). The postseismic displacements recorded at GPS stations close to our PAG survey site [*Cheloni et al.*, 2010] are in broad agreement with the vertical motions we observe.

[5] We compare our measured datasets with previously published theoretical and empirical models that describe measured afterslip from rupture studies following previous earthquakes [*Bucknam et al.*, 1978; *Williams and Magistrale*, 1989; *Marone et al.*, 1991] (Figures 3 and 4). These models have not been optimised to fit our data; they have been plotted relative to day 8, our first observation, using published parameters defined from measured afterslip following previous earthquakes [*Bucknam et al.*, 1978; *Sharp et al.*, 1989; *Williams and Magistrale*, 1989].

4. Discussion

[6] The data for rupture throw, not including syncline subsidence, are indicative of afterslip, showing broad agreement with previously published afterslip models with correlation coefficients ranging from 0.9149–0.9318 (Figure 3). To estimate how much afterslip occurred on the rupture before our measurements began, we utilise field observations 500 m–1500 m SE from our site, PAG by *Boncio et al.* [2010]. They document the widening of a ground fracture by 30–50 mm between the 6th and 25th April and the vertical development of a hangingwall flexure by 25 mm between the 6th April and 19th May; we estimate 15 mm of this vertical motion developed between 6th–14th April. We measured 75 mm of offset across the rupture on the 14th April. If the observations of *Boncio et al.* [2010] apply to our site, we suggest that ~15 mm of this measurement was produced by postseismic deformation on the rupture prior to 14th April. By adding 15 mm to our observation of 13.4 mm of rupture throw observed between 14th April and 8th August, we estimate the total measured afterslip on the rupture since 6th April to be ~30 mm, in broad agreement with the previously published models. This estimate suggests afterslip at PAG is around 50% of the mostly coseismic offset totalling 75 mm observed across the rupture on the 14th April. However, if the postseismic deformation associated with syncline growth are added to those of rupture throw, the models describe such combined motions with lower

[1] Auxiliary materials are available in the HTML. doi:10.1029/2010GL043099.

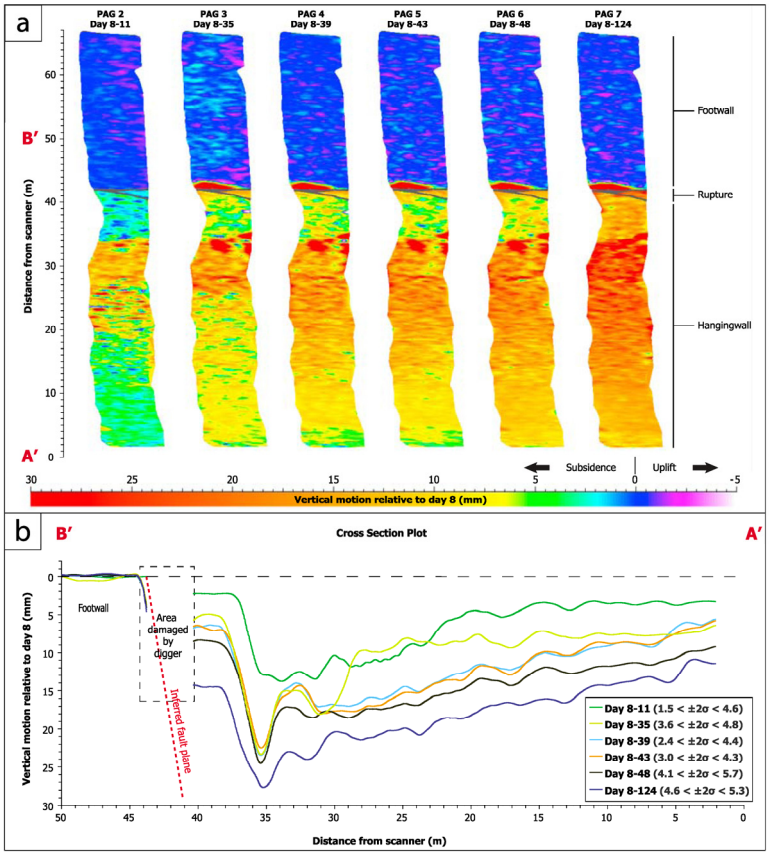

Figure 2. (a) Color map plots showing vertical motion values (mm) in a footwall static reference frame in 3D space for TLS datasets PAG2–PAG7, relative to the first scanned dataset PAG1 (8 days after the earthquake). A time lapse animation of the vertical motions is available in Movie S1. (b) Cross sectional plot taken perpendicular to the main strike of the rupture between A′ and B′. Each plot was calculated using a moving point average with window size 250 points (representing 3 m width × 0.7 m distance along the road), using the vertical motion values from each of the colour map plots in Figure 2a. The boxed zone highlights an area of damage (breaking off of the footwall) the surface rupture received between days 11 and 35 attributed to a digger being driven over it. The similarity of the deformation observed along the rest of the road before and after the digger damage shows that the immediate 2–3 m of footwall was the only part of the road which was vulnerable and subsequently damaged. $\pm 2\sigma$ bounds represent the range of certainty in vertical motion for each cross sectional plot which changes along section due to variations in the smoothness of the road.

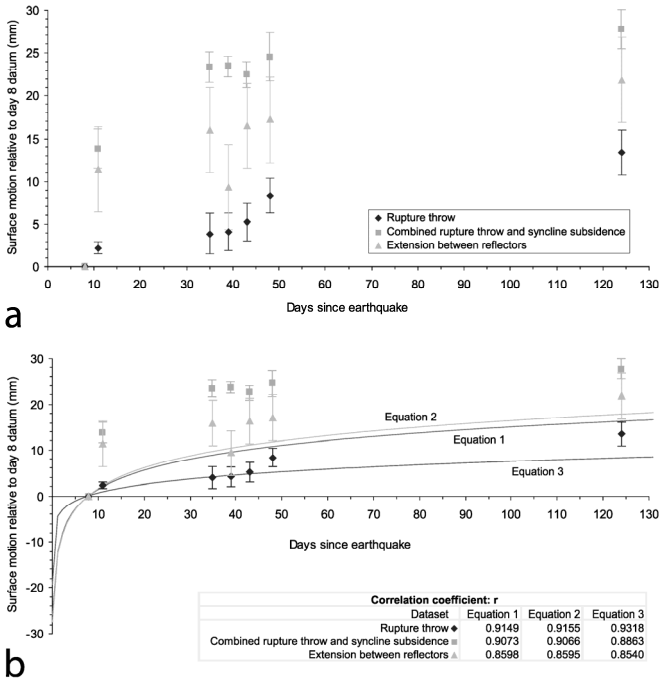

Figure 3. (a) Surface motions for the six TLS datasets (PAG2–PAG7), relative to the initial TLS dataset PAG1, 8 days following the earthquake (Table 1) plotted against time since the earthquake. Error bars represent 2σ (95%) certainty. (b) Graphical comparison of published theoretical and empirical models for afterslip (Equations 1, 2 and 3 in Figure 4) to our datasets, together with their correlation coefficients.

correlation coefficients 0.8863–0.9073, largely because of the relatively rapid syncline subsidence between days 8–11. Between days 8–124, the rate and magnitude of syncline subsidence were comparable to and at times exceeded that of the rupture afterslip, with the combined rupture afterslip and syncline subsidence being approximately twice that of the rupture afterslip at day 124. The similarity in magnitude of the combined rupture throw and syncline subsidence in relation to the data for horizontal extension suggests that hangingwall deformation responsible for syncline growth formed a major component of the postseismic extension at PAG.

[7] Numerous studies suggest the growth of hangingwall synclines are common during normal faulting earthquakes. Hangingwall synclines are observed at many palaeoseismic sites within the Italian Apennines [*D'Addezio et al.*, 1996; *Pantosti et al.*, 1996; *Galli et al.*, 2002; *Galli et al.*, 2008]. Also, surface motions described as 'uplift of the footwall and a warp-like hangingwall subsidence (folding)' were recorded during a study of afterslip on the surface rupture of the 1995 Egion earthquake [*Koukouvelas and Doutsos*, 1996]. Indeed, we have observed progressive development of hangingwall synclines, with similar subsidence in preliminary processing of TLS datasets spanning equivalent time periods at two other sites along the Paganica surface rupture (Figures S2 and S3).

[8] The localised nature of surface motions at PAG produced several centimetres of slip across the rupture that was visible with the naked eye. However, we note that the vertical motions associated with syncline growth would have been missed without the use of TLS, as they were too subtle to observe with the naked eye alone, and no pre-earthquake datum existed in the form of a precise topographic map. This is important because such subtle subsidence associated with hangingwall folding accounts for 52% of the total vertical postseismic deformation. Such deformation may be un-accounted for within empirical slip-magnitude relationships, especially for smaller earthquakes [e.g., *Wells and Coppersmith*, 1994]. If this is the case, we note that in our study, the inclusion of hangingwall deformation would have doubled the surface offset for the given earthquake magnitude, if the total subsidence had not been attributed to a combination of postseismic and coseismic deformation. In palaeoseismic studies such slip-magnitude datasets are used to

$D = a + b\log T$ (1)[1]		$U^P = U_C^S + \alpha' \ln\left[\left(\frac{\beta'}{\alpha'}\right)t + 1\right]$ (2)[2]			$D = at^b$ (3)[3]	
[1]Model 1: Equation defined by least-squares regression of observed displacement data on logarithm of time from the 1976 Guatemala earthquake [*Buckham et al.*, 1978]. D = modeled displacement (mm) a = coseismic rupture offset (mm) b = gradient of best fit line through the data plotted as logarithm of time T = time since earthquake (days)		[2]Model 2: Two variable version of a closed-form solution for afterslip [*Marone et al.*, 1991, after *Scholtz*, 1990] modified to accommodate coseismic measurements, and used to model 1987 Superstition Hills afterslip data [*Sharp et al.*, 1989]. U_P = modeled displacement (mm) U^S_C = coseismic rupture offset (mm) α' = a parameter (mm) defining the friction rate parameter divided by spring stiffness, analogous to the thickness of the velocity strengthening region, the former obtained from best fit to data plotted as logarithm of time β' = coseismic slip velocity in the velocity strengthening region (mm/day)			[3]Model 3: Slip decay model [*Williams and Magistrale*, 1989] describing displacement data from the 1987 Superstition Hills earthquake sites 2M, 2T and 2U. D = modeled displacement (mm) a = coseismic rupture offset (mm) b = decay rate parameter t = time since earthquake (days)	
a (mm)	b	U^S_C (mm)	α'	β'	a (mm)	b
0 (replacement of 50.9 as there is no coseismic component to be compared in our dataset)	13.9	0 (replacement of 237.1 as there is no coseismic component to be compared in our dataset)	65.69	518.1	14.6	0.131
Parameters calculated from data of the 1976 Guatemala earthquake, Zacapa site.		Parameters calculated from data of the 1987 Superstition Hills Earthquake site 2T [*Sharp et al.*, 1989].			Parameters calculated from data of the 1987 Superstition Hills Earthquake, Site 2T.	

Figure 4. Theoretical and empirical afterslip models with parameters obtained from afterslip datasets of previous earthquakes.

estimate palaeoearthquake magnitudes from measured offsets [*Bakun et al.*, 2005; *Vigny et al.*, 2005; *Ryder et al.*, 2007]. Uncertainty in the surface offset for a given magnitude within the slip-magnitude datasets will lead to uncertainty in the palaeoearthquake magnitude for a given offset. Routine TLS surveying permits hangingwall synclines and other off-fault deformation to be quantified and distinguished from rupture slip.

[9] **Acknowledgments.** Funded by NERC grants NE/H003266/1 and NE/E016545/1 and Durham University Doctoral Fellowship (M. Wilkinson). We thank N. De Paola for assistance in the field M. Allen for comments on an earlier draft and D. Stevenson and G. Wilkinson for maintaining computing support. Meng Wei and an anonymous reviewer are thanked for their constructive comments.

References

Amoruso, A., and L. Crescentini (2009), Slow diffusive fault slip propagation following the 6 April 2009 L'Aquila earthquake, Italy, *Geophys. Res. Lett.*, *36*, L24306, doi:10.1029/2009GL041503.

Atzori, S., I. Hunstad, M. Chini, S. Salvi, C. Tolomei, C. Bignami, S. Stramondo, E. Trasatti, A. Antonioli, and E. Boschi (2009), Finite fault inversion of DInSAR coseismic displacement of the 2009 L'Aquila earthquake (central Italy), *Geophys. Res. Lett.*, *36*, L15305, doi:10.1029/2009GL039293.

Bakun, W. H., et al. (2005), Implications for prediction and hazard assessment from the 2004 Parkfield earthquake, *Nature*, *437*, 969–974, doi:10.1038/nature04067.

Boncio, P., A. Pizzi, F. Brozzetti, G. Pomposo, G. Lavecchia, D. Di Naccio, and F. Ferrarini (2010), Coseismic ground deformation of the 6 April 2009 L'Aquila earthquake (central Italy, M_w6.3), *Geophys. Res. Lett.*, *37*, L06308, doi:10.1029/2010GL042807.

Bucknam, R. C., G. Plafker, and R. V. Sharp (1978), Fault movement (afterslip) following the Guatemala earthquake of February 4, 1976, *Geology*, *6*, 170–173, doi:10.1130/0091-7613(1978)6<170:FMAFTG>2.0.CO;2.

Cheloni, D., et al. (2010), Coseismic and initial postseismic slip of the 2009 Mw 6.3 L'Aquila earthquake, Italy, from GPS measurements, *Geophys. J. Int.*, in press.

D'Addezio, G., D. Pantosti, and P. M. De Martini (1996), Palaeoseismologic and geomorphic investigations along the middle portion of the Ovindoli-Pezza Fault (Central Italy), *Ann. Geofis.*, *39*, 663–675.

Emergeo Working Group (2010), Evidence for surface rupture associated with the Mw 6.3 L'Aquila earthquake sequence of April 2009 (central Italy), *Terra Nova*, *22*, 43–51, doi:10.1111/j.1365-3121.2009.00915.x.

Falcucci, E., et al. (2009), The Paganica Fault and Surface Coseismic Ruptures Caused by the 6 April 2009 Earthquake (L'Aquila, Central Italy), *Seismol. Res. Lett.*, *80*, 940–950, doi:10.1785/gssrl.80.6.940.

Galli, P., F. Galadini, M. Moro, and C. Giraudi (2002), New palaeoseismological data from the Gran Sasso d'Italia area (central Apennines), *Geophys. Res. Lett.*, *29*(7), 1134, doi:10.1029/2001GL013292.

Galli, P., F. Galadini, and D. Pantosti (2008), Twenty years of Palaeoseismology in Italy, *Earth Sci. Rev.*, *88*, 89–117, doi:10.1016/j.earscirev.2008.01.001.

Galli, P., et al. (2009), April 6, 2009 L'Aquila earthquake; macroseismic survey, surficial effects and seismotectonic implications, *Ital. J. Quat. Sci.*, *22*, 235–246.

Koukouvelas, I. K., and T. T. Doutsos (1996), Implications of structural segmentation during earthquakes: the 1995 Egion Earthquake, Gulf of Corinth, Greece, *J. Struct. Geol.*, *18*, 1381–1388, doi:10.1016/S0191-8141(96)00071-5.

Mallet, J. L. (1992), GOCAD: A computer aided design program for geological applications, in *Three Dimensional Modeling With Geoscientific Information Systems*, edited by A. K. Turner, pp. 123–141, Kluwer, Netherlands.

Marone, C. J., S. H. Scholtz, and R. Bilham (1991), On the mechanics of Earthquake Afterslip, *J. Geophys. Res.*, *96*, 8441–8452, doi:10.1029/91JB00275.

Michetti, A. M., L. Serva, and E. Vittori (2000), Italy hazard from Capable Faulting, a database of active capable faults of the Italian onshore territory [CD-ROM], report, Agenzia Nazionale Protezione Ambiente, Rome.

Pantosti, D., G. D'Addezio, and F. R. Cinti (1996), Palaeoseismicity of the Ovindoli-Pezza fault, central Apennines, Italy: A history including a large, previously unrecorded earthquake in the Middle Ages (860–1300 A.D.), *J. Geophys. Res.*, *101*, 5937–5959, doi:10.1029/95JB03213.

Roberts, G. P. (2008), Visualisation of active normal fault scarps in the Apennines, Italy: A key to assessment of tectonic strain release and earth-

quake rupture, in *Google Earth Science*, edited by D. De Paor, *J. Virtual Explorer*, *30*(4).

Ryder, I., P. Parsons, T. J. Wright, and G. J. Funning (2007), Post-seismic motion following the 1997 Manyi (Tibet) earthquake: InSAR observations and modeling, *Geophys. J. Int.*, *169*, 1009–1027, doi:10.1111/j.1365-246X.2006.03312.x.

Scholz, C. H. (1990), *The Mechanics of Earthquakes and Faulting*, Cambridge Univ. Press, New York.

Sharp, R. V., et al. (1989), Surface faulting along the Superstition Hills fault zone and nearby faults associated with the earthquakes of 24 November 1987, *Bull. Seismol. Soc. Am.*, *79*, 252–281.

Vigny, C., et al. (2005), Insight into the 2004 Sumatra–Andaman earthquake from GPS measurements in southeast Asia, *Nature*, *436*, 201–206, doi:10.1038/nature03937.

Walters, R. J., J. R. Elliott, N. D'Agostino, P. C. England, I. Hunstad, J. A. Jackson, B. Parsons, R. J. Phillips, and G. Roberts (2009), The 2009 L'Aquila earthquake (central Italy): A source mechanism and implications for seismic hazard, *Geophys. Res. Lett.*, *36*, L17312, doi:10.1029/2009GL039337.

Wells, D. L., and K. J. Coppersmith (1994), New empirical relationships among magnitude, rupture length, rupture width, rupture area and surface displacement, *Bull. Seismol. Soc. Am.*, *84*, 974–1002.

Williams, P. L., and H. W. Magistrale (1989), Slip along the Superstition Hills fault associated with the 24 November 1987 Superstition Hills, California, Earthquake, *Bull. Seismol. Soc. Am.*, *79*, 390–410.

A. M. Blumetti, L. Guerrieri, and E. Vittori, Geological Survey of Italy, High Institute for the Environmental Protection and Research, Via Curtatone, 3, I 00185 Roma, Italy.

A. Bubeck, Geospatial Research Ltd., Department of Earth Sciences, Durham University, Durham DH1 3LE, UK.

P. A. Cowie, School of Geosciences, University of Edinburgh, Drummond Street, Edinburgh EH8 9XP, UK.

K. J. W. McCaffrey and M. Wilkinson, Department of Earth Sciences, South Road, Durham University, Durham DH1 3LE, UK. (maxwell.wilkinson@durham.ac.uk)

A. M. Michetti and G. Sileo, Dipartmento di Scienze Chimiche e Ambientale, Università dell'Insubria, Via Valleggio 11, I-22100, Como, Italy.

R. J. Phillips, Institute of Geophysics and Tectonics, University of Leeds, Leeds LS2 9JT, UK.

G. Roberts, School of Earth Sciences, Birkbeck College, University of London, Malet Street, London WC1E 7HX, UK.

A. Yates, Department of Earth Sciences, Uppsala University, Villavägen 16, SE-75236 Uppsala, Sweden.

Appendix (vii)

‘Distribution and Magnitude of Postseismic Deformation of the 2009 L’Aquila Earthquake (M6.3) Surface Rupture Measured Using Repeat Terrestrial Laser Scanning’ - Published manuscript based on Chapter 5 of this thesis

Geophysical Journal International

Geophys. J. Int. (2012) **189,** 911–922 doi: 10.1111/j.1365-246X.2012.05418.x

Distribution and magnitude of post-seismic deformation of the 2009 L'Aquila earthquake (*M*6.3) surface rupture measured using repeat terrestrial laser scanning

M.W. Wilkinson,[1] K.J.W. McCaffrey,[1] G.P. Roberts,[2] P.A. Cowie,[3] R.J. Phillips,[4] M. Degasperi,[5] E. Vittori[6] and A.M. Michetti[7]

[1] *Department of Earth Sciences, Durham University, UK. E-mail: maxwell.wilkinson@durham.ac.uk*
[2] *Department of Earth and Planetary Sciences, Birkbeck, University of London, UK*
[3] *Department of Earth Science, University of Bergen, Norway*
[4] *School of Earth and Environment, University of Leeds, UK*
[5] *Geological Survey of Trentino, Italy*
[6] *Geological Survey of Italy, High Institute for the Environmental Protection and Research, Rome, Italy*
[7] *Dipartmento di Scienza e Alta Tecnologia, Università dell'Insubria, Como, Italy*

Accepted 2012 February 9. Received 2012 January 17; in original form 2011 July 11

SUMMARY

We captured post-seismic deformation close to the surface rupture of the 2009 L'Aquila earthquake (*M*6.3, central Italy) using repeat terrestrial laser scan (TLS) methods. From 8 to 126 d after the earthquake, we repeatedly laser scanned four road surfaces that intersected the earthquake surface rupture. We modelled vertical near-field deformation, at millimetre-level precision, by comparing subsequent laser scan data sets to the first acquired at each site. The horizontal post-seismic deformation at each site was measured between reflectors paired across the rupture. The TLS data were supplemented by total station data from a fifth site which measured the vertical and horizontal components of post-seismic deformation between two points spanning the rupture. We find post-seismic deformation increased between 44 and 126 d at the southeastern end of the rupture, beneath which a significant gradient in coseismic slip exists within the fault zone. The location, rate of decay and spatially-localized nature of the post-seismic deformation, within tens of metres of the surface rupture suggests it is due to afterslip in the fault zone, driven by increased shear stresses at the edges of regions which slipped coseismically. We note that the magnitude of post-seismic deformation in the far field obtained from InSAR and GPS is not significantly greater than the deformations we have measured close to the rupture. We suggest that shallow, localized afterslip within the fault zone is responsible for the majority of the regional post-seismic deformation field.

Key words: Seismic cycle; Transient deformation; Creep and deformation; Continental neotectonics; Dynamics and mechanics of faulting; Kinematics of crustal and mantle deformation.

1 INTRODUCTION

The 2009 L'Aquila earthquake (M_w 6.3) occurred in the central Italian province of L'Aquila on the April 6 at 3:32 a.m. local time (01:32 UTC). The seismicity was identified to originate from approximately 0.6 to 0.8 m normal sense displacement within a fault zone dipping 54° to the southwest (Walters *et al.* 2009). The Paganica fault, with normal displacement, striking ∼130° N, 6 km east–northeast of the city of L'Aquila was identified as the source of the seismicity. A discontinuous surface rupture was mapped for 2.6 km along the base of the Paganica fault (Vittori *et al.* 2011; Figs 1 and 2). The sharp increase in topographic gradient, which occurs northeastwards across contour 680 m and between sites PA and SP (Fig. 2), indicates the geomorphic expression of the Paganica fault. Each rupture segment displayed a consistent kinematic slip direction of 218° ± 5° (Wilkinson *et al.* 2010). The coseismic offset along these rupture segments was of normal-sense displacement and ranged from hairline cracks with little or no offset to up to 10 cm vertical offset towards the centre of the surface rupture, close to the town of Paganica (Vittori *et al.* 2010).

The L'Aquila earthquake has provided the opportunity for detailed investigation of the magnitude, distribution and rate of decay over time of post-seismic deformation. A study of post-seismic deformation (Amoruso & Crescentini 2009) was conducted at 1400 m depth within the fault zone, using data from two laser strainmeters. The study revealed the propagation of post-seismic slip akin to a diffuse model, while rejecting a model of constant propagation velocity. A study of surface faulting by Boncio *et al.* (2010), revealed

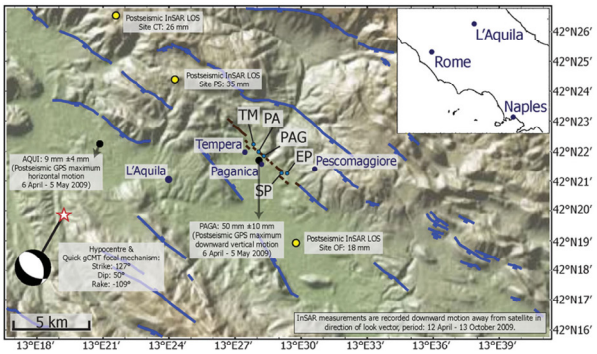

Figure 1. Map of the interpreted active normal faults of the L'Aquila region, and the five study sites PAG, SP, EP, TM and PA. The L'Aquila earthquake surface ruptures are shown in brown (adapted from Michetti *et al.* 2000; Roberts 2008; Falcucci *et al.* 2009; Vittori *et al.* 2011). Additional post-seismic data in the far field from D-InSAR is obtained from Lanari *et al.* (2010). The post-seismic GPS data is from Cheloni *et al.* (2010).

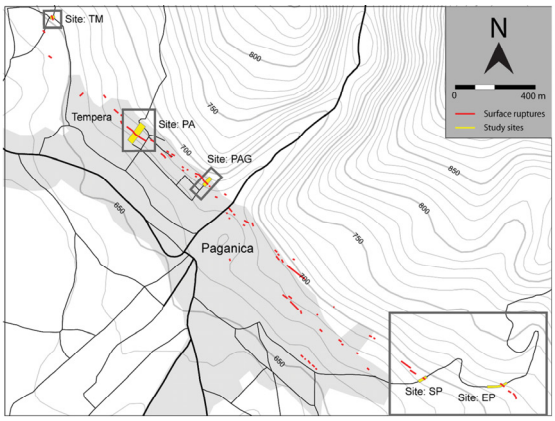

Figure 2. Regional topographic map, detailing the location of the five study sites in yellow. The mapped surface ruptures shown in red after Vittori *et al.* (2011). Black lines represent major and minor roads. The grey shading shows the extent of the urban area around the town of Paganica and its suburbs. Topographic contours are shown in dark grey with a 10 m interval. The boxes around each study site refer to the coverage of the site maps in Fig. 3.

the first evidence of near-field post-seismic deformation immediately after the earthquake. They observed widening of ground fractures by 2 cm between April 6 and April 25 and the deformation of a hangingwall flexure 2.5–3 m wide which opened by 4–5 cm and was vertically offset by ∼2.5 cm. The component magnitudes and rate of decay of post-seismic deformation in the far field were computed by Cheloni *et al.* (2010), who produced an inversion model of the fault zone from two GPS stations (AQUI and PAGA, Fig. 1). They showed that afterslip occurred in regions at the periphery of coseismic slip where increased shear stress is produced by large gradients in coseismic slip, driving afterslip in regions of the fault zone, which did not slip coseismically. A DInSAR analysis of post-seismic displacements in the far field was conducted by Lanari *et al.* (2010). The hangingwall of the Paganica fault was found to be actively deforming with decay times comparable to those of afterslip within the fault zone, suggesting the far-field deformation was driven by fault zone processes. The study identified post-seismic deformation, which was greatest and decayed more rapidly in three discrete regions (PS, CT and OF, Fig. 1).

In this study, we investigate the along-strike distribution and magnitude of post-seismic deformation using repeat Terrestrial Laser Scan (TLS) data sets at four sites (Figs 1 and 2: TM, PAG, SP and EP) spanning the extent of the surface rupture of the Paganica fault, as defined by Vittori *et al.* (2011). We complement these data with that of across-rupture total station measurements from a fifth site (Figs 1 and 2: PA). This multisite approach expands on the previous single-site repeat-TLS study (Wilkinson *et al.* 2010) and provides an insight into the along-rupture magnitude and distribution of post-seismic deformation. Our measurements are confined to surface deformation in the near field within a few tens of metres of the surface

rupture. We compare the magnitude of post-seismic deformation measured in the near-field to far-field values measured from studies of GPS (Cheloni *et al.* 2010) and DInSAR (Lanari *et al.* 2010) to suggest post-seismic deformation on all scales is driven by afterslip within a discrete fault zone. Using measurements of near-field on-rupture post-seismic deformation we provide further evidence to suggest post-seismic deformation within the fault zone occurs in specific regions, which experienced increased shear stresses due to large gradients in coseismic slip.

2 METHOD

Terrestrial Laser Scanning is a ground-based light detection and ranging (LiDAR) technology, which enables exceptionally high-resolution 'point cloud' 3-D digital topography to be acquired, dependent on the machine specification, at lines of sight up to 2 km from the scanner. TLS is often used to document and characterize primary and secondary site effects in earthquake-damaged regions for geological and geo-engineering purposes. Recent examples include reconnaissance reports from the Nigata, Chile, Sendai and Haiti earthquakes by the GEER Association, visualization of surface and structural deformations from the 2004 Nigata earthquake (Kayen *et al.* 2006) and detailed rupture-offset mapping using TLS after the 2010 El-Mayor-Cucapah earthquake (Gold *et al.* 2010).

TLS technology can also be used for detection of change in areas of active deformation, with subtle changes in the geometry of the data sets used to model and infer the resultant deformation occurring between the acquisition of one data set and the next. We employ such an approach in this study to ascertain the magnitude and along rupture distribution of post-seismic deformation at four sites on the surface rupture of the L'Aquila earthquake. A Riegl LMS-z420i terrestrial laser scanner (RIEGL Laser Measurement Systems GmbH, Horn, Austria) was used to acquire a total of twenty three point cloud data sets between 8 and 126 d after the L'Aquila earthquake over four road sites (Table 1; Figs 1 and 2: PAG, SP, EP and TM) cross-cut by the surface rupture of the L'Aquila earthquake. The laser scanner was set up in a level orientation over the same benchmark (Fig. 3: Scan positions) at each site and the point cloud data set collected during each occupation comprised a single scan of the road surface. The relatively short range of the area studied from the scan position (up to 50 m) allowed us to collect data sets with very high spatial density (point spacing of 4–10 mm). The laser scan data sets were corrected for changes in air temperature and pressure between successive scans. When using the Riegl LMS-z420i laser scanner, a fluctuation of either +20 °C in air temperature or –70 mBar in air pressure produce a change of +20 ppm in the range measurement (+1 mm for a range measurement at 50 m). Changes in relative humidity are negligible. An increase of +90 per cent in relative humidity at 20 °C air temperature and 1000 mBar air pressure increases the range measurement by +0.8 ppm. A semi-permanent fixed network of cylindrical reflectors were used at each site to position subsequent point cloud data sets into a preliminary footwall static reference frame relative to the initially acquired point cloud using the Riegl RiSCAN registration software. The point cloud data sets were individually interpolated within GoCAD to produce representative road surfaces for each point cloud data set using the discrete smooth interpolation (DSI) method (Mallet 1992). The DSI method aims to produce an interpolated surface with the smoothest profile possible, while still honouring the input point cloud. The DSI method is particularly suited to produce representative surfaces of essentially smooth features such as road surfaces, as the method omits small-scale noise inherent to the point cloud from the final interpolated surface. Discrete offsets in the road surface due to earthquake rupturing were preserved by interpolating the footwall and hangingwall as separate surfaces. After surface creation, the reflector-calculated preliminary footwall static reference frame is refined. The refinement involves rotating each of the subsequently acquired pointset surfaces such that their footwall surface triangle vertices colocate with those of the initially acquired pointset surface. This surface-to-surface refinement procedure ensures modelled differences in the hangingwall are due to post-seismic deformation and not misalignment of the point clouds. The vertical component of post-seismic deformation was measured by calculating the vertical difference between correspondingly paired triangle vertices of the initial and subsequent surfaces. By seeding each DSI interpolation using a common initial surface and boundary condition, all corresponding triangle vertices from each of the surfaces were created such that only a vertical difference existed between them. The map spacing between neighbouring vertices was set to 10 cm, which is far greater than the horizontal post-seismic deformation measured at the sites. This approach ensured that lateral differences did not exist between vertices, which could upset the calculation of true vertical difference. Each vertical difference calculated between vertices represents the vertical component of surface deformation, which occurred between the acquisitions of the two data sets, at a unique position on the road surface. The calculated vertical differences can be colour-mapped onto the surface (Figs 4a–7a). Cross-sectional plots of the deformation, perpendicular to the main strike of the rupture were produced for each site using a moving point average with window size of 250 points using the vertical difference values for each site (Figs 4b–7b). The moving window represents 3 m width × 0.7 m distance along the road at site PAG, 6 m × 0.35 m at site SP, 9 m × 0.23 m at site EP and 4 m × 0.52 m at site TM. The cylindrical reflectors at each location also enabled us to measure horizontal deformation by comparing the change in horizontal distance between reflector sites paired across the rupture relative to their initial distance during the acquisition of the first data set.

3 RESULTS

3.1 Site: PAG

Site PAG, towards the centre of the surface rupture (Fig. 2) is situated on a rough concrete road on the outskirts of Paganica (Fig. 3c) and has been described previously by Wilkinson *et al.* (2010), but is included here for completeness. The surface rupture cross cuts the concrete road with a NW–SE strike and an initial vertical displacement of ∼7.5 cm observed 8 d after the earthquake. The TLS data acquired at the site consists of seven repeat scans acquired at 8, 11, 35, 39, 43, 48 and 124 d after the earthquake (Table 1). The scan data was cropped to cover a 3 m × 65 m section of the road that spans the hangingwall, rupture and footwall of the Paganica surface rupture. The results of the surface generation and vertical difference measurements describe surface deformation, which are partitioned between afterslip on the rupture and the progressive development of a growing hangingwall trough (Fig. 4). The boxed zone in Fig. 4(b) highlights an area of damage (breaking off of the footwall) the surface rupture received between days 11 and 35 attributed to a vehicle being driven over it. The similarity of the deformation observed along the rest of the road before and after the vehicle damage shows that the immediate 2–3 m of footwall was the only part of the road which was damaged. Both the rupture afterslip and the hangingwall

Table 1. Survey dates and measurements of rupture throw, hangingwall trough subsidence, combined rupture throw and hangingwall trough subsidence and horizontal line of sight extension between reflectors for each of the five data sets, relative to the first measurement acquired at each site.

Date	Data set ID	Location (lat/long)	Days since earthquake	Rupture throw since first data set (mm)	Hangingwall trough subsidence since first data set (mm)	Combined rupture throw and hangingwall trough subsidence since first data set (mm)/Site PA: total vertical deformation (mm)	Horizontal line of sight extension between reflectors since first data set (mm)
2009 April 14	PAG 1		8	–	–	–	–
2009 April 17	PAG 2		11	2.2	11.6	13.8	11.4
2009 May 11	PAG 3	13.471450°E	35	3.9	19.5	23.4	15.9
2009 May 15	PAG 4	42.362631°N	39	4.1	19.4	23.5	9.3
2009 May 19	PAG 5		43	5.2	17.3	22.5	16.4
2009 May 24	PAG 6		48	8.3	16.2	24.5	17.2
2009 August 08	PAG 7		124	13.4	14.3	27.7	21.8
2009 April 17	SP1		11	–	–	–	–
2009 May 14	SP2	13.484543°E	38	6.8	2.7	9.5	7.2
2009 May 18	SP3	42.354447°N	42	7.3	3.3	10.6	16.5
2009 May 21	SP4		45	8.0	3.3	11.3	19.7
2009 August 10	SP5		126	13.1	2.9	16.0	27.6
2009 April 16	EP1		10	–	–	–	–
2009 May 14	EP2	13.489044°E	38	3.3	−3.1	0.2	14.3
2009 May 18	EP3	42.354056°N	42	3.4	−2.2	1.2	15.9
2009 May 22	EP4		46	4.5	−2.2	2.3	10.5
2009 August 09	EP5		125	10.8	4.6	15.4	20.3
2009 April 18	TM1		12	–	–	–	–
2009 May 13	TM2	13.462563°E	37	0.6			4.8
2009 May 17	TM3	42.370022°N	41	0.9	–	–	4.2
2009 May 20	TM4		44	1.7	–	–	2.9
2009 May 23	TM5		47	1.9	–	–	1.4
2009 August 08	TM6		124	2.4	–	–	3.2
2009 April 23	PA1		17	–	–	–	–
2009 May 05	PA2	13.467295°E	31	–	–	3.1	5
2009 May 20	PA3	42.364682°N	44	–	–	7.8	6.3
2009 June 10	PA4		65	–	–	10.8	6.8
2009 June 30	PA5		85	–	–	11.7	12.5
2009 July 29	PA6		114	–	–	13.8	10.1

trough continued to develop with a decaying rate until the end of our survey (Fig. 8a). The maximum rupture afterslip totalled 13.4 ± 2.6 mm. The maximum observed subsidence in the hangingwall trough was 14.3 ± 2.3 mm. The maximum vertical post-seismic deformation observed was 27.7 ± 2.3 mm, from the combined rupture afterslip and hangingwall trough subsidence. The network of five reflector positions (R1–R5, Fig. 3c) were used to calculate the horizontal component of post-seismic deformation, which totalled 21.8 ± 5.0 mm for the 8–124-d period after the earthquake.

3.2 Site: SP

Site SP is situated towards the southeastern end of the surface rupture (Fig. 2), on the tarmac road from Paganica to Pescomaggiore (Fig. 3a). The rupture is defined by a 5–50 cm wide zone of small cracks, striking NE–SE. The cracks were 2–5 mm wide with no apparent vertical displacement when first observed 11 d after the earthquake. Five scans were acquired at 11, 38, 42, 45 and 126 d after the earthquake, spanning an area 6 m × 49 m encompassing the hangingwall, surface rupture and footwall. Surface fitting and vertical differencing show progressive hangingwall subsidence indicative of rupture afterslip, accompanied by the initial development of a trough in the immediate hangingwall of the rupture (Fig. 5). Rupture afterslip was measured with respect to the first scan datum and inferred by projecting the hangingwall surface of each data set into the rupture zone. The maximum afterslip 126 d after the earthquake was 13.1 ± 4.1 mm, calculated from the difference between scan SP1 and SP5. The hangingwall trough developed between data sets SP1 and SP2 (11–38 d), representing 2.7 ± 2.2 mm of vertical subsidence. Further significant growth of the trough was not observed after 38 d. The maximum vertical post-seismic deformation is 16.0 ± 2.2 mm. This figure represents the sum of the afterslip observed between the first and last data acquisitions (13.1 mm), plus the observed subsidence of the hangingwall trough (2.7 mm) over the same period. A network of four reflectors (Fig. 3a, Rs1–Rs4) paired across the rupture moved 27.6 ± 5.0 mm horizontally in the direction of the coseismic slip vector (218°) between SP1 and SP5. The components of post-seismic deformation of each surface relative to the first are shown in Fig. 8(b); they describe deformation increasing at a decaying rate, indicative of afterslip and near-field post-seismic deformation.

3.3 Site: EP

Site EP is located 370 m due east of site SP on the road from Paganica to Pescomaggiore (Fig. 2). The appearance of the rupture is very similar to that at SP, defined by a narrow zone of cracks crossing the road. The cracks had horizontal displacements of 2–5 mm, but no

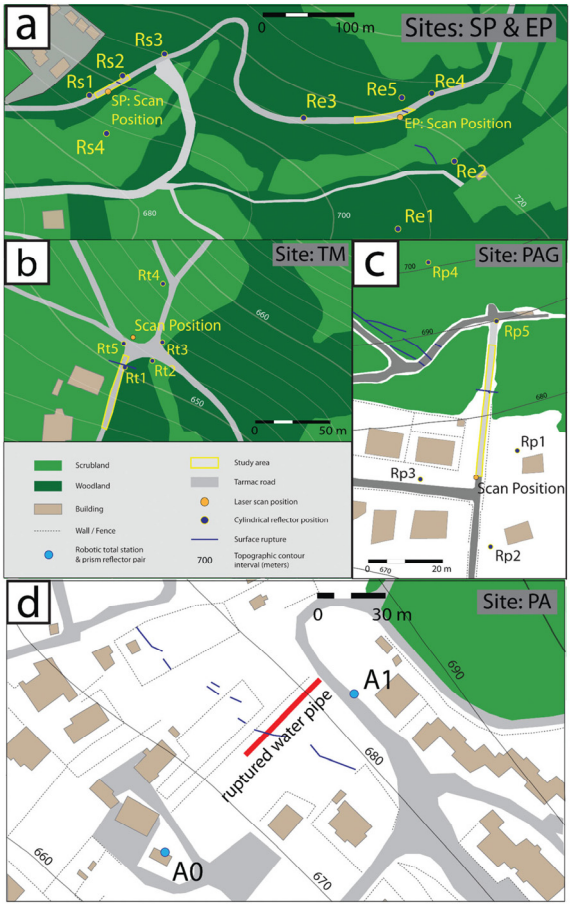

Figure 3. (a–d) Local maps for sites SP and EP, TM, PAG and PA. Land use depicts line of sight restrictions on the reflector network and the extent of the study areas.

vertical displacement observable to the eye in the field. Five scans were acquired at 10, 38, 42, 46 and 125 d after the earthquake of a 9 m × 84 m area, comprising the hangingwall, rupture and footwall. Surface generation and vertical differencing show a trough within the first 4 m of the hangingwall (Fig. 6b: −18 m to −22 m distance from the scanner) that developed between scans EP1 and EP2, along with tilting of the hangingwall towards the rupture between 4 and 50 m from the rupture (−18 m to 50 m distance from the scanner). Hangingwall tilting was contemporaneous with uplift of up to 20 mm at 72 m from the rupture (50 m distance from the scanner). A period of quiescence followed, with little or no change in the surface between EP2 and EP4, except for 2 mm subsidence of the hangingwall from its tilted position. The final scan EP5, acquired 125 d after the earthquake shows significant downthrow of the entire hangingwall by 10.8 ± 3 .8 mm relative to EP1, with additional subsidence of 4.6 mm, creating a hangingwall trough 48 m from the rupture (5–50 m distance from the scanner; Fig. 6b). 10.8 mm of afterslip was observed between 10 and 125 d by projecting the tilted hangingwall into the rupture. The combined magnitude of vertical post-seismic deformation between 10 and 125 d is 15.4 ± 3.1 mm, representing the sum of the maximum afterslip observed (10.8 mm) combined with the observed subsidence of the hangingwall trough (4.6 mm) over the same period. A network of five reflectors (Re1–Re5, Fig. 3a) paired across the rupture were used to measure a horizontal deformation of 20.3 ± 5.0 mm, between 10 and 125 d, resolved in the direction of the coseismic slip vector.

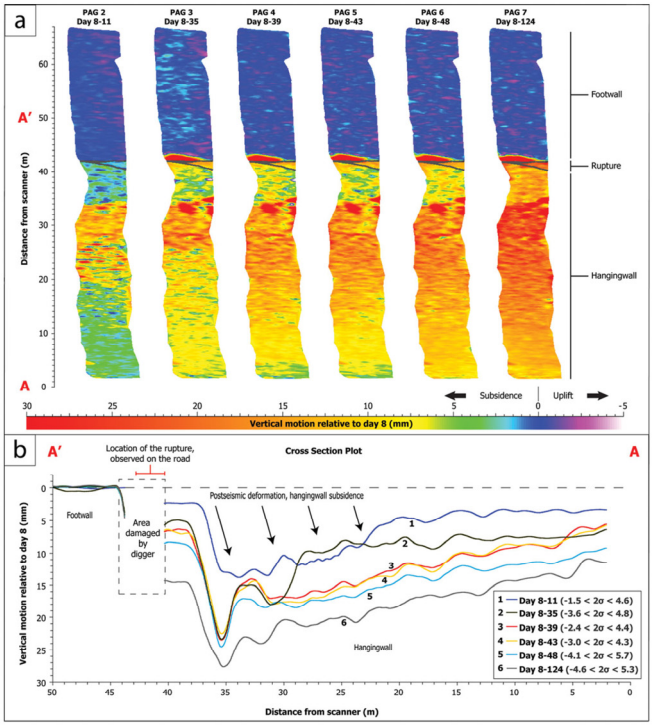

Figure 4. Post-seismic deformation result for site PAG. (a) Colour map plot of vertical deformation (mm) in a footwall static reference frame for subsequent TLS data sets, relative to the initial data set acquired at the site. (b) Cross-sectional plot of the surface deformation between A and A' in (a).

The components of post-seismic deformation of each surface relative to the first are shown in Fig. 8(c). They describe deformation increasing at a decaying rate, indicative of afterslip and near-field post-seismic deformation.

3.4 Site: TM

Site TM is located towards the northwest end of the surface rupture, on the outskirts of the village of Tempera (Fig. 2). The study site is a rough tarmac road (Fig. 3b), 4 m × 51 m, comprising the Paganica surface rupture, hangingwall and footwall. The surface rupture consists of a single crack cross cutting the tarmac road. As observed 12 d after the earthquake, the crack had a horizontal displacement of 8–12 mm, with no vertical offset observable by eye in the field. The site was scanned six times, (12, 37, 41, 44, 47 and 124 d) after the earthquake (TM1–TM6, Table 1). Surface fitting and vertical differencing revealed vertical deformations mostly below the precision of the method (Fig. 7: -2.8 mm $< \pm 2\sigma < 2.8$ mm), suggesting that minimal vertical post-seismic deformation occurred at the site. Most of the vertical deformations are, however, downward and appear to create a subtle depression in the hangingwall between 33 and 63 m distance from the scanner. Values for rupture afterslip were calculated using the vertical deformation of the road in the immediate hangingwall of the rupture. The maximum observed afterslip was 2.4 ± 2.8 mm, occurring between 12 and 124 d after the earthquake. A network of five reflectors paired across the rupture was used to calculate the horizontal component of post-seismic deformation. The horizontal post-seismic deformation observed between 12 and 124 d was 3.2 ± 5.0 mm. The components of post-seismic deformation over the survey period (Fig. 8d) describe deformations below the precision of the method, suggesting little or no post-seismic deformation occurred at this site.

3.5 Site: PA

Site PA is located 400 m northwest of site PAG (Fig. 2). A 40 bar water pipe crosses the Paganica fault at this site and ruptured during the April 6 earthquake and also subsequently, following repair, at 06:00 on April 19. The immediate area of the water pipe was heavily excavated by water leaking the pipe at high pressure following rupture during the April 6 earthquake. Although those sediments, which may have been ruptured, were washed away, surface ruptures remain in the immediate area along strike with coseismic displacements of 10–15 cm (Vittori *et al.* 2011). At this site, we summarize

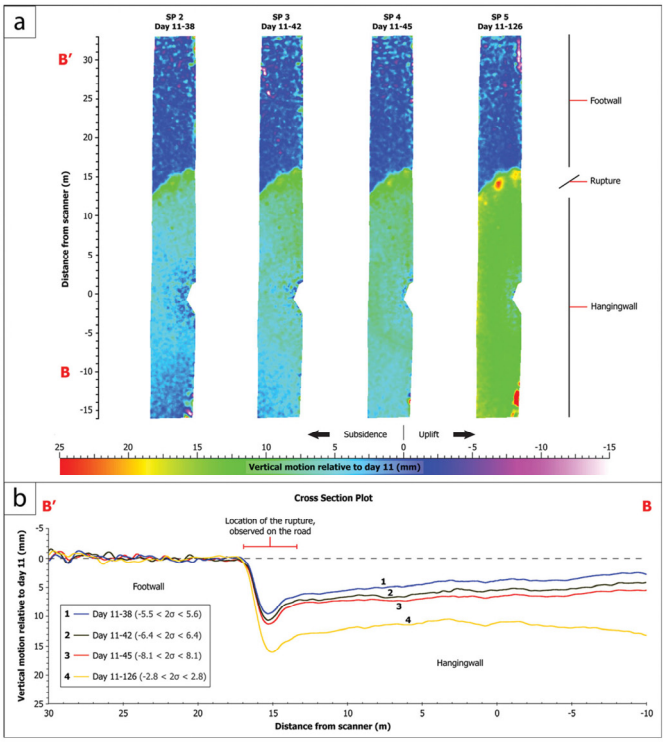

Figure 5. Post-seismic deformation result for site SP. (a) Colour map plot of vertical deformation (mm) in a footwall static reference frame for subsequent TLS data sets, relative to the initial data set acquired at the site. (b) Cross-sectional plot of the surface deformation between B and B' in (a).

data (with permission) from the Geological Survey of Trentino (Degasperi 2010). The Geological Survey installed a Leica TCA2003 automatic total station 63 m in the hangingwall of the rupture (Fig. 3d: point A0). The total station was paired with a staked prism 40 m in the footwall (Fig. 3d: point A1) and set to record the distance to the prism at regular intervals with a precision ± 1.1 mm (1.0 mm +1ppm over ∼100 m distance). The vertical and horizontal components of post-seismic deformation between 17 and 330 d after the earthquake were calculated by comparing subsequent vertical and horizontal distances to the initial measurement. We use the six measurements from 17, 31, 44, 65, 85 and 114 d (Table 1, PA1–PA6), as they span the same time period as the TLS surveys. The data following day 114 show little or no additional post-seismic deformation. The vertical post-seismic deformation observed between 17 and 114 d was 13.8 ± 1.1 mm. The maximum horizontal post-seismic deformation observed was 10.1 ± 1.1 mm over the same period. The measurements of vertical and horizontal deformation increase with a decreasing rate over the study period, indicative of afterslip and near-field post-seismic deformation.

4 DISCUSSION

4.1 Surface change detection

We were able to measure the vertical difference between modelled surfaces with an average precision of ∼3 mm. The selection of smooth road surfaces and close proximity to the scanner produced point cloud data sets of high density and low noise. The figure for average precision was obtained mainly due to the use of the DSI interpolation method and the fact that noise within the point cloud, produced by clock-time errors for two-way traveltime, has a Gaussian distribution about the mean, representing a close approximation to the actual surface. The precision of any repeat scan method is dependent on the precision of the scanner as well as the range, roughness and incidence of the surface to be scanned. An important consideration is that the angle of laser incidence on the road surface becomes progressively more acute with increasing range, assuming the scanner is oriented vertical, looking down the road surface. This increase in incidence with range has the effect of degrading the precision of the returns and increasing the point spacing of the acquired data set. Although the Riegl LMS-z420i

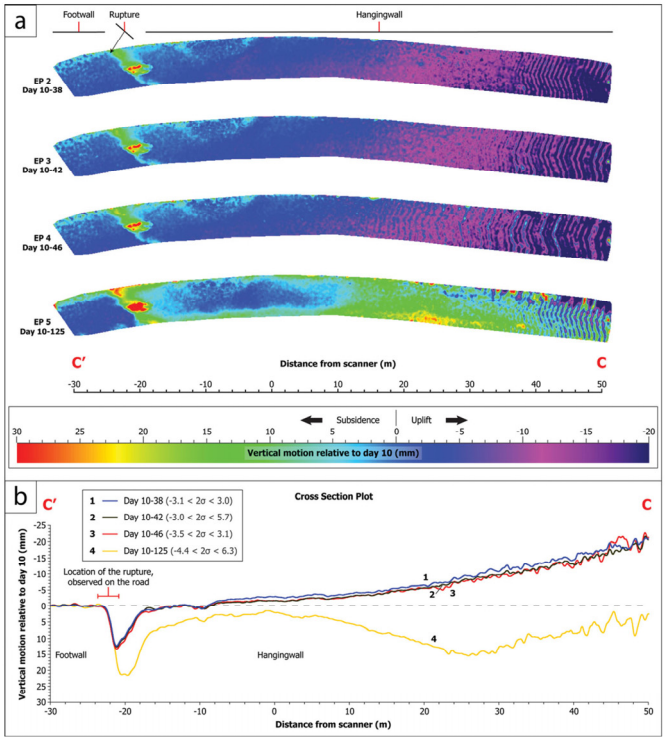

Figure 6. Post-seismic deformation results for site EP. (a) Colour map plot of vertical deformation (mm) in a footwall static reference frame for subsequent TLS data sets, relative to the initial data set acquired at the site. (b) Cross-sectional plot of the surface deformation between C and C' in (a).

has an effective range of 1000 m, we found that due to the effects of reduced incidence at range, repeat scan precision on the order of ∼3 mm could only be obtained for the road sites we selected at distances of up to 50 m. For this study, precisions range from ±1.2 to 8.1 mm (2σ variation of a moving point average based on a rupture parallel moving window of 250 triangle vertices). 'Min $< 2\sigma <$ Max' bounds in Figs 4(b)–7(b) represent the range of certainty in vertical deformation for each cross-sectional plot, which changes along section due to variations in the smoothness of the road. The precision of horizontal deformation measured using the reflector-pair method is ±5.0 mm, due to a precision of ±2.5 mm in the position of a single cylindrical reflector.

4.2 Post-seismic deformation at L'Aquila

Post-seismic surface deformation, including both horizontal and vertical components increased over time at sites PAG, SP, EP and PA (Fig. 8). The rate of deformation declined over our observation period, and is consistent with rate decay laws for afterslip within the fault zone (e.g. Marone *et al.* 1991). In contrast, little deformation, beyond the precision of our method was observed at site TM (Fig. 8d). The location of the five study sites along the Paganica surface rupture (Fig. 2) allowed us to analyse the along-fault distribution of the post-seismic deformation following this earthquake.

The surface expression of rupture afterslip and near-field post-seismic deformation is not consistent along the surface rupture and is highly variable over short distances. The magnitude of the vertical and horizontal components of post-seismic deformation between 8 and 44 d (or the closest measurement dates available at each site) is shown for the five sites in Fig. 9(a). The greatest vertical and horizontal post-seismic deformation over this period occurred at site PAG (22.5 ± 3.3 mm and 16.4 ± 5 mm, respectively), towards the centre of the surface rupture. The observed vertical and horizontal components of post-seismic deformation decrease from site PAG towards sites TM and EP at the NW and SE ends of the rupture, respectively. The vertical and horizontal components of post-seismic deformation between 8 and 126 d (or the closest measurement dates available at each site) is shown for the five sites in Fig. 9(b). The maximum observed vertical and horizontal components of post-seismic deformation are still observed at PAG, with the exception of the horizontal deformation observed at SP. The relative change in the components of post-seismic deformation between 44 and 126 d

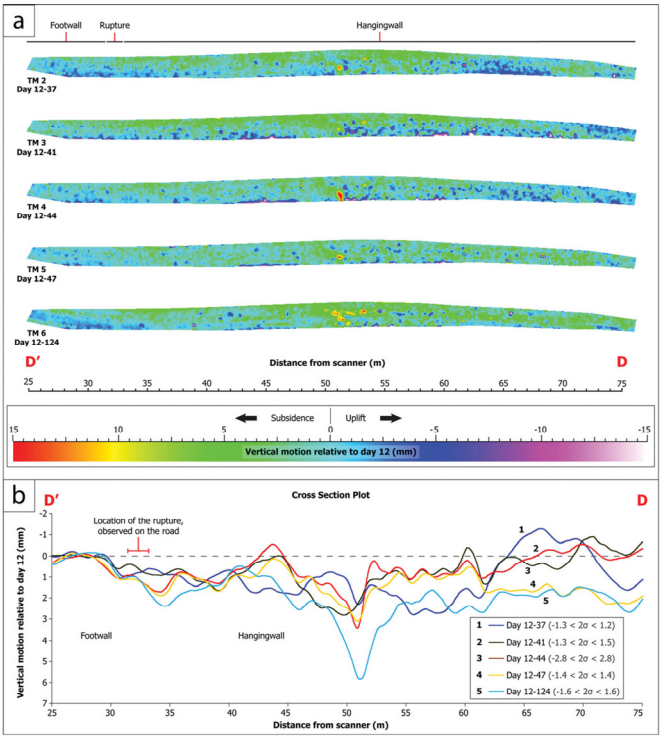

Figure 7. Post-seismic deformation results for site TM. (a) Colour map plot of vertical deformation (mm) in a footwall static reference frame for subsequent TLS data sets, relative to the initial data set acquired at the site. (b) Cross-sectional plot of the surface deformation between D and D' in (a).

is shown in Fig. 9(c). There is a significant increase in deformation over this time period towards the southeastern end of the rupture, observed at sites SP and EP, whereas deformation at TM to the northwest remains low. The vertical and horizontal components of deformation observed at SP increase by 5.4 and 11.1 mm between 42 and 126 d, whereas the vertical and horizontal components of deformation observed at EP increase by 14.2 and 4.4 mm between 42 and 126 d. In comparison the vertical and horizontal components of post-seismic deformation at PAG, towards the centre of the rupture increased by 5.2 and 5.4 mm, respectively.

To illustrate this relative increase in post-seismic deformation at the southeastern end of the rupture, we plotted the maximum observed post-seismic deformation at each site alongside published estimates for the coseismic slip within the fault zone (Fig. 10). The theory of afterslip (Marone *et al.* 1991) dictates that afterslip is driven by coseismic slip deficits (high gradients in coseismic slip) within the fault zone at depth. The unconsolidated material within the fault zone is thought to respond to equilibrate differential shear stresses in the fault zone by the process of gradual creep over time. This behaviour is thought to be responsible for the characteristic decaying rate of afterslip motion observed on surface ruptures. Through the comparison of coseismic and post-seismic fault slip maps produced using far-field GPS data, Cheloni *et al.* (2010) suggested that post-seismic deformation is greatest in regions where shear stress are highest, produced by large gradients in coseismic slip. We plot the coseismic slip within the fault zone sampled at horizontal transects at 1.5 and 3.5 km depth along the length of the fault using values from a modelled coseismic fault slip map inferred from coseismic GPS motions (Cheloni *et al.* 2010; Figs 10a and b). We plot the mean of horizontal and vertical components of the maximum observed post-seismic deformation for each of the five study sites. To directly compare our surface measurements to the modelled coseismic slip within the fault plane, we resolved these magnitudes onto the modelled 54° dipping fault plane, (Table 2, columns 5, 6 and 7 and Fig. 10b, yellow circles). We note that sites SP and EP at the southeastern end of the rupture, where significant increases in post-seismic deformation were observed between 44 and 126 d, are located above a region in the fault zone where the gradient of coseismic slip is high at 3.5 km depth (28 cm change in coseismic slip per km distance along the fault). Sites PA and

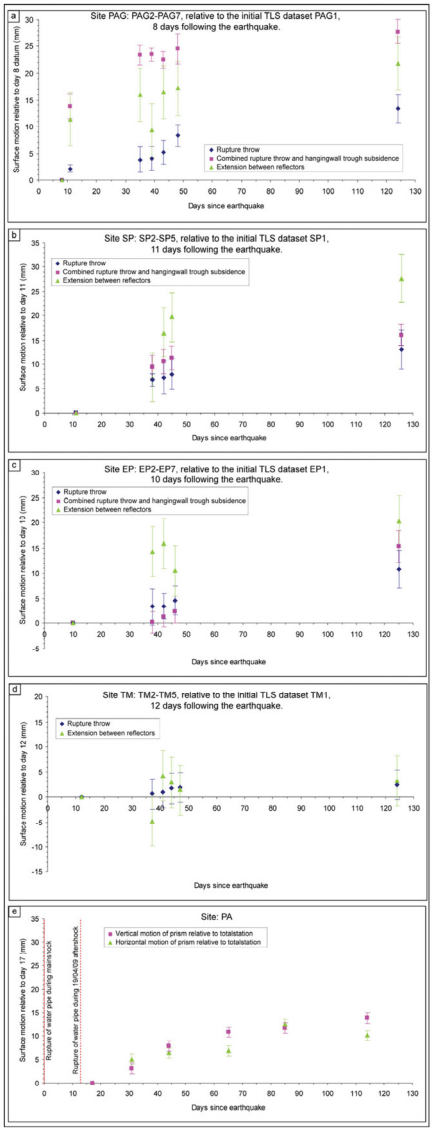

Figure 8. (a–d) Post-seismic deformation measurements for each TLS data set relative to the initial data set, plotted against time since the earthquake. Error bars represent 2σ certainty. (e) Site PA: Horizontal and vertical components of the change in distance between points A0 and A1 (Fig. 3b), relative to the first measurement at day 17.

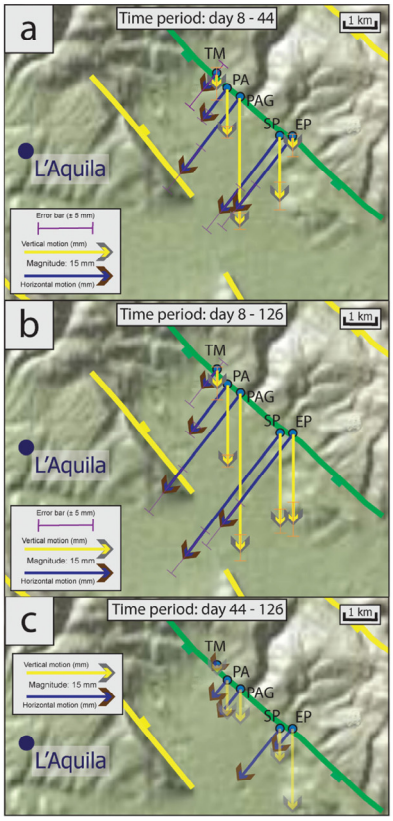

Figure 9. Map distribution of the horizontal and vertical components of post-seismic deformation observed at the five study sites over the period: (a) 8–44 d, (b) 8–126 d and (c) 44–126 d. Arrow lengths and error bars for each measurement scaled from those shown in the legend. The green line represents the inferred subsurface trace of the Paganica fault.

TM which experienced relatively lower values of post-seismic deformation are located above a region where the coseismic slip gradient is of a lesser value at 3.5 km depth (10 cm change in coseismic slip per km distance along the fault). The correlation between the coseismic slip gradient and the increased magnitude of on-rupture post-seismic deformation between 44 and 126 d provides near-field evidence to support the suggestion by Cheloni *et al.* (2010) that post-seismic deformation is driven by high gradients in coseismic slip within the fault zone. A coseismic slip map produced by Atzori *et al.* (2009) from a coseismic interferogram also shows a similar signal of high coseismic slip gradient. We chose not to include this slip map in our analysis as the cell size is slightly greater than the spacing between our sites. The difference in post-seismic deformation between our study sites suggests post-seismic

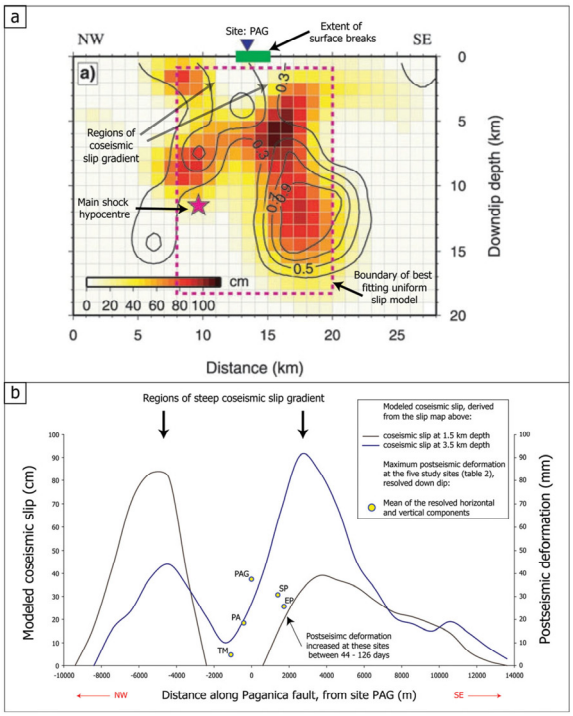

Figure 10. (a) Modelled coseismic fault slip map from Cheloni *et al.* (2010). The contours represent coseismic slip in metres. (b) Plot of the coseismic slip at 1.5 and 3.5 km depth within the fault zone and the maximum observed post-seismic deformation at each study site. The precise positions of peaks in coseismic slip will be affected by the errors estimated through Monte Carlo simulation (see Cheloni *et al.* 2010, supplementary material).

Table 2. The maximum vertical and horizontal components of post-seismic deformation, as observed and resolved as slip in a 54° dipping fault zone.

Site	Survey time frame (days after earthquake)	Maximum observed vertical post-seismic deformation (mm)	Maximum observed horizontal post-seismic deformation (mm)	Maximum observed vertical post-seismic deformation, resolved downdip (mm)	Maximum observed horizontal post-seismic deformation, resolved downdip (mm)	Mean of resolved vertical and horizontal components (mm)
PAG	8–124	27.7	21.8	47.1	26.9	37.0
SP	11–126	16.0	27.6	27.2	34.1	30.7
EP	10–125	15.4	20.3	26.2	25.1	25.7
TM	12–124	2.4	4.2	4.1	5.2	4.7
PA	17–114	13.8	10.1	23.5	12.5	18.0

deformation occurs as a response to a complex pattern of coseismic slip, which produces spatially varying stresses within the fault zone.

The maximum horizontal and vertical components of post-seismic deformation observed in the far field using GPS (Cheloni *et al.* 2010) are 9 mm towards south-southwest (site: AQUI) and 50 mm downward (site: PAGA), respectively (Fig. 1, black arrows). The three areas of maximum line of sight post-seismic displacement (PS, CT and OF) identified by Lanari *et al.* (2010) using SBAS-DInSAR are downward 35, 26 and 18 mm, respectively (Fig. 1, yellow dots, PS, CT and OF). These far-field post-seismic measurements are not significantly greater than the near-field deformation we have measured at sites PAG, PA, SP and EP. This comparison suggests that far-field post-seismic deformation can be attributed to the propagation of near-field post-seismic deformation of similar magnitude. Modelling the propagation of near-field post-seismic deformations into the far field is required to rigorously test this hypothesis, which was beyond the scope of this paper.

5 CONCLUSION

The use of repeat TLS at four sites along the L'Aquila earthquake surface rupture allowed post-seismic deformation on the order of ∼3 mm to be observed at distances of up to 50 m from the laser scanner. The TLS data was complemented by total station data from a fifth site. The measurements of post-seismic deformation from sites PAG, SP, EP and PA show an increase over time with decreasing rate, indicative of afterslip within the fault zone. Surface deformation observed at site TM are within the precision of the method and deemed insignificant. A relative increase in post-seismic deformation was observed between 44 and 126 d at sites SP and EP towards the southeastern end of the rupture. We attribute this increase to a high gradient of coseismic slip within the fault zone beneath these sites and suggest the increase in deformation is driven by increased shear stresses in this part of the fault zone. We note that the magnitude of far-field post-seismic deformation, measured using GPS and InSAR is not significantly greater that the near-field deformation we measured at distances up to 50 m of the rupture. We suggest that localized afterslip within the fault zone, driven by increased shear stresses in regions of high coseismic slip gradient is responsible for the majority of post-seismic deformation on all scales.

ACKNOWLEDGMENTS

Funded by NERC grants NE/H003266/1 and NE/E016545/1 and Durham University Doctoral Fellowship (MW). We thank N. De Paola, A. Yates, A. Bubeck and G. Sileo for assistance in the field, also D. Stevenson and G. Wilkinson for IT support. Two anonymous reviewers and the editor Duncan Agnew are thanked for their thorough comments which greatly improved the manuscript.

REFERENCES

Amoruso, A. & Crescentini, L., 2009. Slow diffusive fault slip propagation following the 6 April 2009 L'Aquila earthquake, Italy, *Geophys. Res. Lett.,* **36,** L24306, doi:10.1029/2009GL041503.

Atzori, S. *et al*., 2009. Finite fault inversion of DInSAR coseismic displacement of the 2009 L'Aquila earthquake (central Italy), *Geophys. Res. Lett.,* **36,** L15305, doi:10.1029/2009GL039293.

Boncio, P., Pizzi, A., Brozzetti, F., Pomposo, G., Lavecchia, G., Di Naccio, D. & Ferrarini, F., 2010. Coseismic ground deformation of the 6 April 2009 L'Aquila earthquake (central Italy, Mw6.3), *Geophys. Res. Lett.,* **37,** L06308, doi:10.1029/2010GL042807.

Cheloni, D. *et al*., 2010. Coseismic and initial post-seismic slip of the 2009 M-w 6.3 L'Aquila earthquake, Italy, from GPS measurements, *Geophys. J. Int.,* **181**(3), 1539–1546, doi:10.1111/j.1365-246X.2010.04584.x.

Degasperi, M., 2010. *Relazione sui monitoraggi nella zona di Paganica*. Provincia Autonoma di Trento, Servizio Geologico, Report Marzo 2010. Available at: http://www.protezionecivile.tn.it/geologico/images/Notizie2010/abruzzo/report_03_2010+ALL.pdf (last accessed 2011 July).

Falcucci, E. *et al*., 2009. The Paganica Fault and surface coseismic ruptures caused by the 6 April 2009 earthquake (L'Aquila, Central Italy), *Seismol. Res. Lett.,* **80**(6), 940–950, doi:10.1785/gssrl.80.6.940.

Gold, P.O. *et al*., 2010. Analyses of coseismic surface rupture from the 4 April 2010 El Mayor-Cucapah earthquake using terrestrial LiDAR, *GSA Abstr. Prog.,* **42**(5), 177.

Kayen, R., Pack, R.T., Bay, S., Sugimoto, S. & Tanaka, H., 2006. Terrestrial-LIDAR visualization of surface and structural deformations of the 2004 Niigata Ken Chuetsu, Japan Earthquake, *Earthq. Spectra J.,* **22**(S1), S147–S162.

Lanari, R. *et al*., 2010. Surface displacements associated with the L'Aquila 2009 Mw 6.3 earthquake (central Italy): new evidence from SBAS-DInSAR time series analysis, *Geophys. Res. Lett.,* **37,** L20309, doi:10.1029/2010GL044780.

Mallet, J.L., 1992. GOCAD: a computer aided design program for geological applications, in *Three Dimensional Modeling With Geoscientific Information Systems*, pp. 123–141, ed. Turner A.K., Kluwer, Netherlands.

Marone, C.J., Scholtz, S.H. & Bilham, R., 1991. On the mechanics of Earthquake Afterslip, *J. geophys. Res. Solid Earth,* **96,** 8441–8452.

Michetti, A.M., Serva, L. & Vittori, E., 2000. Italy hazard from capable faulting, a database of active capable faults of the Italian onshore territory, 32nd Int. Geol. Congress, Rio de Janeiro, August 2000. Internal report of Agenzia Nazionale Protezione Ambiente, Roma (CD).

Roberts, G.P., 2008. Vizualisation of active normal fault scarps in the Apennines, Italy: a key to assessment of tectonic strain release and earthquake rupture, *J. Virtual Explorer,* **30, 4**, doi:10.3809/jvirtex.2008.00197.

Vittori, E. *et al*., 2011. Surface faulting of the April 6th 2009 Mw 6.3 L'Aquila earthquake in central Italy, *Bull. seism. Soc. Am.,* **101,** 1507–1530.

Walters, R.J. *et al*., 2009. The 2009 L'Aquila earthquake (central Italy): a source mechanism and implications for seismic hazard, *Geophys. Res. Lett.,* **36,** L17312, doi:10.1029/2009GL039337.

Wilkinson, M. *et al*., 2010. Partitioned postseismic deformation associated with the 2009 Mw 6.3 L'Aquila earthquake surface rupture measured using a terrestrial laser scanner, *Geophys. Res. Lett.,* **37,** L10309, doi:10.1029/2010GL043099.